GOTTFRIED WILHELM LEIBNIZ UNIVERSITÄT HANNOVER

DOCTORAL THESIS

Metamodel-based uncertainty quantification for the mechanical behavior of braided composites

Von der Fakultät für Bauingenieurwesen und Geodäsie
der Gottfried Wilhelm Leibniz Universität Hannover
zur Erlangung des akademischen Grades

Doktor-Ingenieur (Dr.-Ing.)

genehmigte Dissertation
von

Georgios Balokas M.Sc.

March 24, 2022

Referent: Prof. Dr.-Ing. habil. Raimund ROLFES, Leibniz Universität Hannover
Korreferent: Assoc. Prof. Dr. Marco PETROLO, Politecnico di Torino
Tag der Promotion: 11.03.2022

To my beloved parents, who had almost nothing, but gave me everything...

To my admirable brother, the one and only true doctor...

GOTTFRIED WILHELM LEIBNIZ UNIVERSITÄT HANNOVER

Abstract

Metamodel-based uncertainty quantification for the mechanical behavior of braided composites

The main design requirement for any high-performance structure is minimal dead weight. Producing lighter structures for aerospace and automotive industry directly leads to fuel efficiency and, hence, cost reduction. For wind energy, lighter wings allow larger rotor blades and, consequently, better performance. Prosthetic implants for missing body parts and athletic equipment such as rackets and sticks should also be lightweight for augmented functionality. Additional demands depending on the application, can very often be improved fatigue strength and damage tolerance, crashworthiness, temperature and corrosion resistance etc. Fiber-reinforced composite materials lie within the intersection of all the above requirements since they offer competing stiffness and ultimate strength levels at much lower weight than metals, and also high optimization and design potential due to their versatility. Braided composites are a special category with continuous fiber bundles interlaced around a preform. The automated braiding manufacturing process allows simultaneous material-structure assembly, and therefore, high-rate production with minimal material waste.

The multi-step material processes and the intrinsic heterogeneity are the basic origins of the observed variability during mechanical characterization and operation of composite end-products. Conservative safety factors are applied during the design process accounting for uncertainties, even though stochastic modeling approaches lead to more rational estimations of structural safety and reliability. Such approaches require statistical modeling of the uncertain parameters which is quite expensive to be performed experimentally. A robust virtual uncertainty quantification framework is presented, able to integrate material and geometric uncertainties of different nature and statistically assess the response variability of braided composites in terms of effective properties. Information-passing multiscale algorithms are employed for high-fidelity predictions of stiffness and strength. In order to bypass the numerical cost of the repeated multiscale model evaluations required for the probabilistic approach, smart and efficient solutions should be applied. Surrogate models are, thus, trained to map manifolds at different scales and eventually substitute the finite element models. The use of machine learning is viable for uncertainty quantification, optimization and reliability applications of textile materials, but not straightforward for failure responses with complex response surfaces. Novel techniques based on variable-fidelity data and hybrid surrogate models are also integrated.

Uncertain parameters are classified according to their significance to the corresponding response via variance-based global sensitivity analysis procedures. Quantification of the random properties in terms of mean and variance can be achieved by inverse approaches based on Bayesian inference. All stochastic and machine learning methods included in the framework are non-intrusive and data-driven, to ensure direct extensions towards more load cases and different materials. Moreover, experimental validation of the adopted multiscale models is presented and an application of stochastic recreation of random textile yarn distortions based on computed tomography data is demonstrated.

GOTTFRIED WILHELM LEIBNIZ UNIVERSITÄT HANNOVER

Kurzfassung

Metamodell-basierte Unsicherheitsquantifizierung des mechanischen Verhaltens von geflochtenen Faserverbundwerkstoffen

Die wichtigste Entwurfsanforderung für jede Hochleistungsstruktur ist ein möglichst geringes Eigengewicht. In der Luft- und Raumfahrt- sowie der Automobilindustrie führen leichtere Strukturen direkt zur Erhöhung der Treibstoffeffizienz und damit zur Senkung der Kosten. Bei der Windenergie ermöglicht eine leichtere Bauweise die Anwedung von längeren Rotorblättern und führt somit zu einer gesteigerten Leistung. Prothetische Implantate für fehlende Körperteile und Sportgeräte, wie z.B. Schläger, sollen ebenfalls leicht sein, um deren Funktionalität zu erhöhen. Zusätzliche Anforderungen sind beispielsweise, je nach Anwendung, eine verbesserte Ermüdungsfestigkeit und Schadenstoleranz, Crashfestigkeit, sowie Temperatur- und Korrosionsbeständigkeit. Faserverbundwerkstoffe liegen im Schnittpunkt all dieser Anforderungen, da sie vergleichbare Steifigkeits- und Festigkeitsniveaus bei viel geringerem Gewicht im Vergleich zu Metallen anbieten und aufgrund ihrer Vielseitigkeit ein hohes Optimierungs- und Entwurfspotenzial aufweisen. Eine besondere Unterkategorie der Faser-Kunststoff-Verbunde sind Geflechte, bei denen kontinuierliche Faserbündel um eine Vorform geflochten werden. Das automatisierte Herstellungsverfahren für Geflechte ermöglicht den gleichzeitigen Aufbau von Material und Struktur und damit eine hohe Produktionsrate bei minimalem Materialabfall.

Die mehrstufigen Materialprozesse und die intrinsische Heterogenität sind die Hauptursachen für die Variabilität, welche bei der mechanischen Charakterisierung und der Verwendung von Verbundwerkstoff-Endprodukten vorliegt. Während des Entwurfsprozesses werden konservative Sicherheitsfaktoren angewandt, welche Unsicherheiten berücksichtigen, obwohl stochastische Modellierungsansätze zu rationaleren Schätzungen der Tragfähigkeit und Zuverlässigkeit führen. Solche Ansätze erfordern eine statistische Modellierung der Zufallsparameter, welche in der Regel unter hohen Kosten experimentell bestimmt werden müssen. Es wird ein robustes, virtuelles Framework zur Quantifizierung von Unsicherheiten dargestellt, welches in der Lage ist, materielle und geometrische Unsicherheiten unterschiedlicher Art zu berücksichtigen und die Antwortvariabilität von geflochtenen Verbundwerkstoffen im Hinblick auf die effektiven Eigenschaften statistisch zu bewerten. Für die zuverlässige Vorhersage von Steifigkeit und Festigkeit werden informationsübertragende Multiskalenalgorithmen eingesetzt. Um den numerischen Aufwand der wiederholten Multiskalenmodellauswertungen, welche für den probabilistischen Ansatz erforderlich sind, zu umgehen, sollen intelligente und effiziente Lösungen angewandt werden. Ersatzmodelle werden daher trainiert, um Mannigfaltigkeiten in verschiedenen Maßstäben abzubilden und schließlich die Finite-Elemente-Modelle zu ersetzen. Der Einsatz von maschinellem Lernen ist zwar für die Quantifizierung von Unsicherheiten, die Optimierung und die Zuverlässigkeitsbewertung von textilen Materialien vernünftig, aber für Versagensreaktionen mit komplexen Anwortflächen nicht trivial. Neuartige Techniken basierend auf Daten mit variabler Genauigkeit und hybriden Ersatzmodellen werden ebenfalls berücksichtigt.

Die Zufallsparameter werden anhand ihrer Bedeutung für die entsprechende Antwort mittels varianzbasierter globaler Sensitivitätsanalyseverfahren klassifiziert. Die Quantifizierung der Zufallsparameter in Bezug auf Mittelwert und Varianz kann durch inverse Ansätze auf der

Grundlage der Bayes'schen Inferenz erreicht werden. Alle stochastischen und maschinellen Lernmethoden, die in dem dargestellten Framework angewendet werden, sind nicht-intrusiv und datengesteuert, um eine direkte Erweiterung für weitere Lastfälle und unterschiedliche Materialien zu ermöglichen. Darüber hinaus wird die experimentelle Validierung der verwendeten Multiskalenmodelle vorgestellt und eine Anwendung der stochastischen Rekonstruktion zufälliger Textilgarnverformungen auf der Grundlage von Computertomographiedaten demonstriert.

Acknowledgements

This dissertation signifies the end of my PhD journey. A worthwhile, rewarding and life-changing journey. I am grateful to several people for this. First, I would like to express my gratitude to Prof. Raimund Rolfes for the guidance, motivation and the discussions we had over the years. I believe we had a fruitful and professional collaboration characterized by mutual respect. I would also like to thank the rest of the committee, Assoc. Prof. Marco Petrolo, Prof. Michael Beer and Prof. Andreas Reuter. Special thanks to Marco for writing the report and for being available at all times.

I was extremely lucky to work with two amazing people throughout my PhD who contributed massively to the quality of this work. The first is Dr.-Ing. Steffen Czichon, the man who brought me to Germany in 2016. Steffen was crucial in constructing the research topic of the thesis and, generally, he helped me evolve as a researcher and a professional. His leading and problem-solving skills were extremely motivational. He has my appreciation for his big contribution to my doctoral studies. The second person is Prof. Benedikt Kriegesmann with whom I started collaborating during the second year of my PhD. Benedikt contributed greatly to the technical quality of my thesis with his knowledge in composite materials and probabilistic simulation. I truly admire and appreciate his devotion to science, his enthusiasm, but also the rare talent he has to take anything (text, idea, script etc.) and make it better. Overall, meeting these two persons, who happen to be very good friends and also graduates from the institute of Prof. Rolfes, is one of the best things that happened to me.

Furthermore, thanks to all the people I met and interacted with in my working environments. My colleagues at ELAN-AUSY, my colleagues at TUHH, my project partners during the FULLCOMP project and my hosts at ENSAM Bordeaux. I would also like to thank all the anonymous reviewers of my publications for their comments. Special thanks to Sven Drücker, Johann Körbelin and Niklas Reuter from TUHH for all the help with the testing of my braided specimens. Also, special thanks to my good friend Antonis Armiriotis for helping me with some challenging CAD drawings for the thesis and for his moral support.

Last but not least, I would like to thank my family (Tasos, Sofia and Sotiris) and friends for encouraging me, supporting me but also enduring me all these years of my academic career. This dissertation is dedicated to them.

Hamburg, March 2022 Georgios Balokas

Contents

"Statistical thinking will one day be as necessary for efficient citizenship as the ability to read and write."

H. G. Wells (1866-1946)

Chapter 1

General Introduction

1.1 Introduction and motivation

The current market circumstances are driving the main engineering focus towards cost and process optimization, while concurrently the requirement for lightweight structures with high reliability remains a target. Reducing weight is advantageous in multiple ways, such as fuel efficiency and carbon dioxide emission minimization for aerospace and automotive industries, but also the possibility for larger structures for the wind turbine industry. Additionally, requirements like temperature, fire and corrosion resistance, energy absorption and damage tolerance apply to numerous high-performance structures.

It is clearly not elementary to capture all these aspects from a material point of view. Fiber-reinforced composite materials, however, have the biggest prospect to achieve the above and have, thus, been studied and evolved widely over the last 30-40 years. The combination of highly anisotropic fibers carrying most of the load, with a ductile matrix made of polymeric materials preserving the fiber architecture and protecting the fibers from environmental effects, creates a versatile orthotropic material with high optimization potential. As a result, composite parts are continuously substituting metal parts within industrial applications, since they provide higher stiffness-to-weight and strength-to-weight ratios.

Braided composites belong to the category of textiles or 3D composites and combine structural stability, low cost, as well as attractive damage tolerance and energy absorption abilities. Braiding is defined as a composite material preform manufacturing technique, where a braiding machine deposits continuous, interwined fiber bundles to create desired reinforcing braid architectures before or during the impregnation of the fibers. The mixture of an automated and reproducible process, along with an excellent rate of material deposition for mass-production, has created a plethora of applications in different industrial sectors, such as aeronautics, automotive, civil engineering, medicine and athletics. Relevant examples of braided applications are shown in Fig.1.1.

A convoluted topic for composite design, however, is the presence of uncertainties associated with material heterogeneity and the production processes they encounter. The influence of those uncertainties on the characterization and mechanical response of composites cannot be addressed rigorously via traditional deterministic approaches. In fact, it is rather inefficient to rely on conservative safety factors provided by design codes for a material with such high utilization and exploitation potential. Probabilistic modeling approaches are more appropriate for rational estimations of structural safety and reliability. The main obstacle preventing the global approval of such methods is the need for quantification of all the uncertain parameters involved. The latter would require extensive experimental campaigns and online monitoring of the manufacturing for a direct statistical modeling based on measurements. A practical solution would be the development of virtual uncertainty quantification frameworks, able to integrate

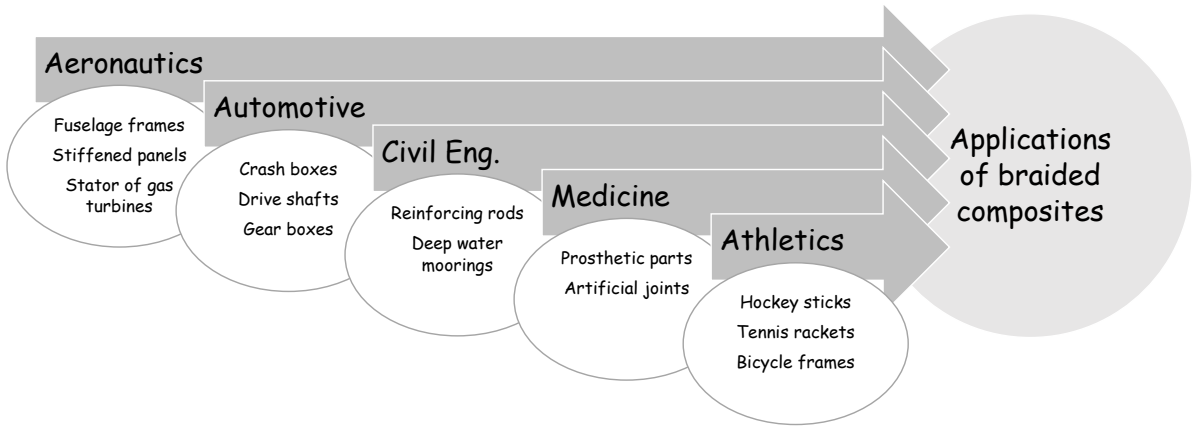

FIGURE 1.1: Sectors of applications for braided composite materials.

the stochastic variability of the material properties and design parameters while statistically assessing the mechanical response.

A further challenge, however, is to develop probabilistic frameworks for complex structures and materials that demand a lot of computational resources for high-fidelity modeling. Braided composites belong to the latter category due to their complicated architecture which can be reliably tacked solely with multiscale modeling. Taking into account the already elevated cost of stochastic analyses due to repeated random simulations, it is evident that smart techniques able to reduce the numerical effort are necessary. Machine learning models consist a valuable tool in this direction, since they can be used as surrogates substituting the demanding numerical simulations in the probabilistic routines, when they are sufficiently trained. A small amount of data required for training is the total numerical cost in this case. This synergy between high-fidelity multiscale modeling, probabilistic methods and machine learning shall be further studied and exploited to efficiently quantify the uncertainties and their effect in braided composite materials and textiles in general.

1.2 State of the art

This section presents a literature review on the modeling of textile composites from the perspective of simulation techniques and uncertainty evaluation, with a special focus on braided composites. The chapter is divided into two parts: first an overview of multiscale methods, manufacturing processes, and mechanical properties prediction, and then applications of uncertainty quantification and machine learning methods.

1.2.1 Textile and braided composites

Modeling of textile composites

Textile or 3D composites have been available and operational for several decades already but still remain one of the most active engineering research topics. Analyzing such materials sets numerical challenges, as detailed models are required in order to capture the complexity of their architecture. Unlike typical composite laminates, the fibers are first assembled to yarns (or tows) and these are subsequently interlaced into specific patterns. Having yarns interlocked in multiple directions offers balance between in-plane and out-of-plane properties. A comprehensive review on textiles including applications can be found in (Mouritz et al., 1999). Reviews focusing on the

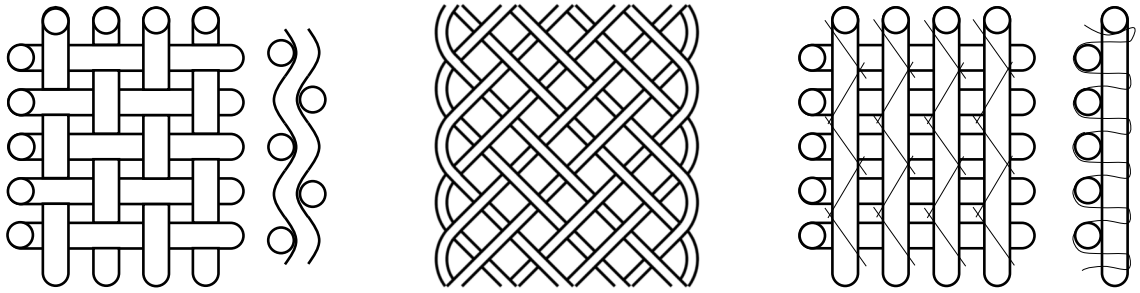

(A) Woven (B) Braided (C) Non-crimp fabric

FIGURE 1.2: Main types of textile architectures: woven (A), braided (B) and non-crimp fabric (C).

finite element (FE) modeling challenges are presented in (Lomov et al., 2011) and (Tan, Tong, and Steven, 1997).

The interlacing pattern of the yarns defines the textile type. There are three basic classes: woven, braided and non-crimp fabrics, as illustrated in Fig.1.2. Woven textiles have two orthogonal yarn families forming a grid. The plain weave is the simplest pattern (Fig.1.2A) as each yarn undulates when meeting another yarn in the vertical direction. More complex patterns, e.g. undulation every two yarns, also exist. Information on the characterization and modeling techniques of woven composites is provided in (Dixit and Mali, 2013). The yarns in braided textiles are interweaved diagonally with a certain angle. Fig.1.2B illustrates a biaxial braiding pattern. In case a family of equally spaced yarns exists aligned to the axial direction, the textile is called a triaxial braid. An informative overview on braided modeling can be found in (Fang and Liang, 2011). Non-crimp fabrics are essentially layers of straight yarns stitched with a lightweight thread, as in Fig.1.2C. The term is derived from the lack of crimp, namely the undulation of the yarns present at the previous types. The reader is referred to (Lomov, 2011) for a detailed review. Another type of relatively limited use is knitted fabrics, in which the yarns are interlaced with each neighboring yarn in a loop (Hasani et al., 2017).

Regarding performance and applicability of the three aforementioned main textile types, the differences lie mostly on the orthogonal interlacement of woven fabrics, as opposed to braided where there is a range of possible angles and, thus, ability to tailor the structural demand according to the load state. Moreover, the extra set of axial yarns of triaxial braids offers more toughness and fatigue strength. Concerning non-crimp fabrics, despite the low-cost production methods in comparison with the other types and the improved strength and stiffness due to the lack of crimp, the reduced drapability of such materials due to the stitching hinders their industrial application.

The mechanical behavior of heterogeneous materials is driven by the properties of their individual components, along with lower-scale geometrical parameters defining their size and spatial distribution. The direct integration of detailed textile architectures to macroscale structural models is impractical, even with the current computational resources. Instead, multiscale modeling provides effective properties for higher-scale simulations, by homogenizing the components of the microstructure via lower-scale models (Kanouté et al., 2009).

A typical multiscale scheme for textile composites is illustrated in Fig.1.3. Based on the concepts of periodicity and statistical ergodicity, the effective mechanical properties of an impregnated yarn can be determined by a microscopic model (order of μm) via fiber and matrix properties. The acquired information passes to the mesoscale (order of mm), where the inner textile geometry

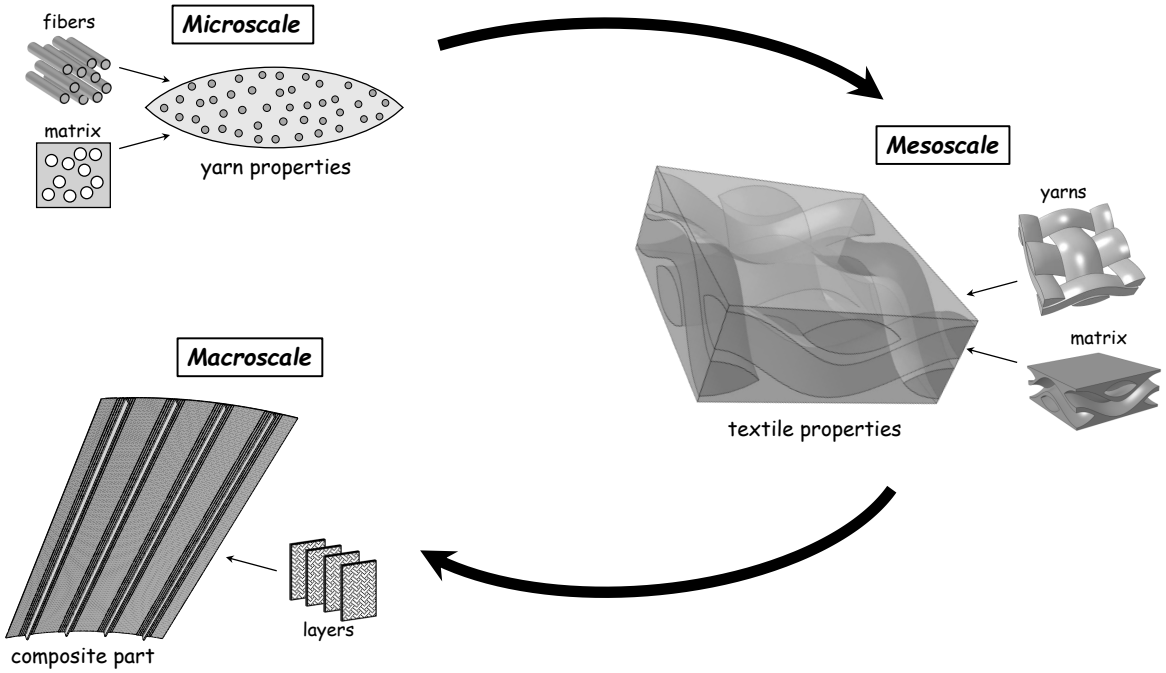

FIGURE 1.3: Typical multiscale information-passing scheme for textile composites: homogenization at microscale level extracting the yarn properties, second homogenization at mesoscale level extracting the textile properties and, finally, analysis of a homogeneous structural part at the macroscale.

is integrated and a second homogenization is performed. Having acquired the textile properties, the macroscale model of interest can be analyzed. In case of a multilayered structure, the classical lamination theory (CLT) can be used assuming the mesoscale model accounts for a single textile layer or, alternatively, a layered mesoscale model and a solid homogeneous macroscopic model can be combined. A handbook on micromechanics and transitioning between scales is given in (Zohdi and Wriggers, 2005).

Multiscale methods for composite materials are divided in two categories: a) hierarchical multiscale methods predicting mechanical properties, where information passes from lower to higher scales, monotonic loading is assumed and models are analyzed sequentially, and b) multiscale and multilevel or FE^2 methods, where information goes both ways and models in different scales are analyzed simultaneously. The latter category allows non monotonic loading as the lower-scale models are updated according to the stress state of the macroscopic model. Such methods have been extensively applied to typical fiber composites, e.g. (Feyel, 1999; Feyel and Chaboche, 2000; Nezamabadi et al., 2015), but are rather expensive computationally. Regarding textiles, there is a limited number of FE^2 studies considering an additional homogenization stage is necessary (Rouf, Liu, and Yu, 2018; Tikarrouchine et al., 2021). Attempts to improve efficiency have been made either by creating databases for the microscopic problem offline and interpolating through the data during the macroscale analysis (Xu et al., 2020; Huang et al., 2021b), or by substituting FE with fast Fourier transforms at the lower scale (Spahn et al., 2014). A recent study combined the two concurring simulations in a single step (Tan, Raju, and Lee, 2020).

Regarding the hierarchical multiscale category, most studies employ FE-based computational homogenization via representative volume elements (RVEs) as in (Ernst et al., 2010) for non-crimp fabrics, in (Patel, Waas, and Yen, 2018) and (Madke and Chowdhury, 2019) for woven,

and in (Aranda-Iglesias et al., 2021) for knitted textiles. This is because the design of textile geometries and the material behavior is easier to be modeled with FE programs. An informative overview of such procedures is given in (Lomov et al., 2007).

Nevertheless, the computational cost and the periodic mesh of the complex geometry remain a challenge. The development of textile modelers like TexGen (Lin, Brown, and Long, 2011; Lin et al., 2012) and WiseTex (Verpoest and Lomov, 2005) offered automated meshes compliant to standard FE software. An extension of TexGen for dimensionally reducible structures, enabling a similar concept like substructures and superelements called mechanics of structure genome, can be found in (Liu et al., 2017). For repeated processes, the voxel mesh approach gained recognition due to its versatility (Kim and Swan, 2003). However, it requires further processing when applied to damage predictions due to stress concentrations at the sharp material interfaces, such as smoothing the interface nodes as in (Fang et al., 2016).

A further alternative regarding the irregular mesh at the interface is the extended finite element method (XFEM), as used in (Kästner, Haasemann, and Ulbricht, 2011). In (Li, Wen, and Aliabadi, 2011), a meshfree method is proposed for the stiffness prediction of woven composites, while Voronoi tessellation has also been employed towards more accurate geometry descriptions (El Said et al., 2016; El Said et al., 2018). Moreover, different approaches have been proposed towards the computational cost reduction, as in (Nasution et al., 2014) where the asymptotic expansion homogenization is employed, while in (Wang et al., 2018) damage predictions based on fast Fourier transforms show fair approximations compared to FE for a braided composite. An overview of analytical models for stiffness prediction is presented in (Hallal, Younes, and Fardoun, 2013).

Manufacturing simulation, characterization and material modeling of braided composites

The braided textile architecture described in the previous section is a result of a manufacturing process called braiding. It is a semi or fully automated procedure which allows versatility in terms of manufacturable shapes and also minimizes material waste, since material and structure are produced concurrently. Concerning machinery, the circular or maypole braiding machine is currently the most commonly used among other types. Its primary concept is based on the motion of a mandrel through a plane formed by radially placed carriers, as illustrated in Fig.1.4 where an isometric view is shown on the left side and a top view focusing on the carrier plane is shown on the right. The carriers support the yarn bobbins, or spools, and move within the horn gears on a sinuous path, half of them clockwise and half counterclockwise. The yarns contact the mandrel at the fell front at specific locations in order to form a helical pattern. The distance between the fell front and the spool plane is the convergence zone, in which the guide rings are also placed to ensure the accurate placement of yarns as the mandrel moves in the direction of the take-up speed. Detailed information on the braiding production process are provided in (Kyosev, 2014; Rana and Fangueiro, 2015), where also other types of braiding procedures are described, such as the Cartesian braiding where the carrier plane is an orthogonal grid instead of circular.

The machine parameters govern the mechanical behavior of the braided structure. For instance, the take-up speed controls the braid angle which is very sensitive for the overall stiffness and strength. Therefore, simulating the manufacturing process has received attention. An overview of simulation approaches is included in (Carey, 2016). Many studies are based on the classical geometric approach first introduced by (Ko, 1987), which established analytical formulations linking process parameters (e.g. take-up speed, mandrel radius etc.) with the braid angle. A similar approach with a visualization tool for 3D preforms is developed in (Potluri et al., 2003). However, those predictions are only accurate for simple circular preforms.

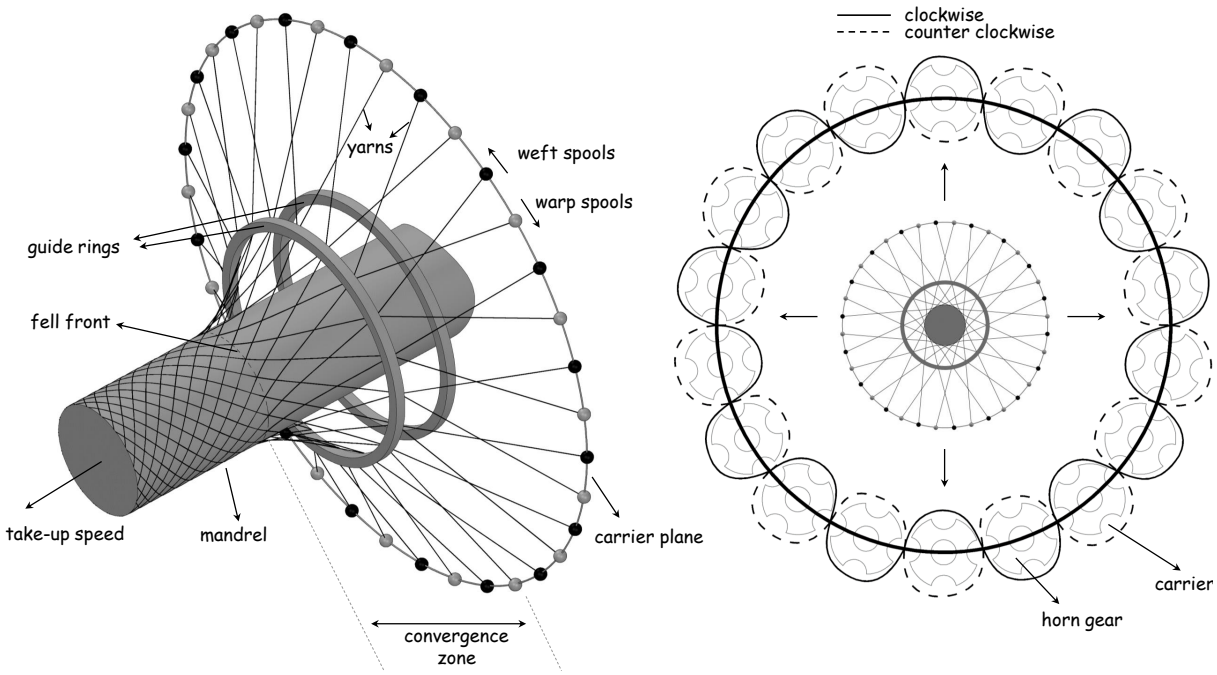

FIGURE 1.4: Operation and terms for a maypole braiding machine: isometric view (left) and top view with details on the carrier plane (right).

An attempt to predict the braid angles for complex, non-axisymmetric preforms was made in (Kessels and Akkerman, 2002), by improving the aforementioned classical theory. A coupling of this formulation with analytical homogenization schemes is provided in (Bigaud, Dréano, and Hamelin, 2005). Alternative analytical approaches based on differential geometry can be found in (Guyader, Gabor, and Hamelin, 2013) and (Na et al., 2014). More recent endeavors include a method correlating process and structure parameters via an oblique coordinate system and curve fitting (Mei et al., 2020) and a method based on the mechanical equilibrium of yarns (Imbert, Finckh, and Gresser, 2021).

Regarding more complex approaches, an inverse kinematics-based formulation was established by (Ravenhorst and Akkerman, 2014), generating the take-up speed for a given braid angle while allowing fast calculations and preforms of variable shape and size. The effect of yarn interactions was later incorporated in (Ravenhorst and Akkerman, 2016). In (Ma, Dong, and Wang, 2016), a strategy based on matrix theory and symbolic operation simulating the carrier movement is proposed. A meshless method simulating the relative movement of multilayer horn gears in order to predict the yarn paths is presented in (Kim, 2017). FE simulations of the complete braiding process are also found in the literature for example, in (Hans et al., 2015; Swery et al., 2017) where also structural modeling is integrated, and in (Wang et al., 2021) for preforms with irregular shapes. However, the computational cost of such simulations remains quite high.

The mechanical characterization of braided composites, whether experimentally or via virtual testing frameworks, is an active research topic with a broad spectrum. Extensive experimental campaigns under multi-axial stress states have been reported in (Cichosz et al., 2016) for biaxial, and in (Wehrkamp-Richter, Hinterhölzl, and Pinho, 2017) for triaxial braided composites and for different braiding angles, including both monotonic and loading-unloading conditions. The free-edge effect (i.e. stress concentration at the free edges of the interface between two plies)

and the strain rate influence for tensile loading have been investigated in (Cai et al., 2021) and (Sun, Liu, and Gu, 2005), respectively. Optical microscopy (Roy, Potluri, and Soutis, 2017) and computed tomography (CT) scans (Ge et al., 2021) have been employed for the identification of tensile failure modes and pore defects. Moreover, compression tests have also been performed e.g. in (Ching Quek et al., 2004; Li et al., 2011; Li et al., 2014) where complex failure modes, including instability phenomena at the yarns, were observed.

Regarding modeling-based characterization, the elastic behavior has been thoroughly investigated via the FE method, e.g. in (Zeng, Wu, and Guo, 2004; Tian et al., 2016; Ni and Wei, 2016), while in (Wehrkamp-Richter, De Carvalho, and Pinho, 2018a) a framework was developed to account for the compaction of the yarns and, thus, RVEs with higher volume fractions were simulated. Furthermore, in order to reduce the computational cost, many analytical approaches have emerged over the years. Classical micromechanical formulas for the elastic prediction of unidirectional (UD) composites were tailored around braided composites in (Hong et al., 2019; Ye et al., 2019). In (Huang, 2000; Zhang, Binienda, and Kohlman, 2014), the bridging model was used to correlate the volume averaged stress increments in the fiber and matrix of braided RVEs, while in (Byun, 2000; Shokrieh and Mazloomi, 2012; Xu and Qian, 2016) the multi-unit cell method was employed, which disassembles the RVE to several unit cells with approximately UD properties. An alternative approach called digital element method using 2-node rod elements for the yarns can be found in (Sun and Sun, 2004).

Predicting the tensile strength response is also mostly based on the FE method, with various approaches employing continuum damage mechanics (CDM) and the Hashin criterion coupled with an elastic damage model for the yarn modeling, e.g. in (Guo-dong, Jun, and Bao-lai, 2009; Ge et al., 2018; Zhu, Li, and Jiang, 2020). Interlaminar progressive failure for the debonding of yarn-matrix interface is also regarded in (Zhang et al., 2015). Alternative approaches include a physically-based smeared-crack model for the yarns and the Drucker-Prager criterion for the matrix in (Wehrkamp-Richter, De Carvalho, and Pinho, 2018b), a pressure dependent elastoplastic matrix damage model with a paraboloidal yield criterion in (He et al., 2019) and an instantaneous stiffness degradation approach with Stassi and Hashin criteria for matrix and yarns, respectively, in (Nobeen et al., 2016). Besides uniaxial loading conditions, the biaxial tension and compression response was studied in (Tian et al., 2018). Concerning compression, an analog micromechanical model accounting for yarn kinking under axial loading has been developed in (McGregor et al., 2007; McGregor et al., 2008), while a combination of Hashin and Hou criteria coupled with a Murakami damage model for the transverse properties can be found in (Zhao et al., 2019). Studies accounting for porosity effects and elevated temperatures can be found in (Gao et al., 2020) and (He et al., 2020), respectively.

A recent trend towards cost-effectiveness is to avoid using FE simulations for characterization. An analytical model based on the subcell concept is proposed in (Dang et al., 2020), able to predict the linear and nonlinear behavior of triaxial braided materials under tension and compression for all uniaxial loading conditions. In (Wang et al., 2020), a concurrent multiscale method is proposed based on fast Fourier transforms for both scales under compressive loading. Finally in (He et al., 2021), a multilevel multiscale method with a reduced order model based on clustering is proposed for longitudinal tensile and compressive loading. Results of the above studies are promising in terms of both accuracy and efficiency.

Besides manufacturing assessment, material characterization and modeling, there are several studies related to the structural design of braided composites. In (Sturm and Heieck, 2015), design principles are developed for braided frames with enhanced energy absorption capacity under bending loads. A study on buckling and post-buckling behavior of stiffened braided panels is presented in (Kosztowny and Waas, 2021), while thermal induced buckling is studied in (Li and Shen, 2009; Li, 2014). Moreover, the considerable delamination resistance has driven

studies towards fatigue assessment, e.g. in (Tate and Kelkar, 2008; Montesano et al., 2013; Zhang, Curiel-Sosa, and Bui, 2018). Optimal design has also received attention, as in (Ghiasi et al., 2010) where a bicycle part was optimized under manufacturing constraints, in (Schatz, Hermanutz, and Baier, 2017) for a braided aircraft propeller, and in (Wu and Viquerat, 2017) where the composite design of hybrid bistable tubes was optimized based on their natural frequencies.

As an overall conclusion, the FE method is dominating regarding the homogenization processes required for the stiffness and strength properties calculation of braided and, in general, textile composite materials. The numerical cost, however, generates a tendency to bypass the FE models when it comes to repeated procedures, as for example the concurrent simulations of FE^2 schemes. Manufacturing-induced effects on the geometry of braided structures are non-negligible and many studies studied the production process simulation from several aspects. Moreover, besides several alternatives reported in this section, the voxel-based mesh is the sole feasible option for automated remeshing of complex and repetitively varying geometries.

1.2.2 Uncertainty quantification and machine learning for composite materials

Probabilistic modeling

The heterogeneous nature and the uncertainties related to the manufacturing processes of fiber composite materials drove the research community towards probabilistic assessments more than 40 years ago (Phoenix, 1978; Fukuda and Chou, 1982). Stochastic approaches allow the integration and propagation of uncertainties to the mechanical response and, thus, enable the justification and quantification of the observed experimental scatters. A noteworthy attempt to report those scatters is made in (Sriramula and Chryssanthopoulos, 2009), where probability models are fitted to ply-level mechanical properties based on experimental data and goodness-of-fit tests, e.g. Kolmogorov-Smirnov. It should be noted that the majority of the studies reported herein are related to typical composite laminates. The probabilistic assessment of textiles is limited and is reported in the last paragraph of this section.

Uncertainty assessment with full probabilistic detail including higher order statistical moments relies mostly on Monte Carlo simulations and, hence, repeated model evaluations. This is affordable for predicting elastic properties as in (Gusev, Hine, and Ward, 2000) and (Melro, Camanho, and Pinho, 2008), where also an algorithm for generating random microstructures with high volume fraction is proposed. In (Stefanou, Savvas, and Papadrakakis, 2015), the synergy of XFEM with brute-force Monte Carlo is demonstrated for the effective properties of composites with randomly-shaped inclusions.

Stochastic perturbation methods based on classical Taylor expansions have also been applied for the elastic prediction in (Kamiński and Kleiber, 2000; Sakata et al., 2008), as they require less model realizations. Variance-reduction methods like importance sampling were used in (Zhang, Shields, and TerMaath, 2020), while the spectral stochastic finite element method (SSFEM) was applied in (Chen and Guedes Soares, 2008) and in (Sasikumar, Suresh, and Gupta, 2015) for laminated composites. In SSFEM the spatial uncertainties are modeled via random fields and the system response is projected in a polynomial chaos basis. A similar approach was applied in (Clément, Soize, and Yvonnet, 2013) together with principal component analysis for reducing the stochastic dimension, accounting also for nonlinear behavior. Non-probabilistic treatment of uncertainties as in (Naskar, Mukhopadhyay, and Sriramula, 2019), is more limited within the literature.

Besides efficiency in terms of minimum model evaluations, numerous studies have dealt with the accurate description of spatial uncertainty via random field modeling. Statistical fitting of spatial stiffness and strength distributions to 2D random fields was performed in (Sasikumar

et al., 2015), based on repeated tests of flat carbon-fiber laminates. The random fiber distribution obtained from scans or microscopy is usually captured by the moving window technique as in (Stefanou, Savvas, and Papadrakakis, 2017; Savvas, Papaioannou, and Stefanou, 2020) for particle-reinforced composites, in (Buryachenko et al., 2003; Koley, Mohite, and Upadhyay, 2019) for long fiber-reinforced composites, and in (Rauter, 2021) for short fiber-reinforced composites.

The accurate recreation of uncertainties for fiber composites is not limited to the random fiber distribution based on cross-sectional images. A recent contribution on the statistical representation of fiber waviness with applications on progressive failure under compression can be found in (Huang et al., 2021a). In (Matveev et al., 2018), the defects occurring due to automated fiber placement (AFP) processes are statistically characterized and their effect to the permeability of the dry preform during resin moulding is studied. Moreover, the recreation of stochastic imperfections on structural level via random fields based on a Fourier methodology and the discrete Karhunen-Loève transform, can be found in (Kriegesmann et al., 2011) for composite cylinders and in (Kriegesmann, Jansen, and Rolfes, 2012) for composite stiffened panels.

The studies already reported propagate the measured uncertainty to the response, since the statistical evaluation of geometrical uncertainties (e.g. volume fraction, imperfections, defects) is feasible through image processing techniques or in-situ inspections. The same does not stand for the inherent uncertainty of composite material properties, such as fiber, matrix and interface properties, as repeated test campaigns are required for the complete statistical characterization. Therefore, inverse approaches, similar to structural health monitoring (SHM) procedures, have been developed towards the identification of material scatters from response data. The randomness of elastic ply properties has been identified from measurements of the displacement field in (Gogu et al., 2013) and in (He, Liu, and Makeev, 2018) via Bayesian updating and optimization, respectively. Eigenfrequencies and modal analysis were used in (Sepahvand and Marburg, 2014) also for the elastic properties identification, while some strength properties based on CLT were included in (Pepper, Montomoli, and Sharma, 2021), where an optimization scheme tailored around Kolmogorov-Smirnov tests was proposed.

Identification of random microscopic parameters is possible by coupling the inverse algorithm with a multiscale approach, as in (Sakata and Ashida, 2010) for elastic constituent properties of particle-reinforced composites, and in (Cappelli et al., 2019) for long-fiber composites. In (Wu, Adam, and Noels, 2018), a Mori-Tanaka elastic model was employed. Regarding strength properties a nonlinear solver and an optimization scheme for the solution of the inverse problem was proposed in (Hu, Fish, and McAuliffe, 2017), while a Bayesian framework based on FE homogenization was presented in (Mustafa, Suleman, and Crawford, 2018). However, the added numerical cost for nonlinear predictions is an issue which has only been moderately addressed, considering also that stochastic inverse problems require more model evaluations than forward uncertainty cases.

Structural reliability is the probability of satisfying a given performance criterion and is evaluated by defining a limit-state function that distinguishes safety and failure (Guedes Soares, 1997). Regarding composite structures, this topic has been addressed on a macro-mechanical level for laminates via the Monte Carlo method in (Jeong and Shenoi, 2000) and (Frangopol and Recek, 2003), and via the stochastic perturbation method in (Onkar, Upadhyay, and Yadav, 2007). The influence of lower-scale parameters on reliability is studied in (Shaw et al., 2010) with Monte Carlo, first and second-order reliability method (FORM and SORM) based on analytical criteria, while in (Omairey, Dunning, and Sriramula, 2018) FE homogenization is performed coupled with Monte Carlo simulations.

As mentioned in the beginning of this section, the stochastic assessment for textile composite materials is rather limited, mainly due to the dual homogenization cost that accompanies them. An attractive research topic is the efficient stochastic characterization of yarn distortion at the cross-section level and out-of-plane waviness from the yarn nominal path based on tomography data, as in (Guo-dong et al., 2009) where a methodology for distorted yarns is proposed based on differential geometry. Markov chains are enabled in (Vanaerschot et al., 2013) and (Vanaerschot et al., 2017) for recreating the random deviations from the nominal yarn path in the cross-section of a woven composite. An inverse approach towards the prediction of elastic properties via modal analysis data for braided composites can be found in (Jiang et al., 2015). The stochastic perturbation method was used in (Zhou et al., 2016) for the random homogenized elastic properties of woven composites, and in (Zhou and Gosling, 2018) for the reliability analysis based on first-ply failure under tension. A framework for the multiscale uncertainty quantification of woven textiles was presented in (Bostanabad et al., 2018), in which Kriging modeling and nested random fields were used. However, even in the presence of metamodeling techniques only a few simulations for the elastic properties were reported. A recent study in (Tao et al., 2020a; Tao et al., 2020b) proposed vine copulas for the stochastic characterization of woven internal geometry and predicted scatters for the effective stiffness and strength properties. Once more, only a few Monte Carlo runs were provided. Consequently, the response samples are not adequate for a full statistical characterization or further quantification usages. Overall, there is a noticeable gap regarding textile uncertainty quantification and methods allowing fast evaluations that can be further used for reliability, optimization, sensitivity etc., especially for failure responses.

Machine learning applications

The employment of machine learning algorithms to fiber composite modeling is relatively recent but advances rapidly. There are two main categories of studies around that subject: uncertainty-related studies and deterministic studies. Studies of the first category train machine learning models in order to substitute expensive simulations for uncertainty quantification purposes. Several applications of artificial neural networks (ANN) can be found, as in (Dey et al., 2016) for stochastic modal analysis of composite plates, in (Zhou et al., 2021) for stochastic strength prediction based on the the microscopic structure, and in (Olivier, Shields, and Graham-Brady, 2021) for predicting the stochastic effective tensile stress-strain response including plastic properties for the matrix. Applications of non-intrusive polynomial chaos expansions (PCE) can be found in (Thapa, Mulani, and Walters, 2019) for stochastic buckling analysis of laminates and in (Thapa et al., 2021) for stochastic progressive failure analysis of laminates. A hybrid ANN-PCE surrogate model was recently developed for stochastic multiscale analysis of composites with multiple spherical inclusions in (Henkes, Caylak, and Mahnken, 2021). Further approaches include a probabilistic multiscale analysis with random voids aided by radial basis functions in (Li et al., 2018), probabilistic modal and buckling analyses of sandwich plates with spline-based adaptive regression in (Dey et al., 2019), and an application of reliability-based design optimization of composite stiffened panels with various surrogate models in (Díaz, Cid Montoya, and Hernández, 2016). An overview on surrogate assisted uncertainty quantification of laminates, including performance comparisons, can be found in (Dey, Mukhopadhyay, and Adhikari, 2017).

Regarding the studies of the second category, machine learning techniques are used to advance the deterministic response prediction in terms of efficiency. Studies able to emulate the complete effective stress-strain response, including the post-failure regime, can be found in (Yang et al., 2020) combining PCA and ANN, and in (Yan et al., 2020) combining regression and classification ANN models. An overview on how ANN can assist the composite constitutive modeling is

provided in (Liu et al., 2021). In (Qi et al., 2019), a decision tree regression model was used to emulate the elastic behavior of a cross-ply laminate. Material and geometric nonlinearities were taken into account in (Liu and Wu, 2019) for multiscale modeling with deep ANN. Moreover, a novel ANN-based failure criterion for yarns able to be integrated in progressive failure modeling of textiles was developed in (Liu et al., 2019), while adaptive sampling and Kriging were used for the first-ply failure envelope prediction in (Tian and Yu, 2021). Applications of classification for cracking detection and clustering for automated inspection of yarn deformations can be found in (Mardanshahi et al., 2020) and (Mendoza et al., 2019), respectively. Finally, non-classical effects regarding composite modeling with shell elements were evaluated combining the Carrera unified formulation and ANN in (Petrolo and Carrera, 2020) and (Petrolo and Carrera, 2021).

Judging from the literature review presented in this chapter, there is an evident gap regarding the probabilistic assessment of textile composites in terms of stiffness and strength prediction but also at a structural part level, mainly due to the high numerical cost, especially concerning the failure response. It is only recently that machine learning methods and metamodels began to be integrated in order to boost the efficiency of multiscale models and approximate important response surfaces that can be used in costly procedures, like optimization, reliability and inverse approaches. However, there is still a disanalogy between typical fiber composites and textile composites. Taking into account the cost of multiscale simulations for a textile composite including progressive material failure, even acquiring a sufficiently large amount data for training a metamodel is challenging and, consequently, yet not fully addressed. Therefore, it is currently a very active research topic with many applications yet to be covered.

1.3 Objectives and outline

The objective of this work is to develop a framework of methods able to evaluate material and geometric uncertainties in braided composites and quantify their effects on their homogenized stiffness and strength. As shown in Fig.1.5, an information-passing multiscale scheme is initially established able to homogenize the elastic and ultimate strength properties of the yarns from the constituent properties at the microscopic level and, consecutively, perform homogenization of stiffness and ultimate strength for a triaxially braided structure at the mesoscale. A progressive failure algorithm is integrated for the strength homogenization. The framework is parametrized to account for uncertainties related to material properties, e.g. the fiber and matrix properties at the microscale and the fibel volume fraction of the yarns, but also production-induced uncertainties, such as the braid angle at the mesoscale which controls the yarn volume content of the braided structure, the out-of-plane waviness of the yarns and the distortions of the yarn shape at a cross-sectional level. Regarding uncertainty quantification, a global sensitivity analysis technique is applied for the classification of the random parameters in terms of importance to the response and exploration of possible dependencies along the different length scales. Furthermore, an inverse uncertainty quantification method based on Bayesian updating for the mean and variance of random parameters is also integrated. In order to make the computational cost of such procedures affordable, metamodels are trained to map the random input with the elastic and strength macroscale response and are used as surrogates instead of the costly FE algorithms, during the demanding in terms of model evaluations uncertainty quantification processes. The framework is non-intrusive so that the extension to different setups, load cases and materials is straightforward.

This thesis is divided into seven chapters in total. In the current introductory section, following the motivation, literature review and objective sections, an overview of the basic theory around probabilities, random variables and random fields is presented in order to assist the comprehension of the core chapters/publications. Finally, a section regarding basic machine

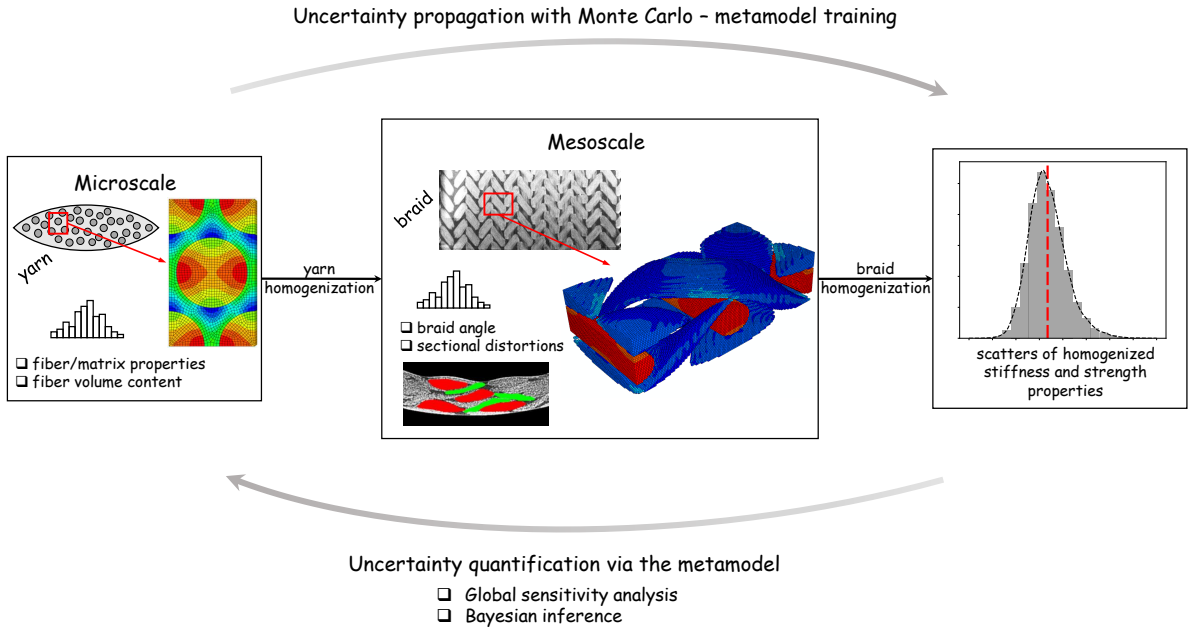

FIGURE 1.5: Overview of the developed framework.

learning terms and processes is documented, covering the fundamentals of training and testing a machine learning algorithm by employing a simple example of polynomial fitting running throughout the section.

Chapter 2 introduces the proposed uncertainty quantification framework for the linear elasticity case, predicting scatters for all parameters of the effective elastic tensor of a triaxially braided material, based on micro and mesoscopic uncertainties. The FE-based homogenization method integrated into the multiscale algorithm is described in detail together with the global sensitivity analysis formulation. Artificial neural networks are used to boost the Monte Carlo procedure of the sensitivity analysis, allowing results for all elastic parameters and providing a clear view on the most important parameters of each load case.

In Chapter 3, the parametrization of random distortions of imperfectly shaped yarns and random deviations of the nominal yarn paths in the interlaminar direction are presented through novel mathematical models. More specifically, Fourier-based random fields are employed for the yarn section representation, able to be calibrated from measurements of the deviations from hypothetically perfect yarn shapes. Regarding the stochastic waviness, a random field formulation based on the Kriging model is presented which considers variance and correlation information in a straightforward manner. Furthermore, the expansion of the framework for the ultimate strength prediction under tension via a progressive failure algorithm is presented, so scatters for both the effective stiffness and strength scatter are presented. Results for both kinds of random imperfections are shown for a braided structure and a discussion concerning the metamodeling potential of those uncertainties is included.

The previously unaddressed problem of mapping randomly generated input with the ultimate strength of a textile composite via machine learning is studied in Chapter 4. The observed complex response surface and the numerical cost of the nonlinear multiscale scheme were dealt with a multi-fidelity strategy and a novel hybrid metamodeling technique. The proposed model integrates artificial neural networks into the kernel of the hierarchical Kriging formulation, providing improved efficiency compared to the original hierarchical Kriging model. The trained

model is used for a global sensitivity analysis of the strength of the braided structure, revealing strong interaction effects between the random input parameters. Several discussions are also included for some numerical aspects of the adopted failure prediction algorithm.

Chapter 5 expands the uncertainty quantification framework further with an inverse approach, able to indirectly characterize uncertainties of microscopic parameters by employing datasets from standard structural tests at higher scales. The approach is able to quantitatively characterize the mean and variance of the governing random parameters, while due to its indirect nature is able to identify scatters of low-scale parameters for which physical testing is challenging. The methodology is based on the combination of Bayesian inference and polynomial chaos metamodeling, which provides sensitivity indices immediately after training. The framework is applied on a UD carbon fiber composite plate, since a textile specimen cannot be used for investigating the matrix properties, as its response is dominated by the interlacing yarns and, therefore, fibers. As a result, a UD specimen must be additionally used for determining the properties of textiles. The experimental campaign utilized herein, includes elastic and failure data and also measurement errors. Thus, there is a clear distinction between aleatoric and systematic errors preventing assumptions which might distort the updated scatter results.

Chapter 6 provides experimental validation for the numerical models and methodologies presented in the previous chapters. The chapter is divided in two subsections. First, the deterministic FE-based braided modeling (middle part of Fig.1.5) is validated against experimental data from the literature in terms of stiffness and strength accuracy at the mesoscale level. The validation is performed via a triaxially braided composite material under axial tension. The second part of the chapter verifies the feasibility of the methodology proposed in Chapter 3 for the stochastic characterization and parametrization of the sectional yarn distortion, by processing CT-scan data of a braided tube specimen. A statistical sample of distorted yarns is collected via image processing, which is then processed to extract the deviations from nominal shapes. A discrete Karhunen-Loève transformation is used to generate random input distortions with the same statistical properties as the data. Finally, the realistic distortion uncertainty is propagated to the effective elastic response of the braided material via the developed probabilistic framework.

Chapter 7 is the closure of this thesis providing the summary of the content and the main conclusions, followed by a future outlook for consecutive research suited for academia but also relevant to industry needs.

1.4 Probability and uncertainty

Uncertainties may affect the behavior of a physical system in an unknown manner, whether of aleatory or epistemic nature. Aleatory (or statistical) uncertainty refers to the inherent randomness in the system (e.g. random earthquake excitation), while epistemic (or systematic) uncertainty refers to partial knowledge or negligence of the system's parameters (e.g. measurement errors). Probability theory is the fundamental tool for modeling and introducing uncertainties to structural engineering applications. This section briefly covers basic definitions on probabilities, random variables and random processes or fields, essential for the next chapters of this thesis. For deeper inquiry, the reader may refer to (Rice, 2007), (Larsen and Marx, 2010) and (Grigoriu, 2002).

1.4.1 Probability theory and random variables

Probability definition

The classical definition of probability as presented in the works of Laplace and Bernoulli, expresses the probability of an event A as the number of successful outcomes $N(A)$ divided by the total number of possible cases $N(\Omega)$. The classical approach served as a predecessor for the frequentist approach of von Mises (Mises, 1981), in which the probability of an event A is its relative frequency of occurrence over an indefinite number of trials:

$$P(A) = \lim_{n\to\infty} \frac{N(A)}{n} \tag{1.1}$$

The axiomatic approach of Kolmogorov (Kolmogorov, 1950) avoids the assumption of equally probable events and of random experiments under the same exact conditions. According to Kolmogorov, the probability P on a set Ω is a function of subsets or events A_i of Ω to $\mathbb{R}$, satisfying the following conditions:

$$P(A_i) \geq 0 \text{ , for } A_i \subset \Omega \tag{1.2}$$

$$P(\Omega) = 1 \tag{1.3}$$

$$P(\bigcup_{i=1}^{\infty} A_i) = \sum_{i=1}^{\infty} P(A_i) \text{ , for } A_1 \cap A_2 ... = \emptyset \tag{1.4}$$

Conditional probability

The conditional probability is a revised probability that considers the known occurrence of another event of the same space. Let A_1 and A_2 be events defined on Ω, with $P(A_2) > 0$. The conditional probability of A_1 assuming the occurrence of A_2 is given as:

$$P(A_1|A_2) = \frac{P(A_1 \cap A_2)}{P(A_2)} \tag{1.5}$$

Bayes' theorem

Based on conditional probabilities, the Bayes' theorem introduces a more subjective perspective by expressing probability as the degree of belief in an event, which is updated in light of new evidence. In case of two events A_1 and A_2, the Bayes' rule relates the conditional probability $P(A_1|A_2)$ with $P(A_1)$ and $P(A_2)$ as follows:

$$P(A_1|A_2) = \frac{P(A_2|A_1)P(A_1)}{P(A_2)} \tag{1.6}$$

where $P(A_1)$ is called the prior or unconditional or marginal probability, $P(A_1|A_2)$ is the posterior probability and $P(A_2)$ is the evidence.

Random variables

A random variable is a function from the sample space of random experiments Ω to $\mathbb{R}$. A discrete random variable takes values from a finite or countably infinite space, whereas a continuous random variable contains an uncountably infinite number of values. The *cumulative distribution function* (CDF) of a random variable X is the probability of X being less or equal to a number x:

$$F_X(x) = P(X \leq x) \tag{1.7}$$

The CDF is the integral of the *probability density function* (PDF) $f_X(x)$, which is given by:

$$F_X(x) = \int_{-\infty}^{x} f_X(x)dx \Rightarrow f_X(x) = \frac{dF_X(x)}{dx} \tag{1.8}$$

The moments of a PDF of a random variable help to characterize its shape. The first moment is the *mean value* given by:

$$\mu(x) = \mathbb{E}[X] = \int_{-\infty}^{+\infty} x f_X(x)dx \tag{1.9}$$

The second central moment provides the *variance* $\sigma^2(x)$ as:

$$\sigma^2(x) = \mathbb{E}[\big(X - \mu(x)\big)^2] = \int_{-\infty}^{+\infty} \big(x - \mu(x)\big)^2 f_X(x)dx \tag{1.10}$$

while its square root is the *standard deviation*. A useful normalized measure of the variance is the *coefficient of variation* (COV), which is given by:

$$\text{COV}(x) = \frac{\sigma(x)}{\mu(x)} \tag{1.11}$$

The above definitions cover the case of continuous random variables, while for the discrete case the integrals are replaced with sums.

Joint distributions

In case of two or more random variables defined on a sample space, their simultaneous behavior is characterized by the joint CDF and PDF. For two random variables X and Y, the joint CDF is given by:

$$F_{X,Y}(x, y) = P(X \leq x, Y \leq y) \tag{1.12}$$

Consequently, the joint PDF is defined as:

$$f_{X,Y}(x, y) = \frac{\partial^2 F_{X,Y}(x, y)}{\partial x \partial y} \Rightarrow F_{X,Y}(x, y) = \int_{-\infty}^{y} \int_{-\infty}^{x} f_{X,Y}(u_X, u_Y)du_X du_Y \tag{1.13}$$

The statistical independence of two random variables X and Y is defined via the joint PDF as:

$$f_{X,Y}(x, y) = f_X(x) f_Y(y) \tag{1.14}$$

The level of association is characterized by the *covariance* and the *correlation* of X and Y. The covariance $C(x, y)$ measures the joint variability and is given by:

$$C(x, y) = \mathbb{E}[\big(X - \mu(x)\big)\big(Y - \mu(y)\big)] = \int_{-\infty}^{y} \int_{-\infty}^{x} \big(u_X - \mu(x)\big)\big(u_Y - \mu(y)\big)du_X du_Y \tag{1.15}$$

while the correlation is a normalized measure defined in terms of covariance by the correlation coefficient $\rho(x, y)$:

$$\rho(x, y) = \frac{C(x, y)}{\sigma(x)\sigma(y)} \tag{1.16}$$

Two random variables can be positively or negatively correlated, but also uncorrelated if:

$$\rho(x,y) = 0 \Rightarrow C(x,y) = 0 \Rightarrow \mathbb{E}[X,Y] = \mu(x)\mu(y) \tag{1.17}$$

1.4.2 Random field theory

When modeling spatial or temporal uncertainties, random/stochastic fields (for space) or processes (for time) are more suitable than random variables.

Random field definition

A random field $H(\mathbf{x},\omega)$ is a mapping from a random event ω to a function of random variables through space $\mathbf{x}$ (Grigoriu, 2002). As illustrated in Fig.1.6 for the 1D case, each infinitely small spatial coordinate x_i is associated with a random variable and each random outcome ω_i provides a single realization $H(\mathbf{x},\omega_i)$ of the random field, which is called sample function.

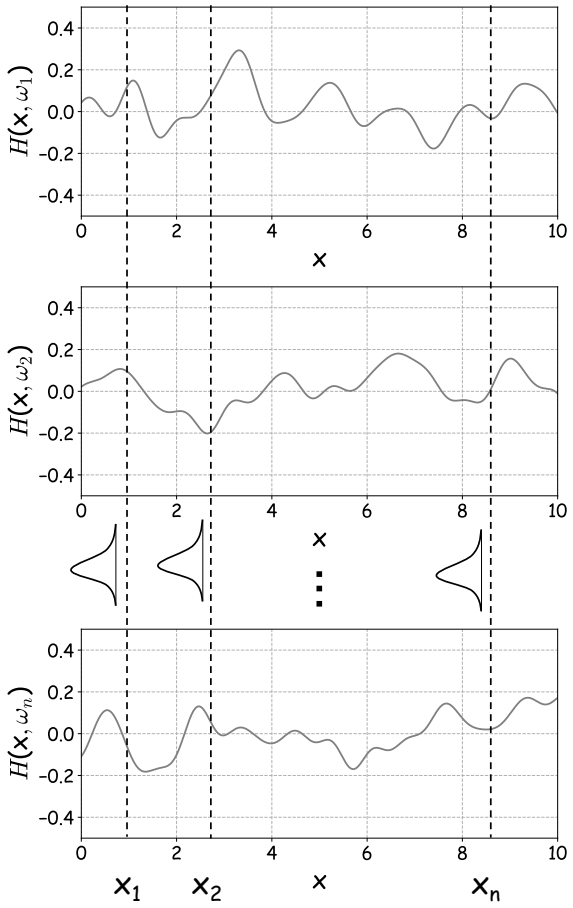

FIGURE 1.6: Illustration of a 1D random field $H(\mathbf{x},\omega)$ within the space interval [0,10]: every fixed random outcome $\omega_1, \omega_2, ..., \omega_n$ provides a sample function of the field (realization) along the $\mathbf{x}$ space, while the family of values for every fixed location $x_1, x_2, ..., x_n$ consists a random variable.

Joint distributions and correlation structure

Considering that a random field $H(\mathbf{x}, \omega)$ is a sequence of random variables $H(x_1), H(x_2), ..., H(x_n)$ for any given spatial coordinate $x_1, x_2, ..., x_n \in \mathbf{x}$, the joint distribution and the correlation structure of these random variables are required for the complete characterization of the field. The joint CDF is the generalization of Eq.1.12, namely:

$$F_{H(x_1),H(x_2),...,H(x_n)}(x_1, x_2, ..., x_n) = P(H(x_1) \leq x_1, H(x_2) \leq x_2, ..., H(x_n) \leq x_n) \tag{1.18}$$

and the derivative gives the joint PDF accordingly.

The *autocorrelation* function expresses the correlation of two random variables $H(x_1)$ and $H(x_2)$ along the $\mathbf{x}$ space:

$$R_H(x_1, x_2) = \mathbb{E}[H(x_1), H(x_2)] = \int_{-\infty}^{+\infty} \int_{-\infty}^{+\infty} \xi_1 \cdot \xi_2 \cdot f_{H(x_1),H(x_2)}(\xi_1, \xi_2) d\xi_1 d\xi_2 \tag{1.19}$$

Accordingly, the *autocovariance* function $C_H(x_1, x_2)$ is given by:

$$C_H(x_1, x_2) = \mathbb{E}\big[\big(H(x_1) - \mu_H(x_1)\big)\big(H(x_2) - \mu_H(x_2)\big)\big] \tag{1.20}$$

The autocovariance function is linked with the autocorrelation by the following equation:

$$C_H(x_1, x_2) = R_H(x_1, x_2) - \mu_H(x_1) \cdot \mu_H(x_2) \tag{1.21}$$

There are several correlation models (or kernels) which can be used for the description of the autocorrelation or autocovariance function, e.g. exponential or square exponential kernel, Matérn etc. Every kernel includes the *correlation length* parameter, which is the distance over which significant loss of correlation occurs. Small correlation lengths lead to high variability within a sample function of $H(\mathbf{x}, \omega)$, while a large correlation length produces a slowly varying sample function. The effect of this parameter for a 1D field within the space interval [0,10] is shown in Fig.1.7, where two sample functions are plotted for different correlation lengths, namely 1 and 5.

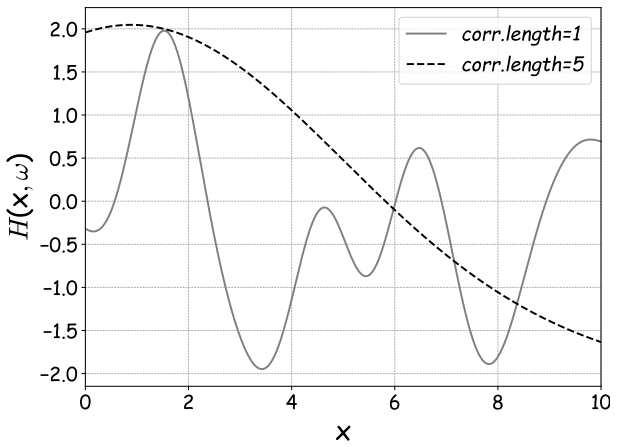

FIGURE 1.7: Effect of the correlation length parameter for a 1D random field $H(\mathbf{x}, \omega)$ within the space interval [0,10].

A measure of correlation between two different random fields $H(\mathbf{x},\omega)$ and $Z(\mathbf{x},\omega)$ at two locations x_1, x_2 is given by the *cross-correlation* function:

$$R_{HZ}(x_1,x_2) = \mathbb{E}[H(x_1),Z(x_2)] = \int_{-\infty}^{+\infty}\int_{-\infty}^{+\infty} \xi_1 \cdot \xi_2 \cdot f_{H(x_1),Z(x_2)}(\xi_1,\xi_2)d\xi_1 d\xi_2 \tag{1.22}$$

The *cross-covariance* function $C_{HZ}(x_1,x_2)$ is, accordingly, given by:

$$C_{HZ}(x_1,x_2) = \mathbb{E}\big[\big(H(x_1)-\mu_H(x_1)\big)\big(Z(x_2)-\mu_Z(x_2)\big)\big] \tag{1.23}$$

Properties

The second-moment characterization of a random field is achieved by identifying its mean and correlation function.

A random field $H(\mathbf{x},\omega)$ is called Gaussian if all random variables $H(x_1,\omega), H(x_2,\omega), ..., H(x_n,\omega)$ have a Gaussian PDF.

A random field is *stationary* (or *homogeneous*) if its joint PDF is independent of the spatial position, thus the mean and variance do not change if shifted in space and do not follow any trends. An illustration of the above definition is shown in Fig.1.8. If all statistics are constant over the space domain the field is called strictly stationary, while if just the mean and autocorrelation are constant the field is called wide-sense stationary.

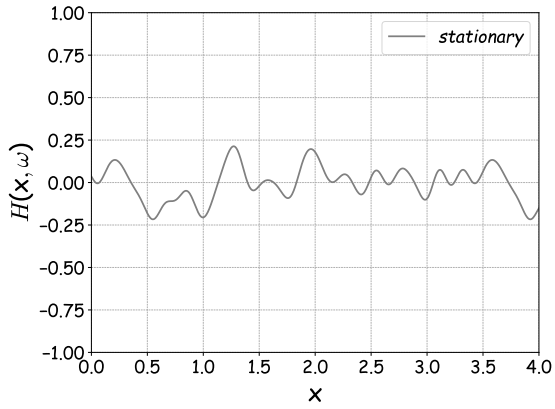

(A) Stationary random field

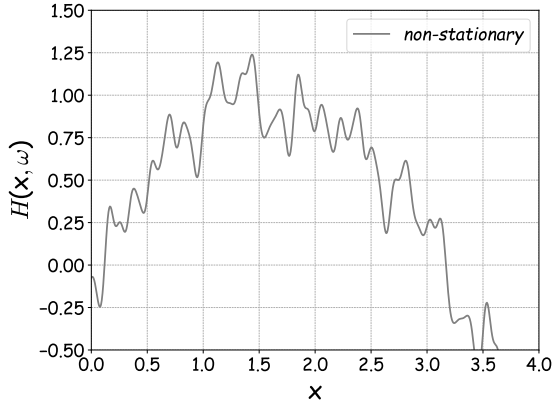

(B) Non-stationary random field

FIGURE 1.8: A sationary and a non-stationary 1D random field within the space interval [0,4].

A stationary random field is called *ergodic* with respect to any statistical property, if this property can be acquired from a single, sufficiently long sample function of the field. For example, in case the sample mean $\frac{1}{n}\sum^{n} H(x_j, \omega_n)$ at a specific location j , is equal to the mean value $\frac{1}{\Omega}\int_{\Omega} H(x,\omega)dx$ of a single sample function over a long space domain Ω, then the random field $H(\mathbf{x},\omega)$ is ergodic in the mean. This property is important when characterizing a random field from measurements, since in the presence of ergodicity the joint PDF of a field can be obtained from just one realization.

Furthermore, it is worth mentioning some famous categories of random processes with distinct properties such as the martingale, the Wiener or Brownian motion process, the Markov process or Markov chain (when discrete) etc. Markov processes are especially important for Markov Chain Monte Carlo algorithms, and according to the Markov property their next value $H(x_{n+1},\omega)$ conditionally to all previous values of the process $H(x_1,\omega), H(x_2,\omega), ..., H(x_n,\omega)$ is only dependent on the current value $H(x_n,\omega)$:

$$P\big(H(x_{n+1},\omega)|H(x_1,\omega), H(x_2,\omega), ..., H(x_n,\omega)\big) = P\big(H(x_{n+1},\omega)|H(x_n,\omega)\big) \tag{1.24}$$

1.5 Machine learning fundamentals

Machine learning allows computers to predict behaviors based on algorithms and example data providing past experience, instead of applying specifically targeted codes. Metamodels (or surrogate models) used for regression problems consist a subclass of machine learning algorithms, which are able to learn how to mimic the behavior of a costly engineering process and, eventually, substitute it. This section provides the basic concepts of machine learning and allows the reader to comprehend the terminology used in the following chapters regarding surrogate modeling for uncertainty quantification. The detailed formulation of the models used in this thesis (artificial neural networks, polynomial chaos expansions and Kriging) are provided within the following chapters. Even though some of these methods have been defined within the literature as response surface methods due to their polynomial nature, they still comply with the fundamental procedures of machine learning, as they are trained in a non-intrusive way without altering the inner structure of the model (black-box approach). The reader may refer to (Alpaydin, 2020) and (Bishop, 2006) for more details on classification and pattern recognition and (Jiang, Zhou, and Shao, 2020) for regression problems.

Categorization of problems

The concept of machine learning lies on training algorithmic models to learn relationships of features or parameters solely by using data in the form of input-output. An algorithm is initially trained (*training phase*) based on a dataset targeting to optimize a performance criterion and then its performance is validated (*testing phase*), ideally, on a different dataset. If accurate predictions for data outside the training dataset are provided, the algorithm has achieved good *generalization* capabilities.

The two basic categories of tasks within machine learning are *classification* and *regression*, and the distinction lies on the type of the output parameters. In case of a boolean output where the aim is assigning each input to a finite number of discrete classes, the task is called classification. For regression problems, the output parameters are continuous variables. The machine learning applications and developments of the current thesis fit the latter category, as the main target is to surrogate costly multiscale models predicting composite properties, by training a regressor-metamodel which can *interpolate* in case the data are not noisy, *extrapolate* (i.e. predict values outside the training range) and, of course, perform regression on noisy data.

Training/learning phase

The training phase is the optimization of the model parameters in order to fit the available (or intelligently selected) data. In case the training dataset includes both the input vectors and the corresponding target outputs, the training follows a *supervised learning* technique. The *unsupervised learning* technique consists of data without any corresponding target values and is mostly common in classification problems. For example, in search of groups within the input data with similar features (*clustering*) or the projection of high dimensional data to lower dimensions (*dimensionality reduction*). Moreover, there are semi-supervised variations enabling *active learning* techniques, where the algorithm can intervene in the data selection and dynamically select new data in order to boost performance. A different strategy not based on target outputs is *reinforcement learning*, where the algorithm interactively discovers appropriate actions by trial and error in order to maximize a reward or avoid a punishment.

The surrogate models of this thesis are based on supervised learning, as most of the regression-based predictive models. The training process consists of selecting the training dataset and tuning the model parameters towards good generalization. The first part is called *design of experiments* in uncertainty quantification and requires efficiency due to the cost of the numerical procedures providing the target outputs. The second part is called *model selection* and depends on the model in-hand.

As an example, let a training set with $\mathbf{x} = \{x_1, ..., x_M\}$ as input and $\hat{\mathbf{y}} = \{\hat{y}_1, ..., \hat{y}_M\}$ as the observed target values. The output is generated by the function $y = \sin(3\pi x)$ with the addition of random noise in every observation. Let also a polynomial function of the form:

$$y(\mathbf{x}, \boldsymbol{\beta}) = \sum_{i=0}^{N} \beta_i x^i \tag{1.25}$$

be the predictive model based on least-squares fitting of coefficients $\{\beta_1, ..., \beta_N\}$, where N is the order of the polynomial. Fig.1.9A shows a prediction when $M = 4$ and Fig.1.9B when $M = 10$, assuming uniform stratified sampling of input points in $[0, 1]$. The polynomial order N equals to 4 in both subfigures. The difference between the predictions is evident, as the small training set results in a poor fit while the larger set provides an acceptable fit. However, it is quite challenging to select an adequate training set in advance, considering also the potential

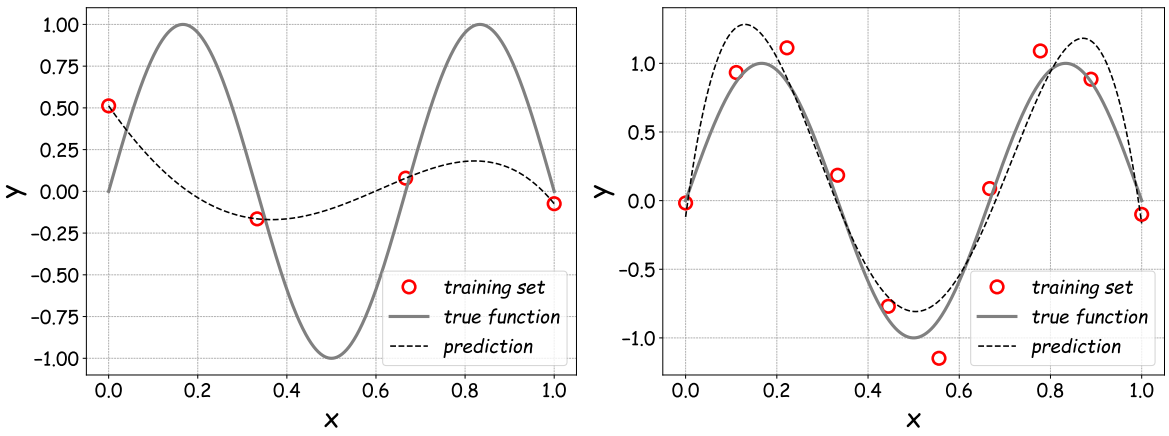

(A) Training set with 4 samples (B) Training set with 10 samples

FIGURE 1.9: Polynomial fitting to a poor training set (A) and an adequate training set (B).

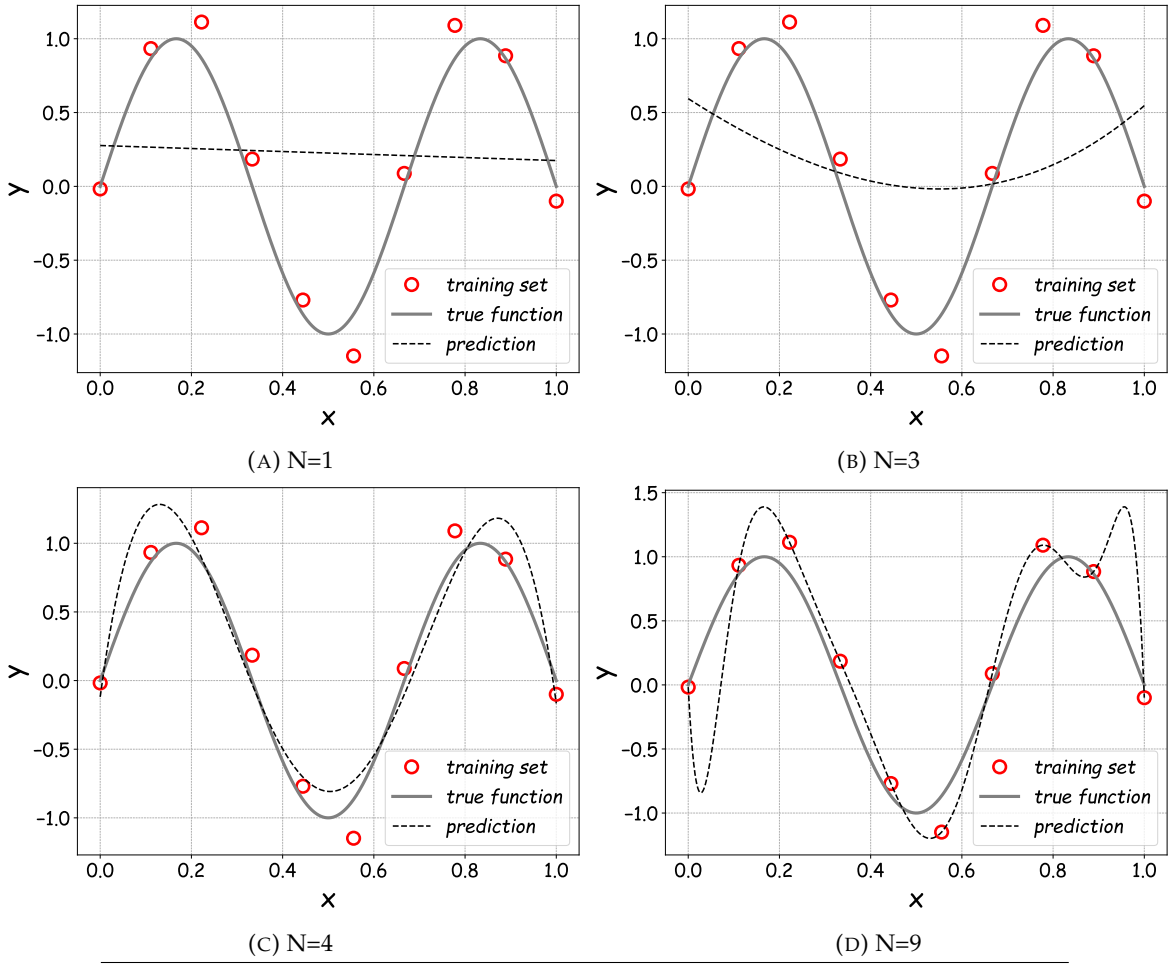

(A) N=1 (B) N=3

(C) N=4 (D) N=9

FIGURE 1.10: Fitting of polynomials with different orders N: underfitting for 1^{st} and 3^{rd} order (A and B), good fitting for 4^{th} order (C) and overfitting for 9^{th} order (D).

cost of acquiring observations.

The same example is used to illustrate the effect of meticulous model selection. The parameter requiring tuning for the linear regression model of Eq.1.25 is the polynomial order N and Fig.1.10 shows its effect for a training dataset of 10 sample points. The 1^{st} (Fig.1.10A) and 3^{rd} order (Fig.1.10B) polynomials do not fit the training data well. This inability of capturing the actual response is also called *bias* in machine learning applications. The 4^{th} order polynomial (Fig.1.10C) approximates the data and the original function quite adequately. The 9^{th} order polynomial (Fig.1.10D) fits the training data perfectly, but it partially oscillates and provides a bad approximation to the original function $y = sin(3\pi x)$. This phenomenon is called *overfitting* and occurs when the model learns the training data too well, ultimately also the noise, and generalizes poorly.

Testing phase

Overfitting is a good reason why machine learning methods need a measurable criterion to assess training and generalization performance. Error metrics are essential for monitoring training and validating models, keeping in mind that visualizations similar to the previous example are not possible for higher dimensions. Moreover, model selection and design of

experiments are mostly based on experience and trial-and-error methods, as there is not a generally accepted strategy except for some rules of thumb.

Once the model is trained, generalization is examined by assembling a new dataset with sample points outside the training set, called the *testing set* or *validation set*. Various error functions exist in order to quantify the prediction uncertainty and obtain an overall assessment of the model, by comparing test predictions against the corresponding target values.

The *mean absolute error* (MAE) and *mean squared error* (MSE) are among the simplest choices of error metrics. Following the concept and nomenclature of the previous curve fitting example, if $\hat{y}_i$ is the target (true) value and $y(x_i, \boldsymbol{\beta})$ is the prediction of the corresponding sample point, they are given by:

$$\text{MAE} = \frac{1}{n}\sum_{i=1}^{n} |y(x_i, \boldsymbol{\beta}) - \hat{y}_i| \tag{1.26}$$

$$\text{MSE} = \frac{1}{n}\sum_{i=1}^{n} \left[y(x_i, \boldsymbol{\beta}) - \hat{y}_i\right]^2 \tag{1.27}$$

where n is the size of the dataset. Assuming a testing set of 100 randomly chosen sample points in [0,1] outside the training set, the above error functions are illustrated in Fig.1.11 as the polynomial order of the model increases. The error calculated from the 10 points of the training set is also included. Both training and testing errors are improving until the 8^{th} order, when the inconsistent increase of the testing error reveals the overfitting of the 9^{th} order (Fig.1.10D). This parametric analysis is representative of a model selection procedure for polynomial-based surrogate models.

Another typical metric for regression problems is the *coefficient of determination* R^2, given by the following formula:

$$R^2 = 1 - \frac{\sum_{i=0}^{n} \left[\hat{y}_i - y(x_i, \boldsymbol{\beta})\right]^2}{\sum_{i=0}^{n} \left[\hat{y}_i - \bar{y}_i\right]^2} \tag{1.28}$$

where $\bar{y}_i$ is the mean of the observed responses. The second term is also called the *fraction of variance unexplained* as due to its denominator is always proportional to the data variance. The closer the value is to 1, the closer the predictions are to the observed responses.

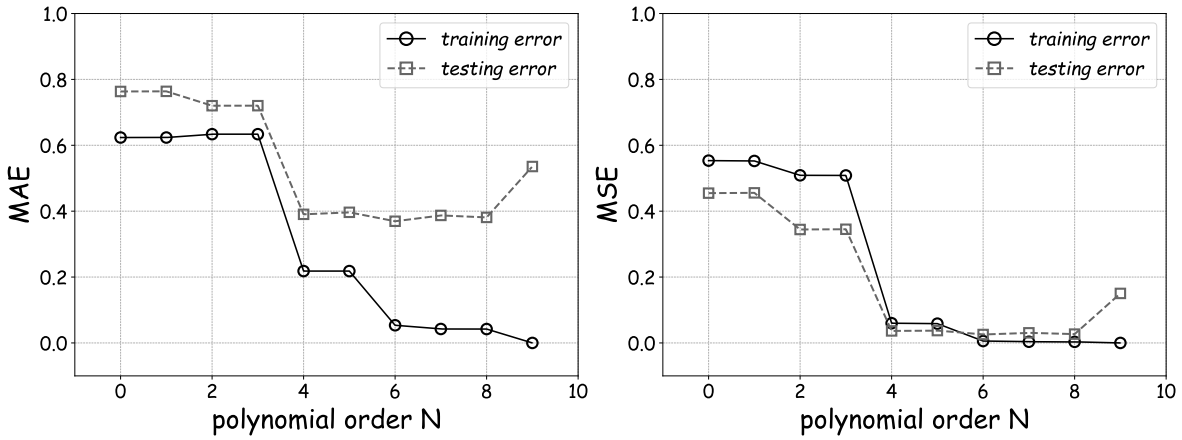

(A) Mean absolute error (B) Mean squared error

FIGURE 1.11: Mean absolute error (A) and mean squared error (B) as an evolution of the polynomial order for both the training and testing sets.

In case there is not enough data for adequate training and testing sets, *cross-validation* methods can be beneficial, since a fraction of data is used for training while all data points are used for validation. For a dataset consisted of M sample points, the *k-fold* cross-validation splits the set to k subsets of equal size $N = M/k$. The model is trained k times, each time using all but one subsets for training and the remaining subset for testing. Assuming an error function E similar to the ones already mentioned, the k-fold error metric is given by:

$$e_{\text{k-fold}} = \frac{1}{k}\sum_{i=1}^{k}\frac{1}{N}\sum_{j=1}^{N} E\big[\hat{y}_j, y_{-i}(x_j, \boldsymbol{\beta})\big] \tag{1.29}$$

where $y_{-i}(x_j, \boldsymbol{\beta})$ is the prediction of the model trained from all subsets except i for the point x_j. A special cross-validation case is the *leave-one-out method* where the number of folds is equal to the number of original sample points ($k = M$).

Bootstrapping can also be used to assess the performance of a predictive model. Several bootstrap subsets are created by resampling datapoints from the original dataset with equal probability (*resampling with replacement*). The model is trained from each subset and the points not sampled from the original set are used as testing set. The errors are collected and the overall bootstrap error is calculated via a leave-one-out strategy as:

$$e_{\text{boot}} = \frac{1}{k}\sum_{i=1}^{k} E_{-i} \tag{1.30}$$

where k is the number of bootstrap subsets and E_{-i} is the error of all subsets except i.

Curse of dimensionality

When machine learning methods are applied in high-dimensional spaces they suffer from the *curse of dimensionality*, which is described as the exponential growth of required samples towards high accuracy with each additional dimension. An example is presented in Fig.1.12 for a set of 1000 sample points drawn from a 2D standard Gaussian distribution. By projecting the data to the lower dimensions X and Y, the samples falling within the area of [1,3] are 15.5% and 14.5%, respectively. However, only 1.15% of the data are covering the equivalent area in 2D, hence it is unlikely to reach good accuracy levels without increasing the number of samples.

An additional barrier is the consequent growth of model parameters which boosts the computational cost during the training phase. Returning to the curve fitting example of Eq.1.25 and assuming d input variables and a 2^{nd} order polynomial, the following formula is developed:

$$y(\mathbf{x}, \boldsymbol{\beta}) = w_0 + \sum_{i=1}^{d}\beta_i x_i + \sum_{i=1}^{d}\sum_{j=1}^{d}\beta_{ij} x_i x_j \tag{1.31}$$

while the number of coefficients grows proportionally to d^2 as the dimension increases. Considering that complex surfaces require higher order polynomials, the method becomes practically ineffective.

Besides the straightforward solution of adding more samples to the learning sets, dimensionality reduction techniques provide a remedy when working in high-dimensional spaces. *Principal component analysis* is an unsupervised method calculating the dimensions with the highest variance via eigenvalue analysis and, eventually, identifying a reduced space with almost the same variance (Jolliffe, 2002). The method of *active subspaces* is a recent variation in which the gaps between the eigenvalues are used instead of their magnitude (Constantine, 2015).

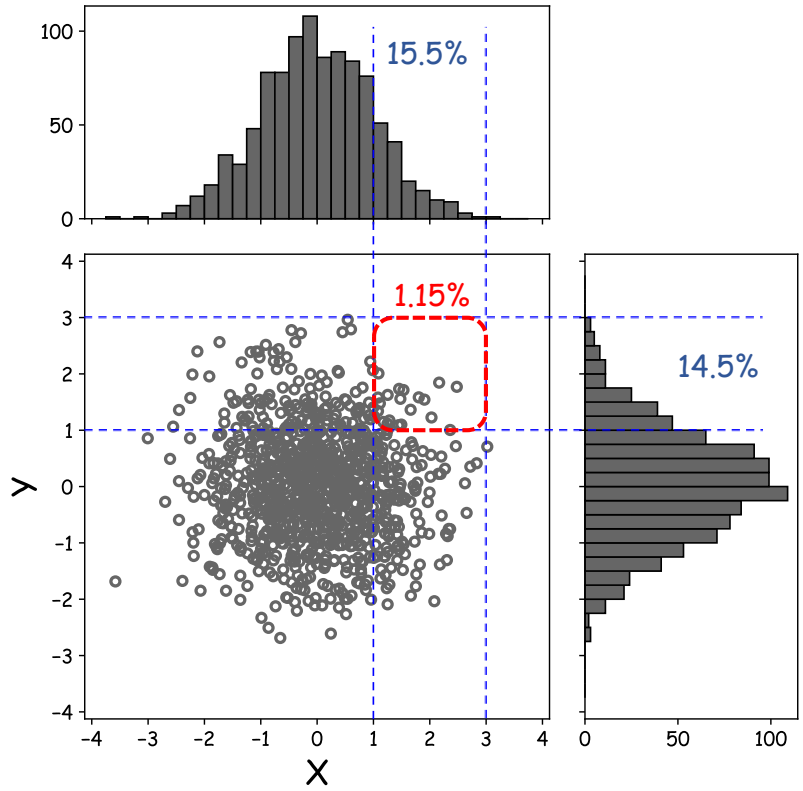

FIGURE 1.12: Illustration of the curse of dimensionality: from 1000 normally distributed points in 2D (μ=0, σ=1) only 1.15% falls within the area of 2±1, whereas the percentage at the 1D projections of the original space is 15.5% and 14.5%.

Chapter 2

Neural Network Assisted Multiscale Analysis for the Elastic Properties Prediction of 3D Braided Composites under Uncertainty

This paper presents an efficient probabilistic framework predicting effective stiffness properties of triaxially braided composites. The framework is based on FE modeling accelerated by artificial neural networks and is able to integrate both material and geometric uncertainties. A classification of the importance of each random input parameter is achieved via global sensitivity analysis.

The paper is published in Composite Structures, Volume 183, 2018, Pages 550–562.

Composite Structures 183 (2018) 550–562

Contents lists available at ScienceDirect

Composite Structures

journal homepage: www.elsevier.com/locate/compstruct

Neural network assisted multiscale analysis for the elastic properties prediction of 3D braided composites under uncertainty

Georgios Balokas [a,*], Steffen Czichon [a], Raimund Rolfes [b]

[a] Structure Development Department, ELAN-AUSY GmbH, Channel 2 Harburger Schloßstr. 24, 21079 Hamburg, Germany
[b] Institute of Structural Analysis, Leibniz Universität Hannover, Appelstraße 9A, 30167 Hannover, Germany

ARTICLE INFO

Article history:
Received 23 January 2017
Revised 1 June 2017
Accepted 13 June 2017
Available online 15 June 2017

Keywords:
Braided composites
Homogenization
Multiscale analysis
Probabilistic analysis
Global sensitivity analysis
Artificial neural networks

ABSTRACT

The stiffness prediction of textile composites has been studied intensively over the last 20 years. It is the complex yarn architecture that adds exceptional properties but also requires computationally expensive methods for the accurate solution of the homogenization problem. Braided composites are of special interest for the aerospace and automotive industry and have thus drawn the attention of many researchers, studying and developing analytical and numerical methods for the extraction of the effective elastic properties. This paper intends to study the effect of uncertainties caused by the automated manufacturing procedure, to the elastic behavior of braided composites. In this direction, a fast FEM-based multiscale algorithm is proposed, allowing for uncertainty introduction and response variability calculation of the macro-scale properties of 3D braided composites, within a Monte Carlo framework. Artificial neural networks are used to reduce the computational effort even more, since they allow for rapid generation of large samples when trained. With this approach it is feasible to apply a variance-based global sensitivity analysis in order to identify the most crucial uncertain parameters through the costly Sobol indices. The proposed method is straightforward, quite accurate and highlights the importance of realistic uncertainty quantification.

1. Introduction

Even though composite materials have been available for several decades already, they are steadily one of the most active engineering research topics. This is justified by their excellent performance in terms of stiffness-to-weight and strength-to-weight ratio, fatigue strength, corrosion resistance, stability and impact properties and numerous other advantages over conventional engineering metals. Composite structures are mainly separated into two categories according to the fiber architecture: laminated composites (a bundle of unidirectional laminas) and 2D or 3D textile composites (where the fibrous reinforcements are interlaced in multi-directions). In textiles, the linear assemblage of the fibers into yarns and the consequent bonding/interlocking of the yarns into specific patterns, add through-the-thickness reinforcement and thus balance between in-plane and out-of-plane properties. A review on textile composites can be found in [1], whereas modeling challenges are investigated and documented in [2]. In [3], a review emphasizing on woven textiles is presented.

Braided composites consist a class of textiles, increasingly used in a wide variety of high-performance industry applications in aerospace, automotive and marine sectors. Braiding can be defined as a composite material preform manufacturing technique where a braiding machine deposits continuous, interwined, fiber tows (yarns) to create desired reinforcing braid architecture before or during the impregnation of the fibers, according to [4]. The combination of an automated and reproducible process together with an excellent rate of material deposition for mass-production of high-level structures, is the main reason for the attention braided composites have received. Nevertheless, analysis of such materials sets challenges and computational obstacles, as it requires very detailed models in order to capture the complexity of braided structures. Review papers on braided describing modeling challenges and trends, can be found in [4,5].

In most problems of engineering and applied mechanics, only the macroscopic mechanical behavior is of interest. However, in composites and generally in heterogeneous materials, the mechanical properties of the individual components along with other lower-scale parameters defining their spatial and size distribution

* Corresponding author.
E-mail address: Georgios.Balokas@elan-ausy.com (G. Balokas).

http://dx.doi.org/10.1016/j.compstruct.2017.06.037
0263-8223/

(e.g. volume fractions etc.), govern in fact the overall mechanical behavior. Hence, attributes of micro and meso scale are extremely important for a better understanding of the elemental properties of those materials. On that account, various modeling approaches for predicting the effective elastic properties of braided composites have been developed, with the intention to describe accurately and efficiently the connection between micromechanical characteristics and macro stiffness properties. A review on the stiffness prediction modeling approaches is offered in [4]. An attractive analytical micromechanics model able to also predict the inelastic and strength behavior (called bridging), is presented in [6], while another analytical model based on numerical simulation and mathematical modeling after analyzing the microstructure of the braided preforms, can be found in [7]. Besides analytical, plenty of numerical multiscale models can be found in the literature, like [8] which is based on the homogenization variational principle and [9] where use of the TexGen mesoscale modeling software is made. In [10], a recent study concerning the friction consideration in a novel interface constitutive model is presented, whereas in [11] a comparison is performed between periodic meshes and a more efficient freely generated mesh of the braided unit-cell. A complete study on elastic prediction of braided composites using both analytical and numerical models is presented in [12]. Recently, an interesting numerical study accounting for the pore defects effect on the elastic properties of braided was offered in [13]. A general information-passing multiscale numerical approach is presented and used in [14,15], enabling material nonlinearity introduction and providing not only stiffness but also strength.

Due to the multiphase and heterogeneous nature of composites, uncertainties are of great substance. Therefore the variability in elastic constants needs to be considered in the mechanical response analysis of composite structures. In principal, uncertainties are classified as either aleatory (inherent randomness in the system) or epistemic (due to partial knowledge of the problem and parameters). A noteworthy attempt to compile and classify the uncertainty modeling approaches for composite structures was made in [16], where it is stated that regarding composite materials, aleatory uncertainty typically refers to fiber and matrix characteristics, manufacturing variations etc., whereas epistemic may be associated with the type of experimental and modeling methods being used. Recent studies [17,18] showed that aleatory uncertainty and specifically fiber waviness, plays an important role in compressive failure of polymer composites by triggering fiber kinking. Significant work regarding the aleatory uncertainty assessment of composite shells and the coupling with current design methods has been performed in [19,20].

Consequently, the scatter in the mechanical properties due to aleatory uncertainty is a dynamic research field, with various approaches considering the probabilistic homogenization problem. Linear perturbation techniques were introduced in [21], while approximate solutions of the elastic response aided by Kriging models were presented in [22]. The influence of random inclusions in the microstructure by applying the extended finite element method (XFEM) was described in [23], whereas the study in [24] established the synergy of Monte Carlo simulation (MCS) and the XFEM for the homogenization problem with random microstructures. A variety of probabilistic approaches in carbon fiber reinforced polymers can be found in [25]. Moreover, the implementation of surrogate (or meta) models becomes a necessity when it comes to the stochastic assessment of such materials. Reviews on neural network (NN) applications in composite materials can be found in [26,27], while a recent review covering a variety of surrogates (polynomial chaos, radial basis functions, Kriging etc.) is presented in [28]. Stochastic optimization is also a field of application for the above models [29,30]. NN have been also used for forming processes simulations [31] while an interesting approach that couples polynomial approximations and NN is offered in [32].

However, the aforementioned work concerns only continuous unidirectional fiber laminate composites. It is only recently that a perturbation technique for the stochastic homogenization of woven composites was proposed in [33], which theoretically could be applied in any textile, though being perturbation-based is limiting information on the shape of the elastic parameters probability density functions (PDFs) and also investigates exclusively uncertainties caused by the material properties of the constituents. A study adding scatter information on braided composites was offered in [34], but it is founded more on model updating based on experimental data, than on probabilistic homogenization modeling for the variability calculation. Also there is not information about the exact source of uncertainty.

In this paper, a probabilistic FEM-based method is proposed for the prediction of the elastic constants of braided composites, under various sources of aleatory uncertainty. The algorithm is based on a Monte Carlo framework so that statistical characteristics of the elastic response can be described in full detail. Uncertainties are covering a wide range of imperfections that can be caused from manufacturing processes, while the numerical tools used in the method allow random properties to be inserted independently. As a result, the effect of every random input can be measured with the aid of a sensitivity analysis technique. With the mesoscale modeler used in the proposed methodology, important geometric properties for a braided material can be taken into account. To further improve the efficiency of the costly Monte Carlo technique and sensitivity analysis, artificial Neural Networks are implemented as surrogate models, decreasing the computational cost by orders of magnitude. The proposed method is applied on a typical triaxial 3D braided model.

2. Homogenization scheme

2.1. Theoretical approach

Consider a macrostructure that is heterogeneous on a lower scale. Let a continuous body of this heterogeneous material denoted M, with multiple phases (Fig. 1). The governing equilibrium and kinematic equations for a solid mechanics problem posed on this structure are:

$$div(\boldsymbol{\sigma}) + \rho\, \boldsymbol{b} = \rho\, \ddot{\boldsymbol{u}} \qquad in\ R \tag{1}$$

$$\boldsymbol{\sigma} = \mathscr{C}\, \boldsymbol{\varepsilon} \tag{2}$$

where $\boldsymbol{\sigma}$ is the stress tensor, $\boldsymbol{\varepsilon}$ is the strain tensor, $\boldsymbol{b}$ are the acting body forces, ρ is the body density and $\mathscr{C}$ is the elasticity tensor of the constitutive equation (Eq. (2)). The essential and natural boundary conditions (BCs) respectively are:

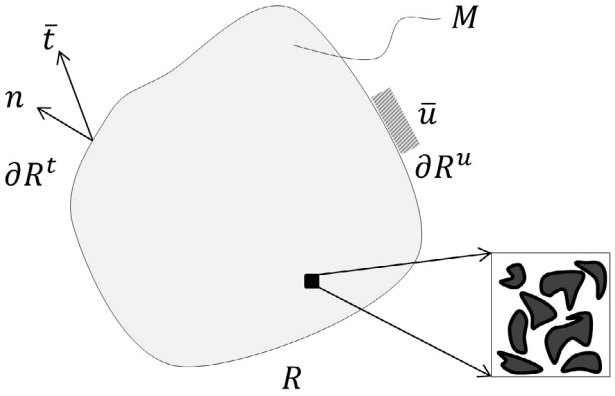

Fig. 1. Heterogeneous material M of the macrostructure in domain R, subjected to essential and natural boundary conditions on surfaces ∂R^u and ∂R^t respectively.

$$\boldsymbol{u} = \bar{\boldsymbol{u}} \qquad on\ \partial R^u \tag{3}$$

$$\boldsymbol{t} = \boldsymbol{\sigma}\,\boldsymbol{n} = \bar{\boldsymbol{t}} \qquad on\ \partial R^t \tag{4}$$

where $\boldsymbol{n}$ is the unit vector normal to the surface ∂R^t where the traction $\bar{\boldsymbol{t}}$ is applied. Due to the presence of heterogeneities, the density and the explicit form of the constitutive equation fluctuate from phase to phase, rendering the solution of the problem very challenging in its original form. The subject of homogenization is the determination of approximate effective quantities ρ^* and $\mathscr{C}^*$, so that the problem of the homogeneous effective material M^* with the same BCs would be solvable.

In essence, the homogenization process is performed on a representative volume element (RVE) of the heterogeneous material which is defined by Hill [35] as the smallest sample entirely typical of the whole mixture on average. So after several averaging procedures, the homogenization problem degenerates to the following RVE problem under quasistatic conditions:

Determine $\boldsymbol{u}$ so that:

$$div(\boldsymbol{\sigma}) = 0 \quad in\ volume\ V\ of\ RVE \tag{5}$$

subject to BCs such that:

$$\boldsymbol{\sigma}^* \cdot \boldsymbol{\varepsilon}^* = \frac{1}{|V|}\int_V \boldsymbol{\sigma}\cdot\boldsymbol{\varepsilon}\, dV \tag{6}$$

Eq. (6) is known as the Hill's energy averaging theorem and states that the strain energy of the homogenized macrocontinuum, with macroscopic stress and strain tensors $\boldsymbol{\sigma}^*$ and $\boldsymbol{\varepsilon}^*$ respectively, has to be equal to that of the microstructured RVE, with $\boldsymbol{\sigma}$ and $\boldsymbol{\varepsilon}$ being the corresponding microscopic quantities.

When the solution of the previous problem is obtained, the effective constitutive formulation is determined by relating $\boldsymbol{\sigma}^*$ to $\boldsymbol{\varepsilon}^*$. For an elastic orthotropic material, the generalized stress–strain constitutive law of Eq. (2) is given via:

$$\begin{Bmatrix}\sigma_1\\ \sigma_2\\ \sigma_3\\ \tau_{23}\\ \tau_{31}\\ \tau_{12}\end{Bmatrix} = \begin{bmatrix}\mathscr{C}_{11} & \mathscr{C}_{12} & \mathscr{C}_{13} & 0 & 0 & 0\\ \mathscr{C}_{21} & \mathscr{C}_{22} & \mathscr{C}_{23} & 0 & 0 & 0\\ \mathscr{C}_{31} & \mathscr{C}_{32} & \mathscr{C}_{33} & 0 & 0 & 0\\ 0 & 0 & 0 & \mathscr{C}_{44} & 0 & 0\\ 0 & 0 & 0 & 0 & \mathscr{C}_{55} & 0\\ 0 & 0 & 0 & 0 & 0 & \mathscr{C}_{66}\end{bmatrix}\begin{Bmatrix}\varepsilon_1\\ \varepsilon_2\\ \varepsilon_3\\ \gamma_{23}\\ \gamma_{31}\\ \gamma_{12}\end{Bmatrix} \tag{7}$$

The inverse of the macroscopic stiffness matrix $\boldsymbol{S} = \mathscr{C}^{-1}$ is the compliance (or flexibility) matrix. The elastic properties can be determined from compliance constants by applying separately uniaxial normal/shear stresses in each direction/plane and restricting the remaining degrees of freedom. The compliance matrix as a function of the engineering constants has the following form:

$$\begin{Bmatrix}\varepsilon_1\\ \varepsilon_2\\ \varepsilon_3\\ \gamma_{23}\\ \gamma_{31}\\ \gamma_{12}\end{Bmatrix} = \begin{bmatrix}\frac{1}{E_1} & -\frac{\nu_{21}}{E_2} & -\frac{\nu_{31}}{E_3} & 0 & 0 & 0\\ -\frac{\nu_{12}}{E_1} & \frac{1}{E_2} & -\frac{\nu_{32}}{E_3} & 0 & 0 & 0\\ -\frac{\nu_{13}}{E_1} & -\frac{\nu_{23}}{E_3} & \frac{1}{E_3} & 0 & 0 & 0\\ 0 & 0 & 0 & \frac{1}{G_{23}} & 0 & 0\\ 0 & 0 & 0 & 0 & \frac{1}{G_{31}} & 0\\ 0 & 0 & 0 & 0 & 0 & \frac{1}{G_{12}}\end{bmatrix}\begin{Bmatrix}\sigma_1\\ \sigma_2\\ \sigma_3\\ \tau_{23}\\ \tau_{31}\\ \tau_{12}\end{Bmatrix} \tag{8}$$

The compliance matrix is naturally symmetric due to Maxwell's reciprocal theorem:

$$\frac{\nu_{ij}}{E_i} = \frac{\nu_{ji}}{E_j} \tag{9}$$

2.2. Numerical implementation

This study employs the open-source software TexGen [36] for the treatment of the homogenization problem. TexGen is a 3D solid modeler of textile structures at unit-cell level, developed at the University of Nottingham. It allows user-friendly modeling of the complex yarn architecture through either graphical user interface or Python scripting. The fact that yarns are simulated as solid volumes representing the approximate bounds of the fibers contained within them, makes the modeling feasible through simply defining the path nodes and the cross-section of the yarns.

TexGen approaches the unit-cell according to the principles documented in [37], where only translational symmetry transformations are employed (reflectional or rotational symmetries are excluded). This results in major advantages, as the unit-cell can be subjected to arbitrary combinations of macroscopic stresses and strains with a single set of BCs, but also can be applicable to nonlinear problems of any nature. Periodic BCs are applied on the unit-cell in order to satisfy Eq. (6), based on the following relations between the macroscopic strains and the relative displacements at a point P in the unit-cell to those at P' as the image of P in another cell:

$$\begin{aligned} u' - u &= (x'-x)\varepsilon_x^0 + (y'-y)\gamma_{xy}^0 + (z'-z)\gamma_{xz}^0\\ v' - v &= (y'-y)\varepsilon_y^0 + (z'-z)\gamma_{yz}^0\\ w' - w &= (z'-z)\varepsilon_z^0 \end{aligned} \tag{10}$$

where x, y and z are the coordinates of point P, u, v and w are the displacements at the same point, the respective symbols with an apostrophe are associated with the point P' (an image of P) and $\varepsilon_x^0, \varepsilon_y^0, \varepsilon_z^0, \gamma_{yz}^0, \gamma_{xz}^0, \gamma_{xy}^0$ are the macroscopic strains. In obtaining the displacement field of Eq. (10), the following kinematic constraints are applied:

$$\begin{aligned} &u = v = w = 0\\ &\frac{\partial w}{\partial x} = \frac{\partial v}{\partial x} = \frac{\partial w}{\partial y} \qquad at\ \ x = y = z = 0 \end{aligned} \tag{11}$$

The exact procedure on how to derive the periodic BCs from this formulation, is referred to [37].

TexGen has the ability to automatically produce an input file for the ABAQUS commercial FE package [38], including all necessary data about geometry, materials and support of the unit-cell. The ABAQUS implementation of the periodic BCs involves the use of an equation for the representation of the relative displacement of two node sets at opposite boundaries (faces, edges etc.), equal to the displacement of a dummy node. In this manner the unit-cell deformation is controlled by applying BCs to the dummy node.

Regarding the elastic properties extraction, concentrated loads are applied on those dummy nodes separately in every necessary direction, which are related to the macroscopic stresses through virtual work equilibrium [37]. For example, if a force F_x is applied to the degree of freedom ε_x^0 of a unit-cell while all the other extra degrees of freedom are free from constraints, the work done by the force is:

$$W = \frac{1}{2}F_x\varepsilon_x^0 \tag{12}$$

The strain energy stored in the unit-cell can be expressed in terms of the macroscopic stresses and strains as:

$$E = \frac{1}{2}\int_V \sigma_x^0\varepsilon_x^0\, dV = \frac{1}{2}V\sigma_x^0\varepsilon_x^0 \tag{13}$$

where σ_x^0 is the macroscopic normal X stress and V is the unit-cell volume. Equating W to E results in the following relationship for the X-direction:

$$\sigma_x^0 = \frac{F_x}{V} \tag{14}$$

The effective longitudinal modulus of the material would then be obtained as:

$$E_x^0 = \frac{\sigma_x^0}{\varepsilon_x^0} = \frac{F_x}{V\varepsilon_x^0} \quad \text{when} \quad F_y = F_z = F_{yz} = F_{zx} = F_{xy} = 0 \tag{15}$$

The forces are applied volumetrically so that all stresses similar to Eq. (14) would be unitary. As a result, the displacement output from the FE analysis at the dummy nodes will represent the strain and according to Eq. (15), the moduli would simply be the inverse of calculated strains. The remaining effective properties for an orthotropic material are obtained accordingly (six load cases in total).

3. Global sensitivity analysis for Monte Carlo simulation

The inherent probabilistic nature of most design parameters hampers the deterministic treatment of engineering problems and leads to analysis under uncertainty. In a probabilistic model with multiple discrete sources of uncertainty, sensitivity analysis offers the impact of each random input to the total output variability of the model. Hence, the system complexity can be reduced and the cause-and-effect relationship can be explained.

This paper applies a variance-based global sensitivity analysis (GSA) that is able to describe the sensitivity pattern of a model, through a full decomposition of the output variance into terms corresponding to the input parameters and their interactions. The principal advantages of such techniques over local sensitivity analyses are the consideration of the whole input space, the applicability in nonlinear responses and the ability to measure effects of interaction in non-additive systems [39].

3.1. Formulation

Consider a model $y = f(x_1, x_2, \dots\ x_k)$ with y a scalar. Given that f is a square integrable function over the k-dimensional unit hypercube Ω^k, the model may be decomposed in the following way [40]:

$$f = f_0 + \sum_i f_i + \sum_{j>i} f_{ij} + \ldots + f_{12\ldots k} \tag{16}$$

where $f_i = f_i(x_i), f_{ij} = f_{ij}(x_i, x_j)$ etc. All the terms in the functional decomposition are orthogonal. Consequently, they can be calculated using the conditional expectations of the model output y as:

$$\begin{aligned} f_0 &= E(y) \\ f_i &= E(y|x_i) - E(y) \\ f_{ij} &= E(y|x_i, x_j) - f_i - f_j - E(y) \end{aligned} \tag{17}$$

If Eq. (16) is squared and integrated, appears the expression:

$$\int f^2 d\boldsymbol{x} - f_0^2 = \sum_i \int f_i^2 dx_i + \sum_{j>i} \int f_{ij}^2 dx_i dx_j + \ldots + \int f_{12\ldots k}^2 dx_1 dx_2 \ldots dx_k \tag{18}$$

The left part of Eq. (18) is the total variance of output y and the terms of the right part are decomposed variance terms with respect to the sets of the input x_i. With the aid of Eq. (17) the final expression for the variance decomposition is reached:

$$Var(y) = \sum_{i=1}^{k} V_i + \sum_{j>i}^{k} V_{ij} + \cdots + V_{12\ldots k} \quad \text{where} \quad \begin{aligned} V_i &= Var_{x_i}(E_{x_{\sim i}}(y|x_i)) \\ V_{ij} &= Var_{x_{ij}}(E_{x_{\sim ij}}(y|x_i, x_j)) - V_i - V_j \quad etc. \end{aligned} \tag{19}$$

The $x_{\sim i}$ notation indicates the set of all variables except x_i. A direct variance-based measure of sensitivity called first-order sensitivity index or first order Sobol index, can be obtained by dividing the term of interest from the decomposed variance by the unconditional variance $Var(y)$:

$$S_i = \frac{V_i}{Var(y)} \tag{20}$$

This is the contribution to the output variance of the main effect of x_i, therefore it measures the effect of varying x_i alone, but averaged over variations in other input parameters. It is normalized by the total variance to provide a fractional contribution.

3.2. Monte Carlo implementation

In the majority of cases, the model does not allow for an analytical evaluation of the integrals in the variance decomposition. Thus, GSA is performed through estimators for the Sobol indices, emerging from a sampling technique within a Monte Carlo framework. A summary of the estimators described so far in the literature is documented in [41]. In this paper we use the following estimator for the first order index:

$$V_i = Var_{x_i}(E_{x_{\sim i}}(y|x_i)) \approx \frac{1}{N}\sum_{j=1}^{N} f(B)_j (f(A_B^i)_j - f(A)_j) \tag{21}$$

In the above equation, N is the problem-dependent base sample (large enough sample size for the Monte Carlo procedure to converge) and $f(A), f(B), f(A_B^i)$ are the model outputs of the input matrices A, B and A_B^i respectively. The sample matrices are generated as follows [39]: A and B are two (N, k) matrices with random sample points of the input space, where k is the number of random inputs. Matrix A_B^i is identical with A, except that its ith column is substituted with the ith column of B $(i = 1, \ldots, k)$. As a result, k matrices similar to A_B^i are required, which leads to a total computational cost of $N(k+2)$ simulations.

The accuracy of the estimators is highly dependent on N. So computational expense is a problem when the model needs considerable time for a single simulation (e.g. FE model). In addition, the convergence of the Sobol index (Eq. (20)) might require a large sample N when approximated with an estimator (Eq. (21)), regardless if the crude Monte Carlo problem has already converged for a smaller size. The potential excessive cost of the Sobol indices has guided researchers to alternative techniques, like polynomial chaos expansions [42,43].

4. Artificial neural networks

Artificial neural networks, or simply neural networks (NN), are mathematical models based on biological nervous systems, with the ability to learn their environment by example through training via samples. In principal, they are used as a Machine Learning method for a variety of applications, such as prediction, pattern recognition, decision making etc. For engineering mechanics, they are mostly considered as surrogate (or meta) models for the rapid mapping between given input and output quantities. Their massively parallel structure composes a very fast information-processing mechanism, which can enhance the efficiency of numerical simulations by producing extreme amount of results with trivial computational effort. As a result, the use of NN can practically eliminate any limitation on the scale of the problem and the sample size used for MCS.

4.1. Basic neural network structure

A neural network consists of at least three layers: the input, the output and one hidden layer. In general there might be several hidden layers. Terminology is borrowed from neuroscience, as the units (nodes) inside every layer are called neurons, while the links between them are called synapses. Although there are numerous

different NN architectures (e.g. radial basis function networks, Kohonen self-organizing networks, recurrent networks among others [44]), the most commonly used for surrogate modeling in engineering are the multilayer feed-forward NN.

A typical configuration of a single layer feed-forward network is demonstrated in Fig. 2. The input neurons (squares) do not process information and only connect the network to the external environment, as terminal points. The neurons of the hidden layer (circles) process information coming from a previous layer and feed their output to the next layer. The hidden denotation originates from the lack of directly observable data. Thus, information is propagated in a single direction, from the input data towards the output (feed-forward). It is noted that there is no connection among neurons of the same layer.

Regarding the processing neurons, their interior structure is summarized in the lower part of Fig. 2. For every connection between neurons there is a weight parameter w_{ij}, which corresponds to the influence of each of the preceding neurons. Every input x_i received by the neuron is multiplied with the corresponding weight and then the sum of those products is calculated by the following formula:

$$z_j = \sum_{i=1}^{n} x_i w_{ij} + b \tag{22}$$

where b is a bias term allowing the neuron to cover a wider range. The result is sent through a nonlinear transfer function called activation function, where the nonlinearity of the decision boundary is introduced. Common activation functions are the sign function and sigmoid functions like the logistic or the hyperbolic tangent function etc.

4.2. Training process

Training a NN is a challenging task, as the problem of overfitting is lurking. The learning procedure is based on a general function optimization problem, where the weights are adjusted in order for the mapping to approximate closely the training set. The objective function is the sum squared error between the predicted output $t(\boldsymbol{w})$ and the target output y_0:

$$E(w_{ij}) = \frac{1}{2}\sum [t(w_{ij}) - y_0]^2 \tag{23}$$

In the minimization process, the weights of all the synapses are modified until the desired error level is achieved or the maximum number of cycles is reached. The weights are updated through an iterative procedure:

$$w_{ij}^{(t+1)} = w_{ij}^{(t)} + \Delta w_{ij} \tag{24}$$

where Δw_{ij} is the correction of the weight at the tth learning step, which is calculated by the following formula:

$$\Delta w_{ij} = -n\frac{\partial E}{\partial w_{ij}} \tag{25}$$

where n is a small parameter adjusting the correction each time, called learning rate. The algorithm described above is called backpropagation algorithm [44].

The definition of overfitting is the poor generalization ability of a NN despite the very small error prediction over the training data. The learning process is so powerful that guides the NN to learn the train data "too well". However, due to the large amount of neurons involved, the error for new predictions (outside the training data) is large. An illustrative example is given in Fig. 3 for the 2D space (scalar input and output), where an overfitting of the training sample (Fig. 3a) is contradicted with a good fit for the exact same data (Fig. 3b).

There are several methods able to rectify the overfitting problem, with the most popular among others being the early stopping of the training and the regularization of the error function [45]. The first one involves a fraction of the sample data being used as a validation dataset, whose error is monitored over the iterations and stops training if its value increases rapidly. Regularization is the intention to smoothen the network's response by modifying the objective function. The idea emerged because of the excessive output variability observed by large weights.

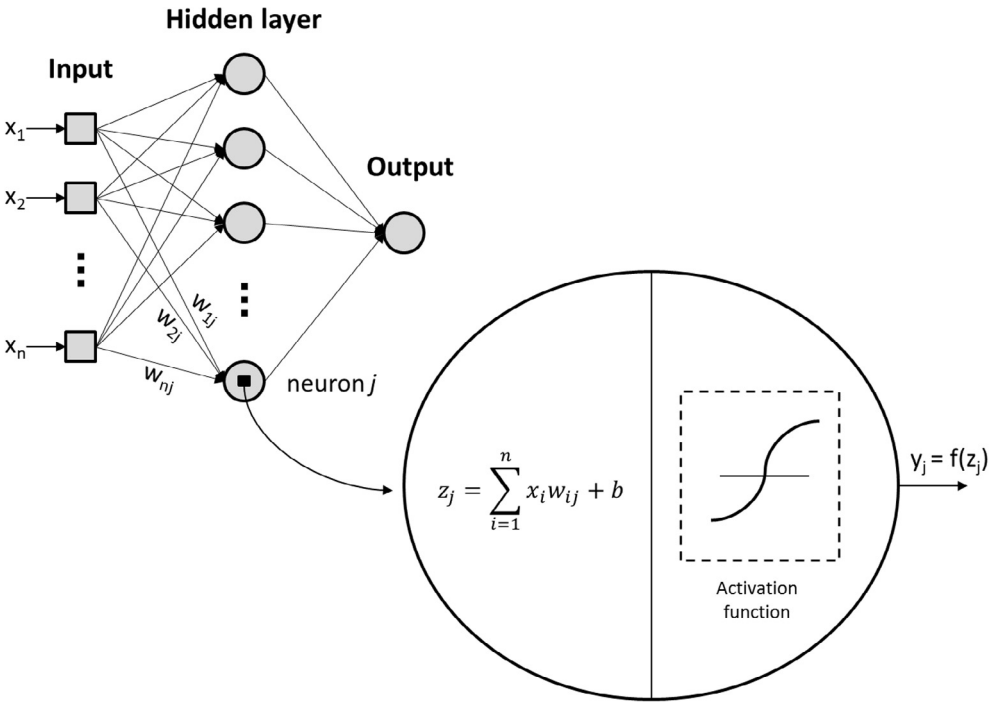

Fig. 2. Architecture of a single layer feed-forward network and neuron structure.

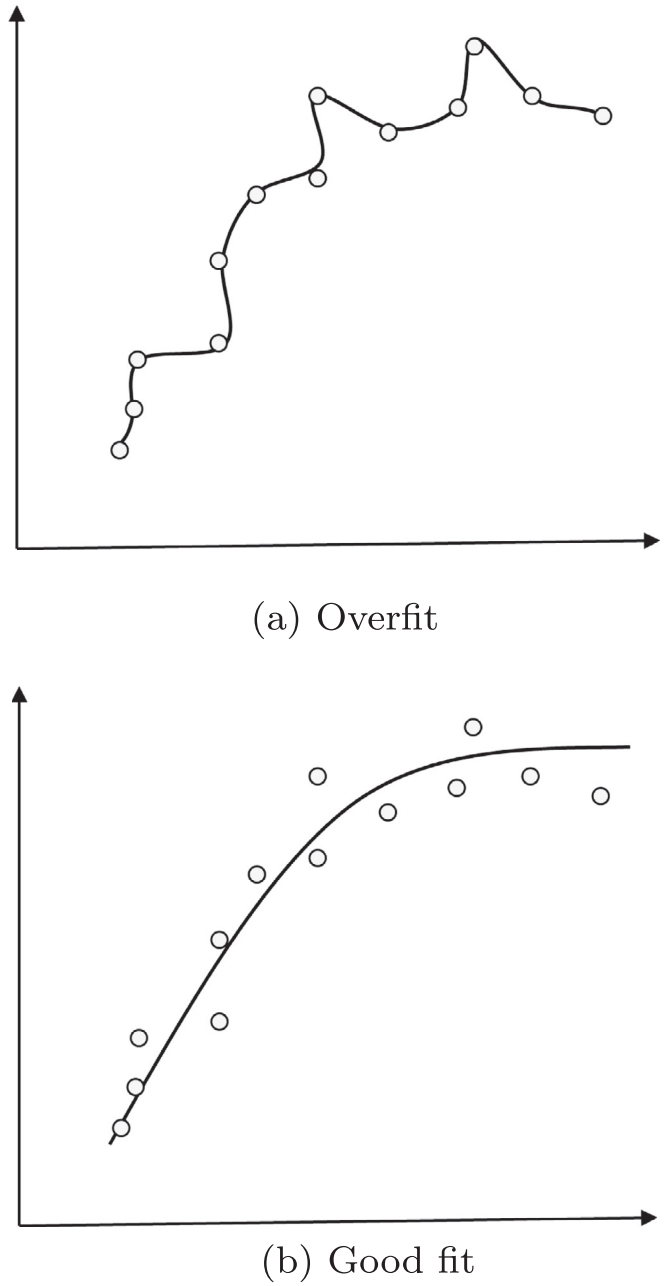

Fig. 3. Overfitting example.

5. Proposed methodology

As mentioned in the introduction, the proposed method is used for the probabilistic analysis of 3D braided composite structures in a Monte Carlo framework. However, it is not limited on braided because the use of TexGen as a modeler allows for any kind of textile composite. Even though the problem is linear, the method is based on the versatile tool of MCS and is, therefore, able to calculate the complete PDF of the response (not just low order moments or probabilities of exceedance of a prescribed value etc.).

Moreover, the method not only allows for material property related uncertainties, but also for geometric uncertainties at the unit-cell level, such as braid and undulation angles. Uncertainties are distinct and due to the clear boundaries between the scales, the variability propagation towards higher levels can be predicted. The division of the uncertainties enables sensitivity analysis and subsequently offers the identification of the parameter with the most crucial effect. The algorithm is quite efficient but the performance is further accelerated by using NN for the repetitive procedure of MCS.

5.1. Multiscale algorithm

Python scripting provides great synergy between the preprocessing in TexGen and the post-processing in ABAQUS. Hence, the algorithm can be implemented in Python in a straightforward manner. The parametric geometrical model of the unit-cell at the mesoscale is scripted with the functions provided by TexGen, with respect to geometric variable of interest, which will be potentially used as an uncertainty. Building a unit-cell textile model requires definition of the yarn paths, the yarn cross-sections and the yarn repeats within a domain. Since the model simulates the yarns as solids, homogenization of their material properties needs to be performed.

The algorithm is much faster if analytical expressions for the microscale material behavior are used and since the Chamis model [46] has been found quite accurate for laminate composites, it is applied for the micro-to-meso scale transition. The yarns in a textile-based composite are essentially unidirectional continuous fiber composites, so the applicability of the model is valid. The transversely isotropic properties of the yarn according to the Chamis model are governed by the following expressions:

$$\begin{aligned} E_{11} &= V_f E_{f,11} + (1 - V_f) E_m \\ E_{22} = E_{33} &= \frac{E_m}{1 - \sqrt{V_f}\left(1 - \frac{E_m}{E_{f,22}}\right)} \\ G_{13} = G_{12} &= \frac{G_m}{1 - \sqrt{V_f}\left(1 - \frac{G_m}{G_{f,12}}\right)} \\ G_{23} &= \frac{G_m}{1 - V_f\left(1 - \frac{G_m}{G_{f,23}}\right)} \\ \nu_{12} = \nu_{13} &= \nu_m + V_f(\nu_{f,12} - \nu_m) \\ \nu_{23} &= V_f \nu_{f,23} + V_m\left(2\nu_m - \frac{\nu_{12}}{E_{11}} E_{22}\right) \end{aligned} \tag{26}$$

where $E_{f,11}, E_{f,22}, G_{f,12}, G_{f,23}, \nu_{f,12}$ and $\nu_{f,23}$ are the transversely isotropic material properties of the fibers, E_m, G_m and ν_m are the isotropic material properties of the polymer matrix and V_f is the yarn volume fraction (percentage of the volume of fibers inside the volume of the yarn).

The next step is to call ABAQUS via Python, for the FE solution of the input file generated by TexGen. It is noted that a mesh convergence study is necessary for the trade-off between accuracy and efficiency in order to adjust the voxel mesh parameters of the unit-cell. Once the model is solved, the effective elastic properties of the macroscale (assumed orthotropic) are extracted with a script implementing the process described in Section 2.2. The procedure described so far needs to be automated in order to generate a sample through Monte Carlo analysis.

The generated sample is used as a training dataset for a NN in MATLAB [47]. An early stopping method is used in order to further improve generalization. In this technique, which is enclosed in MATLAB NN tool, the available data are divided into three subsets: the training, validation and testing set. The training set is used for the procedure described in Section 4.2 (gradient computation and weights updating). The validation set is used as a separate dataset whose error is monitored during the training, so that the generalization performance is evaluated. During the initial phase of training the validation error normally decreases, along with the training error. When the network begins to overfit the data, the validation

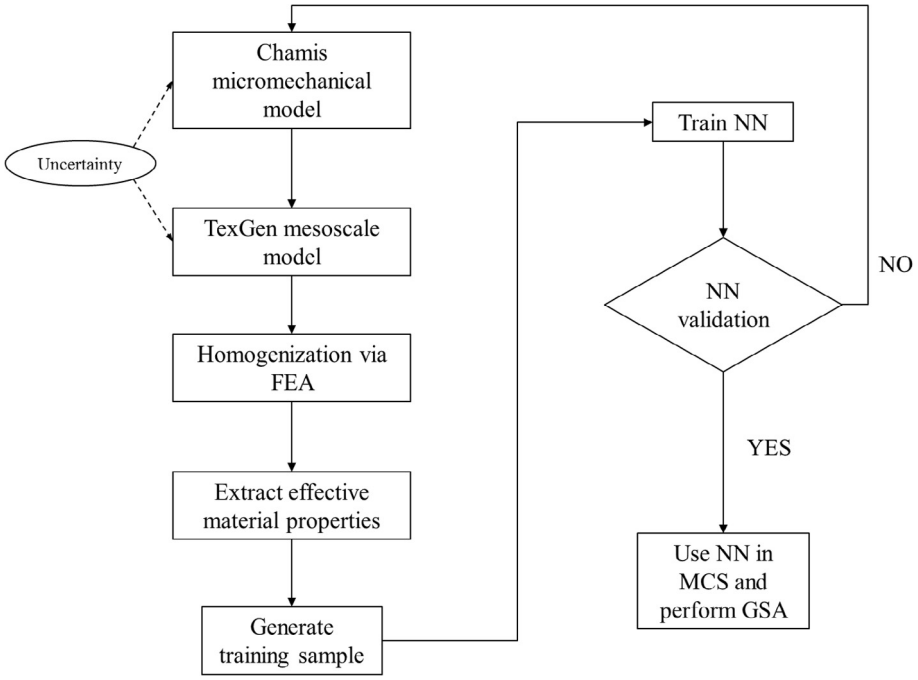

Fig. 4. A flow chart of the proposed methodology.

error begins to rise and the training process is stopped. The weights and biases at the minimum error are adopted. Finally, the testing dataset is used strictly after the training process has finished and offers a representative error which can be expected from absolutely new data. In our study, the input data are randomly divided so that 70% of the samples are assigned to the training set, 15% to the validation set and 15% to the testing set.

Afterwards, the NN is evaluated through a target value for the mean squared error of the prediction. If the criterion is met, the NN is used for the MCS, enabling the fast extraction of excessive response samples for the effective material properties. Furthermore, a GSA framework for the calculation of the Sobol indices can be scripted, for the case of a vector input of uncertainties, according to the formulation of Section 3. If the error is larger than the threshold, the NN needs to be redesigned, either in terms of a new dataset or number of layers and neurons.

A schematic description of the aforementioned methodology is presented in Fig. 4. Uncertainties can be introduced either in the microscale (Chamis micromechanical model), or in the mesoscale through parametric scripting for the unit-cell geometry. As mentioned previously, at least the left part of the chart is required to be automated, as the training of the NN could be performed manually. Nevertheless, it is considered much more efficient to automate the entire algorithm by coupling Python with the MATLAB NN tool. The post-processing for the calculation of the Sobol sensitivity indices is also scripted in Python.

5.2. Experimental validation

The combination of Chamis model, TexGen and ABAQUS for the numerical extraction of the elastic properties, is validated through selected experimental results studied in [48]. This study obtained, among others, the mechanical properties of a triaxial braided carbon/epoxy composite and investigated the effect of the braid angle. Three different braid architectures with a braid angle of $30^\circ, 45^\circ$ and 60° are each tested in their longitudinal and transverse direction. The values for these cases are presented in Fig. 5 in comparison with the numerical prediction of the multiscale modeling, represented by the solid lines, for the cases of E_1 and E_2. The accuracy is satisfactory, even though there are some approximation errors introduced by the scaling of the results due to volume fraction discrepancies.

6. Numerical examples

6.1. Model description

The model examined herein, can be specified as a typical 3D triaxial braided composite. Triaxial means that the yarns run in three directions. The axial (or warp) yarns lay straight and equally spaced, while the weft yarns interlace the axial yarns at an angle, according to the pattern shown in Fig. 6a. The layer architecture is based on a CT scan conducted on a braided tubular structure.

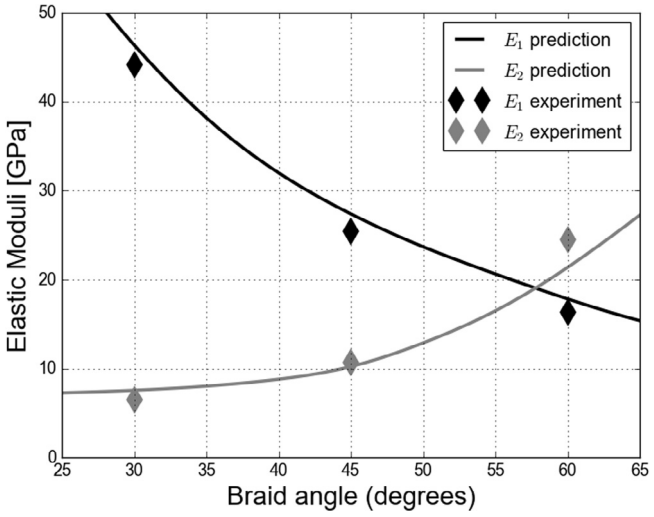

Fig. 5. Comparison of the proposed multiscale methodology (solid lines) with experimental values.

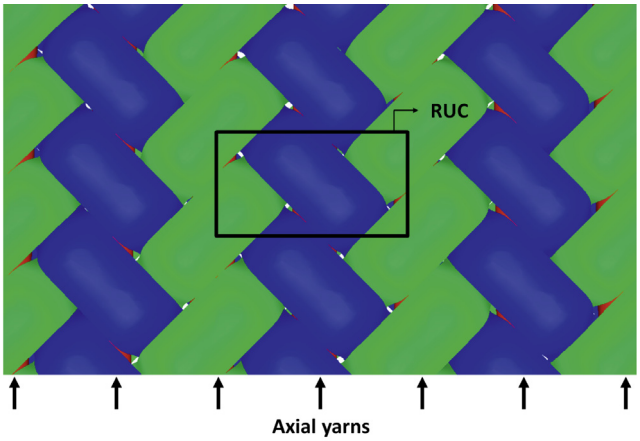

(a) Braiding pattern and RUC

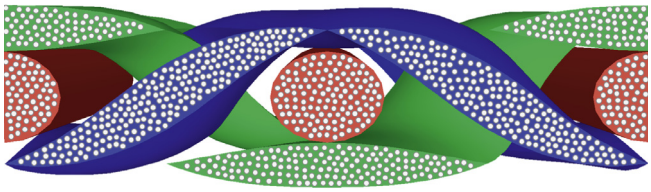

(b) Cross-section

Fig. 6. Triaxial braiding pattern: (a) Top view, (b) Side view (cross-section)

A cross-section of the braiding pattern is presented in Fig. 6b, where the heterogeneity of the yarns is emphasized by illustrating the embedded fibers. The section area of the weft yarns (green and blue) is lenticular (intersection of two circles), while the axial yarns (red) are of elliptical shape.

The representative unit-cell (RUC) extracted from the braiding pattern for the TexGen modeling (Fig. 6a) is presented in Fig. 7a in an isometric projection. The in-plane angle between the weft yarn and the axial yarn is the braid angle (BA) and the out-of-plane angle that the weft yarns are forming within the cell thickness, is the undulation angle (UA). These two geometric variables consist the most significant structural parameters of the mesoscale for a braided composite, considering that they are fully correlated with the unit-cell volume fraction (percentage of the volume of yarns inside the volume of the unit-cell). Fig. 7b presents the meshed unit-cell model in ABAQUS (matrix is excluded for visibility reasons). Characteristics from AS4 Carbon Fibers and EPON 9504 resin for the polymer matrix are used. Material properties selected from [49], are summarized together with the mesoscale geometric properties in Table 1.

Table 1
Material and geometric parameters of braided model.

Parameter	Mean value
Longitudinal fiber modulus E_{f1}	227.53 GPa
Transverse fiber modulus E_{f2}	16.55 GPa
Shear fiber modulus G_{f12}	24.82 GPa
Shear fiber modulus G_{f23}	6.89 GPa
Fiber Poisson's ratio υ_{12}	0.2
Fiber Poisson's ratio υ_{23}	0.25
Matrix Young's modulus E_m	3.5 GPa
Matrix Poisson's ratio υ_m	0.38
Yarn volume fraction (YVF)	70%
Braid angle (BA)	45°
Undulation angle (UA)	57°

6.2. Microscale uncertainty – A single case

As mentioned in Section 5.1, uncertainties could be introduced either in the microscale through the Chamis model (fiber/matrix properties, volume fraction etc.), or in the mesoscale through parametric scripting for the geometric parameters of interest (braid and undulation angles, yarn section shapes etc.), which have a direct impact on the unit-cell volume fraction and consequently the effective macro properties. In this section, the yarn volume fraction (V_f in Eq. (26)) is considered as an uncertainty and we present its effect to the output macro-properties, from a statistical point of view.

Despite the fact that most of the uncertain quantities appearing in practical engineering problems are non-Gaussian in nature, the Gaussian assumption is often used due to its simplicity and the lack of relevant experimental data. To that end, the yarn volume fraction is modeled as a Gaussian random variable, with mean value according to Table 1 and coefficient of variation (COV) equal to 10%. COV is defined as the ratio of the standard deviation over the mean value and is used in this study as a unitless measure for both input and output variability, representing the second statistical moment.

Fig. 8 presents the required simulations for a sufficient representation of the COV of the effective macroscopic properties. As shown, statistical convergence is practically achieved after 400 simulations, which means that for the PDF roughly 1000 simulations would surely be an adequate estimation. The evolution of the mean value is not presented since the convergence is almost instant.

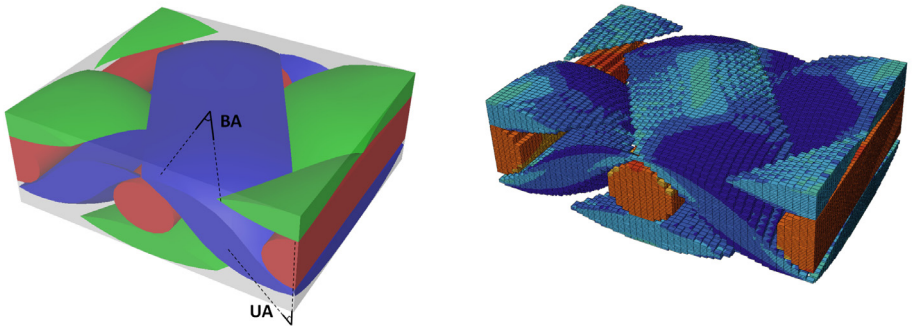

(a) TexGen model (b) FE model

Fig. 7. Representative unit-cell mesoscale model.

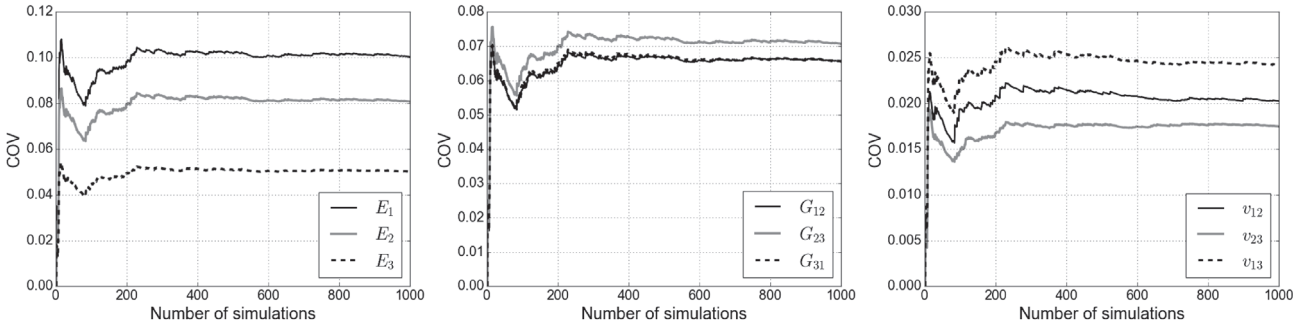

(a) Longitudinal moduli (b) Shear moduli (c) Poisson's ratios

Fig. 8. Statistical convergence of COV for the effective properties.

The response PDFs are calculated with the aid of the kernel density estimation method (KDE), which is a fundamental data smoothing technique, where inferences about the population are made based on a finite data sample [50]. In Fig. 9, we compare the response after 1000 crude MCS (which is considered as a reference solution) and after 1000 simulations with a trained NN, according to the methodology described in Section 5.1, for E_1, E_2 and E_3. It is observed that the accuracy of the NN-assisted algorithm is very good, providing that the NN is well trained. In general, the problem described in this paper does not need more than one hidden layer for good NN performance. On average, a training sample of 40–60 input/output sets is sufficient and the neurons should not be more than 10. The exact number of neurons is always dependent on the size of the training sample. In Fig. 10a, an illustrative error plot of the data sets against the internal iterations of a well trained NN is presented, while the convergence of the response with respect to the size of the sample used for training is presented in Fig. 10b in terms of cumulative distribution functions (CDFs) and in Fig. 10c in terms of PDFs. All three plots correspond to the response of the longitudinal modulus E_1, while

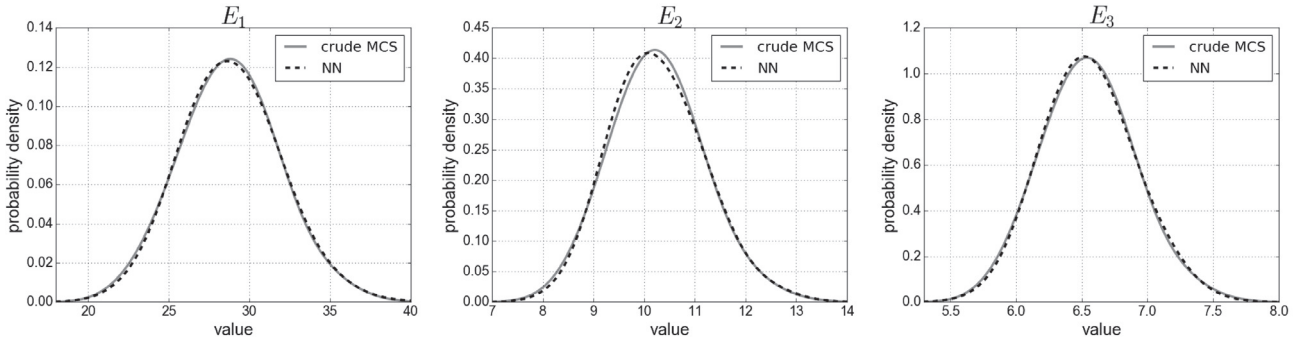

(a) (b) (c)

Fig. 9. Accuracy of the proposed NN-aided method (values in GPa).

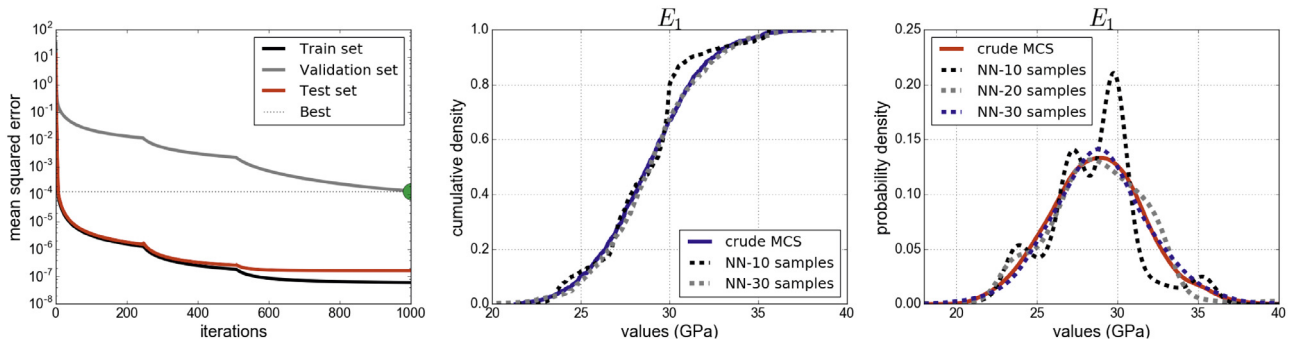

(a) Mean squared error curves (b) CDF convergence (c) PDF convergence

Fig. 10. Training information.

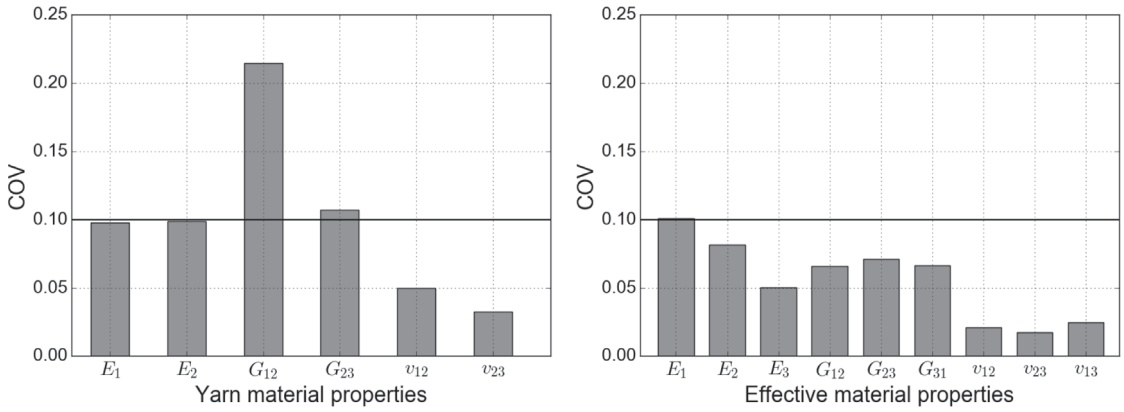

(a) Mesoscale variability (b) Macroscale variability

Fig. 11. Variability propagation through the scales.

the hidden layer holds 5 neurons for this case. Naturally, convergence can be achieved more easily for the CDF case, since the data are going through an additional integration procedure.

To further boost the training procedure, a Latin Hypercube Sampling (LHS) technique could be used for a more efficient choice of the input sample, as the random variables are sampled from the complete range of their possible values, ensuring a smaller sample size is required [51]. Since the relation between the elastic properties and the V_f is almost linear [52], the PDF shape in Fig. 9 is Gaussian. Skewness is expected to be introduced by other uncertain parameters, like the braid and undulation angles, where the relation is nonlinear as in Fig. 5 (see also [12,48,53]), in case they dominate the response. In terms of efficiency, an Intel Core i7-3770 processor required 195600 s (3260 min) for 1000 crude MCS realizations, while 1000 realizations with a trained NN were performed in 10.53 s (0.1755 min).

Regarding the uncertainty propagation, the response variability is calculated in both the mesoscale and the macroscale phase. Results are illustrated in bar charts for all material properties involved, in Fig. 11. An horizontal solid line is drawn at the COV level of 10% as a reference to the input variation. It is worth noting the slight reduction of the variability through the scales, especially the high G_{12} variability of the yarns in the mesoscale, which however does not increase the output samples of the macroscale.

6.3. Sensitivity analysis – General case

The efficiency provided by the NN, enables the application of the variance-based GSA described in Section 3, since it is costless to perform the large number of simulations required for the convergence of the Sobol index estimation. Several uncertain parameters are considered herein and through the total output variance decomposition, it is straightforward to draw conclusions about the statistical importance and impact of each input.

The selected random input parameters are inspired from possible uncertainties caused by manufacturing procedures. We choose the following 6 random properties from Table 1: E_{f1}, E_{f2}, G_{f12}, YVF, BA and UA. The first four parameters are introduced in the microscale, while the last two in the mesoscale and they are all considered as the most influential according to some preliminary analyses and the literature. The mean values are summarized in Table 1. Concerning the input variance, all four random variables of the microscale have a COV equal to 10%, while the COV of the mesoscale geometric variables (BA and UA) is selected so that the induced COV of the unit-cell volume fraction does not exceed 3%. This assumption maintains the simulation realistic, but also abides with the modeling limitation of the non-consideration of the yarns' contact and intersection.

The output variability is presented in Fig. 12. The in-plane elastic moduli E_1 and E_2 gather the highest COV levels, which makes sense due to the geometric variation of the yarns in the mesoscale. This is also related with the slight skewness introduced in the PDF shapes of those moduli, as shown in Fig. 13a and b. In this figure, the output histograms along with the PDF shapes according to the KDE method and the best fit among known probability distributions, are presented. Most of the effective properties are of Gaussian shape. The highest skewness is obtained in E_2 (Fig. 13b) and v_{12} (Fig. 13g), implying they are profoundly sensitive to the mesoscale uncertainties.

Results of the variance-based GSA are demonstrated in Fig. 14, in terms of evolution of each Sobol index (Eq. (20)) over the number of simulations. It is highlighted that this illustration is preferable in comparison with the table values after a standard number of simulations (which is the trend in the literature), in order to be certain that the indices have converged. In all subfigures there are solid lines indicating the indices limits of 0 and 1. The variance of the shear moduli (Figs. 14d, e and f) is dominated by the yarn volume fraction variability. E_2 and v_{12} are indeed governed by the braiding angle input as assumed (Figs. 14b and g) and

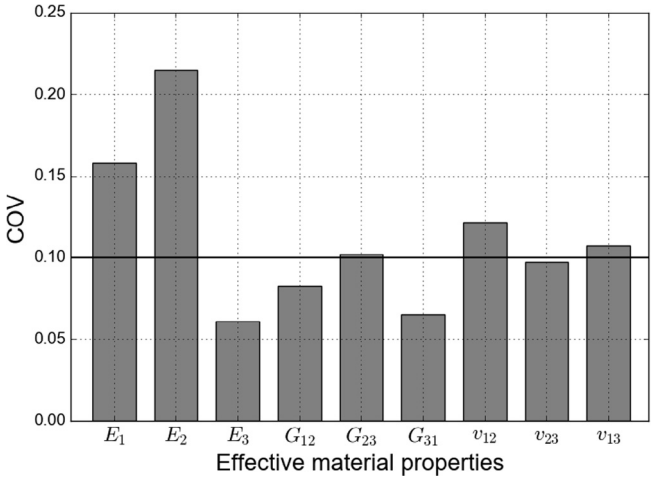

Fig. 12. Output variability for the general case.

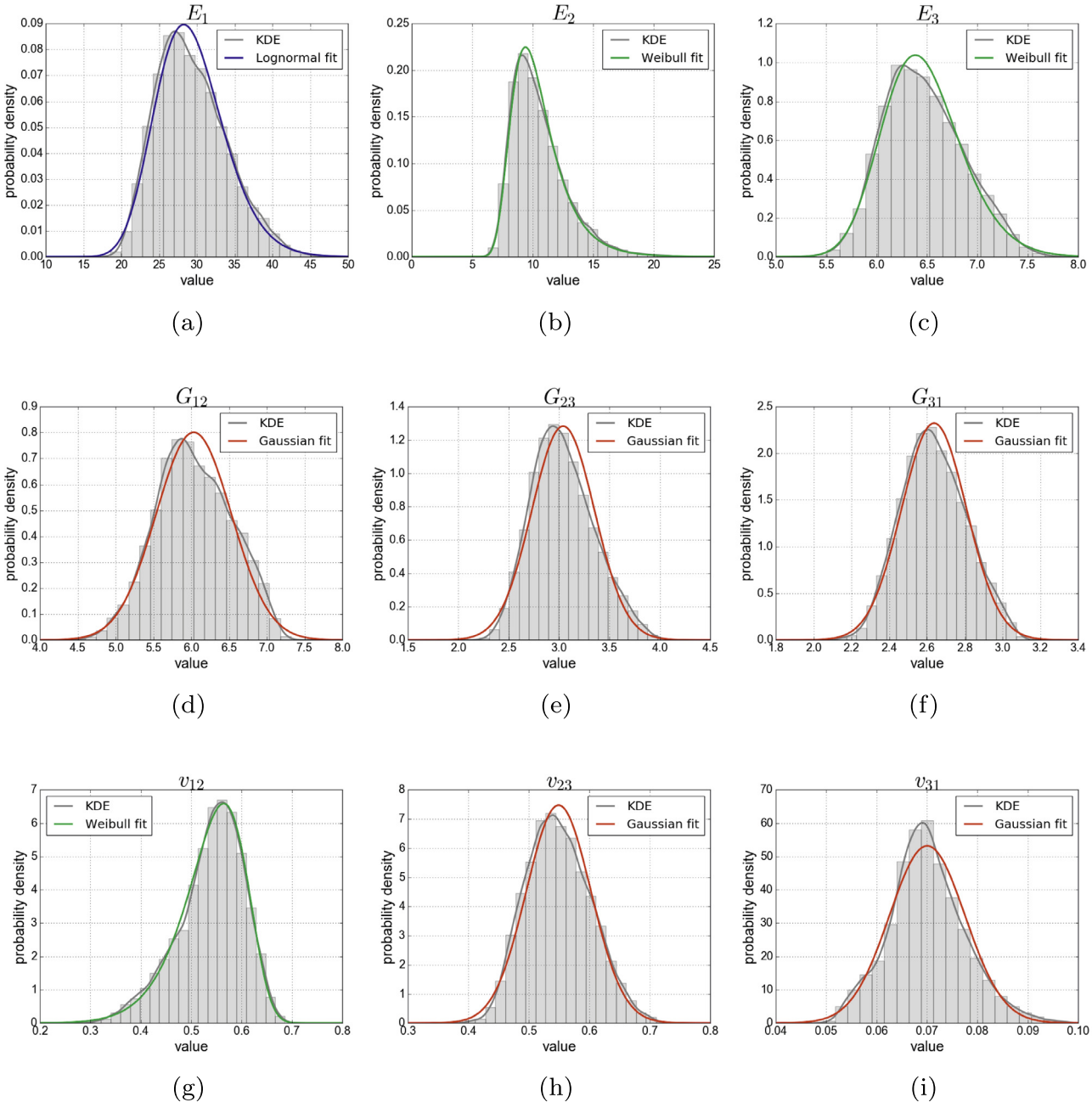

Fig. 13. Histograms of the effective mechanical properties and best fits.

the skewness of the PDFs is explained. In general, the yarn volume fraction seems as the most influential parameter, together with the braid angle. The undulation angle does not seem to have a noteworthy variability impact on the elastic properties. It is also noted that some of the output parameters required up to 8000 simulations to converge.

7. Concluding remarks

Uncertainties due to manufacturing imperfections affect the elastic behavior of braided composites. In this paper, a method is described for the effective properties prediction under uncertainty for textile composites. A multiscale model of a triaxial braided composite is presented and the effect of several micro and meso scale uncertainties is investigated. The developed algorithm is modeling a unit-cell at the mesoscale over TexGen, with homogenized yarn properties through an analytical model. Numerical homogenization is performed via ABAQUS and the effective mechanical properties are extracted with a Python post-processing script. Response variability is calculated via trained NN in the core of Monte Carlo simulation, thus results can be obtained with orders of magnitude less computational effort compared to the standard procedure. Sensitivity analysis is performed through a global technique, by measuring the contribution of the uncertain parameters to the output variance through the Sobol indices. Both material and geometric related uncertainties can be introduced. With reliable uncertainty measurements the method can solve accurately the forward uncertainty propagation problem

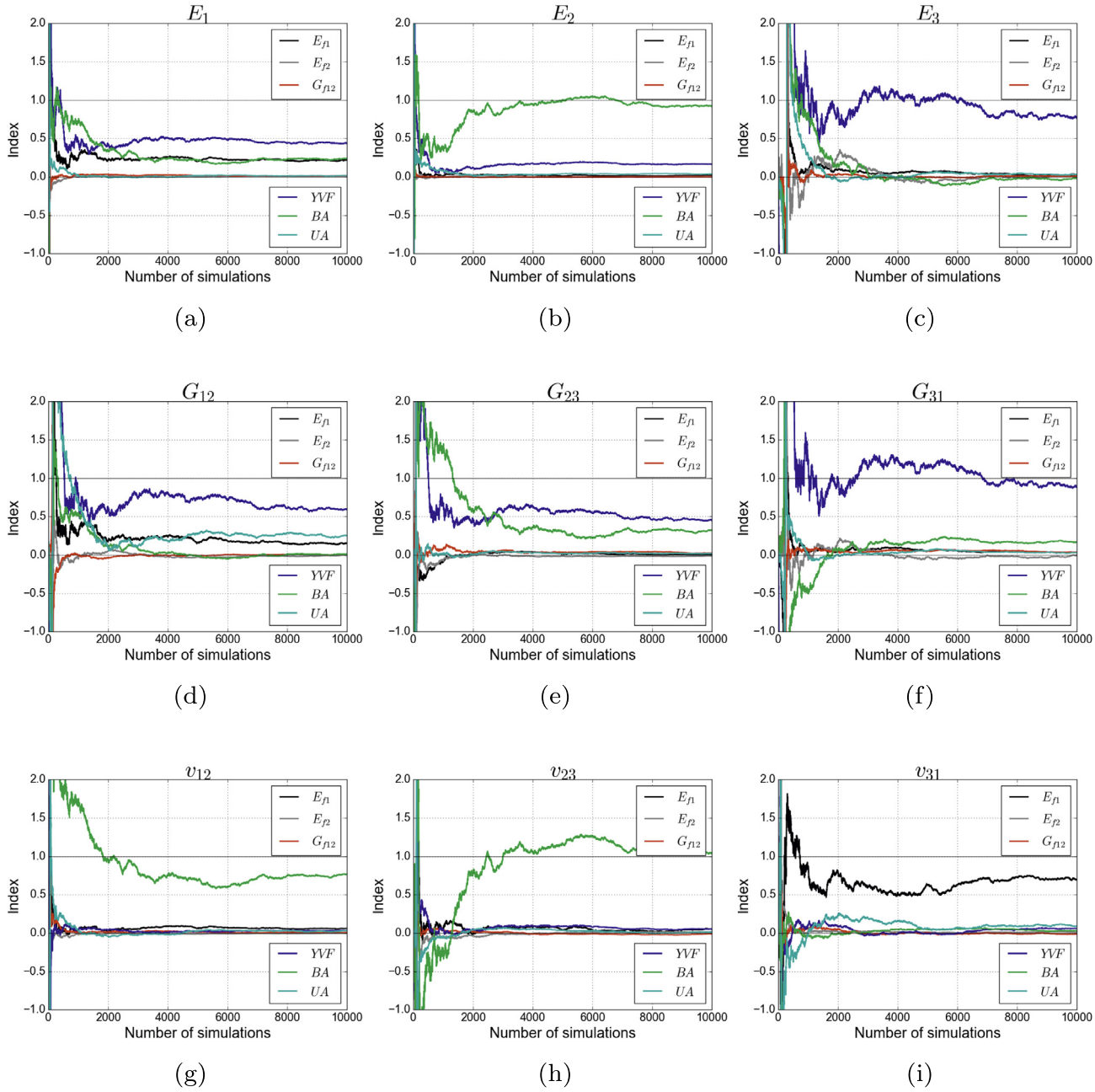

Fig. 14. Sobol indices.

and provide accurate PDFs for the effective properties of braided macrostructures, that could be later used for reliability analyses. The method can be extended to consider the contact between the yarns with an ad hoc code.

Acknowledgments

This work is implemented within the framework of the research project "FULLCOMP: Fully Integrated Analysis, Design, Manufacturing and Health-Monitoring of Composite Structures" under European Union's Horizon 2020 research and innovation program and is funded by the European Commission under a Marie Sklodowska-Curie Innovative Training Networks Grant (No. 642121) for European Training Networks (ETN). The provided financial support is gratefully acknowledged by the authors.

References

[1] Byun JH, Chou TW. Modelling and characterization of textile structural composites: A review. J Strain Anal Eng Des 1989;24(4):253–62.
[2] Lomov SV, Perie G, Ivanov DS, Verpoest I, Marsal D. Modeling three-dimensional fabrics and three-dimensional reinforced composites: challenges and solutions. Text Res J 2011;81(1):28–41.
[3] Dixit A, Mali HS. Modeling techniques for predicting the mechanical properties of woven-fabric textile composites: A review. Mech Compos Mater 2013;49(1):1–20.
[4] Ayranci C, Carey J. 2D braided composites: A review for stiffness critical applications. Compos Struct 2008;18(1):43–58.
[5] Fang G, Liang J. A review of numerical modeling of three-dimensional braided textile composites. J Compos Mater 2011;45(23):2415–36.
[6] Huang ZM. The mechanical properties of composites reinforced with woven and braided fabrics. Compos Sci Technol 2000;60(4):479–98.
[7] Tang ZX, Postle R. Mechanics of three-dimensional braided structures for composite materials – Part II: Prediction of the elastic moduli. Compos Struct 2001;51(4):451–7.

[8] Chen L, Tao XM, Choy CL. Mechanical analysis of 3-D braided composites by the finite multiphase element method. Compos Sci Technol 1999;59(16):2383–91.
[9] Zhang C, Xu X. Finite element analysis of 3D braided composites based on three unit-cells models. Compos Struct 2013;98:130–42.
[10] Zhang C, Curiel-Sosa JL, Bui TQ. A novel interface constitutive model for prediction of stiffness and strength in 3D braided composites. Compos Struct 2017;163:32–43.
[11] Zhang C, Curiel-Sosa JL, Bui TQ. Comparison of periodic mesh and free mesh on the mechanical properties prediction of 3D braided composites. Compos Struct 2017;159:667–76.
[12] Zhang C, Binienda WK, Kohlman LW. Analytical model and numerical analysis of the elastic behavior of triaxial braided composites. J Aerosp Eng 2014;27(3):473–83.
[13] Dong J, Huo N. A two-scale method for predicting the mechanical properties of 3D braided composites with internal defects. Compos Struct 2016;152:1–10.
[14] Ernst G, Vogler M, Hühne C, Rolfes R. Multiscale progressive failure analysis of textile composites. Compos Sci Technol 2010;70:61–72.
[15] Rolfes R, Vogler M, Czichon S, Ernst G. Exploiting the structural reserve of textile composite structures by progressive failure analysis using a new orthotropic failure criterion. Comput Struct 2011;89:1214–23.
[16] Sriramula S, Chryssanthopoulos K. Quantification of uncertainty modelling in stochastic analysis of FRP composites. Compos A 2009;40:1673–84.
[17] Bishara M, Rolfes R, Allix O, Revealing complex aspects of compressive failure of polymer composites – Part I: Fiber kinking at microscale. Compos Struct 2017;169:105–115.
[18] Bishara M, Vogler M, Rolfes R, Revealing complex aspects of compressive failure of polymer composites – Part II: Failure interactions in multidimensional laminates and validation. Compos Struct 2017;169:116–128.
[19] Kriegesmann B, Rolfes R, Hühne C, Temer J, Arbocz J. Probabilistic design of axially compressed composite cylinders with geometric and loading imperfections. Int J Struct Stab Dyn 2010;10(4):623–44.
[20] Kriegesmann B, Rolfes R, Hühne C, Kling A. Fast probabilistic design procedure of axially compressed composite cylinders. Compos Struct 2011;93(12):3140–9.
[21] Kamiński M, Kleiber M. Perturbation based stochastic finite element method for homogenization of two-phase elastic composites. Comput Struct 2000;78(6):811–26.
[22] Sakata S, Ashida F, Zako M. Kriging-based approximate stochastic homogenization analysis for composite materials. Comput Methods Appl Mech Eng 2008;197(21–24):1953–64.
[23] Savvas D, Stefanou G, Papadrakakis M, Deodatis G. Homogenization of random heterogeneous media with inclusions of arbitrary shape modeled by XFEM. Comput Mech 2014;54(5):1221–35.
[24] Stefanou G, Savvas D, Papadrakakis M. Stochastic finite element analysis of composite structures based on material microstructure. Compos Struct 2015;132:384–92.
[25] Kamiński M, Pawlak A. Various approaches in probabilistic homogenization of the CFRP composites. Compos Struct 2015;133:425–37.
[26] El Kadi H. Modeling the mechanical behavior of fiber-reinforced polymeric composite materials using artificial neural networks – A review. Compos Struct 2006;73:1–23.
[27] Zhang Z, Friedrich K. Artificial neural networks applied to polymer composites: a review. Compos Sci Technol 2003;63:2029–44.
[28] Dey S, Mukhopadhyay T, Adhikari S. Metamodel based high-fidelity stochastic analysis of composite laminates: A concise review with critical comparative assessment. Compos Struct 2017;171:227–50.
[29] Rouhi M, Rais-Rohani M, Najafi A. Probabilistic analysis and optimization of energy absorbing components made of nanofiber enhanced composite materials. Compos Struct 2013;100:144–53.
[30] Jansson N, Wakeman WD, Månson J-AE. Optimization of hybrid thermoplastic composite structures using surrogate models and genetic algorithms. Compos Struct 2007;80:21–31.
[31] Bui TQ, Tran AV, Shah AA. Improved knowledge-based neural network (KBNN) model for predicting spring-back angles in metal sheet bending. Int J Model Simul Sci Comput 2014;5(2):1350026.
[32] Dey S, Naskar S, Mukhopadhyay T, Gohs U, Spickenheuer A, Bittrich L, Sriramula S, Adhikari S, Heinrich G. Uncertain natural frequency analysis of composite plates including effect of noise – A polynomial neural network approach. Compos Struct 2016;143:130–42.
[33] Zhou XY, Gosling PD, Pearce CJ, Ullah Z, Kaczmarczyk L. Perturbation-based stochastic multi-scale computational homogenization method for woven textile composites. Int J Solids Struct 2016;80:368–80.
[34] Jiang D, Li Y, Fei Q, Wu S. Prediction of uncertain elastic parameters of a braided composite. Compos Struct 2015;126:123–31.
[35] Hill R. Elastic properties of reinforced solids: Some theoretical principles. J Mech Phys Solids 1963;11:357–72.
[36] Lin H, Brown LP, Long AC. Modelling and simulating textile structures using TexGen. Adv Mater Res 2011;331:44–7.
[37] Li S, Wongsto A. Unit cells for micromechanical analyses of particle-reinforced composites. Mech Mater 2004;36:543–72.
[38] ABAQUS, Documentation, Dassault Systèmes Simulia Corp. Providence RI 2014.
[39] Saltelli A, Ratto M, Andres T, Campolongo F, Cariboni J, Gatelli D, Saisana M, Tarantola S. Global sensitivity analysis. The primer. John Wiley and Sons; 2008.
[40] Sobol IM. Global sensitivity indices for nonlinear mathematical models and their Monte Carlo estimates. Math Comput Simul 2001;55:271–80.
[41] Saltelli A, Annoni P, Azzini I, Campolongo F, Ratto M, Tarantola S. Variance based sensitivity analysis of model output. Design and estimator for the total sensitivity index. Comput Phys Commun 2010;181:259–70.
[42] Sudret B. Global sensitivity analysis using polynomial chaos expansions. Reliab Eng Syst Saf 2008;93:964–79.
[43] Crestaux T, Le Maître O, Martinez JM. Polynomial chaos expansion for sensitivity analysis. Reliab Eng Syst Saf 2009;94:1161–72.
[44] Fausett L. Fundamentals of neural networks. Prentice Hall; 1994.
[45] Swingler K. Applying neural networks: a practical guide. Academic press; 1996.
[46] Chamis CC. Mechanics of composite materials: Past, present, and future. J Compos Technol Res 1989;11:3–14.
[47] MATLAB, Release 2014b, The MathWorks Inc., Natick, Massachusetts, United States; 2014.
[48] Wehrkamp-Richter T, Humbs M, Schultheiss D, Hinterhölzl R, Damage characterization of triaxial braided composites under tension using full-field strain measurement. In: The 19th international conference on composite materials. Montreal, Canada; 2013.
[49] Kelkar AD, Whitcomb JD. Technical report: Characterization and structural behavior of braided composites. U.S. Department of Transportation, Federal Aviation Administration; 2009.
[50] Klemelä J. Smoothing of multivariate data: Density estimation and visualization. Wiley; 2009.
[51] Stein M. Large sample properties of simulations using Latin hypercube sampling. Technometrics 1987;29:143–51.
[52] Sun H-Y, Qiao X. Prediction of the mechanical properties of three-dimensional braided composites. Compos Sci Technol 1996;57:623–9.
[53] Deng Y, Chen X, Wang H. A multi-scale correlating model for predicting the mechanical properties of tri-axial braided composites. J Reinf Plast Compos 2013;32(24):1934–55.

Chapter 3

Stochastic Modeling Techniques for Textile Yarn Distortion and Waviness with 1D Random Fields

In this paper, a probabilistic framework integrating stochastic manufacturing-induced geometrical imperfections of textile yarns is proposed. The study includes methodologies for the distortion of the yarn's shape and the deviations from their nominal path. The effects of the above defects are investigated via a forward uncertainty propagation application of a triaxially braided composite for both effective stiffness and strength properties.

The paper is published in Composites Part A: Applied Science and Manufacturing, Volume 127, 2019, 105639.

Composites Part A 127 (2019) 105639

Contents lists available at ScienceDirect

Composites Part A

journal homepage: www.elsevier.com/locate/compositesa

Stochastic modeling techniques for textile yarn distortion and waviness with 1D random fields

Georgios Balokas[a,*], Benedikt Kriegesmann[a], Steffen Czichon[b], Raimund Rolfes[c]

[a] Structural Optimization for Lightweight Design, Hamburg University of Technology, Hamburg, Germany
[b] Fraunhofer Institute for Wind Energy Systems IWES, Bremerhaven, Germany
[c] Institute of Structural Analysis, Leibniz Universität Hannover, Hannover, Germany

ARTICLE INFO

Keywords:
Braided composites
Yarn distortion
Yarn waviness
Stochastic modeling
Random fields
Kriging

ABSTRACT

Within the concept of simulation approaches for manufacturing-induced imperfections of composite structures, this work proposes modeling frameworks for the consideration of stochastic deviations concerning the yarns of textile composite materials. The random distortion of a yarn's cross-section, is addressed by flexible 1D Fourier-based random fields, with the potential to be calibated from measurements of the deviations from the nominal yarn shape and their statistical characteristics. Furthermore, a Kriging-based modeling approach is presented, able to randomize any nominal yarn path in short or long range problems, considering data for the correlation and variance in a straightforward manner. The effects of defects due to stochastic yarn distortion and waviness, are investigated by simulating a forward uncertainty propagation problem of a triaxially braided composite material. The response variability concerning stiffness and strength for different uncertainty levels is highlighted, while several comments are offered regarding numerical issues and potential surrogate modeling techniques.

1. Introduction

Mechanical properties and behavior of textile composites can be analyzed with multiple methods. Internal complexity of the mesoscale (level of individual tows $\approx 10^{-3}$ m) is the main reason for the excessive use of the finite element method (FEM) when it comes to such materials. However, even when numerical multiscale analyses are performed, mostly an ideal representative volume element (RVE) is assumed, without consideration of any geometrical imperfections. In fact, manufacturing procedures of composite materials introduce several sorts of defects.

For textiles, the first process step is the insertion of the fibers into the resin impregnation system (resin bath), and then the assembly into yarns/tows and the forming of their nominal shape. Afterwards, the forming of the textile architecture follows, by interlacing the yarns through processes like braiding, weaving, stitching and filament winding. The tension of the yarns over the preform might cause distortion of some cross-sections along the yarn path, or of the nominal path itself. Especially for braiding, the jamming action (tightening/straightening of the yarns after every machine cycle) adds an extra pinch to the yarn geometry. The dry fabric is then impregnated with resin, so that the curing process begins, which is another main source of imperfections [1,2].

Processes like resin transfer molding (RTM) are common for such fabrics due to their scale. They exhibit a high level of compaction during RTM, in order to reach considerable fiber volume fractions. Pultrusion might also be applied, in which the fabric is pulled through a mechanism directly after the curing chamber, or is cured while being pulled through a heated die. Such processes induce out-of-plane compression and cause the yarns to pressure each other. Other manufacturing factors which are potential sources of defects, are thermal processing, filament winding, storage, deformation during moving, etc. In industrial practice, their influence is taken into account by knock-down factors, which are derived from experimental tests. For reducing experimental effort, the uncertainties need to be taken into account by realistic and reliable simulations.

The issue of geometrical imperfections and spatial variability modeling of fiber yarns due to manufacturing processes, is mainly partitioned in the literature into two problems: (a) the deformation of yarns in a cross-sectional level and the divergence from ideally elliptical or lenticular shapes, mostly expressed as *yarn distortion*, and (b) the deviations from the assumed perfect trajectories of the yarn paths, a concept predominantly entitled as *yarn waviness*. It should be clarified that for most textile composites where weft yarns have an inherent

* Corresponding author.
E-mail address: georgios.balokas@tuhh.de (G. Balokas).

https://doi.org/10.1016/j.compositesa.2019.105639
Received 29 March 2019; Received in revised form 15 September 2019; Accepted 17 September 2019
Available online 21 September 2019
1359-835X/

periodic variation (called trend), the term yarn waviness stands for the additional stochastic deviations, besides the systematic variation. Yarn waviness can be modeled for short-range, meaning that deviations are limited within the size of a unit cell, or long-range yarn paths.

Production-induced imperfections have been basically handled by researchers as uncertainties, thusly modeled within a stochastic approach. Nevertheless, several studies with a deterministic scope can be found, aiming for a precise representation of an architecture, captured by scanning particular textile specimens. Šejnoha and Zeman [3] described the unit cell of a plain weave textile with several independent parameters, which were used as design variables to a minimization routine, aiming to approximate the macroscopic behavior of a measured material. Mahadik and Hallet [1] examined the influence of yarn waviness on the compressive strength and failure properties of a woven textile composite, however purely from an experimental point of view. An interesting paper by Green et al. [4], highlighted that idealized multiscale models overestimate stiffness and strength of woven composites, by comparing results with experimental data. A numerical tool based on the multi-chain digital element method, was used to predict the deformations during weaving and molding, which were transferred to unit-cell models implemented with the TexGen software [5], leading to distorted sections and yarn paths. The realistic models produced results closer to the experimental data. Furthermore, Xu and Qian [6] recently developed an analytical model able to include the yarn distortion effect, by introducing the twist angle of interior yarn filaments and predict the elastic tensor of the material. Finally, a recent study by Wang et al. [7] investigated the jam-action-induced yarn deformation, by perturbing the centerline of the yarns of a braided composite and developing a progressive failure algorithm for the stress-strain response on a macroscale level.

As far as the stochastic modeling is concerned, two main approaches have been widely applied in the literature. The first one was introduced by Yushanov and Bogdanovich [8,9] and is based on a stochastic metric theory. The random yarn path is specified by a position vector in a parametric form, which is bisected into a deterministic and a stochastic part. The key point of this approach is the local stochastic metric basis, through which the orientation of the random yarn is obtained. The stochastic stiffness matrix can then be evaluated with an orientation averaging procedure. Wang and Wang [10–12] expanded this theory, to be able to consider yarn distortion as well. Moreover, Guo-dong et al. [13] implemented this method into a multiscale algorithm to also predict the strength of four-directional braided composites. In all, although the method only needs the mean path and standard deviations of the local tangents as uncertainty input, implementing the theoretical formulation to an actual model is not straightforward, as it demands a solid background on differential geometry.

The second approach, was initially proposed by Blacklock et al. [14]. At first, the centroid path vector is once again decomposed into a non-stochastic, periodic part and a second part where the stochastic deviations are added. The level of information extracted from CT scans, is increased by the usage of the Reference Period Collation (RPC) method, which was first introduced by Bale et al. [15] to classify deviations into stochastic and non-stochastic. Subsequently, a virtual specimen generator is established. In order to model stochastic deviations corresponding to the specimen, a Markov Chain Monte Carlo (MCMC) method is calibrated from the correlation matrix having been extracted from the data. The original study of Blacklock et al. generated low-order representations for a rather obsolete binary model. A following study [16] expanded the method to 3D yarn representations.

Vanaerschot et al. have studied the yarn waviness problem and worked extensively on the latter method. In [17], they extended the characterization procedure to polymer textiles arranged in a laminate with different topology. In [18], the virtual specimen generator was implemented via the WiseTex software [19] for a woven textile laminate. A novel approach for the representation of long-range yarn variations can be found in [20]. Random fields generated with the Karhunen-Loève expansion are used, so that the cross-correlation between different yarns is also considered, aside from the auto-correlation within the same yarn. Moreover, a general and instructive paper discussing different modeling techniques is presented in [21], while in [22] a recent extension towards more sophisticated 3D textile composites is provided, considering yarn distortion as well. Applications of this technique in permeability of fabrics were recently published [23,24]. Skordos and Sutcliffe [25] were among the first to employ random fields for yarn misalignment modeling and study the effect on the forming of woven composites. The generation of random realizations was performed without MCMC. There are also some further studies available, independent from the two basic stochastic modeling approaches described above [26–28].

The stochastic techniques previously reported, contain a certain level of complexity, especially when it comes to implementation. This paper proposes alternative modeling methods (one for each problem) based on the random field theory, able to simulate yarn distortion and waviness in a straightforward manner. Both formulations rely on the concept of randomizing a motif (systematic or recurring theme) with a clear pattern, with the first one inspired from random inclusions studies, while the second uses Gaussian Process/Kriging modeling. The proposed methodologies are flexible enough to allow calibration from captured data and, thus, lead to realistic stochastic mesoscale simulations. To the authors' knowledge, random fields have not been applied for yarn distortion modeling in previous studies, while a thorough discussion is made on the advantages of the proposed Kriging approach over existing waviness modeling methods (Section 3.4). The theoretical modeling is presented in detail and applied to a 3D triaxially braided composite with short-range spatial deviations. The current study provides a forward uncertainty quantification problem for the elastic and ultimate tensile strength properties extraction, yet with arbitrary input due to lack of experimental data. The effect of the yarn distortion and waviness to both stiffness and strength output variability is highlighted. Moreover, the methodology is designed to fit FE models and is, herein, implemented via the voxel method [29,30]. Numerical issues arising from this approach are discussed as well. Finally, some remarks are made about the feasibility of surrogate models.

2. Yarn distortion modeling

2.1. General description

It is widely evident from CT-scan captured images that textiles display a considerable amount of asymmetries on a cross-sectional level. Modeling the yarn section in the mesoscale as e.g. a perfect ellipse, is a rough approximation which in most cases leads to over or understatements, concerning response and results. It is obvious by observing images from the literature [31,2,32] like in Fig. 1, that almost all shapes deviate in a random manner, for both the orthogonal and angle interlock woven architecture, while the basic trend could be either an ellipse, a power ellipse, or a lenticular shape (e.g. section between two circles). Occasionally, the cross-section could exhibit a greater number of waves on the perimeter, leading to highly irregular shapes.

Previous attempts to simulate this effect included the characterization of distortion through a twist angle, which is a description of the twist extent of the yarn about the tangent vector of the yarn path, and consequently representation of the angle with a random variable [11]. The modified stochastic metric theory [10] additionally uses the semi-major and minor axes of the cross-section. More simplified approaches also existing in the literature, with only random diameters or cross-section heights and widths [24,26], are not suitable for tailoring the randomly distorted shapes. More flexibility in the variation of the section shape along its perimeter, can be achieved with a one-dimensional (1D) random field. In the next section, a formulation which can simulate the spatial variability of the distorted yarns by randomizing a trend

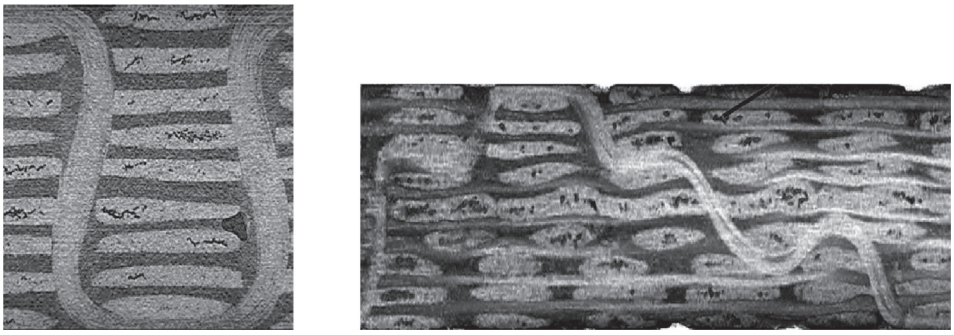

(a) Orthogonal woven textile (b) Angle interlock woven textile

Fig. 1. Mesoscale cross-sections of yarns [32].

shape (e.g. an ellipse or a lenticular shape), is proposed.

2.2. Formulation

The methodology is inspired from former studies on the stochastic representation for random inclusions of arbitrary shape in multiphase materials [33,34]. These inclusions (also called "rough circles") are generated within the context of level set functions and are expressed as random functions of the form:

$$\psi(\boldsymbol{x}, \theta) = \|\boldsymbol{x} - \boldsymbol{c}\| - R(\phi(\boldsymbol{x}), \theta) \tag{1}$$

where $\boldsymbol{x}$ is the spatial location of a point in the domain, $\boldsymbol{c}$ is the center of the arbitrary inclusion, $R(\phi(\boldsymbol{x}), \theta)$ is the radius of the inclusion expressed as a random field, $\phi(\boldsymbol{x})$ is the polar angle at position $\boldsymbol{x}$ which lies within the interval $[0, 2\pi]$ and lastly θ stands for the randomness of a quantity. The random field for the radius of the rough circle, is defined as [34]:

$$\begin{aligned} R(\phi, \theta) = \; & 0.2 + 0.03Y_1(\theta) + 0.015\{Y_2(\theta)\cos(k_1\phi) \\ & + Y_3(\theta)\sin(k_1\phi) + Y_4(\theta)\cos(k_2\phi) + Y_5(\theta)\sin(k_2\phi)\} \end{aligned} \tag{2}$$

In the above equation $Y_i(\theta) \in U(-\sqrt{3}, \sqrt{3})$, with $i = 1, ..., 5$, are independent and identically distributed, uniform random variables. Y_1 controls the mean reference radius, while the rest of the random variables control the amplitude of the deviation from the rough circle. The period of oscillations of the random shape around the perfect circle is defined from the two deterministic constants k_1 and k_2 inside the harmonic functions. The choice of the parameters (0.2, 0.03, 0.015) is not justified by these studies.

However, it is evident that Eq. (2) is derived from a Fourier series, restricted to describe a superposition of two distortions with wave lengths k_1 and k_2. As an extension, a more general description of the random field would be:

$$R(\phi, \theta) = \frac{a_0}{2} + \sum_{i=1}^{\infty} a_i(\theta)\cos(i\phi) + b_i(\theta)\sin(i\phi) \tag{3}$$

In order to get the same representation from the generic Eq. (3) and its subset (Eq. (2)), the Fourier coefficients are determined by:

$$\begin{aligned} a_0 = 0.2 + 0.03Y_1, \quad a_{k_1} = 0.015Y_2, \quad a_{k_2} = 0.015Y_4, \\ b_{k_1} = 0.015Y_3 \quad \text{and} \quad b_{k_2} = 0.015Y_5 \end{aligned} \tag{4}$$

where if $i \neq k_1$ and $i \neq k_2$, the coefficients are equal to zero.

The basic idea for implementing the above to the stochastic yarn distortion problem, is that random fields in the form of Eq. (2) or Eq. (3) can be tailored around any desired section shape, just by expressing the section into the polar coordinate system and expanding the semi-minor and semi-major axes accordingly. Consider, for instance, an elliptical shape in a parametric form, given width w and height h. It is described as:

$$X(t) = \frac{w}{2}\cos(2\pi t), \qquad 0 \leqslant t \leqslant 1 \tag{5}$$

$$Y(t) = \frac{h}{2}\sin(2\pi t), \qquad 0 \leqslant t \leqslant 1 \tag{6}$$

If the width and height expand to random fields, namely:

$$\begin{aligned} w(\phi, \theta) = \; & w_0 + 0.03Y_1(\theta) + 0.015\{Y_2(\theta)\cos(k_1\phi) \\ & + Y_3(\theta)\sin(k_1\phi) + Y_4(\theta)\cos(k_2\phi) + Y_5(\theta)\sin(k_2\phi)\} \end{aligned} \tag{7}$$

$$\begin{aligned} h(\phi, \theta) = \; & h_0 + 0.03Y_1(\theta) + 0.015\{Y_2(\theta)\cos(k_1\phi) \\ & + Y_3(\theta)\sin(k_1\phi) + Y_4(\theta)\cos(k_2\phi) + Y_5(\theta)\sin(k_2\phi)\} \end{aligned} \tag{8}$$

where w_0 and h_0 are the mean values, Eq. (5) and (6) turn into random fields as well, thus can form a random elliptical shape for every realization θ. Fig. 2 presents such realizations and also the effect of the constants k_1 and k_2, for an ellipse of width 0.5 mm and height 0.2 mm. The Y_1 variable was kept constant for Fig. 2b, Fig. 2c and Fig. 2d, in order to demonstrate the distortion level.

The weft yarns of braided textiles are mostly simulated with lenticular cross-sections, because of the jamming-action of the braiding machine and the consequent stretching around the preform. Let two circles of radii r_1 and r_2 on a common Cartesian coordinate system, offset vertically by distances $o_1 < r_1$ and $o_2 < r_2$ from the coordinate center. The lenticular shape is defined as their intersection and all the above parameters can be calculated from the desired width w, height h and distortion d of the section (Fig. 3):

$$r_1 = \frac{w^2 + (h - 2d)^2}{4(h - 2d)} \tag{9}$$

$$r_2 = \frac{w^2 + (h + 2d)^2}{4(h + 2d)} \tag{10}$$

$$o_1 = -r_1 + \frac{h}{2} \tag{11}$$

$$o_2 = r_2 - \frac{h}{2} \tag{12}$$

For the particular case of a symmetric section, the distortion parameter d equals to zero. The reader is referred to Appendix A for the mathematical proof of Eq. (10). The parametric equations for the lenticular section are given as:

$$X(t) = \begin{cases} r_1\sin\gamma, & \text{if } 0 \leqslant t \leqslant 0.5 \\ r_2\sin\gamma, & \text{if } 0.5 \leqslant t \leqslant 1 \end{cases} \tag{13}$$

$$Y(t) = \begin{cases} r_1\cos\gamma + o_1, & \text{if } 0 \leqslant t \leqslant 0.5 \\ -r_2\cos\gamma + o_2, & \text{if } 0.5 \leqslant t \leqslant 1 \end{cases} \tag{14}$$

where the angle γ is calculated by the following formula:

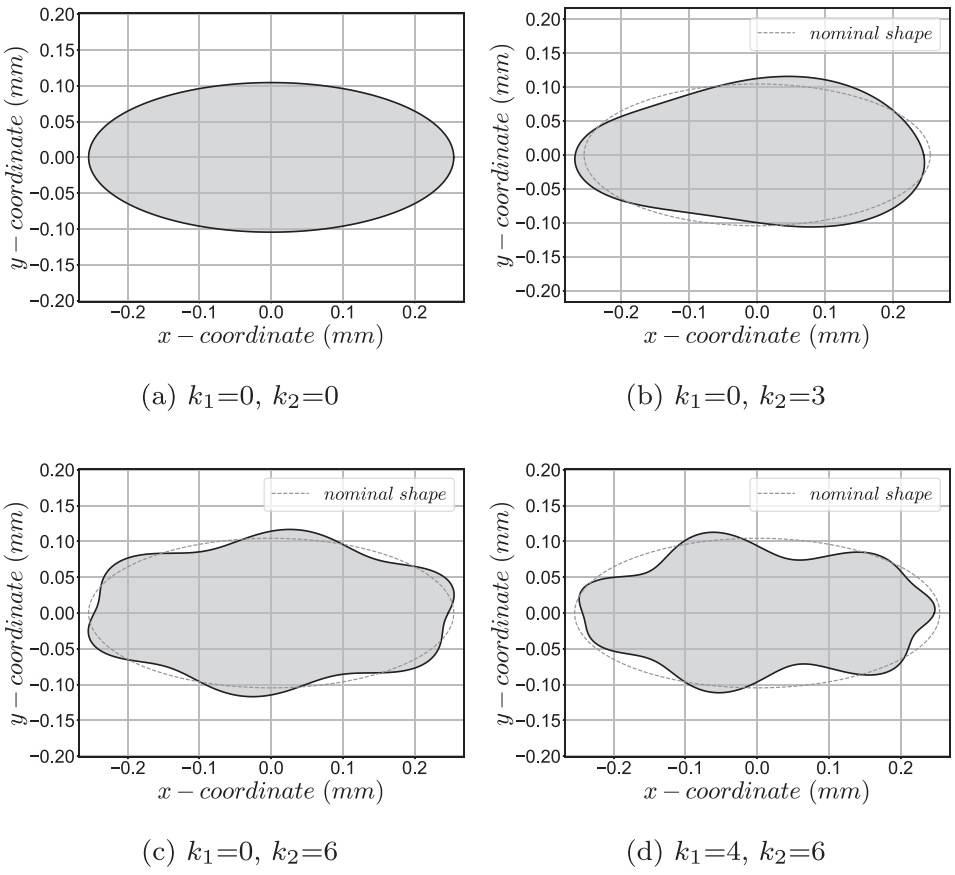

Fig. 2. Randomly generated elliptical cross-sections.

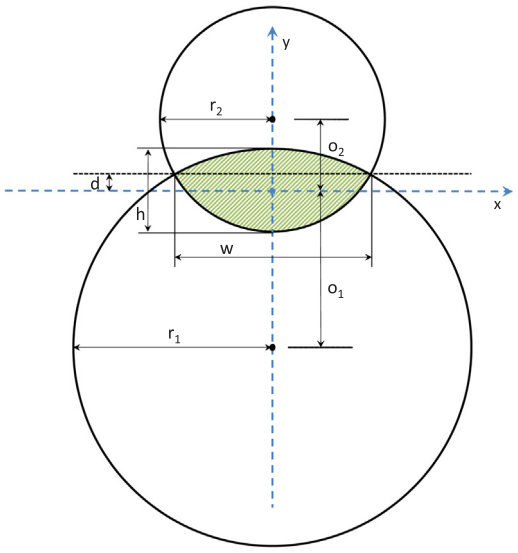

Fig. 3. Lenticular shape definition. (For interpretation of the references to colour in this figure legend, the reader is referred to the web version of this article.)

$$\gamma = \begin{cases} (1-4t)\arcsin\left(\frac{w}{2r_1}\right), & \text{if } 0 \leqslant t \leqslant 0.5 \\ (-3+4t)\arcsin\left(\frac{w}{2r_2}\right), & \text{if } 0.5 \leqslant t \leqslant 1 \end{cases} \tag{15}$$

As in the elliptical case, uncertainty is introduced through the expansion of the size parameters into random fields: $w = w(\phi, \theta)$ and $h = h(\phi, \theta)$ (see Eqs. (7) and (8)). The stochastic equations are obtained by propagating the uncertainties to Eqs. (13) and (14). Results for random realizations are shown in Fig. 4 for different cases of k_1, k_2, for a lenticular section of $w = 1$ mm and $h = 0.2$ mm. Once again, Y_1 was kept constant for Fig. 4b, c and d, in order to demonstrate the distortion level.

It is noted that using the Fourier series of Eq. (3) requires to carefully choose the amplitudes a_i and b_i as well as the upper limit of the series. On the other hand, the great advantage of the general approach is that in case of measurement data availability for the yarn distortion, the Fourier coefficients and their stochastic distribution can be determined directly from the data. A similar methodology as in [35] could be used for this purpose, e.g. use of the discrete Karhunen-Loève transformation to the measured data covariance matrix, which leads to uncorrelated Fourier coefficients describing the stochastic distribution of deviations from the nominal yarn shape. Furthermore, the correlation between adjacent yarns (cross-correlation) can be modelled by correlating the Fourier coefficients of the yarn cross sections (e.g. correlating $a_i^k(\theta)$ and $a_i^j(\theta)$ for yarns k and j). In case of available measurement data, these correlations can be determined as a function of the distance $\phi(\boldsymbol{x})$ of the cross sections. That way it could be possible to avoid modelling of textile compaction to obtain yarn shapes at crossover locations.

2.3. Modeling implementation

Implementation of the above formulation to a FE analysis, demands a modeling software that treats yarns as solid volumes, representing the approximate bounds of the fibers contained within them. This is feasible with a textile software such as WiseTex or TexGen, where yarn paths are represented by a 1D curve defined in 3D space, while yarn sections are described by 2D shapes emerging when cutting the yarn by a plane perpendicular to the yarn path tangent. The proposed methodology ensures continuity of the random section, thus application to the

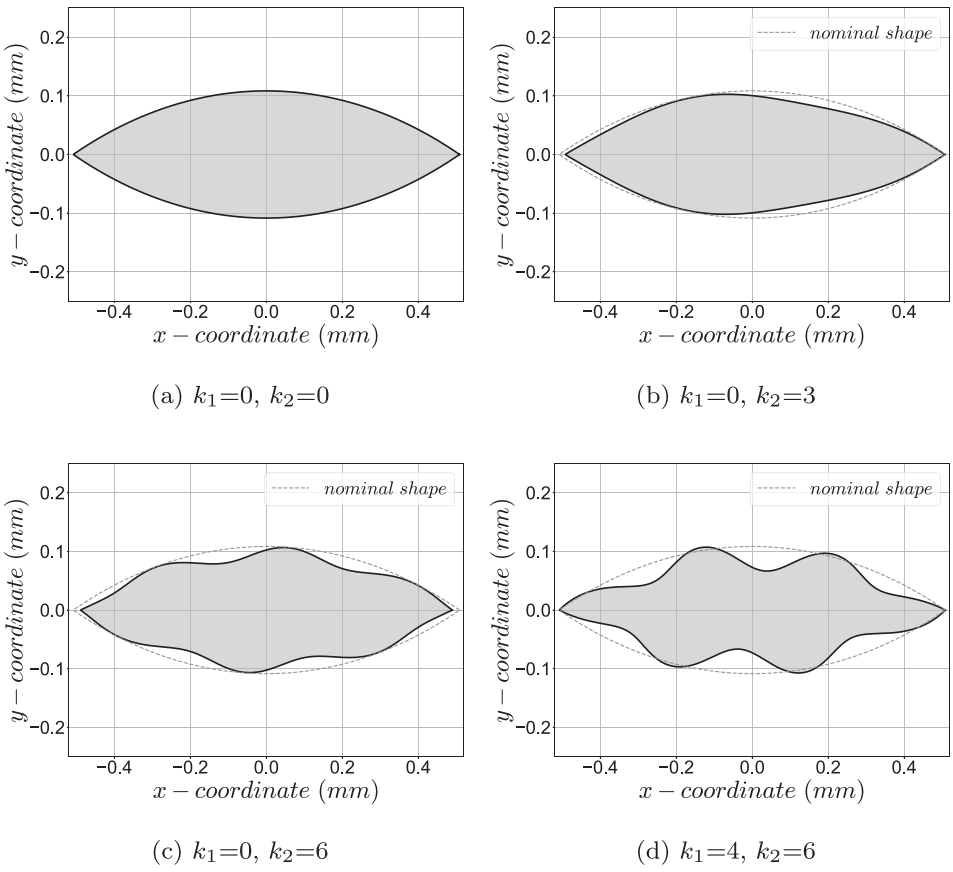

Fig. 4. Randomly generated lenticular cross-sections.

aforementioned softwares is evidently feasible.

Fig. 5 presents TexGen models of an elliptical, warp yarn (red) and a lenticular, interwined, weft yarn (green), as would emerge from a braiding process. In Fig. 5b the cross-sections are randomly generated to account for distortion, as opposed to Fig. 5a, where the ideal model is illustrated. This snapshot could represent distortion due to compaction, as the cross-sections, even though randomly generated, are constant along the yarn path. Implementation of variable sections is also feasible, and even with different oscillation periods, by modifying k_1, k_2 on each discrete section along the yarn length. This occurs because of the interpolation algorithms of TexGen between specified cross-sections, defined as:

$$C(t, \mu) = A(t) + [B(t) - A(t)]\mu, \quad 0 \leqslant t \leqslant 1, \quad 0 \leqslant \mu \leqslant 1 \tag{16}$$

where $C(t)$ is the interpolated section between sections $A(t)$ and $B(t)$ and μ varies from 0 to 1 linearly with the distance between them. Options for linear spline, natural cubic spline and Bezier spline interpolation are offered. Such techniques could be potentially used for pinching modeling, induced by jamming-action. An example is shown in Fig. 6.

3. Yarn waviness modeling

3.1. General description

Contrary to the common assumption in numerical studies, warp and weft yarn geometrical paths of textile composites are neither straight, nor perfectly harmonic. In fact, physical samples show random fluctuations from the trajectory of the ideal paths, as in Fig. 7 where processed images of textile layers from the literature are shown, after CT image enhancement techniques.

As mentioned in the introduction, this problem has first been addressed with a local stochastic metric basis theory, and later with a MCMC methodology able to generate stochastic paths complying with data from physical samples. The early approach requires good knowledge of differential geometry, while the random walk transition matrix of the MCMC method could be troublesome to generate. A novel approach, employing the Kriging model for generating stochastic deviations of yarn paths, is presented in the next section.

3.2. Formulation

The basic principle of the yarn waviness problem, regardless which method is being used, is that yarn paths can be statistically represented by partitioning their components into periodic, systematic variations and non-periodic, stochastic deviations. In mathematical terms, each yarn position (x_i, y_i) on the centerline, can be regarded as shifted by a deviation vector (u_i, v_i) from the location $(\bar{x}_i, \bar{y}_i)$, that the yarn would hypothetically have in the perfect path:

$$(x_i, y_i) = (\bar{x}_i, \bar{y}_i) + (u_i, v_i) \tag{17}$$

The Kriging model (also known as Gaussian process modeling) axiomatically holds the distinction between trend and deviation. Let $\boldsymbol{x} = \{x_i, \ i = 1,...,N\}$ be a vector of the input space (called experimental design - ED) and Y the corresponding scalar output. The basic assumption is that Y can be approximated by a single realization of a Gaussian random field:

$$Y \approx M(\boldsymbol{x}) = \boldsymbol{\beta}^T \boldsymbol{f}(\boldsymbol{x}) + \sigma^2 Z(\boldsymbol{x}) \tag{18}$$

The first term $\boldsymbol{\beta}^T \boldsymbol{f}(\boldsymbol{x}) = \sum_{i=1}^{P} \beta_i f_i(x)$ characterizes the trend of the field via linear regression, with $\boldsymbol{\beta}$ being the coefficient vector and $\boldsymbol{f}$ the set of P-order regression functions (generally Vandermode polynomials). The variance term includes the Kriging variance σ^2 and a zero-mean, unit variance Gaussian random field $Z(\boldsymbol{x})$. The spatial correlation of Kriging

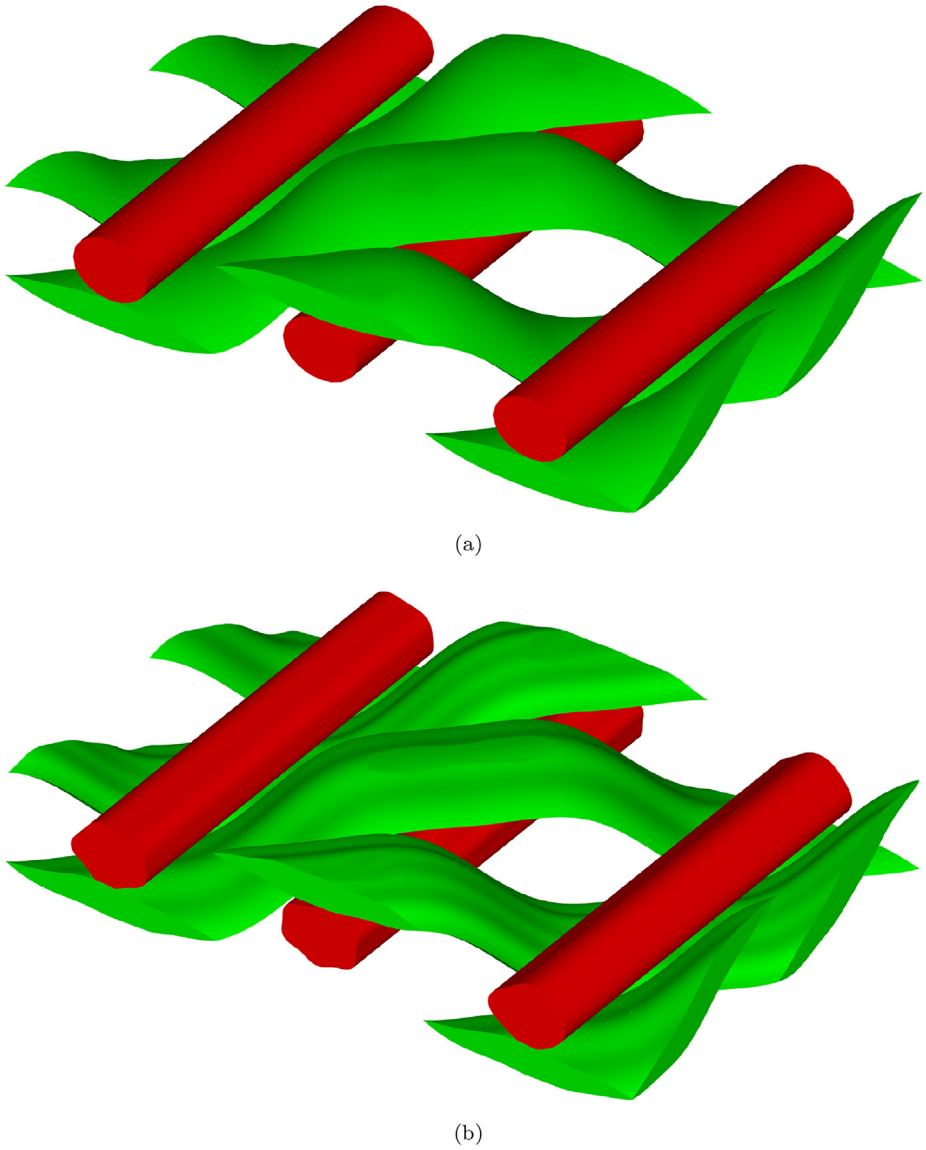

Fig. 5. Modeling representation of yarn distortion: (a) perfect model and (b) randomly generated imperfections. (For interpretation of the references to colour in this figure legend, the reader is referred to the web version of this article.)

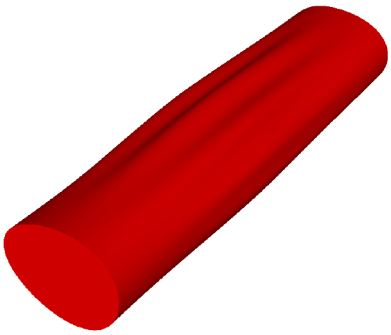

Fig. 6. Yarn pinch modeling via interpolation of variable, randomly generated sections. (For interpretation of the references to colour in this figure legend, the reader is referred to the web version of this article.)

is controlled by the autocorrelation function of $Z(\boldsymbol{x})$, namely $R(|x - x'|;\theta)$ for two points x and x', where θ are the correlation length parameters to be computed. Assuming a kernel type (e.g. exponential, square exponential, Matérn, etc.) for the above function, the correlation matrix $\boldsymbol{R}$ of the ED is computed:

$$\boldsymbol{R} = \begin{bmatrix} R(x_1, x_1) & R(x_1, x_2) & \dots & R(x_1, x_N) \\ R(x_2, x_1) & R(x_2, x_2) & \dots & R(x_2, x_N) \\ \vdots & \vdots & \ddots & \vdots \\ R(x_N, x_1) & R(x_N, x_2) & \dots & R(x_N, x_N) \end{bmatrix} \tag{19}$$

Kriging parameters $\boldsymbol{\beta}$ and σ^2 are calibrated via the generalized least-squares method, for a specific value of the correlation length parameter of the Gaussian field $\hat{\theta}$, as:

$$\boldsymbol{\beta}(\hat{\theta}) = (\boldsymbol{F}^T\boldsymbol{R}^{-1}\boldsymbol{F})^{-1}\boldsymbol{F}\boldsymbol{R}^{-1}Y \tag{20}$$

$$\sigma_y^2(\hat{\theta}) = \frac{1}{N}(Y - \boldsymbol{F}\boldsymbol{\beta})^T\boldsymbol{R}^{-1}(Y - \boldsymbol{F}\boldsymbol{\beta}) \tag{21}$$

where $\boldsymbol{F}_{ij} = \{f_j(x_i),\ i = 1, \dots, N,\ j = 0, \dots, P\}$ is the regression matrix at the input design points. For the calculation of the optimum correlation length $\hat{\theta}$, a minimization procedure should be applied in either of the following estimates:

$$\hat{\theta}_{ML} = \text{arg}min\left[\frac{1}{N}(Y - \boldsymbol{F}\boldsymbol{\beta})^T\boldsymbol{R}^{-1}(Y - \boldsymbol{F}\boldsymbol{\beta})(det\boldsymbol{R})^{\frac{1}{N}}\right] \tag{22}$$

$$\hat{\theta}_{CV} = \text{arg}min\left[Y^T\boldsymbol{R}^{-1}diag\left(\boldsymbol{R}^{-1}\right)^{-2}\boldsymbol{R}^{-1}Y\right] \tag{23}$$

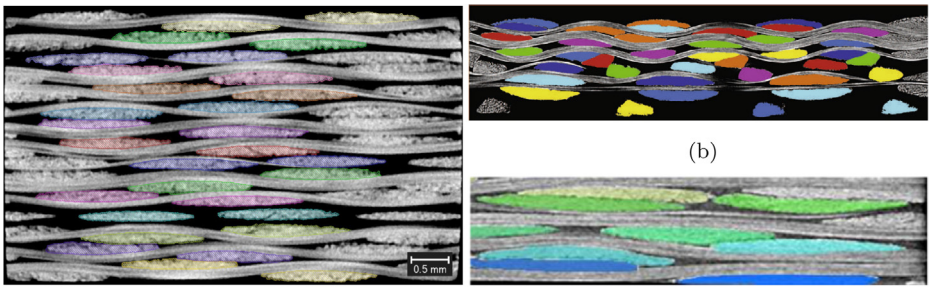

Fig. 7. Yarn waviness illustration from different sources: (a) [12], (b) [22] and (c) [17]. (For interpretation of the references to colour in this figure legend, the reader is referred to the web version of this article.)

where ML stands for Maximum Likelihood and CV for Cross-Validation. The latter approach is more robust if the autocorrelation function is not known a priori, according to [36]. Consequently, predicting the response of a new point $x_0 \notin \boldsymbol{x} = \{x_i,\ i = 1,...,N\}$of the input space, is feasible with the following formulas for the mean value and variance:

$$\mu(x_0) = \boldsymbol{f}(x_0)^T\boldsymbol{\beta} + \boldsymbol{r}(x_0)^T\boldsymbol{R}^{-1}(Y - \boldsymbol{F\beta}) \tag{24}$$

$$\sigma^2_{\hat{y}}(x_0) = \sigma^2_y\left(1 - \langle \boldsymbol{f}(x_0)^T\boldsymbol{r}(x_0)^T\rangle \begin{bmatrix} 0 & \boldsymbol{F}^T \\ \boldsymbol{F} & \boldsymbol{R} \end{bmatrix}\begin{bmatrix} \boldsymbol{f}(x_0) \\ \boldsymbol{r}(x_0) \end{bmatrix}\right) \tag{25}$$

where $\boldsymbol{r}(x_0) = R(|x_0 - x_i|;\hat{\boldsymbol{\theta}})$ is the correlation between the unknown point x_0 and the ED $\boldsymbol{x}$, while $\boldsymbol{f}(x_0)$ is the set of regression functions evaluated at x_0. It must be noted that Kriging is an exact interpolator, meaning that:

$$\mu(x_i) = M(x_i), \quad \sigma^2_{\hat{y}}(x_i) = 0, \qquad \forall\ x_i \in \boldsymbol{x} \tag{26}$$

3.3. Modeling implementation

The yarn waviness is taken into account by mapping the variation of the yarn path to the coordinates along the center line. Assuming that the centerline coordinates are given in a 3D Cartesian system (Fig. 8a), the first step is to establish a transformation into a 2D system (Fig. 8b), where x coordinate is the in-plane direction of the yarn and y the out-of-plane direction (undulation). The 2D system allows acquiring the systematic yarn position $(\bar{x}_i, \bar{y}_i)$ of Eq. (28). A few pairs are enough as an ED, to fit a Kriging model describing the function $\bar{y}_i = f(\bar{x}_i),\ i = 1,\ ...,N$.

Afterwards, by applying the formulation described in the previous section, the yarn path can be fully represented by the Kriging predictor $\mu(x)$ of Eq. (24), for any point x outside the ED. Once the systematic curve is predicted, random path generations can eventually be extracted from Eq. (18), where the parameters $\boldsymbol{\beta}$ and σ^2 have already been computed from the training procedure (Eq. (20)), while a zero-mean, unit variance random field realization $Z(\boldsymbol{x})$, can be generated by either the spectral representation method [37], or the Karhunen-Loève expansion [38]. Formulation for simulating a random field with the spectral representation method can be found in Appendix B.

For illustrative purposes, the proposed approach is demonstrated on a non-periodic, harmonic function. Let the function $f(x) = x\sin(x)$ within the interval [0, 10]. Considering 10 equally spaced points within this interval as an ED, the Kriging predictor $\mu(x)$ of Eq. (24) can perfectly represent the function with just a first-order Vandermode polynomial, as shown in Fig. 9, where the black, dashed line is the exact function and the blue, continuous line is the Kriging representation. Nevertheless, when using Eq. (18) for generating random paths, the regression order p should be slightly higher, depending on the data size N available (by definition $p \leqslant N$). Artificial oscillations due to Runge's phenomenon must be avoided. Random generations with the use of Eq. (18) are also visible in the same figure. Considering the kernel type, a Gaussian kernel was employed for both this example and the application of the next section and is highly recommended due to its strong generalization capabilities.

The correlation and variance factors of the zero-mean Gaussian field $Z(\boldsymbol{x})$ of Eq. (18), offer flexibility to the Kriging representation and add desired characteristics to the random path. The effect of the correlation length parameter is presented in Fig. 10a. It is evident that Kriging is able to "wrap" the random generation around the systematic, non-stochastic curve effectively. The effect of variance is shown in a parametric plot in Fig. 10b, for a constant correlation length value. The aforementioned variance parameter of $Z(\boldsymbol{x})$, is not to be confused with the scalar Kriging variance parameter $\sigma^2_{\hat{y}}$ of Eq. (21).

3.4. Discussion

From a purely mathematical perspective, the essential target here is to generate non-stationary random fields tailored around specific

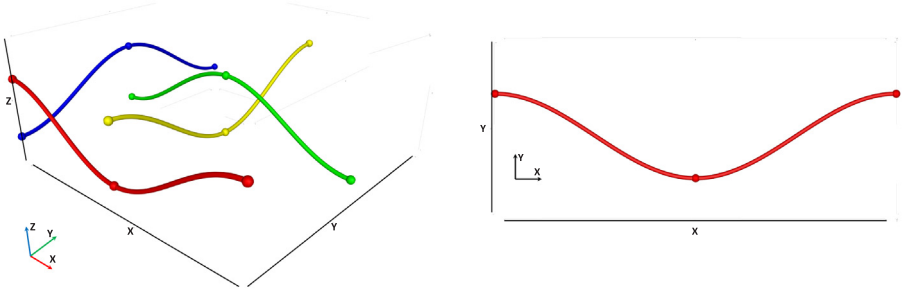

(a) 3D Cartesian coordinate system (b) 2D plane system

Fig. 8. Coordinate system transformation in TexGen. (For interpretation of the references to colour in this figure legend, the reader is referred to the web version of this article.)

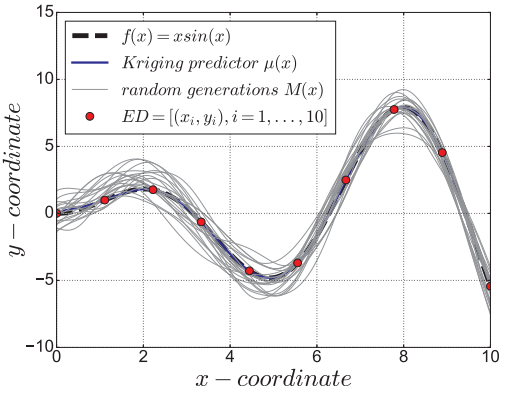

Fig. 9. Kriging random generations of a non-periodic harmonic function. (For interpretation of the references to colour in this figure legend, the reader is referred to the web version of this article.)

trends. The proposed methodology holds several advantages. As mentioned, the random Kriging paths can be calibrated with specific statistical characteristics, by adjusting the correlation and variance parameters of the zero-mean random field $Z(\boldsymbol{x})$. This means that correlation information from scanned samples, can be directly introduced into the Kriging formulation, either by extracting correlation lengths from the deviations' correlation matrix and putting them into the kernel of the autocorrelation function of $Z(x)$, or if using the Karhunen-Loève expansion, by decomposing the actual correlation matrix [21]. Reconstruction of random paths is then straightforward, as there is no need for a MCMC algorithm.

In addition, smoothing operations due to the discrete nature of Markov Chains are not required, which makes the proposed modeling attractive. Another drawback of the Markov Chain approach is the inability to simulate cross-correlated data between different yarns. As a series expansion method, the proposed approach can take cross-correlation into account [39], while being more efficient than the Karhunen-Loève approach in [20], as there is no integral equation to be solved numerically. Furthermore, besides short-range periodic paths extracted from RPC methods, Kriging is also able to represent non-periodic paths. Such cases could rise from symmetry-breaking features (e.g. heat exchangers, aerofoils, etc.), when attempting to quantify randomness on aperiodic, long-range textile preforms.

Random deviations of the fiber yarn path could as well be modeled with Fourier series. The procedure is similar to the one given in Section 2.2 for the yarn cross-section. However, compared to the Kriging model the following drawbacks emerge: (i) as mentioned, the random yarn path is not necessarily a periodic function. Modeling a non-periodic function is possible with Fourier series, but leads to inaccuracies at the edges of the domain of the approximated function [40]. (ii) The spatial correlation of the points along the yarn path is captured by the correlation of the (large number of) Fourier coefficients. Adjusting the deviation amplitude or frequency is much less straightforward compared to Kriging, because a multitude of Fourier coefficients needs to be modified at the same time, in order to describe effects as shown in Fig. 10. (iii) For a small number of measurement points (i.e. large distance), the number of Fourier coefficients that may be used is limited. When using Fourier terms with a period similar to -or smaller than- the distance of two measurement points, an artificial short wave oscillation is introduced in the approximation. The Kriging model however, provides a smooth approximation even for a small number of points.

4. Application to a 3D triaxially braided multiscale model

4.1. Model description

The effect of yarn distortion and short-range yarn waviness is demonstrated herein, within a multiscale framework of a triaxially braided material model. The proposed modeling approaches are applied on a mesoscale level to create random RVEs with stochastic geometric imperfections. The response variability is calculated in terms of macroscale stiffness and strength scatter. The model is a typical 3D triaxially braided layer, where the axial (or warp) yarns lay straight and equally spaced, while the weft yarns interlace the axial yarns at an angle, according to the pattern shown in Fig. 11a. An isometric view of the RVE extracted from this pattern and its dimensions, are presented in Fig. 11b. The section area of the weft yarns (green and blue) is lenticular while the axial yarns (red) are of elliptical shape. Regarding the material properties, AS4 Carbon Fibers and EPON 9504 resin for the polymer matrix are used. The values are given in Table 1 along with some geometrical model parameters. For further information regarding the model, the reader is referred to [41].

4.2. Stiffness and strength prediction algorithms

The response this study will focus on, is the effective stiffness and strength properties of the macroscale. Reliable estimation of the mechanical properties for such complex materials requires numerical multiscale schemes. Regarding the elastic properties, a two-step homogenization scheme is employed as in a previous study by the authors [41].

As a first step, assuming transversely isotropic properties for the carbon fibers and isotropic properties for the matrix on the microscale, the effective stiffness properties of the yarns are calculated with the Chamis analytical criterion [42]. For the second step, these properties are provided to the mesoscale RVE, where a numerical homogenization

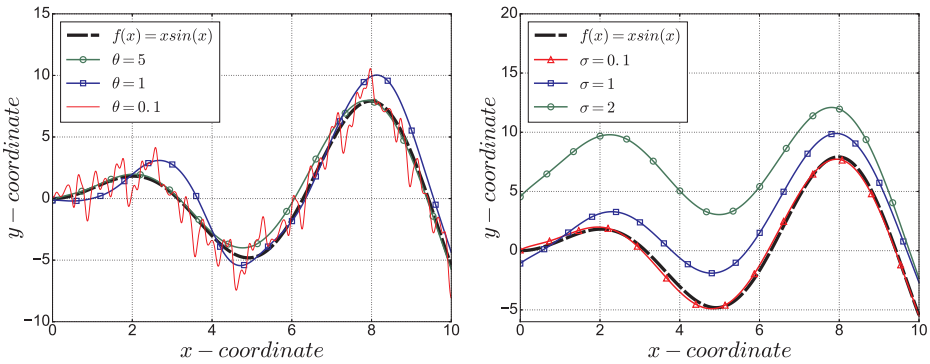

(a) Correlation length influence (b) Variance influence

Fig. 10. Parametric plots in terms of correlation and variance for randomly generated Kriging representations of a non-periodic harmonic function. (For interpretation of the references to colour in this figure legend, the reader is referred to the web version of this article.)

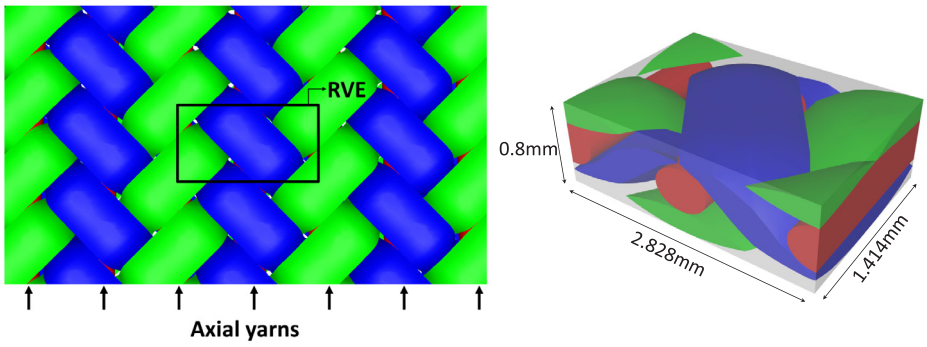

(a) Braiding pattern and RVE (b) RVE mesoscale model

Fig. 11. Triaxial braiding pattern: (a) Top view, (b) TexGen RVE mesoscale model. (For interpretation of the references to colour in this figure legend, the reader is referred to the web version of this article.)

Table 1
Material and geometric parameters of braided model.

Parameter	Symbol	Value
Longitudinal fiber modulus	E_{f1}	227.53 GPa
Transverse fiber modulus	E_{f2}	16.55 GPa
In-plane shear fiber modulus	G_{f12}	24.82 GPa
Out-of-plane shear fiber modulus	G_{f23}	6.89 GPa
In-plane fiber Poisson's ratio	v_{12}	0.2
Out-of-plane fiber Poisson's ratio	v_{23}	0.25
Tensile fiber strength	X_{ft}	3.16 GPa
Compressive fiber strength	X_{fc}	0.728 GPa
Matrix Young's modulus	E_m	3.5 GPa
Matrix Poisson's ratio	v_m	0.38
Matrix tensile strength	X_{mt}	60.18 MPa
Matrix compressive strength	X_{mc}	107.37 MPa
Matrix plastic yield	σ_y	69 MPa
Yarn volume fraction	YVF	80%
Braid angle	BA	45°
Undulation angle	UA	57°
Total fiber volume fraction	VF_{tot}	48–50%

is performed with TexGen for the computation of the effective orthotropic stiffness properties of the braided layer at the macroscale. Periodic boundary conditions along with the unit-stress method are applied, while a voxel mesh is created in Abaqus [43] for the numerical solution of all six load cases required for the elastic tensor. For detailed information on the numerical homogenization procedure, the reader is referred to [41].

Concerning strength properties, the current study deals with the ultimate strength prediction of the macroscale, solely under uniaxial tension. Once more, a two-step multiscale scheme is employed, however both steps include FE models in this case. For the micro-to-mesoscale transition, a typical hexagonal RVE arrangement is applied in order to extract the effective strength properties of the yarns. Prescribed displacement boundary conditions according to Barbero [45] are applied, whereas the required load cases for longitudinal tension/compression, transverse tension/compression, in-plane shear and out-of-plane shear properties are shown in Fig. 12. The fiber material model is considered as linear elastic up to brittle failure, according to a maximum stress criterion:

$$\begin{aligned} \sigma_f &\geqslant X_{ft} \\ |\sigma_f| &\geqslant X_{fc} \end{aligned} \tag{27}$$

while the matrix accounts for both permanent deformation due to plasticization, according to the von Mises plasticity model of Abaqus, and fracture failure initiation according to the Christensen criterion [46]:

$$\frac{\sigma_{vm}^2}{X_{mc}X_{mt}} + \left(\frac{1}{X_{mt}} - \frac{1}{X_{mc}}\right) I_1 \geqslant 1 \tag{28}$$

The above criterion is a modified version of von Mises, considering the discrepancy between compressive and tensile strength due to the hydrostatic pressure (σ_{vm} is the von Mises stress and $I_1 = \sigma_1 + \sigma_2 + \sigma_3$ is the first stress invariant). All symbols are reported in Table 1.

At the second step of the strength prediction algorithm, the mesoscale RVE extracted from TexGen is properly modified to account for failure of the yarns and matrix, while the stresses are monitored within a displacement control solution method. Initiation of failure for the yarns is predicted according to the Hashin criterion [47], where the following four failure modes (fibre failure in tension, fibre failure in compression, matrix failure in tension and matrix failure in compression respectively) are associated with the yarn damage:

$$\left(\frac{\sigma_1}{X_t}\right)^2 + \frac{\tau_{12}^2 + \tau_{13}^2}{S_{12}^2} = 1 \qquad (\sigma_1 > 0) \tag{29}$$

$$-\sigma_1 = X_c \qquad (\sigma_1 < 0) \tag{30}$$

$$\left(\frac{\sigma_2 + \sigma_3}{Y_t}\right)^2 + \frac{\tau_{23}^2 - \sigma_2\sigma_3}{S_{23}^2} + \\ + \frac{\tau_{12}^2 + \tau_{13}^2}{S_{12}^2} = 1 \ (\sigma_2 + \sigma_3 > 0) \tag{31}$$

$$\left[\left(\frac{Y_c}{2S_{23}}\right)^2 - 1\right]\frac{\sigma_2 + \sigma_3}{Y_t} + \left(\frac{\sigma_2 + \sigma_3}{2S_{23}}\right)^2 + \\ + \frac{\tau_{23}^2 - \sigma_2\sigma_3}{S_{23}^2} + \frac{\tau_{12}^2 + \tau_{13}^2}{S_{12}^2} = 1 \qquad (\sigma_2 + \sigma_3 < 0) \tag{32}$$

In these equations, σ_i is the stress component in i direction, τ_{ij} are the components of the shear stresses and X_t, X_c, Y_t, Y_c, S_{12}, S_{23} are the effective strength properties of the yarns, having been extracted from the previous step (see also Fig. 12). The matrix material model remains the same as in the first step.

The progressive damage model is implemented for all scales as a user defined field subroutine (USDFLD) in Abaqus, based on the instantaneous stiffness degradation concept. Namely, when stresses at an integration point of the model satisfy the failure initiation criterion, its stiffness is reduced to a specific value according to the relevant failure mode and the respective degradation factor. It is a popular choice among researchers [48–50], since it can be easily implemented while not adding any convergence difficulties to the progressive failure algorithm. Especially for probabilistic analyses, this is a viable option since convergence, robustness and efficiency are assured, as opposed to an UMAT approach. The algorithm is illustrated in a flow chart for better comprehension (Fig. 13), including the degradation factors chosen for both scales according to [44]. It should be noted, that after damage localization (post-failure path) the described approach is not

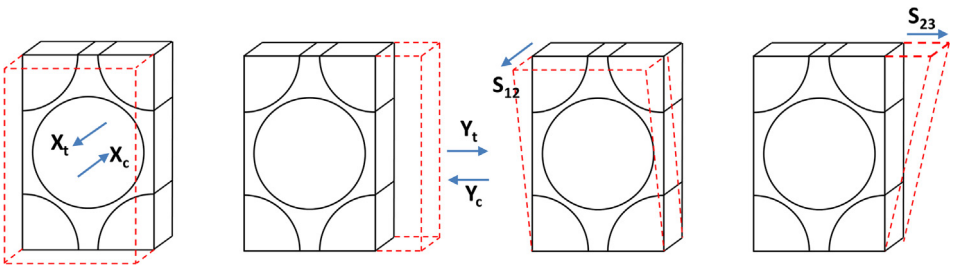

Fig. 12. Hexagonal microscale RVE and required load cases for the effective yarn properties. (For interpretation of the references to colour in this figure legend, the reader is referred to the web version of this article.)

reliable; firstly, because the homogenization problem under periodic conditions becomes ill-posed, but also because the error due to the energy dissipation negligence would become crucial. Moreover, the assumption of small strains (geometrically linear analysis) becomes invalid after damage initiation.

Table 2 presents the results of the previously discussed multiscale methodologies for stiffness and strength prediction, if applied to the braided model of Section 4.1, when no uncertainties have yet been implemented (deterministic case). It is highlighted, that the nonlinear response is highly dependent on whether the yarns are in contact or not. As shown in Fig. 14, a stiffer model with a volume fraction of 49.86% reaches a failure strength of 230.967 MPa, while a slightly less stiff model (V_f = 47.98%) with a thin film of matrix around the yarns, reaches a higher ultimate strength (281.081 MPa). For this study, the unfavorable case of the stiffer model will be used as nominal response, while the distortion and waviness variability is expected to cover all possible scenarios.

4.3. Numerical issues

The complex braided architecture of the mesoscale seen in Fig. 11, requires high-fidelity FE modeling to be sufficiently captured. Meshing such surfaces with tetrahedral elements (i.e. conformal meshing) may result in bad element shapes, and since the mesh generation needs to be automated, this approach cannot be applied. The voxel (volume pixel) technique is based on hexahedral elements of the same size with aspect ratio of one. This technique offers easier mesh generation, with elements of higher accuracy than those of conformal meshes, and can discretize in a robust way models of high complexity.

The voxel mesh is adopted in this study due to the robustness and the complete lack of bad elements; features vital for a study of probabilistic nature. Convergence analyses have been conducted for both the stiffness and strength outputs, and the results are presented in Fig. 15. In both plots, the horizontal axis labeled as "voxels", accounts for the number of elements located in the direction of the longest aspect of the RVE. For the strength case of Fig. 15b, the top horizontal axis demonstrates the convergence related to the number of analysis steps in Abaqus, due to the USDFLD subroutine. The routine has access to material point quantities only at the start of each increment (explicit approach), hence the accuracy of the results is also step-dependent [43]. As a trade-off between accuracy and efficiency, 120 voxels (equals to 700920 DOFs) where each of them has an aspect of approximately 0.02 mm, and 120 steps are selected for all analyses further on. The above mesh choice is also assumed sufficient to represent the geometric

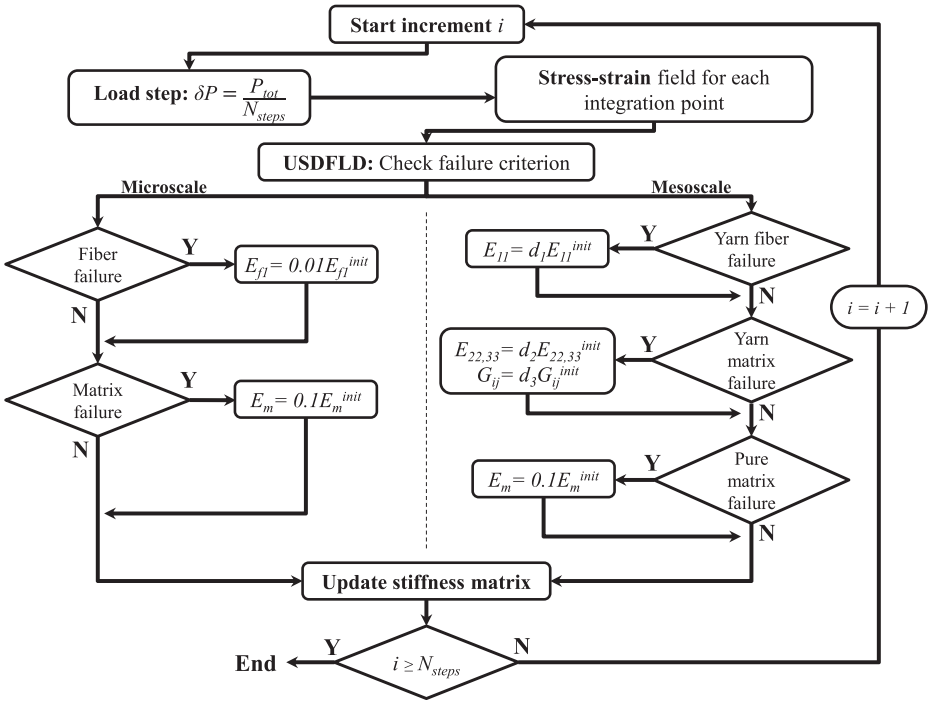

Fig. 13. Strength prediction algorithm via USDFLD approach: the microscale model reduces the fiber stiffness by 1% and the matrix stiffness by 10% for each failed element; for the mesoscale model where the Hashin criterion is applied, d_1 equals to 0.07 for tension (Eq. (29)) and 0.2 for compression (Eq. (30)), while d_2 equals to 0.14 for tension (Eq. (31)) and 0.4 for compression (Eq. (32)). For combined shear longitudinal or transverse damage, the shear moduli of the yarn G_{12}, G_{13} and G_{23} are degraded as well by $d_3 = 1 - (1 - d_1)(1 - d_2)$ [44].

Table 2
Deterministic results of the triaxially braided model.

Mesoscale (yarn)					Stiffness (GPa)				
	E_{11}	E_{22}	E_{33}	G_{12}	G_{13}	G_{23}	ν_{12}	ν_{13}	ν_{23}
	182.72	11.88	11.88	8.38	8.38	4.69	0.24	0.24	0.27
					Strength (MPa)				
	X_t	X_c	Y_t	Y_c	S_{12}	S_{23}			
	2546.62	590.63	43.38	160.15	41.68	31.33			
Macroscale (layer)					Stiffness (GPa)				
	E_{11}	E_{22}	E_{33}	G_{12}	G_{13}	G_{23}	ν_{12}	ν_{13}	ν_{23}
	34.53	12.05	7.46	7.09	3.17	3.68	0.52	0.07	0.55
					Strength (MPa)				
	X_t^{ult}								
	230.97								

deviations for the stochastic analysis of distorted yarn sections and waviness.

Nonetheless, the voxel technique carries some burdens as well. A fine voxel mesh is computationally demanding and combined with probabilistic methods of repetitive type, could be proven prohibitive. Another issue is the possible oscillation of stresses at the matrix/yarn boundary because of the pointy interface surfaces, which may affect strength predictions. Several studies have addressed this problem, by applying non-local methods and smoothening either the stresses or the voxel geometry. Other studies however, have shown that for uniaxial cases the error can be neglected [51,30]. The focus of the current study is on variability due to aleatory uncertainties. Such systematic modeling errors (epistemic uncertainty) will not affect the variance results and will not be considered. They will, nonetheless, be investigated in a future study entirely dedicated to uncertainty quantification of textiles' strength properties.

Another numerical issue is the intersections between yarns that could possibly emerge in a stochastic realization of the distorted geometry. TexGen eliminates most of the small intersections as the mesh is generated, via a method based on interference depth, which iteratively adjusts the node position in the volume mesh until the intersection is reduced to a given tolerance [5]. This of course leads to slight loss of yarn volume, which adds an extra error to the procedure. A potential gross error was avoided in this work, with a simple threshold in the algorithm and an acceptance-rejection sampling technique (accept only the samples found less than this threshold value, while in the opposite case generate another sample).

5. Response variability estimates

The triaxially braided layer presented in the previous section, is investigated herein under stochastic yarn distortion and waviness. The purpose of this study is to implement the proposed uncertainty modeling framework and examine the scatter of the response, in terms of stiffness and strength at a macroscale level. Due to lack of data, a forward uncertainty propagation problem is implemented, while parametric analyses with respect to the distortion and waviness amplitude of the input, are performed. The random RVE used in the multiscale scheme, composes a short-range application of spatial variations. As a result, the cross-correlation between different yarns is not taken into account. However, as discussed in Section 3.4, the methodology is able to incorporate this assumption.

5.1. Yarn distortion

The same level of distortion was introduced for both the warp (elliptical shape) and weft (lenticular shape) yarns of the model. The random cross-section of the yarns is assumed constant along the RVE. Three parametric cases were conducted with an increasing distortion amplitude, namely $k_1 = 0$, $k_2 = 3$, $k_1 = 0$, $k_2 = 6$ and $k_1 = 4$, $k_2 = 6$. These are the same cases used in Section 2.2, so a graphical sense of the distortion level can be acquired from Figs. 2 and 4. However, the value of random parameter Y_1, which controls the mean reference width and height, thus the volume of the yarns, was kept constant in these figures. A sense of the maximum deviations that can occur from the nominal sections, can be acquired by calculating an extreme value for the most distorted case with $k_1 = 4$, $k_2 = 6$. A potential maximum deviation of 0.05 mm from Fig. 4d for the lenticular yarns, if added with an extreme case of variability for Y_1 (e.g. three standard deviations away from the mean) results in a total maximum deviation of 0.15 mm. According to measurements from a twill carbon fabric in [24], this value is within realistic range. Moreover, the variance values for yarn heights and widths

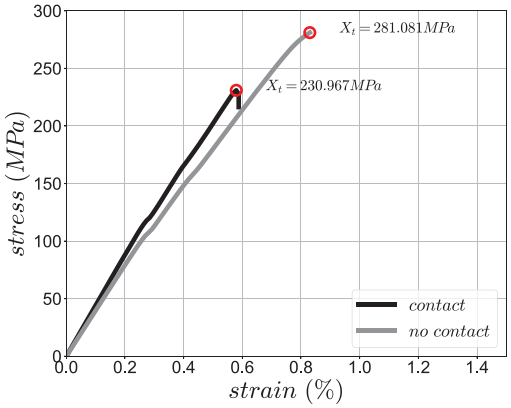

(a) Uniaxial tension response comparison

(b) Contact between yarns

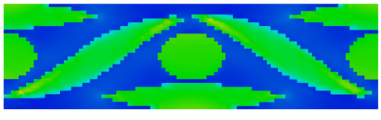

(c) No contact between yarns

Fig. 14. Comparison of nonlinear behavior regarding the contact of the yarns. (For interpretation of the references to colour in this figure legend, the reader is referred to the web version of this article.)

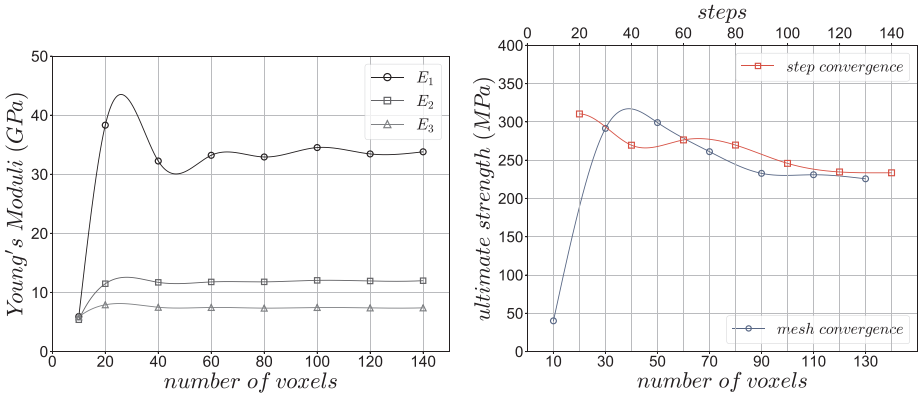

(a) Mesh convergence for stiffness response (b) Mesh and step convergence for strength response

Fig. 15. Convergence analysis of the voxel-based FE model. (For interpretation of the references to colour in this figure legend, the reader is referred to the web version of this article.)

found in the same reference (in terms of coefficient of variation (COV), a normalized measure of variance equal to the standard deviation σ, divided by the mean value μ), are comparable with the COV offered by Y_1, for example for the width of the elliptical yarns (Eq. 7): $\text{COV}(w) = \sigma(0.03Y_1)/0.5 = 0.03/0.5 = 6\%$.

5.1.1. Stiffness properties

Seeking for an adequate number of random simulations, the COV is plotted against the increasing amount of model evaluations. The response variability of all elastic parameters has practically converged after 300 Monte Carlo simulations, as it can be seen in Fig. 16, for the case of $k_1 = 0$, $k_2 = 3$. The same stands for the rest of the cases.

Regarding the variability estimation, it is shown in Fig. 17a that the majority of the parameters lies in the range of 8–10%. So even for mildly distorted shapes ($k_1 = 0$, $k_2 = 3$), the response variability is significant. It is also evident that yarn distortion affects equally the longitudinal and transverse stiffness ($\text{COV}(E_1) \approx \text{COV}(E_2)$). Variability slightly increases for the medium distortion case ($k_1 = 0$, $k_2 = 6$), while for the extreme case of $k_1 = 4$, $k_2 = 6$, it drops. This could be justified from the filtering of intersections between the yarns and the adjustments made from TexGen; the stiffness is highly dependent on the volume fraction of the RVE, hence the filtering of intersections between wavy shapes causes small insensitivity to the volume fraction and consequently to the stiffness.

An estimation for the shape of the probability density function (PDF) of E_1, is illustrated in Fig. 17b. The rest of the major elastic parameters (E_2, E_3, G_{12}) are omitted as they have similar shapes. The strong correlation between the PDFs of the elastic parameters and the volume fraction, for this type of uncertain input, is something to be further investigated. However, as an illustration a scatter plot is shown in Fig. 18 for the case of $k_1 = 0$, $k_2 = 3$. It is noted that the PDFs of Fig. 17b are also similar to the PDF of yarn volume fraction extracted from measurements in [24].

5.1.2. Strength properties

Concerning the strength variability for the case of uniaxial tension in the longitudinal yarns' direction, the scatter levels were found higher compared to the stiffness (≈ 13%). An interpretation for the higher COV level in comparison with stiffness, is that failure is a more local-oriented phenomenon and distortions are very likely to act as damage initiation areas. Once again, 300 Monte Carlo simulations were enough for the COV to converge (Fig. 19), for all three cases performed. If the scatter of the stress-strain curves is plotted, it can be seen that two major subgroups are forming. Fig. 20a displays the case of mild distortion ($k_1 = 0$, $k_2 = 3$), where the first core is located around a value of 230 MPa and the second around 280 MPa. This could be expected from the discussion made in Section 4.2 regarding the effect of contact between yarns.

A more interesting remark can be made from the parametric PDF plot of Fig. 20b. Even though the mode with the higher strength value is more probable for the first case ($k_1 = 0$, $k_2 = 3$), the median approximates the lower value mode as the distortion level increases. This is considered reasonable in terms of physical interpretation, and highlights the importance of uncertainty quantification for such input data.

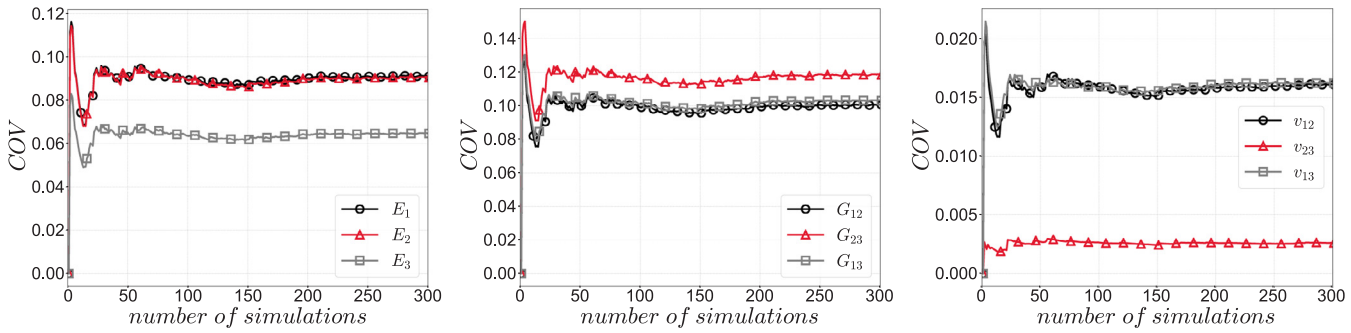

(a) Young's moduli (b) Shear moduli (c) Poisson's ratios

Fig. 16. Variation convergence of elastic properties under stochastic yarn distortion, for the case $k_1 = 0$, $k_2 = 3$. (For interpretation of the references to colour in this figure legend, the reader is referred to the web version of this article.)

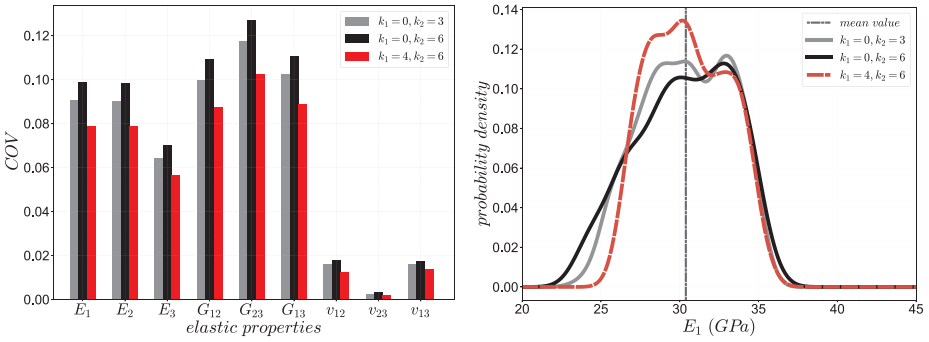

(a) Response variability (b) Probability density estimation for E_1

Fig. 17. Variability and density estimation of the stiffness properties. (For interpretation of the references to colour in this figure legend, the reader is referred to the web version of this article.)

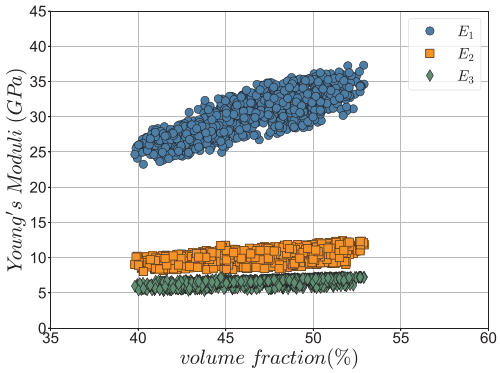

Fig. 18. Scatter plot of stiffness against the fiber volume fraction for the case of $k_1 = 0$, $k_2 = 3$. (For interpretation of the references to colour in this figure legend, the reader is referred to the web version of this article.)

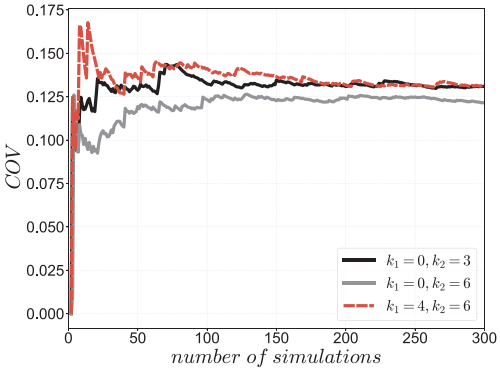

Fig. 19. Variation convergence of strength under stochastic yarn distortion. (For interpretation of the references to colour in this figure legend, the reader is referred to the web version of this article.)

5.2. Yarn waviness

In this section, stochastic waviness is introduced to the weft yarns of the model. The modeling framework presented in Section 3, allows calibration in terms of variance (σ) and correlation (θ). In order to explore the effects of both, a general case is first chosen as a baseline, with $\sigma = 3$ and $\theta = 1$. Then, the second case weakens the correlation scale to $\theta = 0.4$ to examine possible effects, while the variance is fixed. Finally, the input variance is boosted in the third case to $\sigma = 4$, for the same correlation length as in the baseline case. Graphical representations for the three cases mentioned are shown in Fig. 21, where the black line is a part of the nominal yarn path in 2D, while the grey lines are random path generations. The maximum deviations from the nominal paths, are roughly 0.25 mm (Fig. 21a,b) and 0.50 mm (Fig. 21c), which according to the literature [52,53] lie within possible amplitudes for textiles. Regarding the variance levels, the COV values for the waviness offered in [53], put the chosen input into context, as the calculated COV of 23% at the straight yarn segment ($x = 2$mm) of Fig. 21a, lies well within range. Regarding the correlation length values, the two cases of $\theta = 1$ and $\theta = 0.4$, could be interpreted as one with no dips (change of wave phase) at the straight yarn segments and one with at least one dip. The terminology is borrowed from [17], where dips where observed from measurements of a 2/2 twill weave.

5.2.1. Stiffness properties

Regarding the elastic properties, all response samples converge smoothly within the 300 performed simulations. Fig. 22 confirms the latter, for the baseline case of $\sigma = 3$ and $\theta = 1$. Convergence is ensured for the other parametric cases as well. A comparative bar plot for an overview on the elastic response variability, is presented in Fig. 23. In most cases, the variance ranges between 5 and 10%; however, the transverse stiffness exceeds this range and consequently, so does the Poisson's ratio ν_{12}. As opposed to Section 5.1.1, the transverse stiffness is more sensitive than the longitudinal, since variability is implemented only to the weft yarns, which are interlacing the axial, unaltered warp yarns. Concerning the parametric cases, the rough paths after the correlation decrease ($\theta = 0.4$), do not have a crucial effect on the variability, although they tend to lower it, presumably because of the interactions and the slight loss of volume. On the other hand, the variance increase of the third parametric analysis ($\sigma = 4$), boosts indeed the response variability, but not to a great extent.

The effect of stochastic waviness to the weft yarns and the sensitivity of the transverse direction, is also evident from the density estimations of Fig. 24. The PDF of E_1 is mainly unimodal and approximates a normal distribution (Fig. 24a). On the contrary, the PDF of E_2 is highly skewed, with a second mode rising on the right part, meaning that nonlinearities are introduced due to the asymmetric spatial variations.

5.2.2. Strength properties

The scatter of the ultimate tensile strength for the stochastic waviness case is quite large. The COV reaches the value of 20%, while it has the most fluctuating behavior among all other cases reported so far, within the span of the 300 Monte Carlo runs performed. As shown in Fig. 25, all three parametric analyses converge approximately to the same value, while the case with the shortest correlation length ($\sigma = 3$, $\theta = 0.4$ - Fig. 21b) has the most irregular behavior until convergence.

However, the variability extent is relatively misleading, since the scatter plot of the baseline case ($\sigma = 3$, $\theta = 1$) in Fig. 26a, shows that there is a principal spread around 100 MPa and then some higher

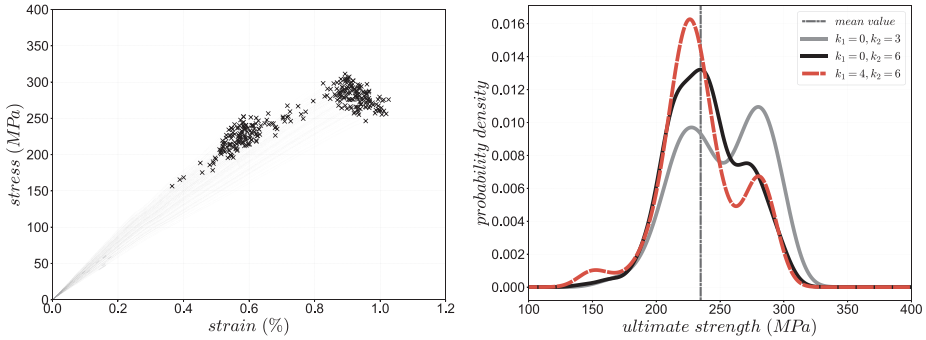

(a) Scatter of nonlinear curves (k_1=0, k_2=3) (b) Probability density estimation

Fig. 20. Scatter plot and density estimation of the ultimate tensile strength under stochastic yarn distortion. (For interpretation of the references to colour in this figure legend, the reader is referred to the web version of this article.)

dispersed results, which are of course stretching the overall variance. This is also illustrated in terms of probability density estimation in Fig. 26b.

The reason behind the large response variability is linked with the rather low median value of roughly 100 MPa. The assumption of uncorrelated yarns results in asymmetries within the RVE. Therefore, damage localization can occur at different locations and also quite earlier than the nominal case. So even though some local damage could be followed by a strengthening part (which was often the case for many realizations close to the median), the method considers as failure the first softening occurrence, due to the assumptions discussed in Section 4.2. Moreover, it is evident from Fig. 26b that this problem is rather insensitive to the modifications of variance and correlation. This is probably connected with the short scale of this application, meaning that changes in the variation of the yarn path within the RVE range, are hard to be reflected in the strength response of the longitudinal direction.

5.3. Surrogate modeling

The proposed probabilistic modeling framework could be also applied for uncertainty quantification purposes (e.g. global sensitivity analysis) or reliability analysis. However, the excessive number of necessary evaluations of the high-fidelity FE model, raises a prohibitive computational burden. Bypassing the FE simulation with a surrogate model holds as a remedy, as these models can reduce the computational effort by orders of magnitude. For formulating and applying surrogate models to uncertainty quantification problems, the reader is referred to [41,54]. These references explain how to map uncorrelated random variables with the desired response, by using artificial neural networks, polynomial chaos expansions and Kriging models. Yet approximating the response function when sampling random fields might be demanding, depending on the stochastic dimension of the problem or the discretization of the model.

Towards an efficient surrogate-based stochastic FE methodology, some comments are made herein concerning the problems of yarn distortion and waviness, by utilizing the described braided use case. For the yarn distortion problem, a dimensionality reduction could be achieved by using as an input vector the five uniform random variables of Eq. 2, instead of the uncertain input parameters emerging from the spatial discretization of the field. In this manner, the input space is independent from the size of the field and the FE model, so an efficient training procedure can be accomplished. Regarding the accuracy, a comparison between a surrogate model (Kriging) and a conventional Monte Carlo approach for predicting the E_1 scatter, shows sufficient convergence in terms of cumulative distribution function (CDF) (Fig. 27a), but also point-to-point for 50 samples outside the training dataset. (Fig. 27b).

The prediction considering yarn waviness via surrogates is harder and requires more training data. Depending on the problem, a similar dimensionality reduction as before can be used, for example mapping the phase angle of the spectral representation method (see Appendix B) to the output, instead of the coordinates of the random field representing the yarn. This technique was first proposed by Giovanis and Papadopoulos [55], but even though it was tested for the current use case, the results were not satisfactory, while due to the interpolation of TexGen between the path points, not many of them are required. Consequently, the training was performed by mapping the undulation coordinates of the yarns with the response and the results are presented in Fig. 28.

Evidently, the accuracy of the latter figure is not ideal and further investigation is worthwhile. What is even more challenging is the emulation of the strength prediction, which requires more advanced methods in order to be accurate (e.g. hybrid surrogates, adaptive techniques, etc.) This will be investigated in a future work regarding uncertainty quantification of the nonlinear behavior of textiles. It should be finally noted, that further efficiency can be reached for all cases, if the training samples emerge from a space-filling technique, such as latin hypercube sampling [55].

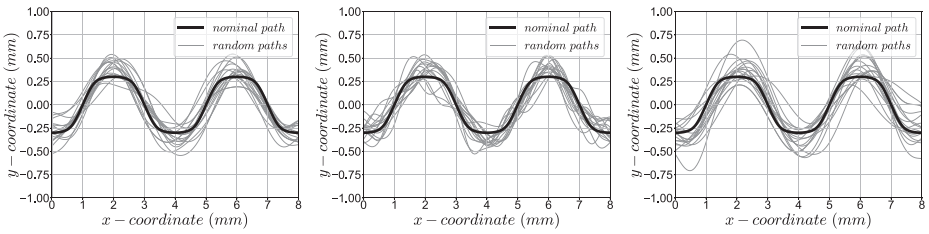

(a) $\sigma = 3$, $\theta = 1$ (b) $\sigma = 3$, $\theta = 0.4$ (c) $\sigma = 4$, $\theta = 1$

Fig. 21. Yarn waviness parametric cases.

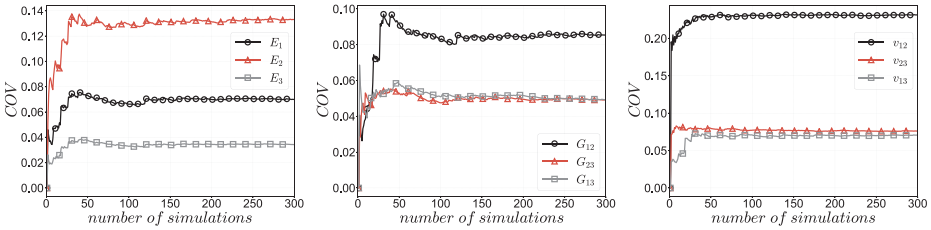

(a) Young's moduli (b) Shear moduli (c) Poisson's ratios

Fig. 22. Variation convergence of elastic properties under stochastic yarn waviness ($\sigma = 3$, $\theta = 1$). (For interpretation of the references to colour in this figure legend, the reader is referred to the web version of this article.)

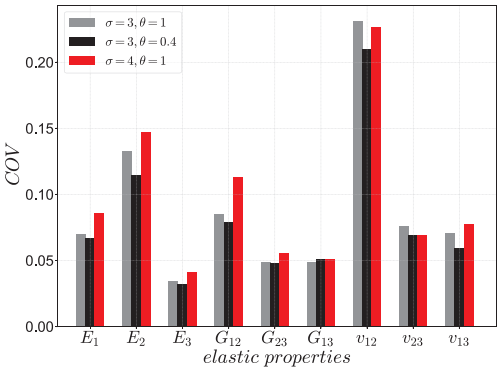

Fig. 23. Response variability of stiffness properties under stochastic yarn waviness. (For interpretation of the references to colour in this figure legend, the reader is referred to the web version of this article.)

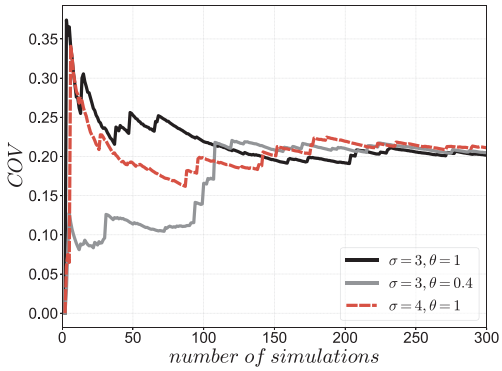

Fig. 25. Variation convergence of strength under stochastic yarn waviness. (For interpretation of the references to colour in this figure legend, the reader is referred to the web version of this article.)

6. Concluding remarks

This paper presented two methodologies, for the integration of random geometric imperfections of textile yarns, into numerical modeling procedures of probabilistic nature. Random, production-induced distortions of the yarns' cross-section, are modeled as random fields via a Fourier series-based procedure, inspired from studies of random inclusions for heterogeneous media. Application of such stochastic imperfections to a multiscale algorithm, predicting the stiffness and strength of a triaxially braided composite layer, showed that variability levels due to distortions are non-negligible. A big part of the response variability was caused by the volume fraction variation (≈ 7%), when the stiffness variability was found ≈ 10% and the equivalent of ultimate strength ≈ 13%. The parametric cases performed, highlighted the importance of imperfection modeling, especially for localization-driven behaviors, such as strength response. The second modeling approach uses the Kriging formulation to generate random yarn paths, based on sample points characterizing a nominal (average) yarn path and a simple manifold transformation. In case measurement data are available, calibration concerning correlation and variance is straightforward, while the application of stochastic waviness to the interlacing yarns of the braided model, revealed significant scatter of the linear response in the transverse direction and severe effects on the strength capacity. Results seem to be less affected by the fiber volume fraction variability (≈ 6%) in this case, for both stiffness and strength parameters. The elastic response variability levels for both yarn distortion and waviness are found to be within the range offered by similar studies [10,11]. The proposed methodologies will be tested with experimental data derived from CT-scans in a future endeavor, while another challenge is the accurate mapping of the random fields to the nonlinear response, with appropriate surrogate modeling techniques.

Acknowledgments

This work was implemented within the framework of the research project "FULLCOMP: Fully Integrated Analysis, Design, Manufacturing

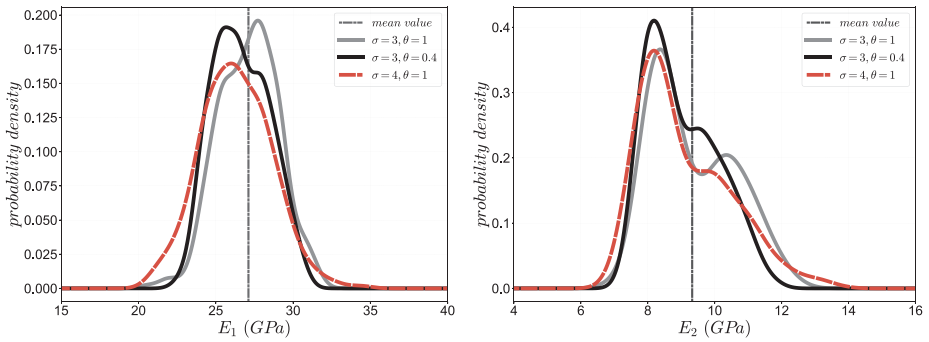

(a) Probability density estimation for E_1 (b) Probability density estimation for E_2

Fig. 24. Density estimation of the stiffness under stochastic yarn waviness. (For interpretation of the references to colour in this figure legend, the reader is referred to the web version of this article.)

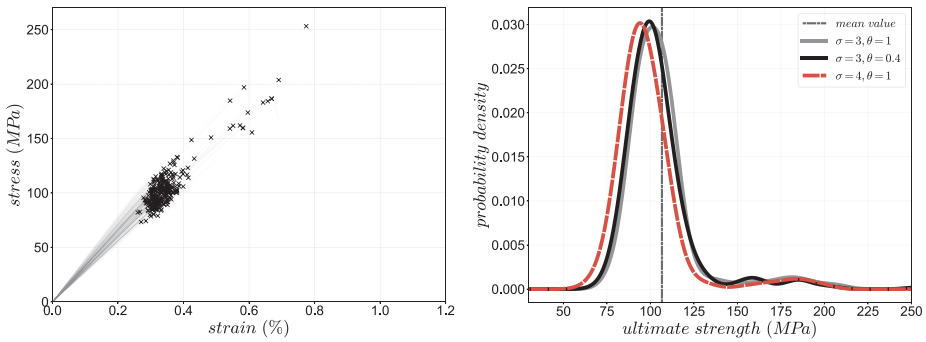

(a) Scatter of nonlinear curves ($\sigma = 3$, $\theta = 1$) (b) Probability density estimation

Fig. 26. Scatter plot and density estimation of the ultimate tensile strength under stochastic yarn waviness. (For interpretation of the references to colour in this figure legend, the reader is referred to the web version of this article.)

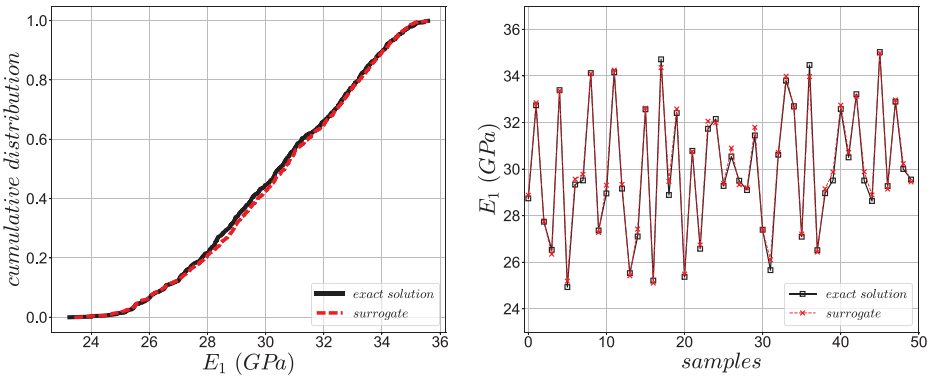

(a) Comparison of CDFs (b) Point-to-point comparison

Fig. 27. Verification of the surrogate model for yarn distortion. (For interpretation of the references to colour in this figure legend, the reader is referred to the web version of this article.)

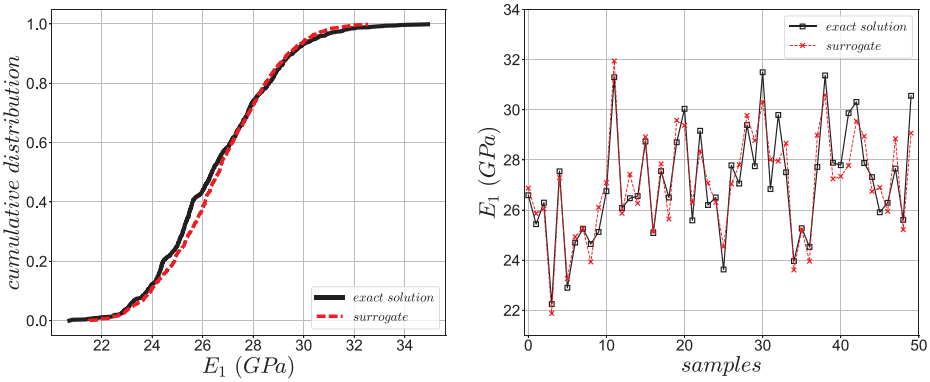

(a) Comparison of CDFs (b) Point-to-point comparison

Fig. 28. Verification of the surrogate model for yarn waviness. (For interpretation of the references to colour in this figure legend, the reader is referred to the web version of this article.)

and Health-Monitoring of Composite Structures". and has received funding from the European Unions Horizon 2020 research and innovation programme under the Marie Skłodowska-Curie grant agreement No 642121. The provided financial support is gratefully acknowledged by the authors.

Appendix A. Function of lenticular shape parameters with intersecting circles' radii

There is a relationship between the radii of the intersecting circles that form the lenticular section and its dimensions. For the general asymmetric case ($d \neq 0$), the radii are given by Eqs. (9) and (10). The proof of those equations is similar. If we consider Eq. (10), by applying the Pythagorean theorem on the triangle formed by r_2, vertical axis y and the radical line (connecting the two points of intersection), which is hatched in Fig. 29, we get:

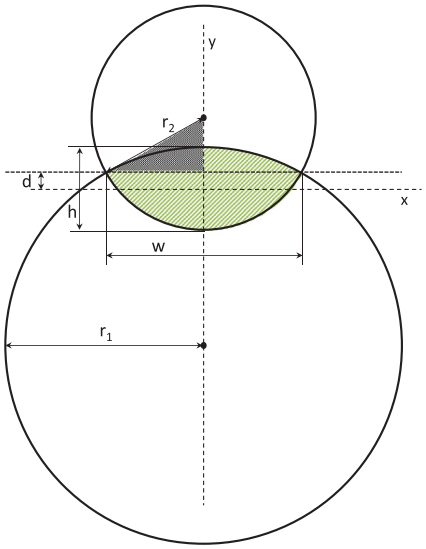

Fig. 29. Lenticular shape. (For interpretation of the references to colour in this figure legend, the reader is referred to the web version of this article.)

$$r_2^2 = \left(\frac{w}{2}\right)^2 + \left(r_2 - \frac{h}{2} - d\right)^2 \tag{A.1}$$

Expanding, rearranging and solving for r_2 gives:

$$r_2^2 = \frac{w^2}{4} + \left(r_2 - \frac{(h+2d)}{2}\right)^2 \tag{A.2}$$

$$\cancel{r_2^2} = \frac{w^2}{4} + \cancel{r_2^2} - \cancel{2} r_2 \frac{(h+2d)}{\cancel{2}} + \frac{(h+2d)^2}{4} \tag{A.3}$$

$$r_2(h+2d) = \frac{w^2}{4} + \frac{(h+2d)^2}{4} \tag{A.4}$$

$$r_2 = \frac{w^2 + (h+2d)^2}{4(h+2d)} \tag{A.5}$$

Appendix B. Spectral representation method for random field simulation

Spectral representation method expands the random field as a series of cosine functions with random phase angles. A one-dimensional, homogeneous random field $\hat{f}(\boldsymbol{x})$, truncated after N terms, is given by the following formula:

$$\hat{f}(\boldsymbol{x}) = \sqrt{2} \sum_{i=1}^{N} A_i \cos(\omega_i \boldsymbol{x} + \phi_i) \tag{B.1}$$

where ϕ_i, $i = 1, \ldots, N$ are independent and uniformly distributed random phase angles within the range $[0, 2\pi]$. The coefficients A_i are defined as follows:

$$A_0 = 0, \quad A_i = \sqrt{2 S_{f_0}(\omega_i) \Delta\omega}, \quad i = 1, \ldots, N \tag{B.2}$$

where S_{f_0} is the power spectral density function, which is a real non-negative function of the frequencies. These frequencies are given by:

$$\omega_i = i\Delta\omega = i\frac{\omega_u}{N}, \quad i = 1, \ldots, N \tag{B.3}$$

where ω_u is the upper cut-off wave number, after which the power spectrum becomes practically zero. The A_0 coefficient is chosen zero so that the temporal mean value averaged over the whole simulation time $T_0 = 2\pi/\Delta\omega$ of the generated stochastic field $\hat{f}(\boldsymbol{x})$ remains zero. The simulated process of Eq. (B.1) is asymptotically Gaussian as $N \to \infty$ and ergodic in the mean and in correlation due to the central limit theorem [37]. The same procedure is generalized for the cases of two and three dimensional random fields.

References

[1] Mahadik Y, Hallett SR. Effect of fabric compaction and yarn waviness on 3D woven composite compressive properties. Compos Part A: Appl Sci Manuf 2011;42:1592–600.
[2] Green SD, Long AC, ElSaid BSF, Hallett SR. Numerical modelling of 3D woven preform deformations. Compos Struct 2014;108:747–56.
[3] Šejnoha M, Zeman J. Micromechanical modeling of imperfect textile composites. Int J Eng Sci 2008;46:513–26.
[4] Green SD, Matveev MY, Long AC, Ivanov D, Hallett SR. Mechanical modelling of 3D woven composites considering realistic unit cell geometry. Compos Struct 2014;118:284–93.
[5] Lin H, Brown LP, Long AC. Modelling and simulating textile structures using TexGen. Adv Mater Res 2011;331:44–7.
[6] Xu K, Qian X. Analytical prediction of the elastic properties of 3D braided

composites based on a new multiunit cell model with consideration of yarn distortion. Mech Mater 2016;92:139–54.
[7] Wang R, Zhang L, Hu D, Liu X, Cho C, Li B. Progressive damage simulation in 3D four-directional braided composites considering the jamming-action-induced yarn deformation. Compos Struct 2017;178:330–40.
[8] Yushanov SP, Bogdanovich AE. Stochastic theory of composite materials with random waviness of the reinforcements. Int J Solids Struct 1998;35(22):2901–30.
[9] Yushanov SP, Bogdanovich AE. Fiber waviness in textile composites and its stochastic modeling. Mech Compos Mater 2000;36(4):501–32.
[10] Wang H, Wang Z. A variable metric stochastic theory of textile composites with random geometric parameters of yarn cross-section. Compos Struct 2015;126:78–88.
[11] Wang H, Wang Z. Quantification of effects of stochastic feature parameters of yarn on elastic properties of plain-weave composite. Part 1: Theoretical modeling. Compos Part A: Appl Sci Manuf 2015;78:84–94.
[12] Wang H, Wang Z. Quantification of effects of stochastic feature parameters of yarn on elastic properties of plain-weave composite. Part 2: Statistical prediction vs. mechanical experiments. Compos Part A: Appl Sci Manuf 2016;84:147–57.
[13] Guo-dong F, Jun L, Yu W, Bao-Iai W. The effect of yarn distortion on the mechanical properties of 3D four-directional braided composites. Compos Part A: Appl Sci Manuf 2009;40:343–50.
[14] Blacklock M, Bale H, Begley M, Cox B. Generating virtual textile composite specimens using statistical data from micro-computed tomography: 1D tow representations for the Binary Model. J Mech Phys Solids 2012;60:451–70.
[15] Bale H, Blacklock M, Begley M, Marshall D, Cox B, Ritchie R. Characterizing three-dimensional textile ceramic composites using synchrotron X-ray micro-computed-tomography. J Am Ceram Soc 2012;95(1):392–402.
[16] Rinaldi RG, Blacklock M, Bale H, Begley MR, Cox BN. Generating virtual textile composite specimens using statistical data from micro-computed tomography: 3D tow representations. J Mech Phys Solids 2012;60:1561–81.
[17] Vanaerschot A, Cox BN, Lomov SV, Vandepitte D. Stochastic framework for quantifying the geometrical variability of laminated textile composites using micro-computed tomography. Compos Part A: Appl Sci Manuf 2013;44:122–31.
[18] Vanaerschot A, Cox BN, Lomov SV, Vandepitte D. Stochastic multi-scale modelling of textile composites based on internal geometry variability. Comput Struct 2013;122:55–64.
[19] Verpoest I, Lomov SV. Virtual textile composites software wisetex: Integration with micro-mechanical, permeability and structural analysis. Compos Sci Technol 2005;65(15–16):2563–74.
[20] Vanaerschot A, Cox BN, Lomov SV, Vandepitte D. Simulation of the cross-correlated positions of in-plane tow centroids in textile composites based on experimental data. Compos Struct 2014;116:75–83.
[21] Vanaerschot A, Cox BN, Lomov SV, Vandepitte D. Multi-scale modelling strategy for textile composites based on stochastic reinforcement geometry. Comput Meth Appl Mech Eng 2016;310:906–34.
[22] Vanaerschot A, Panerai F, Cassell A, Lomov SV, Vandepitte D, Mansour NN. Stochastic characterisation methodology for 3-d textiles based on micro-tomography. Compos Struct 2017;173:44–52.
[23] Bodaghi M, Vanaerschot A, Lomov SV, Correia NC. On the variability of mesoscale permeability of a a 2/2 twill carbon fabric induced by variability of the internal geometry. Compos Part A: Appl Sci Manuf 2017;101:394–407.
[24] Bodaghi M, Vanaerschot A, Lomov SV, Correia NC. On the stochastic variations of intra-tow permeability induced by internal geometry variability in a 2/2 twill carbon fabric. Compos Part A: Appl Sci Manuf 2017;101:444–58.
[25] Skordos AA, Sutcliffe MPF. Stochastic simulation of woven composites forming. Compos Sci Technol 2008;68:283–96.
[26] Chudoba R, Vořechovský M, Konrad M. Stochastic modeling of multi-filament yarns: I. Random properties within the cross-section and size effect. Int J Solids Struct 2006;43:413–34.
[27] Vořechovský M, Chudoba R. Stochastic modeling of multi-filament yarns: II. Random properties over the length and size effect. Int J Solids Struct 2006;43:435–58.
[28] Abdiwi F, Harrison P, Koyama I, Yu WR, Long AC, Corriea N, Guo Z. Characterising and modelling variability of tow orientation in engineering fabrics and textile composites. Compos Sci Technol 2012;72:1034–41.
[29] Doitrand A, Fagiano C, Irisari F-X, Hirsekorn M. Comparison between voxel and consistent meso-scale models of woven composites. Compos Part A: Appl Sci Manuf 2015;73:143–54.
[30] Ernst G, Vogler M, Hühne C, Rolfes R. Multiscale progressive failure analysis of textile composites. Compos Sci Technol 2010;70(1):61–72.
[31] Ali A, Shah SM, Bozar S, Kazici M, Keskin B, Kaleli M, Aky S. Metal-free polymer/MWCNT composite fiber as an efficient counter electrode in fiber shape dye-sensitized solar cells. Nanotechnology 2016;27(38):384003.
[32] Saleh MN, Yudhanto A, Lubineau G, Soutis C. The effect of z-binding yarns on the electrical properties of 3d woven composites. Compos Struct 2017;182:606–16.
[33] Stefanou G, Savvas D, Papadrakakis M. Stochastic finite element analysis of composite structures based on material microstructure. Compos Struct 2015;132:384–92.
[34] Stefanou G, Nouy A, Clement A. Identification of random shapes from images through polynomial chaos expansion of random level-set functions. Int J Num Meth Eng 2009;79(2):127–55.
[35] Kriegesmann B, Rolfes R, Hühne C, Kling A. Fast probabilistic design procedure for axially compressed composite cylinders. Compos Struct 2011;93:3140–9.
[36] Bachoc F. Cross Validation and Maximum Likelihood estimations of hyper-parameters of Gaussian processes with model misspecification. Comput Stat Data Anal 2013;66:55–69.
[37] Shinozuka M, Deodatis G. Simulation of stochastic processes by spectral representation. Appl Mech Rev (ASME) 1991;44(4):191–203.
[38] Ghanem R, Spanos P. Stochastic finite elements: a spectral approach. New York: Springer-Verlag; 2000.
[39] Vořechovský M. Simulation of simply cross correlated random fields by series expansion methods. Struct Saf 2008;30(4):337–63.
[40] Kriegesmann B. Probabilistic design of thin-walled fiber composite structures PhD Dissertation Hannover: Institute of Structural Analysis, Leibniz University of Hannover; 2012.
[41] Balokas G, Czichon S, Rolfes R. Neural network assisted multiscale analysis for the elastic properties prediction of 3D braided composites under uncertainty. Compos Struct 2018;183:550–62.
[42] Chamis CC. Mechanics of composite materials: past, present, and future. J Compos Technol Res 1989;11:3–14.
[43] ABAQUS. Documentation. Providence (RI): Dassault Systèmes Simulia Corp.; 2014.
[44] Warren KC, Lopez-Anido RA, Vel SS, Bayraktar HH. Progressive failure analysis of three-dimensional woven carbon composites in single-bolt, double-shear bearing. Compos Part B: Eng 2016;84:266–76.
[45] Barbero E. Finite element analysis of composite materials. Florida: CRC Press, Taylor and Francis Group; 2007.
[46] Christensen RM. A comprehensive theory of yielding and failure for isotropic materials. J Eng Mater Technol 2007;129(2):173–81.
[47] Hashin Z. Failure criteria for unidirectional composites. J Appl Mech 1980;47(2):329–34.
[48] Xu L, Jin CZ, Ha SK. Ultimate strength prediction of braided textile composites using a multi-scale approach. J Compos Mater 2014;49(4):477–94.
[49] Wang C, Zhong Y, Adaikalaraj PFB, Ji X, Roy A, Silberschmidt VV, Chen Z. Strength prediction for bi-axial braided composites by a multi-scale modelling approach. J Mater Sci 2016;51:6002–18.
[50] Nobeen NS, Zhong Y, Francis BAP, Ji X, Chia ESM, Joshi SC, Chen Z. Constituent materials micro-damage modeling in predicting progressive failure of braided fiber composites. Compos Struct 2016;145:194–202.
[51] Matveev MY, Long AC, Jones IA. Modelling of textile composites with fibre stength variability. Compos Sci Technol 2014;105:44–50.
[52] Gommer F, Brown LP, Brooks R. Quantification of mesoscale variability and geometrical reconstruction of a textile. J Compos Mater 2015;50(23):3255–66.
[53] Karahan M, Lomov SL, Bogdanovich AE, Mungalov D, Verpoest I. Internal geometry evaluation of non-crimp 3D orthogonal woven carbon fabric composite. Compos Part A: Appl Sci Manuf 2010;41:1301–11.
[54] Balokas G, Kriegesmann B, Czichon S, Böttcher A, Rolfes R. Advances in predictive models and methodologies for numerically efficient linear and nonlinear analysis of composites. In: Petrolo M, editor. PoliTO Springer series. Cham: Springer; 2019. Ch. Metamodel-based uncertainty quantification for the mechanical behavior of braided composites.
[55] Giovanis DG, Papadopoulos V. Spectral representation-based neural network assisted stochastic structural mechanics. Eng Struct 2014;84:382–94.

Chapter 4

A Variable-Fidelity Hybrid Surrogate Approach for Quantifying Uncertainties in the Nonlinear Response of Braided Composites

This paper addresses the problem of efficient stochastic failure prediction for textiles. A multi-fidelity scheme and a novel hybrid NN-Kriging surrogate model are proposed towards the uncertainty quantification of the failure response of a braided material under tension. A global sensitivity analysis is applied indicating important interaction effects among the random input.

The paper is published in Computer Methods in Applied Mechanics and Engineering, Volume 381, 2021, 113851.

Available online at www.sciencedirect.com
ScienceDirect
Comput. Methods Appl. Mech. Engrg. 381 (2021) 113851
Computer methods in applied mechanics and engineering
www.elsevier.com/locate/cma

A variable-fidelity hybrid surrogate approach for quantifying uncertainties in the nonlinear response of braided composites

Georgios Balokas[a,*], Benedikt Kriegesmann[a], Steffen Czichon[b], Raimund Rolfes[c]

[a] *Hamburg University of Technology, Structural Optimization for Lightweight Design, Am Schwarzenberg-Campus 4, 21073 Hamburg, Germany*
[b] *Fraunhofer Institute for Wind Energy Systems IWES, Am Seedeich 45, 27572 Bremerhaven, Germany*
[c] *Leibniz University Hannover, Institute of Structural Analysis, Appelstraße 9A, 30167 Hannover, Germany*

Received 2 December 2020; received in revised form 26 March 2021; accepted 2 April 2021
Available online 23 April 2021

Abstract

The ultimate strength prediction of textile composite materials requires high-fidelity FE modeling with information-passing multiscale schemes and damage initiation and propagation algorithms. The numerical demand of this procedure together with the complexity of the observed response surface, hampers the quantification of uncertainties contributing to the scatter of strength values. This study proposes a surrogate methodology able to efficiently emulate the nonlinear multiscale procedure, based on a combination of artificial neural networks and Kriging modeling under a variable-fidelity framework. A triaxially braided textile under longitudinal tension is used as a use-case and the methodology is employed to identify the most critical parameters in terms of variance via a global sensitivity analysis technique. Results show strong interaction effects between the uncertain parameters. The approach is non-intrusive and can be easily extended to other types of textiles and load cases.

Keywords: Braided composites; Failure prediction; Sensitivity analysis; Uncertainty quantification; Variable-fidelity; Surrogate modeling

1. Introduction

Composite materials have a predominant role in research, design and production of lightweight structures for aerospace, energy and automotive sectors. High strength and stiffness conditional to weight, toughness, thermal conductivity and energy absorption are a few of their primary advantages over other material types. A challenging fact, however, is the observed scatter of the mechanical response parameters, due to their heterogeneous nature and the multiple manufacturing stages they encounter, which results in uncertainty occurring at different spatial scales.

The investigation of these uncertainties through the development and employment of probabilistic methods, has grown over the last 10–15 years. Concerning the parameters governing the elastic behavior of typical composites, there are numerous uncertainty assessment studies with both analytical and numerical homogenization techniques [1,2]. The statistical relation between lower and higher scales, in terms of elastic parameters, has been also addressed for particle-reinforced composites [3,4]. Textile composites are a special category, consisting of yarns/tows (i.e. linear assemblage of fibers) interlocked within the plies into specific patterns [5]. They have

* Corresponding author.
E-mail address: georgios.balokas@tuhh.de (G. Balokas).

https://doi.org/10.1016/j.cma.2021.113851
0045-7825/

gained attention because of the enhancement regarding specific properties (e.g. delamination resistance, tailorability, through-thickness reinforcement etc.), while due to their demanding numerical modeling, surrogate models are implemented for the quantification of uncertainty [6,7].

The stochastic failure prediction is certainly more complex. For thin-walled structures, failure is mainly driven by buckling, which can be used for estimating the probability of failure or identifying uncertainties related to stiffness and fiber volume content [8,9]. When it comes to material nonlinearities, uncertainty quantification has been moderately addressed including applications of composite laminates [10,11], short-fiber [12] and particle-reinforced composites [13]. Regarding textile composites, there are only a few studies dealing with the uncertainties in the nonlinear response [14,15], in which the results are based on limited model evaluations. As a result, only the first two statistical moments can be reliably estimated.

This is due to the complexity of textile materials regarding their failure response and the necessity of demanding finite element (FE) models for an accurate and reliable prediction. For uncertainty quantification (UQ) procedures like variance-based sensitivity analysis or Bayesian inference, but also for the integration in optimization routines, the required number of model evaluations might reach the order of 10^4–10^5 [6,9], so the training of a surrogate model is a precondition. However, even training such a surrogate requires a significant amount of model evaluations because of the complex failure response surface and the numerous parameters of the problem. Recently, variable-fidelity methods have been proposed for demanding problems of this sort, able to assist the training procedures with faster evaluations of lower fidelity [16–18].

In this study, the unaddressed problem of emulating the nonlinear response of textile composites is investigated. The proposed solution is based on training artificial neural networks for the surrogate modeling of the yarn properties and on a novel variable-fidelity framework for the mesoscale simulations, which integrates an artificial neural network into the Hierarchical Kriging formulation. The algorithm employs the step size of the nonlinear analysis as a novel fidelity parameter, ensuring sufficient correlation and considerable reduction in computing resources. The method is applied to a 3D triaxially braided structure, towards the UQ of its failure behavior under longitudinal uniaxial tension. By employing the successfully trained surrogate model, the identification of the most critical parameters related to the ultimate strength of the braided material is achieved via a variance-based global sensitivity analysis. The method is non-intrusive in the sense that it could be easily extended to other textile types or load cases by modifying solely the FE model. The sensitivity results reveal interactions between the input parameters of the problem, which justifies the plethora of necessary samples for a sufficient surrogate training.

The remaining of the paper is organized as follows: Section 2 recapitulates the theory of homogenization and describes the multiscale modeling approach. Section 3 recalls the basic formulation of artificial neural networks and Kriging and describes their integration to a global sensitivity analysis framework. The latter models are combined to assemble the proposed variable-fidelity analysis procedure in Section 4 and the application of the proposed approach to a braided composite is presented in Section 5. Finally, Section 6 points out the major conclusions of the present study.

2. Deterministic failure prediction modeling

2.1. Computational homogenization

The formulation for an elastostatic macroscale problem of a continuous body under small strains is given by:

$$\nabla \cdot \bar{\boldsymbol{\sigma}}^T + \bar{\boldsymbol{b}} = 0 \tag{1}$$

$$\bar{\boldsymbol{\sigma}} = C : \bar{\boldsymbol{\varepsilon}} \tag{2}$$

$$\bar{\boldsymbol{\varepsilon}} = \nabla_s \cdot \bar{\boldsymbol{u}} \tag{3}$$

where ∇ and ∇_s are the gradient and symmetric gradient operators, $\bar{\boldsymbol{\sigma}}$ and $\bar{\boldsymbol{\varepsilon}}$ are the macroscopic stress and strain tensors, $\bar{\boldsymbol{u}}$ is the displacement vector and $\bar{\boldsymbol{b}}$ are the acting body forces. The material behavior is characterized by the generalized constitutive law of Eq. (2) and the elasticity tensor C.

The solution of this problem given a heterogeneous body is intractable. Instead, effective homogeneous properties are extracted under the assumption that any material point is associated to a statistically representative volume element (RVE) on a lower scale. The characteristic length of this scale should be much smaller than the macroscale one. The equilibrium state of the RVE with volume Ω in absence of body forces, is then formulated as [19]:

$$\nabla \cdot \boldsymbol{\sigma}(\boldsymbol{x})^T = 0, \quad \forall\, \boldsymbol{x} \in \Omega \tag{4}$$

$$\boldsymbol{\sigma} = C_{\Omega} : \boldsymbol{\varepsilon} \tag{5}$$

where C_{Ω} is the elastic tensor that varies due to the different phases of the RVE. Any constitutive law can be introduced for each phase, thus assuming a progressively damaging microstructure, a typical constitutive law of a phase R is of the form:

$$\boldsymbol{\sigma}(\boldsymbol{x}) = \big(1 - d(\boldsymbol{x})\big) C_{\mathrm{R}} : \boldsymbol{\varepsilon}(\boldsymbol{x}), \quad \forall \boldsymbol{x} \in R \subset \Omega \tag{6}$$

where $d \in [0, 1)$ is a scalar damage variable and C_{R} is the stiffness tensor of the phase.

A basic principle in homogenization theory is the Hill–Mandel equation, through which energy consistency between every material point on the macroscale and the associated RVE is established in an average sense:

$$\bar{\boldsymbol{\sigma}} \cdot \bar{\boldsymbol{\varepsilon}} = \frac{1}{|\Omega|} \int_{\Omega} \boldsymbol{\sigma} \cdot \boldsymbol{\varepsilon} \, d\Omega \tag{7}$$

The above is typically enforced in practice by applying periodic boundary conditions (PBCs) on the RVE, e.g. periodicity on the displacement field $\boldsymbol{u}$ and anti-periodicity on the traction field $\boldsymbol{t}$ by mapping opposite boundaries [19]:

$$\boldsymbol{u}(x^{+}) = \boldsymbol{u}(x^{-}), \quad \forall x^{+} \in \partial\Omega^{+}, \ \forall x^{-} \in \partial\Omega^{-} \tag{8}$$

$$\boldsymbol{t}(x^{+}) = -\boldsymbol{t}(x^{-}), \quad \forall x^{+} \in \partial\Omega^{+}, \ \forall x^{-} \in \partial\Omega^{-} \tag{9}$$

The coupling between the scales can then be performed via the volume average of the microscopic stress and strain values as:

$$\bar{\boldsymbol{\sigma}} = \frac{1}{|\Omega|} \int_{\Omega} \boldsymbol{\sigma} \, d\Omega \quad , \quad \bar{\boldsymbol{\varepsilon}} = \frac{1}{|\Omega|} \int_{\Omega} \boldsymbol{\varepsilon} \, d\Omega \tag{10}$$

When the nonlinear stress–strain behavior of a heterogeneous material is of interest, the effective curves are obtained from the above equations, according to the numerical discretization of the RVE. For example, in a finite element (FE) approach the macroscopic stresses can be extracted in each solution step, by applying strains corresponding to specific load cases, through appropriate degrees of freedom on the RVE, and by calculating:

$$\bar{\boldsymbol{\sigma}} = \frac{1}{|\Omega|} \int_{\Omega} \boldsymbol{\sigma} \, d\Omega \approx \frac{1}{\Omega_{tot}} \sum_{k=1}^{N_p} \boldsymbol{\sigma}^{k} \Omega^{k} \tag{11}$$

where N_p is the total number of integration points. The above procedure is valid until the localization of damage within the RVE, as then the problem under PBCs becomes ill-posed and the small strains assumption is violated.

2.2. Multiscale strength prediction algorithm and material modeling

A high-fidelity estimation of the mechanical properties for textile composite materials (or fabrics) is feasible through numerical multiscale schemes, since the heterogeneities and their complex patterns inside the material architecture have significantly lower length scales than the final structure. The final textile geometry is specified in two stages: the assemblage of the fibers into yarns and the consequent bonding/interlocking of the yarns into specific patterns in multiple directions. Accordingly, a two-step homogenization scheme is fitting, initially on a microscopic level ($\approx 10^{-6}$ m) to predict the yarn behavior and then on a mesoscale level ($\approx 10^{-3}$ m) for the extraction of the textile layer's properties [6,20].

In this work, the probabilistic assessment of the tensile strength properties of a braided fabric is of interest. Hence, a two-scale information-passing algorithm is used, computing the stiffness and strength properties of each scale and transferring the data from lower to higher scales, as shown in Fig. 1. Due to the incorporated uncertainties and the local periodicity assumption (i.e. periodicity only in a small proximity of each macroscopic point) the term statistical volume element (SVE) is used from now on, instead of the RVE [21]. Failure criteria are applied for each constituent (fibers, matrix, interface and yarns) and a continuous damage approach is employed for addressing the material degradation of the progressively damaging system. The last part of Fig. 1 illustrates the dependency of the layer's stiffness and strength properties in the macroscale, on the material properties of the constituents on lower scales (C_{Ω}, C_{R}), but also on geometric properties like volume fractions, yarn angles etc., represented with

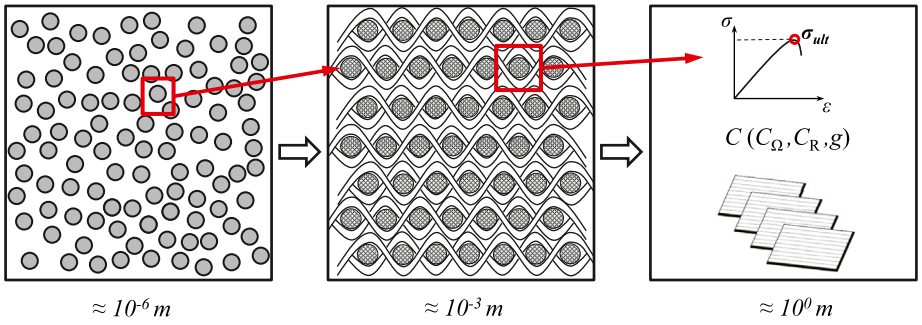

Fig. 1. 2-step multiscale scheme: from microscale (left) to macroscale (right).

the vector $\boldsymbol{g}$. Eventually, the homogenized layer properties can be used in a composite layup for the formulation of a macroscale model.

Regarding the material laws of the constituents, carbon fibers were used in this work which exhibit a transversely isotropic behavior and follow a linear elastic law until brittle failure, governed by a maximum stress criterion of the form:

$$\begin{aligned} &\sigma_f \geq X_{ft} \\ &\sigma_f \leq |X_{fc}| \end{aligned} \tag{12}$$

where X_{ft} and X_{fc} are the fiber strengths in tension and compression. Matrix regions are simulated with an isotropic material following the von Mises plasticity model. Fracture initiation is modeled by a modified von Mises criterion [22] as:

$$\frac{\sigma_{vm}^2}{X_{mc}X_{mt}} + \left(\frac{1}{X_{mt}} - \frac{1}{X_{mc}}\right) I_1 \geq 1 \tag{13}$$

considering the discrepancy between compressive and tensile strength due to the hydrostatic pressure, where σ_{vm} is the von Mises stress, $I_1 = \sigma_1 + \sigma_2 + \sigma_3$ is the first stress invariant and X_{mt} and X_{mc} are the matrix strengths in tension and compression, respectively.

The yarns essentially behave like unidirectional continuous fiber composites, so they are modeled with transversely isotropic properties. The failure initiation is characterized by the Hashin criterion [23], accounting for the following four different failure modes: fiber failure in tension ($\sigma_1 > 0$), fiber failure in compression ($\sigma_1 < 0$), matrix failure in tension ($\sigma_2 + \sigma_3 > 0$) and matrix failure in compression ($\sigma_2 + \sigma_3 < 0$). The corresponding expressions to each of the above modes are:

$$\left(\frac{\sigma_1}{X_t}\right)^2 + \frac{\tau_{12}^2 + \tau_{13}^2}{S_{12}^2} = 1 \tag{14}$$

$$-\sigma_1 = X_c \tag{15}$$

$$\left(\frac{\sigma_2 + \sigma_3}{Y_t}\right)^2 + \frac{\tau_{23}^2 - \sigma_2\sigma_3}{S_{23}^2} + \frac{\tau_{12}^2 + \tau_{13}^2}{S_{12}^2} = 1 \tag{16}$$

$$\left[\left(\frac{Y_c}{2S_{23}}\right)^2 - 1\right]\frac{\sigma_2 + \sigma_3}{Y_t} + \left(\frac{\sigma_2 + \sigma_3}{2S_{23}}\right)^2 + \frac{\tau_{23}^2 - \sigma_2\sigma_3}{S_{23}^2} + \frac{\tau_{12}^2 + \tau_{13}^2}{S_{12}^2} = 1 \tag{17}$$

where σ_i is the stress component in i direction, τ_{ij} are the components of the shear stresses and X_t, X_c, Y_t, Y_c, S_{12}, S_{23} are the effective strength properties of the yarns (X stands for the longitudinal direction, Y for the transverse, S for the shear and the subscripts t for tension and c for compression).

The progression of damage is addressed with a Murakami-type degradation model, meaning that the material properties are reduced in a single step once the failure criterion is met [24,25]. This approach, also known as instantaneous stiffness degradation, is straightforward in terms of implementation, but also much more efficient than a gradual degradation approach, since the damage variables of Eq. (6) are constant, instead of solution-dependent. To ensure numerical stability, the stiffness matrix is kept positive by enforcing the physical conditions reported in [25] and by keeping the off-diagonal terms of the damaged compliance matrix unaffected.

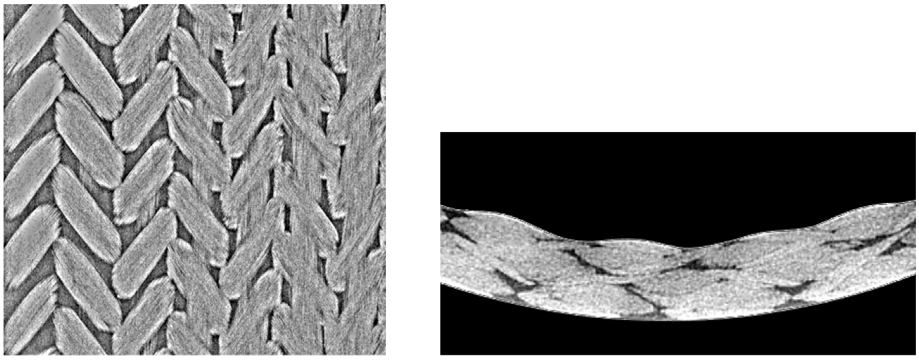

(a) (b)

Fig. 2. CT images from cylindrical braided specimen: (a) diamond braiding pattern and (b) cross-section segment.

For the case of an orthotropic textile material in 3D, the aforementioned matrix has the following form:

$$S(d_i) = \begin{bmatrix} \frac{S_{11}}{1-d_1} & S_{12} & S_{13} & 0 & 0 & 0 \\ S_{12} & \frac{S_{22}}{1-d_2} & S_{23} & 0 & 0 & 0 \\ S_{13} & S_{23} & \frac{S_{33}}{1-d_2} & 0 & 0 & 0 \\ 0 & 0 & 0 & \frac{S_{44}}{1-d_3} & 0 & 0 \\ 0 & 0 & 0 & 0 & \frac{S_{55}}{1-d_3} & 0 \\ 0 & 0 & 0 & 0 & 0 & \frac{S_{66}}{1-d_4} \end{bmatrix} \tag{18}$$

The choice of damage variables in this study is based on the work of Warren et al. [26], thus d_1 corresponding to longitudinal damage due to fiber rupture is 0.93 for tension (Eq. (14)) and 0.8 for compression (Eq. (15)), while d_2 corresponding to transverse damage due to matrix cracking is 0.86 for tension (Eq. (16)) and 0.6 for compression (Eq. (17)). For combined shear, longitudinal or transverse damage, variables d_3 and d_4 are equal to $1-(1-d_1)(1-d_2)$. The matrix located between the yarns for the mesoscale, as well as within the fibers for the microscale has a pure matrix damage variable of 0.9. For the microscopic fiber damage the stiffness is dropped to 1% of the initial value. A flow chart of the progressive failure algorithm can be found in a previous work by the authors [15].

2.3. Modeling approach

The model under investigation in this work is based on a triaxially braided cylindrical specimen, following a diamond braiding pattern [5] which can be visualized in Fig. 2a, an image extracted from a computed tomography (CT) scan. The axial (or warp) yarns lay straight and equally spaced, while the weft yarns interlace the axial yarns at a specified angle. According to the manufacturer, the plies of the specimen vary along its length. The cross section of Fig. 2b has 3 plies, however severe nesting effects are visible due to high compaction.

The exact material properties of the constituents are unknown, thus typical AS4 carbon properties are used for the nominal values of the fiber properties, according to a published report on braided material characterization [27]. The values are summarized in Table 1. The compressive strength value is missing from the above report, so a value from a similar material is used from the literature [28]. Regarding the matrix, the same document uses an EPON 9504 resin, however information like the hardening curves are missing. Hence, a RIM 135 epoxy resin is used from [20], which has very similar stiffness and strength values, but also the tensile and shear hardening curves available. The nominal matrix properties are reported in Table 2.

Without loss of generality, this work deals only with the ultimate strength response of a single braided layer under uniaxial tension in the longitudinal direction. The same procedures can be followed for calculating tensile

Table 1
AS4 carbon fiber properties.

Parameter	E_{f1} (GPa)	E_{f2} (GPa)	G_{f12} (GPa)	G_{f23} (GPa)	υ_{12}	υ_{23}	X_{ft} (MPa)	X_{fc} (MPa)
Value	227.53	16.55	24.82	6.89	0.2	0.25	4150	3000

Table 2
RIM 135 resin matrix properties.

Parameter	E_m (GPa)	G_m (GPa)	υ_m	X_{mt} (MPa)	X_{mc} (MPa)	X_{ms} (MPa)
Value	3.35	1.24	0.35	69	120	55

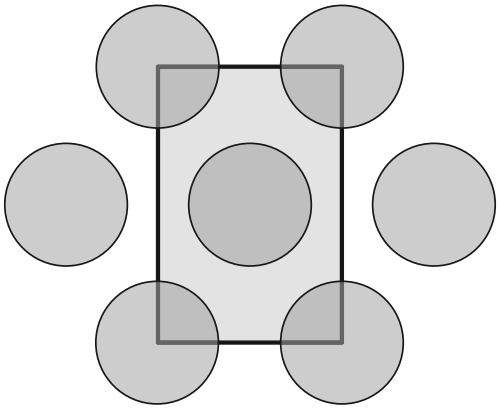

Fig. 3. SVE with hexagonal fiber arrangement for the microstructure.

properties in other directions, by changing the boundary conditions on the mesoscale level. The commercial software Abaqus [29] is employed for all FE calculations. The damage progression algorithm is implemented as a user defined field subroutine (USDFLD). This routine works in an explicit approach, meaning that the material point quantities are only accessed at the start of each increment. The accuracy of the results depends on the size of the time increment, hence in order to ensure this, a convergence analysis was carried out by the authors in [15].

2.3.1. Yarn properties (micro-to-meso transition)

The microstructure of the yarns is similar to that of a unidirectional laminate in terms of fibers, matrix and interface. The random fiber positioning as in Fig. 1 (left), can be well approximated by a periodically structured fiber pattern [21]. Thus, a typical SVE assuming a hexagonal fiber arrangement is used, as illustrated in Fig. 3. The appropriate load cases for the virtual testing of the SVE can be found in [15,20].

Regarding geometry, the fiber diameter is $7 \cdot 10^{-6}$ m and the fiber volume fraction in the SVE is 80%. This relatively high value is typical for textiles due to the extra fiber (yarn) placement process e.g. weaving or braiding, as the final fiber volume fraction at the macroscale must remain at a satisfactory level (≈50%–60%). Given the diameter d_f and the volume fraction V_f, the SVE in-plane dimensions X,Y are calculated from the nonlinear system below:

$$\begin{aligned} V_f &= \frac{\pi {d_f}^2}{2\mathrm{XY}} \\ \mathrm{Y} &= \mathrm{X}\ \tan(60^\circ) \end{aligned} \tag{19}$$

The SVE thickness (out-of-plane) can be chosen arbitrarily.

For the transverse and shear load cases which are matrix-driven, a cohesive traction-separation law was used to account for potential debonding between matrix and fiber. The interface damage initiation is described with a quadratic stress criterion of the form:

$$\left(\frac{\langle \sigma_n \rangle}{N_{\max}}\right)^2 + \left(\frac{\sigma_s}{S_{\max}}\right)^2 + \left(\frac{\sigma_t}{T_{\max}}\right)^2 = 1 \tag{20}$$

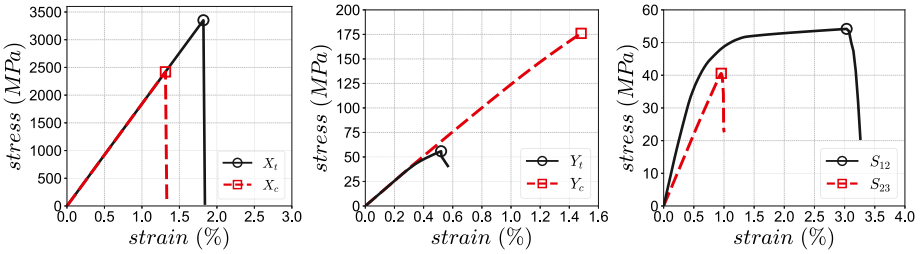

Fig. 4. Stress–strain curves for the yarn properties: (a) longitudinal direction, (b) transverse direction and (c) in-plane and out-of-plane shear.

Table 3
Yarn mechanical properties.

Parameter	Value		Units
	FEM	Analytical	
E_{11}	182.526	182.694	GPa
E_{22}	11.312	11.688	GPa
G_{12}	8.098	8.252	GPa
G_{23}	4.403	4.652	GPa
v_{12}	0.23	0.23	–
v_{23}	0.2659	0.2562	–
X_t	3351.28	3332.22	MPa
X_c	2420.23	2391.43	MPa
Y_t	55.856	63.803	MPa
Y_c	176.065	192.841	MPa
S_{12}	54.186	50.066	MPa
S_{23}	40.575	–	MPa

where σ_n is the normal stress perpendicular to the cohesive zone, σ_s, σ_t are the shear stresses and $N_{\max}$, $S_{\max}$ and $T_{\max}$ are the corresponding maximum allowable stresses. The modeling is implemented with the cohesive zone approach of Abaqus, allowing for an energy-based evolution of damage via the Benzeggagh–Kenane formulation of mixed fracture modes [29]. Assuming isotropic interface failure, all allowable stresses were set to 57 MPa and the fracture energy for all modes to 280 J/m^2 [30].

The results for the yarn properties after the virtual testing of the micro-SVE are shown, in terms of stress–strain plots, in Fig. 4. The stiffness values are calculated from the tangent of the curves in the elastic region. Both stiffness and ultimate strength results are gathered in Table 3. Values from analytical criteria of composite materials are also provided where available, for comparison/verification purposes. The well known Chamis criterion [31] is used for verification of the stiffness properties. For the strength properties there is not a unified framework of equations, especially for the matrix-driven strength properties. This is mainly due to the several potential failure modes that can be triggered (e.g. matrix failure, plasticization, debonding etc.) The formulas used herein can be found in [8,32]. The small discrepancies observed (e.g. for Y_t, Y_c) are justified by the inability of the criteria to capture more than one failure mode.

2.3.2. Braided layer properties (meso-to-macro transition)

The mesoscale SVE is modeled with the textile design software TexGen [33]. The braiding pattern is shown in Fig. 5a and an isometric view of the SVE with its outer dimensions in Fig. 5b. The warp yarns have an elliptical cross-section while the weft yarns follow a lenticular shape [15]. The fiber volume fraction of the SVE is 48%, considering the nominal braid angle is 45°.

The voxel mesh technique is used to discretize the SVE for the FE solution. It is a hexahedral-based mesh where all elements have the same size with an aspect ratio of one. Thus it provides meshes of accepted accuracy for models of high geometrical complexity, e.g. geometries resulting from topology optimization routines, or automated re-meshing algorithms accounting for geometrical variations [34]. A mesh convergence study can be found in the authors' previous study [15].

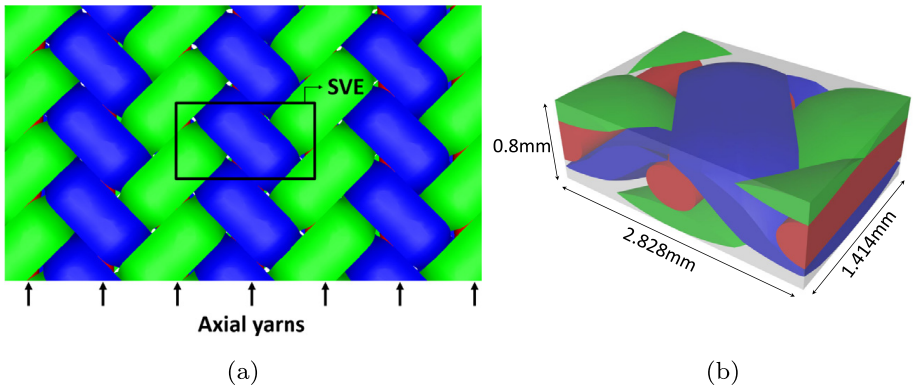

Fig. 5. Triaxial braiding pattern: (a) Top view, (b) TexGen SVE mesoscale model.

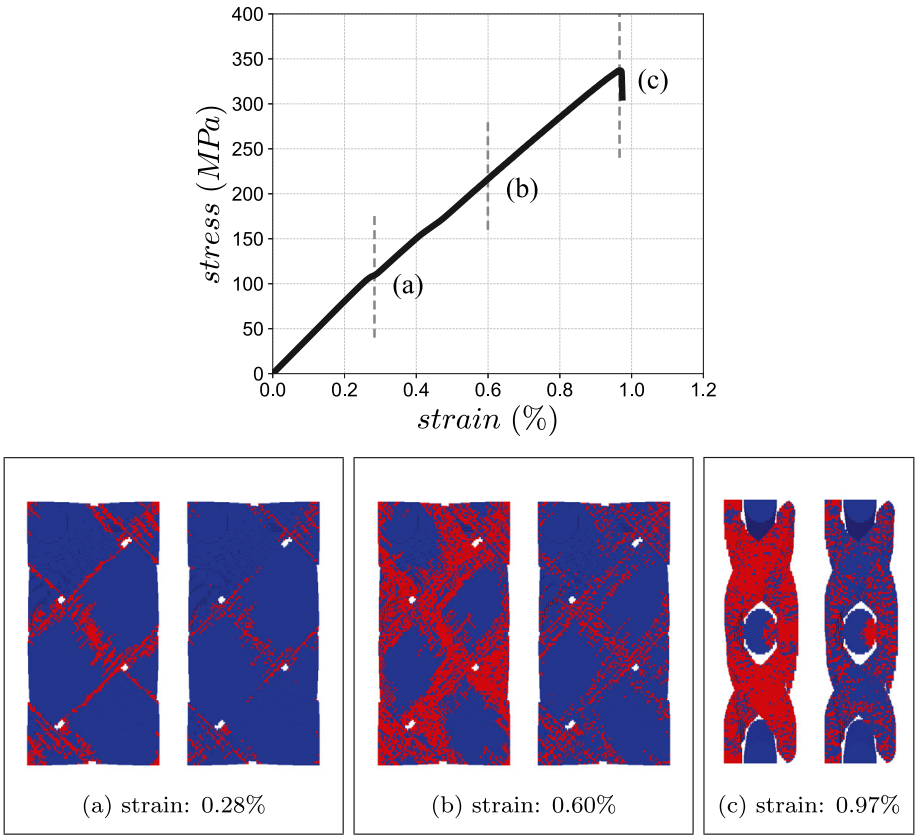

Fig. 6. Stress–strain curve of braided layer and damage levels for three levels a, b and c corresponding to the subplots (in each subplot the left figure corresponds to the matrix tensile failure mode and the right to the fiber tensile failure mode).

The response curve for the SVE under uniaxial longitudinal tension is shown in the upper part of Fig. 6, together with some damage plots of the yarns for three states along the loading history (Fig. 6a, b and c). In each of these states, the plot on the left corresponds to the tensile damage of the matrix (Eq. (16)), while the one on the right to the tensile damage of the fibers within the yarns (Eq. (14)), since those are the governing failure modes. The damage progressively expands throughout the weft yarns, until the warp yarns fail at point c, which is the ultimate strength state. The ultimate strength value of 337.15 MPa is considered within realistic range according to [24,25,27], considering the differences in volume fraction levels and material types within the different studies.

There are two numerical issues worth discussing that rise from the failure prediction method described. The first is the energy dissipation due to failure, which is ignored by the instantaneous stiffness degradation approach. Even though there is a physical inconsistency, it can be easily seen that the energy loss is not critical until the peak of

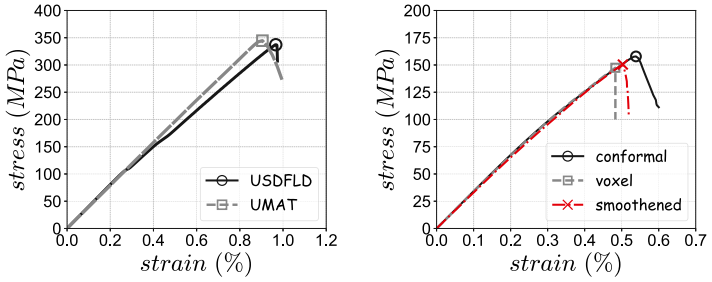

(a) (b)

Fig. 7. Verification of the modeling approach through comparisons: (a) Instantaneous stiffness (USDFLD) and continuous stiffness (UMAT) degradation approach and (b) conformal, voxel and smoothened voxel approach.

the homogenized curve, by plotting the internal and external work of the SVE, hence the homogenized strength is not affected. The post-failure path is anyway not reliable, as noted in Section 2.1. The same deduction is reached, if the adopted approach is directly compared with a continuous stiffness degradation scheme. A Matzenmiller energy-based damage evolution model was implemented in an UMAT subroutine for Abaqus [35], with the Hashin criterion for damage initiation, for the same use-case braided model. The results against the adopted USDFLD approach are shown in Fig. 7a, where discrepancies are negligible. It is noted that the UMAT approach is about 8 times slower than the USDFLD.

The second issue is the voxel mesh approach and its fidelity regarding strength prediction, due to possible oscillations of stresses at the sharp matrix–yarn interfaces. Indeed a conformal mesh (i.e. tetrahedral elements) would be more accurate for textile geometries, however creating one is quite challenging and often results in bad element shapes. Besides, uncertainty quantification requires numerous analyses and, therefore, an automated and robust pre-process is a prerequisite. Nonetheless, the stress concentrations that may emerge from a voxel mesh are not so severe for uniaxial loading cases. Alternatively, smoothing the voxel geometry at the interfaces is a possible remedy.

A comparison between a conformal, a voxel and a smoothened voxel mesh is presented in Fig. 7b. The geometry of the model was herein modified (smaller sections towards a smaller volume fraction) in order to be conformally meshed. For the smoothing, a modified Laplacian algorithm was used [36], based on iteratively moving the node coordinate of interest x_i towards the barycenter created by the neighboring nodes, with the transfer function $x'_i = x_i + \lambda \Delta x_i$, where $\Delta x_i = \sum_{j \in i^*} w_{ij}(x_i - x_j)$ is the Laplacian and j is a node in the neighborhood of i. The weights w_{ij} are non-negative values adding up to unity for each node. The scaling factor $0 < \lambda < 1$ is changing sign in every iteration to prevent shrinkage. For this example, 15 smoothing iterations were performed, as more would lead to highly distorted elements. The figure verifies that the error is not severe and could indeed be improved by smoothing. Since the error is small and the cost of smoothing is considerable (use of nearest-neighbors algorithm), it will not be employed in this study.

3. Variance-based global sensitivity analysis with surrogate models

3.1. Global sensitivity analysis formulation

In an uncertainty quantification framework, global sensitivity analysis (GSA) is a tool to classify the importance of each random input parameter in terms of variance. Considering the whole bounded input space, this technique decomposes the output variability into normalized fractions corresponding to the input variables and their possible interactions.

Assuming a square integrable function $y = f(x_1, x_2, \dots\ x_k)$ over the k-dimensional unit hypercube Ω^k, the following decomposition is feasible [37]:

$$f = f_0 + \sum_i f_i(x_i) + \sum_{j>i} f_{ij}(x_i, x_j) + \cdots + f_{12\dots k}(x_1, x_2, \dots, x_k) \tag{21}$$

For brevity, the following nomenclature is applied: $f_i(x_i) = f_i$, $f_{ij}(x_i, x_j) = f_{ij}$ etc. Since all the terms are orthogonal, they can be calculated using the conditional expectations of the scalar output y as:

$$f_0 = E(y) \tag{22}$$

$$f_i = E(y|x_i) - E(y) \tag{23}$$

$$f_{ij} = E(y|x_i, x_j) - f_i - f_j - E(y) \tag{24}$$

By raising the terms of Eq. (21) to the power of 2 and integrating, the following statement appears:

$$\int f^2 d\boldsymbol{x} - f_0^2 = \sum_i \int f_i^2 dx_i + \sum_{j>i} \int f_{ij}^2 dx_i dx_j + \cdots + \int f_{12\ldots k}^2 dx_1 dx_2 \ldots dx_k \tag{25}$$

where on the left is the total variance of y and on the right are the decomposed variances with respect to the input $\boldsymbol{x} = \{x_1, x_2, \ldots, x_k\}$. The final expression is reached after substituting Eqs. (22)–(24):

$$\sigma^2(y) = \sum_{i=1}^{k} V_i + \sum_{j>i}^{k} V_{ij} + \cdots + V_{12\ldots k} \tag{26}$$

$$\text{where} \quad V_i = \sigma_{x_i}^2(E_{x_{\sim i}}(y|x_i)) \tag{27}$$

$$V_{ij} = \sigma_{x_{ij}}^2(E_{x_{\sim ij}}(y|x_i, x_j)) - V_i - V_j \quad \text{etc.} \tag{28}$$

The $x_{\sim i}$ notation stands for the set of all variables except x_i. The first-order sensitivity index (or first order Sobol index) for the variable x_i, measures the additive effect and is obtained as a fraction of the unconditional variance $\sigma^2(y)$:

$$S_i = \frac{\sigma_{x_i}^2(E_{x_{\sim i}}(y|x_i))}{\sigma^2(y)} \tag{29}$$

while the total Sobol index accounts also for higher order interactions [38]:

$$S_i^T = \frac{E_{x_{\sim i}}(\sigma_{x_i}^2(y|x_i))}{\sigma^2(y)} = 1 - \frac{\sigma_{x_{\sim i}}^2(E_{x_i}(y|x_i))}{\sigma^2(y)} \tag{30}$$

For models which cannot be solved analytically, a sampling procedure is applied for the solution of the integrals. The estimators used in this work are the following:

$$S_i \approx \Big[\frac{1}{N}\sum_{j=1}^{N} f(B)_j (f(A_B^i)_j - f(A)_j)\Big] / \sigma^2(y) \tag{31}$$

$$S_i^T \approx \Big[\frac{1}{2N}\sum_{j=1}^{N} (f(A)_j - f(A_B^i)_j)^2\Big] / \sigma^2(y) \tag{32}$$

In these equations, A and B are two (N, k) matrices with random samples from the input space, where k is the input dimension and N is the number of evaluations. Matrix A_B^i is identical with A, except that its i^{th} column is substituted with the i^{th} column of B $(i = 1, \ldots, k)$.

Estimators of this sort might require up to 10^5 realizations in order to converge, which makes them impractical for demanding numerical models. Therefore, the use of surrogates instead of the original models is vital.

3.2. Surrogate models

Surrogate modeling (or metamodeling) in computational engineering denotes the replacement of intensive simulators by proxy mathematical models that are cheap to evaluate. Such models are able to emulate predefined input–output relationships, even if a model is not available but only data sets exist, which is common in machine learning applications.

In the context of UQ, if $\boldsymbol{x} = \{x_i,\ i = 1, \ldots, k\}$ is a random input vector, with k being the total amount of input random variables, and if $\Omega(\boldsymbol{x})$ is the model simulating a physical process, then the statistical characteristics of the scalar quantity of interest (QoI) $y \in \mathbb{R}$ (could also be multidimensional), are obtained by propagating the

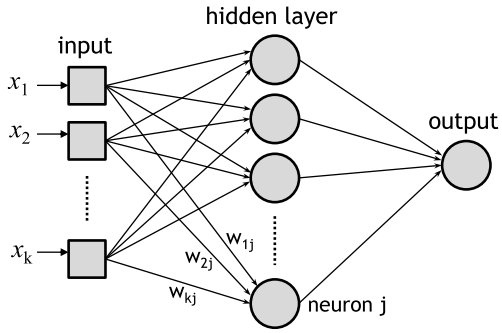

Fig. 8. Configuration of a single layer feed-forward artificial neural network.

uncertainty in $\boldsymbol{x}$ multiple times (random realizations). A surrogate is a low-cost approximation of the original model of the form:

$$\Omega(\boldsymbol{x}) = \hat{\Omega}(\boldsymbol{x}, \boldsymbol{a}) + \epsilon \tag{33}$$

where ϵ is the approximation error and the vector $\boldsymbol{a}$ includes the parameters which are tuned during the training process according to a small set of model runs, called the experimental design (ED). Once trained, the surrogate $\hat{\Omega}(\boldsymbol{x}, \boldsymbol{a})$ can produce extreme amounts of results with trivial computational effort and, therefore, bypass the sampling over the original model $\Omega(\boldsymbol{x})$. The next sections present a brief overview of the formulation for two powerful surrogate types, namely artificial neural networks and Kriging.

3.2.1. Artificial neural networks

Artificial neural networks (ANN) are rapid information-processing systems with a parallel architecture of nodes (neurons), able to handle high dimensional data of discrete or continuous nature [39]. They consist of at least three layers: the input, the output and one (or more) hidden layers. The neurons inside every layer are linked by the so-called synapses. Deep learning methods [40] involve ANNs with many hidden layers, however for structural engineering applications with continuous variables, typically no more than one layer is required.

A typical single-layer ANN configuration, assuming an input vector $\boldsymbol{x} = \{x_i,\ i = 1, \ldots, k\}$, is shown in Fig. 8. The input neurons (squares) do not process information and only connect the network to the external environment. The neurons of the hidden layer (circles) process information coming from a previous layer and feed their output to the next layer. Information is propagated only in a single direction (feed-forward network). For every synapse there is a weight parameter w_{ij} corresponding to the importance of the preceding neuron. Every neuron j calculates a weighted sum of the form:

$$z_j = \sum_{i=1}^{k} x_i w_{ij} + b \tag{34}$$

where b is a bias term allowing the neuron to cover a wider range. Each result is going through an activation function, usually of sigmoid type, in which the nonlinearity of the decision boundary is introduced.

The training procedure is essentially the inference of the weights by minimizing the sum squared error between the predicted output $t(w_{ij})$ and the target output y:

$$\min_{w_{ij}}\big(E(w_{ij})\big) = \min_{w_{ij}}\left\{\frac{1}{2}\sum[t(w_{ij}) - y]^2\right\} \tag{35}$$

Throughout the optimization process, the weights of all synapses are updated until the desired error level or the maximum number of cycles is reached. The weights are updated via an iterative procedure:

$$w_{ij}^{(t+1)} = w_{ij}^{(t)} + \Delta w_{ij} \tag{36}$$

where Δw_{ij} is the correction of the weight at the t^{th} learning step, which is calculated by the gradient:

$$\Delta w_{ij} = -n\frac{\partial E}{\partial w_{ij}} \tag{37}$$

where n is a small parameter adjusting the correction each time, called learning rate. This algorithm is known as back-propagation algorithm, because the residual error is spread back to the neurons in order for the weights to be updated. A fraction of the input data set is used as a validation set and an early stopping criterion is applied in case of overfitting [6].

3.2.2. Kriging

Kriging (a.k.a. Gaussian process regression) is a series expansion method that approximates the original function by a single realization of a Gaussian random field [41]:

$$\Omega(\boldsymbol{x}) \approx \boldsymbol{\beta}^{\mathrm{T}} \boldsymbol{f}(\boldsymbol{x}) + \sigma^2 Z(\boldsymbol{x}) \tag{38}$$

where $\boldsymbol{\beta}$ is a vector of hyper parameters multiplying the set of P-order regression functions $\boldsymbol{f}$, σ^2 is a scalar hyper parameter characterizing the variance and $Z(\boldsymbol{x})$ a zero-mean, unit variance Gaussian random field. The first term of Eq. (38) defines the trend of the surrogate, whereas the second the local deviations.

Regarding the training, if an ED data set of size N is assumed, the hyper parameters $\boldsymbol{\beta}$ and σ^2 are calculated via the generalized least-squares method, depending on the correlation length parameter of the Gaussian field $\hat{\boldsymbol{\theta}}$, as:

$$\boldsymbol{\beta}(\hat{\boldsymbol{\theta}}) = (\boldsymbol{F}^T \boldsymbol{R}^{-1} \boldsymbol{F})^{-1} \boldsymbol{F} \boldsymbol{R}^{-1} y \tag{39}$$

$$\sigma^2(\hat{\boldsymbol{\theta}}) = \frac{1}{N} (y - \boldsymbol{F}\boldsymbol{\beta})^{\mathrm{T}} \boldsymbol{R}^{-1} (y - \boldsymbol{F}\boldsymbol{\beta}) \tag{40}$$

where $\boldsymbol{F}$ is the regression matrix, $\boldsymbol{R}$ is the correlation matrix of the ED for a certain kernel type and y is the actual output of the ED. The correlation length $\hat{\boldsymbol{\theta}}$ inserting the above equations, is extracted through an optimization routine from either of the following expressions:

$$\hat{\boldsymbol{\theta}}_{\mathrm{ML}} = \arg\min \left[\frac{1}{N} (y - \boldsymbol{F}\boldsymbol{\beta})^{\mathrm{T}} \boldsymbol{R}^{-1} (y - \boldsymbol{F}\boldsymbol{\beta}) |\boldsymbol{R}|^{\frac{1}{N}} \right] \tag{41}$$

$$\hat{\boldsymbol{\theta}}_{\mathrm{CV}} = \arg\min \left[y^{\mathrm{T}} \boldsymbol{R}^{-1} \mathrm{diag}(\boldsymbol{R}^{-1})^{-2} \boldsymbol{R}^{-1} y \right] \tag{42}$$

where ML stands for Maximum Likelihood and CV for Cross-Validation and $|\boldsymbol{R}|$ is the determinant of the correlation matrix.

The use of Kriging as a surrogate relies on using the following predictor μ for points $x_0 \notin x = \{x^i,\ i = 1, \ldots, N\}$ outside the ED:

$$\mu(x_0) = \boldsymbol{f}(x_0)^{\mathrm{T}} \boldsymbol{\beta} + \boldsymbol{r}(x_0)^{\mathrm{T}} \boldsymbol{R}^{-1} (y - \boldsymbol{F}\boldsymbol{\beta}) \tag{43}$$

where $\boldsymbol{r}(x_0) = \boldsymbol{R}(|x_0 - x_i|; \hat{\boldsymbol{\theta}})$ is the correlation between the unknown point x_0 and the ED, while $\boldsymbol{f}(x_0)$ is the set of regression functions evaluated at x_0. Adjustable parameters able to help the training process are the order of the regression functions $\boldsymbol{f}$, the correlation kernel type (e.g. Gaussian, Matérn etc.) and a stable optimization algorithm for the calculation of $\hat{\boldsymbol{\theta}}$. The clear distinction between trend and variance in the Kriging formulation offers great flexibility for hierarchical approaches [16] and non-stationary calibrations [15].

4. Proposed variable-fidelity approach

4.1. Overview of variable-fidelity surrogate methods

Variable-fidelity (VF) or multi-fidelity surrogates are approximations combining information from at least two different models in terms of accuracy (fidelity) and cost. The model differences could lie in the discretization level, dimensionality reduction, simplifications in mathematical or numerical description etc., assuming that there is good correlation between them regarding the QoI. As a result, if constructing a surrogate model requires an excessive amount of training samples, or if the original high-fidelity (HF) model is computationally prohibitive even for a few samples, a VF surrogate approach is a viable trade-off [16–18].

VF surrogate methods, as well as the multi-level Monte Carlo (MLMC) [42], are founded on the linearity of the expectation operator. Meaning that if H is a high-fidelity and L a low-fidelity (LF) approximation of a QoI, the following sum stands:

$$\mathbb{E}(H) = \mathbb{E}(L) + \mathbb{E}(H - L) \approx \frac{1}{N_L} \sum_{i=1}^{N_L} L^{(i)} + \frac{1}{N_H} \sum_{i=1}^{N_H} (H^{(i)} - L^{(i)}) \tag{44}$$

where the number of cheap evaluations N_L could be much bigger than N_H. As a generalization, a variable-fidelity surrogate model Ω_V can replace a high-fidelity surrogate Ω_H, assisted by a lower fidelity surrogate Ω_L in the following manner:

$$\Omega_V(\boldsymbol{x}, \boldsymbol{a}) = \Omega_V(\Omega_L(\boldsymbol{x}), \boldsymbol{a}) \approx \Omega_H(\boldsymbol{x}) \tag{45}$$

where $\boldsymbol{x}$ a vector from the input space and $\boldsymbol{a}$ a vector of tuning parameters, which is calculated by a limited number of HF data.

The simplest type of VF surrogate uses a scaling function to map the input space with a scalar parameter representing the error between fidelity levels. If k is the dimension of the input space, a LF surrogate is first trained with $x_i,\ i = 1, \ldots, N \in \mathbb{R}^k$ points. Then, a subset of points $x_i,\ i = 1, \ldots, M \subset N$ is chosen and is used as a training set for the HF surrogate. The scaling factor $\alpha_i,\ i = 1, \ldots, M$ can be of additive or multiplicative form:

$$\alpha_i = HF(x_i) - LF(x_i) \quad \text{or} \quad \frac{HF(x_i)}{LF(x_i)},\ i = 1, \ldots, M \tag{46}$$

where $LF(x_i)$ and $HF(x_i)$ are the low and high fidelity model evaluations. The second surrogate is then trained from $\mathbb{R}^k$ to $\mathbb{R}^1$ to establish the mapping $x_i \mapsto \alpha_i,\ i = 1, \ldots, M$. The final form of the VF surrogate is obtained as:

$$\Omega_V(\boldsymbol{x}) = \Omega_L(\boldsymbol{x}) + \boldsymbol{\alpha} \quad \text{or} \quad \Omega_L(\boldsymbol{x}) * \boldsymbol{\alpha} \tag{47}$$

An alternative approach is the so-called space mapping, where the second surrogate model is a direct $\mathbb{R}^1 \mapsto \mathbb{R}^1$ mapping from the LF outcome to the HF outcome.

Although the latter approaches are useful for local approximations, they are often greedy when the whole region of the input space is of interest. A more powerful VF surrogate is the hierarchical Kriging approach [16], in which the trend term of Eqs. (38) and (43), as presented in Section 3.2.2, is substituted by a Kriging model trained with LF data, instead of the regression functions of the original model. The enhanced VF predictor is given by:

$$\mu_V = \boldsymbol{\beta}\mu_L + \boldsymbol{r}^{\mathrm{T}}\boldsymbol{R}^{-1}(y_H - \boldsymbol{F}\boldsymbol{\beta}) \tag{48}$$

where μ_L is the predictor of the LF Kriging model, y_H is the output vector of the original HF model. The remaining terms represent the same parameters as in Section 3.2.2. It is noted that the entire term related to the deviations from the trend depends solely on the output of the HF level. It is clear from the latter formula, that any surrogate method can be integrated in the trend, besides the original Kriging. Indeed, Schöbi et al. [43] used polynomial chaos expansions which performed well in their studied cases.

4.2. Hybrid hierarchical surrogate method

In order to overcome the computational obstacles set by the demanding FE simulation of a textile SVE and to construct a fast and reliable surrogate method suitable for UQ schemes, a VF surrogate enabling ANNs and hierarchical Kriging is proposed.

Among other solid advantages, hierarchical Kriging is flexible in terms of the correlation between different levels and does not require the HF training set to be a subset of the LF dataset, which would require a costly nearest-neighbor type of algorithm for the selection. A further enhancement allowed by the versatility of this model, is the integration of ANNs in the trend of Eq. (48), as the predictor μ_L of the LF model. Such a machine learning technique discards limitations regarding the input dimension, the processing speed and the data complexity because of its parallel structure. Moreover, it has been found to require less or equal training samples for sufficient accuracy than series expansion methods [44].

Concerning the type of different fidelity levels, the failure prediction algorithm described in Section 2, allows the use of the step size, or equivalently the total number of steps. As mentioned, the step should be kept small towards a high fidelity simulation, resulting of course in longer FE runs, due to the explicit approach of the USDFLD subroutine. However, choosing fewer steps still drives the results towards the correct direction with good correlation and simultaneously decreases the analysis cost. In this study, 20 steps were chosen for the LF models and 150 steps for the HF ones, resulting to a reduction of 7.5 times. The option of the step for the proposed VF approach was preferred to the obvious choice of the mesh size, because the combination of the automatic voxel

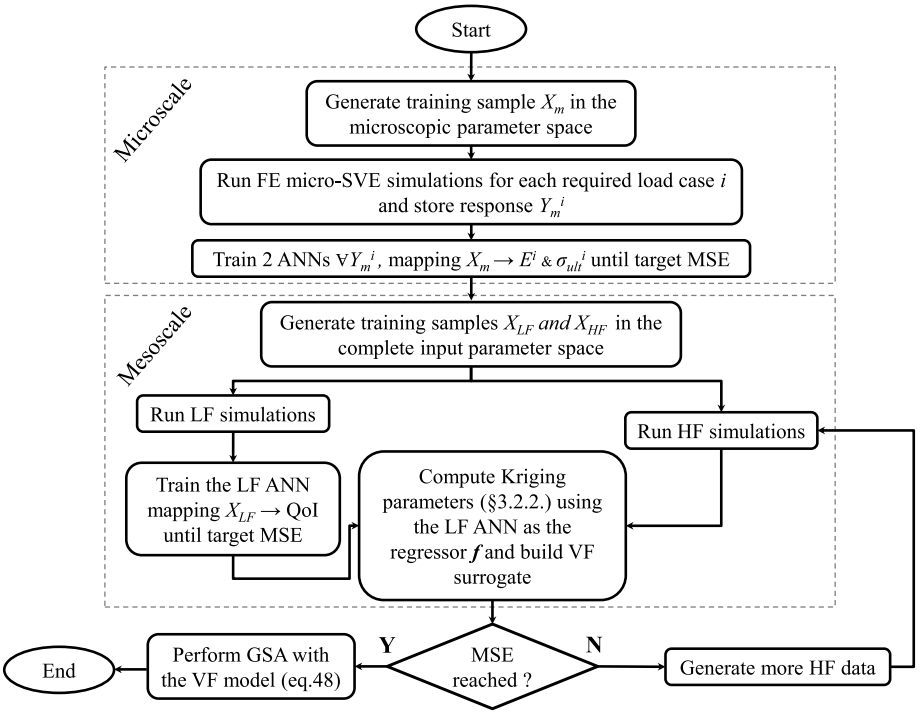

Fig. 9. Flow chart of the proposed VF method.

mesh generation and the variability of a geometric parameter (e.g. the braid angle) could introduce small, but non negligible, numerical noise.

The proposed approach is described in the flow chart of Fig. 9. Initially, the micro-to-meso transition established by the FE models providing the yarn properties (Section 2.3.1), is surrogated by ANNs. Within every necessary load case, one ANN predicts the stiffness and one the ultimate strength value. It is also possible to train one model to predict both the above parameters, yet it would be slightly less accurate. The micro-SVE FE models are not very computationally demanding and their response can be captured with relatively few samples, as it will be shown in the next section. Hence, there is no need for a VF approach in this part of the algorithm.

Subsequently, two different training sets are generated for the LF and HF model evaluations. At this point, all random parameters to be investigated within the UQ framework should be included, from both the micro and the mesoscale. The different fidelity FE models could run in parallel, while the trained ANNs from the previous step are used to accelerate the process. The LF data are used to train the ANN model of the LF mesoscale SVE, which is later used as the trend of the hierarchical VF model. The required Kriging parameters $\boldsymbol{\beta}$, σ^2, $\hat{\boldsymbol{\theta}}$ (Eqs. (39)–(42)) are estimated based on the HF data and the $\boldsymbol{F}$ matrix is filled by the LF surrogate. Provided that the ANNs from the previous stages are suitably trained, the only way to increase the accuracy of the VF model without increasing the correlation between levels, is to increase the number of HF data.

5. Uncertainty quantification: analysis and results

The VF approach presented in Section 4.2, is applied towards the global sensitivity analysis of a triaxially braided composite, using the model and properties given in Section 2. The random input consists of material and geometrical parameters that were found important for the elastic behavior in an older study [6], as well as strength parameters likely to play a role in the damage behavior, under the longitudinal uniaxial tension load case. Specifically, the following eight parameters are considered as random: the longitudinal fiber stiffness (E_{f1}), the volume fraction of the yarns (YV_f), the axial fiber tensile strength (X_{ft}), the tensile matrix strength (X_{mt}), the compressive matrix strength (X_{mc}), the cohesive stiffness (E_{coh}), the cohesive strength (X_{coh}) and the braiding angle (BA). The first seven of those are introduced at the microscale and propagated towards higher scales through the yarn properties, whereas the braiding angle variation is introduced at the mesoscale SVE. It should be noted that the spatial variation of the effective properties cannot be captured by the current modeling and that ideally they should be simulated as random fields. However, due to the lack of correlation data, random variables are considered.

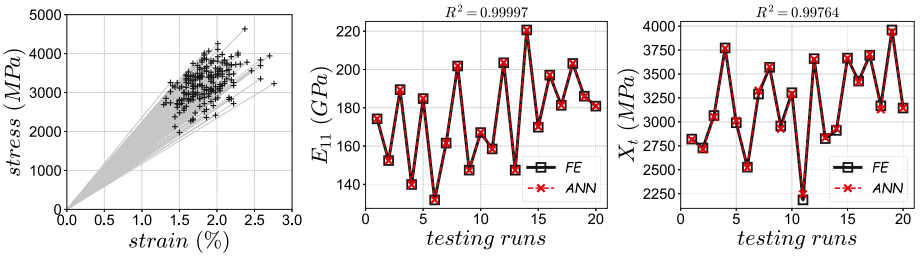

(a) (b) (c)

Fig. 10. Performance of longitudinal tension surrogate models: (a) scatter of model evaluations, (b) evaluation of stiffness surrogate (50 training samples) and (c) evaluation of strength surrogate (90 training samples).

5.1. Experimental design

The nominal values of the random vector are reported in Section 2. The training sample points for all EDs are generated by an optimal Latin Hypercube sampling algorithm [45], for an efficient filling of the input space. It is also noted that all sampling methods are one-shot (e.g. all samples are generated at the same time), as no adaptive techniques are used for simpler implementation. Regarding the scatter, all parameters of the random vector follow a Gaussian distribution with a coefficient of variation (COV $= \sigma/\mu$) of 10%, except the YV_f which follows a truncated Gaussian distribution up to 0.9 for physical consistency.

5.2. Training results and verification in all fidelity levels

In total, 10 surrogate training procedures are performed within the proposed approach: eight surrogate models for the mapping of the microscopic properties to the properties of the yarns (micro-to-meso transition, 2 surrogates for each load case), one surrogate for the LF level of the meso-SVE and one final VF hybrid surrogate using both the LF model and HF data of the meso-SVE (Fig. 9). The training procedure and the validity of the surrogate modeling is verified by direct comparisons of the trained models against the original FE models. Data sets of 20 points outside the training state, are used for that purpose at each stage of the proposed approach.

As an approximation error metric, the coefficient of determination R^2 is given by the formula:

$$R^2 = 1 - \frac{\sum_{i=1}^{N}(y_i - \hat{y}_i)^2}{\sum_{i=1}^{N}(y_i - \bar{y}_i)^2} \tag{49}$$

where y_i is the true response, $\hat{y}_i$ is the respective prediction of the trained surrogate, $\bar{y}_i$ is the mean of the true responses and N is the total number of samples. The values of R^2 are bounded in [0,1] where the better fit is the closer to 1. Point-to-point comparison plots and the respective coefficients of determination are presented for all aforementioned surrogate models, as well as the required training samples for each case.

Starting from the eight ANN surrogates emulating the micro-SVE response, Fig. 10 illustrates the response for the longitudinal tension case. The scatter of the original model evaluations in the stress–strain plane, is shown in Fig. 10a, the stiffness surrogate in Fig. 10b and the strength surrogate in Fig. 10c, reporting also R^2 for each case. The response surface is quite smooth as the damage behavior is governed by the fiber strength, hence the surrogate prediction is exceptional with 50 training sample points for E_{11} and 90 for X_t.

The cases of transverse tension, in-plane and out-of-plane shear are bit more demanding for the training of the nonlinear response. Fig. 11 illustrates the transverse tension case, where the response scatter is bigger due to multiple failure modes. Nevertheless, the performance is fully satisfactory as shown in Fig. 11b and c, with 150 training points for E_{22} and 200 for Y_t. The same stands for the shear cases (Figs. 12 and 13), even though the behavior, as illustrated in the scatter plots, is more complex and highly nonlinear. To reach this performance level, 400 model evaluations were used in the training set of S_{12} and S_{23}. The elastic behavior is always easier to capture, with 50 samples for G_{12} and 60 for G_{23}.

Overall, the ANNs emulating the micro-SVE response perform well, as the biggest error is around 1%, when in fact the model evaluations required are not prohibitive considering the micro-SVE FE model. The number of neurons in the hidden layer of these 8 surrogates ranges from 6 (simpler cases) to 15 (more complex cases).

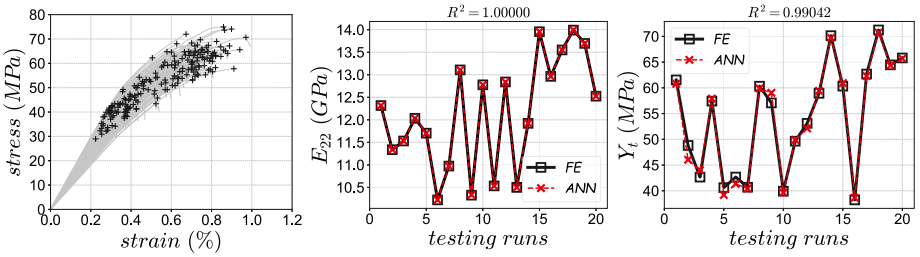

(a) (b) (c)

Fig. 11. Performance of transverse tension surrogate models: (a) scatter of model evaluations, (b) evaluation of stiffness surrogate (150 training samples) and (c) evaluation of strength surrogate (200 training samples).

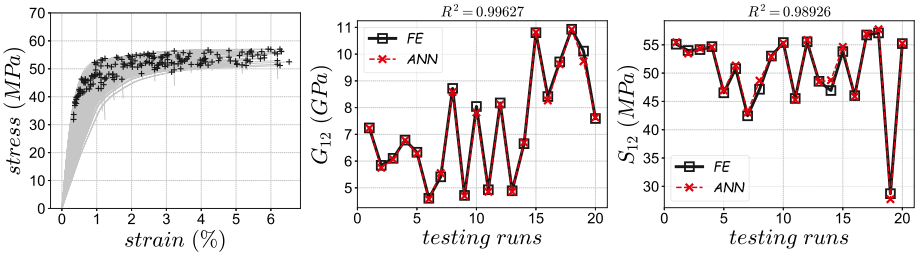

(a) (b) (c)

Fig. 12. Performance of in-plane shear surrogate models: (a) scatter of model evaluations, (b) evaluation of stiffness surrogate (50 training samples) and (c) evaluation of strength surrogate (400 training samples).

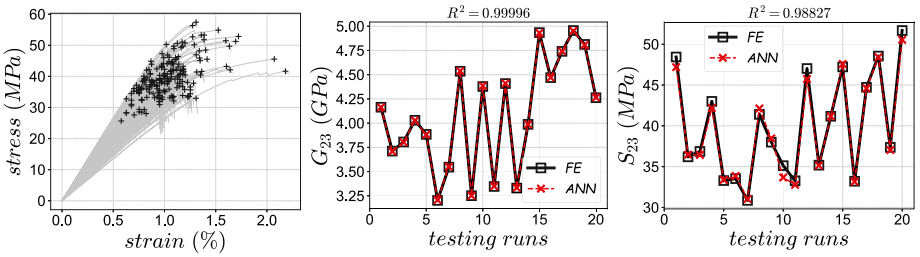

(a) (b) (c)

Fig. 13. Performance of out-of-plane shear surrogate models: (a) scatter of model evaluations, (b) evaluation of stiffness surrogate (60 training samples) and (c) evaluation of strength surrogate (400 training samples).

Moving on to the mesoscale simulations, the lower fidelity FE model evaluations are used to train an ANN mapping the microscopic and mesoscopic input parameters with the ultimate tensile strength (QoI), which is used as a kernel in the hybrid hierarchical approach described in Section 4.2. The scatter of the LF model evaluations is shown in Fig. 14a and the point-to-point comparison against the original FE modeling in Fig. 14b. The LF surrogate required 2000 samples and 35 neurons in order to reach the illustrated performance. In order to further boost the generation of the training data set, the microscale surrogate models previously described were applied. However, the original FE micro-SVEs were used to calculate the reference response for the 20 training runs shown in the evaluation plot (Fig. 14b).

Furthermore, 100 HF model evaluations were used as the training data set for the hierarchical VF surrogate methodology. The response scatter is shown in Fig. 14a together with the LF data. The evaluation plot of the final VF surrogate shown in Fig. 14c, illustrates an adequate performance against 20 HF reference FE simulations, where the total approximation error is calculated as 4% ($R^2 = 0.96$). The hierarchical ANN–Kriging surrogate works with an exponential kernel and the cross-validation expression (Eq. (42)) for the correlation length calculation. A differential-evolution algorithm is employed for the optimization procedure.

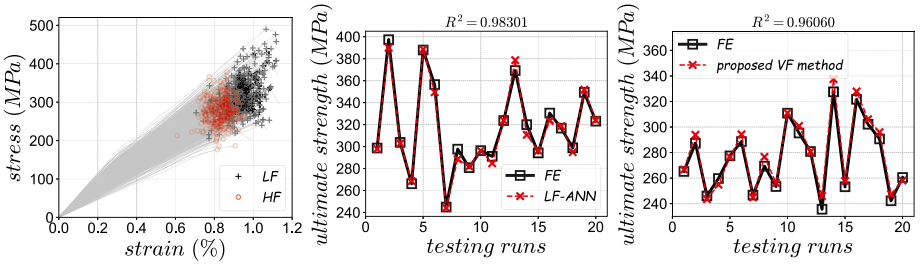

(a) (b) (c)

Fig. 14. Performance of LF and VF surrogate models: (a) scatter of LF and HF model evaluations, (b) evaluation of LF surrogate (2000 LF training samples) and (c) evaluation of hybrid VF surrogate (100 HF training samples).

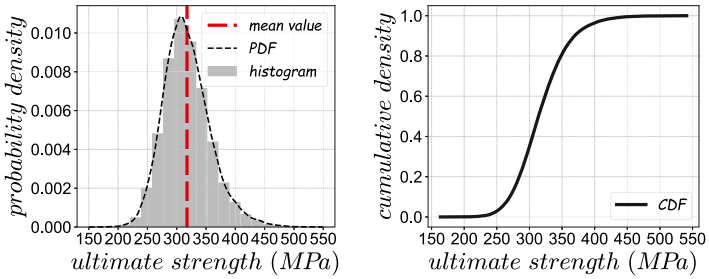

(a) (b)

Fig. 15. Statistics of response variability: (a) probability density function and (b) cumulative density function.

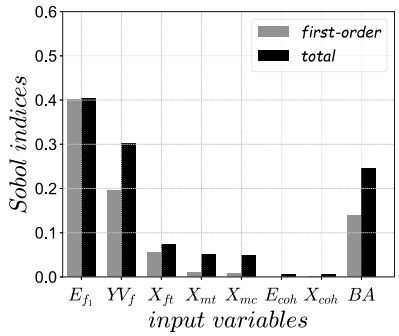

Fig. 16. GSA results: first-order and total Sobol indices.

5.3. Sobol indices

The trained surrogate model enables the necessary rapid mapping for UQ purposes. The GSA methodology described in Section 3.1, is applied towards the identification of the most critical parameters of the input vector for the probabilistic response of the QoI. The same scatter is applied to all random input parameters, with a COV of 10%. To acquire a sense of the response variability, the normalized histogram with a fitted probability density function (PDF) and the cumulative distribution function (CDF) are demonstrated in Fig. 15. The output mean and standard deviation are equal to 317.55 MPa and 40.48 MPa respectively, which results in a response COV of 13%. The PDF is slightly skewed, even though all inputs are symmetrically distributed, displaying the nonlinearity of the input–output relationship.

The results of the variance-based GSA are illustrated in a bar plot form in Fig. 16. Both the first-order and the total indices are visible for each parameter. A first interpretation is that the contribution is distributed, as there is not a single parameter with a dominating percentage. The parameters related to the elastic behavior are more influential than the ones related to strength. The fiber stiffness, followed by the fiber volume content of the yarns and the braiding angle have the lead, while the fiber and matrix strengths have a less profound effect to the response

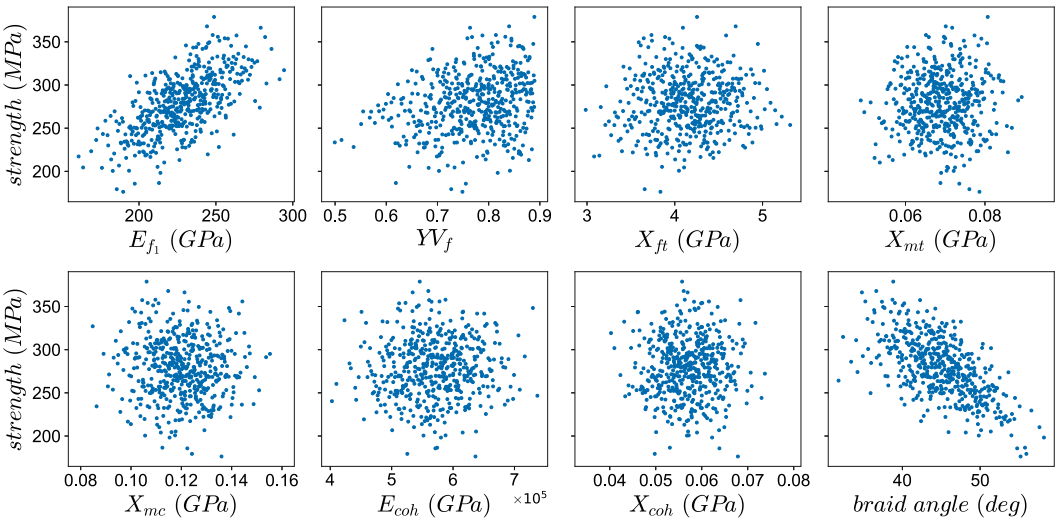

Fig. 17. Scatter plots of each input parameter against the ultimate tensile strength.

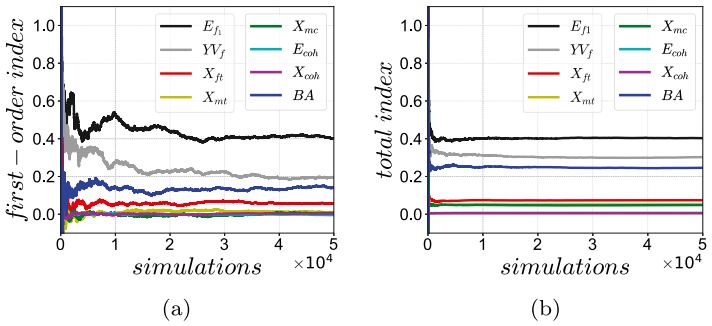

Fig. 18. Evolution of first-order (a) and total (b) Sobol indices over the number of model evaluations.

variability. The interface properties do not contribute much due to the load case under investigation. Moreover, it should be noted that geometrical parameters like the volume fraction and the braiding angle play an important role, a fact that proves the validity of the focus shift towards manufacturing improvement and optimization.

An element maybe even more interesting, is the clear presence of interactions between the input variables. It can be observed from the sum of the first-order indices ($0.8<1$), but also more specifically from the differences of certain variables between the first-order and the total index. The interactions explain the non-smooth response surface and consequently, the difficulty in training accurately a surrogate model able to emulate the response and the requirement for a variable fidelity approach. An explanation for the variables with strong interaction effects is the multiscale nature of the problem under investigation, as the biggest discrepancies are observed at variables from different length scales (YV_f and BA) and variables which are introduced in both scales (X_{mt} and X_{mc}).

A fast way to verify the GSA results and avoid possible mistakes, is the visualization of the scatter of each input parameter against the QoI. The scatter plots are presented in Fig. 17, where the clouds formed from the points are in line with the sensitivity results of the GSA. Moreover, it is meaningful to check the convergence of the Sobol indices by plotting their evolution over the number of model evaluations. The plots in Fig. 18 verify that such an analysis would be prohibitive without using an effective surrogate model, since the first order indices start converging after 35.000 simulations.

6. Concluding remarks

The nonlinear behavior of textile composites within an uncertainty quantification framework has barely been addressed due to the difficulties in approximating the complex response surfaces. A surrogate modeling methodology is proposed herein for the solution of this problem, allowing for the variance-based global sensitivity analysis

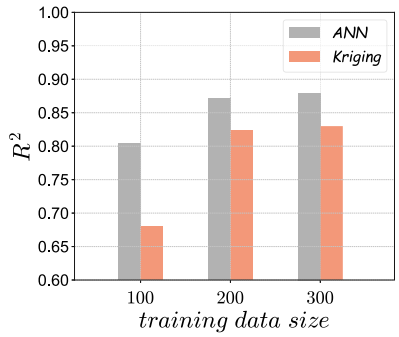

Fig. A.19. Performance comparison between ANN and Kriging for LF training sets of increasing size.

of a progressively damaging triaxially braided composite layer. The microscopic properties are mapped to the yarn properties with artificial neural networks, enabling a fast micro-to-meso scale transition. A novel variable-fidelity surrogate model is presented for the emulation of the demanding braided SVE, which modifies the already established Hierarchical Kriging into a more powerful surrogate, by using a neural network for the low fidelity approximations. The use of the step size as the fidelity level allows a 7.5 times cost reduction without compromising the accuracy levels due to the simultaneous application of automatic voxel mesh generation and geometric variabilities. In total, only 100 HF runs were required for an approximation error of 4%.

The results of the GSA did not identify a single parameter as the governing factor, but rather a spread of the contribution to the yarn volume fraction, the fiber longitudinal stiffness and the braiding angle variation. The differences between first-order and total Sobol indices for several parameters revealed the interactions of the input properties, which can be justified by the multiscale nature of the problem. Moreover, the Sobol indices were found to converge at around 35.000 simulations, proving the necessity of a metamodeling solution.

The proposed approach is non-intrusive and can be applied to any type of textile and load case. Additionally, several future prospects could rise with respect to different focal points, e.g. if the material characterization is the main concern, a VF approach combining USDFLD routines for the LF runs and precise UMAT routines for the HF runs, or voxel meshes for LF runs and conformal meshes for HF runs for load cases with considerable shear phenomena. Finally, in the presence of experimental strength values, the integration of the surrogate model into a Bayesian updating scheme is straightforward and a potential future endeavor of the authors.

Declaration of competing interest

The authors declare that they have no known competing financial interests or personal relationships that could have appeared to influence the work reported in this paper.

Acknowledgments

The provided financial support from the European Union's Horizon 2020 research and innovation programme FULLCOMP under the Marie Skłodowska-Curie grant agreement No 642121 is gratefully acknowledged by the authors.

Appendix. Performance comparison between ANN–Kriging and Hierarchical Kriging

The proposed approach of the ANN–Kriging VF surrogate is compared with the Hierarchical Kriging approach. Since the second part of Eq. (48) is identical for both approaches, the predictor of the trend will be compared using LF data for training. So it is essentially a comparison of ANN versus Kriging performance with the LF data. Fig. A.19 presents the coefficient of determination of each surrogate, using training data sets of increasing size. The same data set was used for training both surrogates and the coefficient of determination was calculated against the same reference data set. The ANN surrogate performs better for all three cases for this specific problem, while the number of parameters to be estimated and tuned is larger for the Kriging approach (polynomial order, correlation length, kernel etc.).

References

[1] X.F. Xu, X. Chen, Stochastic homogenization of random elastic multi-phase composites and size quantification of representative volume element, Mech. Mater. 41 (2) (2009) 174–186.

[2] X.Y. Zhou, P.D. Gosling, C.J. Pearce, L. Kaczmarczyk, Z. Ullah, Perturbation-based stochastic multi-scale computational homogenization method for the determination of the effective properties of composite materials with random properties, Comput. Methods Appl. Mech. Engrg. 300 (2016) 84–105.

[3] G. Stefanou, D. Savvas, M. Papadrakakis, Stochastic finite element analysis of composite structures based on mesoscale random fields of material properties, Comput. Methods Appl. Mech. Engrg. 326 (2017) 319–337.

[4] D. Savvas, I. Papaioannou, G. Stefanou, Bayesian identification and model comparison for random property fields derived from material microstructure, Comput. Methods Appl. Mech. Engrg. 365 (2020) 113026.

[5] Y. Kyosev, Braiding Technology for Textiles: Principles, Design and Processes, Woodhead Publishing, Waltham, MA, 2014.

[6] G. Balokas, S. Czichon, R. Rolfes, Neural network assisted multiscale analysis for the elastic properties prediction of 3D braided composites under uncertainty, Compos. Struct. 183 (2018) 550–562.

[7] R. Bostanabad, B. Liang, J. Gao, W.K. Liu, J. Cao, D. Zeng, X. Su, H. Xu, Y. Li, W. Chen, Uncertainty quantification in multiscale simulation of woven fiber composites, Comput. Methods Appl. Mech. Engrg. 338 (2018) 506–532.

[8] M. Thapa, S.B. Mulani, R.W. Walters, Stochastic multi-scale modeling of carbon fiber reinforced composites with polynomial chaos, Compos. Struct. 213 (2019) 82–97.

[9] L. Cappelli, G. Balokas, M. Montemurro, F. Dau, L. Guillaumat, Multi-scale identification of the elastic properties variability for composite materials through a hybrid optimisation strategy, Composites B 176 (2019) 107193.

[10] M.J. Bogdanor, C. Oskay, S.B. Clay, Multiscale modeling of failure in composites under model parameter uncertainty, Comput. Mech. 56 (3) (2015) 389–404.

[11] G. Mustafa, A. Suleman, C. Crawford, Probabilistic first ply failure prediction of composite laminates using a multi-scale M-SaF and Bayesian inference approach, J. Compos. Mater. 52 (2) (2018) 169–195.

[12] L. Wu, K. Zulueta, Z. Major, A. Arriaga, L. Noels, Bayesian inference of non-linear multiscale model parameters accelerated by a deep neural network, Comput. Methods Appl. Mech. Engrg. 360 (2020) 112693.

[13] M. Bansal, I. Singh, B. Mishra, K. Sharma, I. Khan, A two-scale stochastic framework for predicting failure strength probability of heterogeneous materials, Compos. Struct. 179 (2017) 294–325.

[14] W. Tao, P. Zhu, C. Xu, Z. Liu, Uncertainty quantification of mechanical properties for three-dimensional orthogonal woven composites. Part II: Multiscale simulation, Compos. Struct. 235 (2020) 111764.

[15] G. Balokas, B. Kriegesmann, S. Czichon, R. Rolfes, Stochastic modeling techniques for textile yarn distortion and waviness with 1D random fields, Composites A 127 (2019) 105639.

[16] Z.-H. Han, S. Görtz, Hierarchical Kriging model for variable-fidelity surrogate modeling, AIAA J. 50 (9) (2012) 1885–1896.

[17] P.S. Palar, T. Tsuchiya, G.T. Parks, Multi-fidelity non-intrusive polynomial chaos based on regression, Comput. Methods Appl. Mech. Engrg. 305 (2016) 579–606.

[18] M. Kast, M. Guo, J.S. Hesthaven, A non-intrusive multifidelity method for the reduced order modeling of nonlinear problems, Comput. Methods Appl. Mech. Engrg. 364 (2020) 112947.

[19] C. Miehe, A. Koch, Computational micro-to-macro transitions of discretized microstructures undergoing small strains, Arch. Appl. Mech. 72 (4–5) (2002) 300–317.

[20] G. Ernst, M. Vogler, C. Hühne, R. Rolfes, Multiscale progressive failure analysis of textile composites, Compos. Sci. Technol. 70 (1) (2010) 61–72.

[21] M. Ostoja-Starzewski, Material spatial randomness: From statistical to representative volume element, Probab. Eng. Mech. 21 (2) (2006) 112–132.

[22] R.M. Christensen, A comprehensive theory of yielding and failure for isotropic materials, J. Eng. Mater. Technol. 129 (2) (2007) 173–181.

[23] Z. Hashin, Failure criteria for unidirectional fiber composites, J. Appl. Mech. 47 (2) (1980) 329–334.

[24] L. Xu, C.Z. Jin, S.K. Ha, Ultimate strength prediction of braided textile composites using a multi-scale approach, J. Compos. Mater. 49 (4) (2015) 477–494.

[25] N.S. Nobeen, Y. Zhong, B.A. Francis, X. Ji, E.S. Chia, S.C. Joshi, Z. Chen, Constituent materials micro-damage modeling in predicting progressive failure of braided fiber composites, Compos. Struct. 145 (2016) 194–202.

[26] K.C. Warren, R.A. Lopez-Anido, S.S. Vel, H.H. Bayraktar, Progressive failure analysis of three-dimensional woven carbon composites in single-bolt, double-shear bearing, Composites B 84 (2016) 266–276.

[27] A.D. Kelkar, J.D. Whitcomb, Characterization and Structural Behavior of Braided Composites, Final Report DOT/FAA/AR-08/52, U.S. Department of Transportation Federal Aviation Administration.

[28] A. Kaddour, M. Hinton, Input data for test cases used in benchmarking triaxial failure theories of composites, J. Compos. Mater. 46 (19–20) (2012) 2295–2312.

[29] ABAQUS, Documentation, Dassault Systèmes Simulia Corp., Providence RI, 2014.

[30] E.J. Barbero, Finite Element Analysis of Composite Materials, CRC Press, 2007.

[31] C.C. Chamis, Mechanics of composite materials: Past, present, and future, J. Compos. Technol. Res. 11 (1) (1989) 3–14.

[32] B.D. Agarwal, L.J. Broutman, K. Chandrashekhara, Analysis and Performance of Fiber Composites, fourth ed., Wiley, Hoboken, New Jersey, 2017.

[33] H. Lin, L.P. Brown, A.C. Long, Modelling and simulating textile structures using texgen, Adv. Mater. Res. 331 (2011) 44–47.

[34] P. Frey, B. Sarter, M. Gautherie, Fully automatic mesh generation for 3-D domains based upon voxel sets, Internat. J. Numer. Methods Engrg. 37 (16) (1994) 2735–2753.
[35] A. Matzenmiller, J. Lubliner, R.L. Taylor, A constitutive model for anisotropic damage in fiber-composites, Mech. Mater. 20 (2) (1995) 125–152.
[36] S.K. Boyd, R. Müller, Smooth surface meshing for automated finite element model generation from 3D image data, J. Biomech. 39 (7) (2006) 1287–1295.
[37] I.M. Sobol, Global sensitivity indices for nonlinear mathematical models and their Monte Carlo estimates, Math. Comput. Simulation 55 (1) (2001) 271–280.
[38] A. Saltelli, P. Annoni, I. Azzini, F. Campolongo, M. Ratto, S. Tarantola, Variance based sensitivity analysis of model output. Design and estimator for the total sensitivity index, Comput. Phys. Comm. 181 (2) (2010) 259–270.
[39] L. Fausett, Fundamentals of Neural Networks: Architectures, Algorithms, and Applications, Prentice-Hall, Inc., USA, 1994.
[40] A. Oishi, G. Yagawa, Computational mechanics enhanced by deep learning, Comput. Methods Appl. Mech. Engrg. 327 (2017) 327–351.
[41] J. Sacks, W.J. Welch, T.J. Mitchell, H.P. Wynn, Design and analysis of computer experiments, Statist. Sci. 4 (4) (1989) 409–423.
[42] K.A. Cliffe, M.B. Giles, R. Scheichl, A.L. Teckentrup, Multilevel Monte Carlo methods and applications to elliptic PDEs with random coefficients, Comput. Vis. Sci. 14 (1) (2011) 3.
[43] R. Schöbi, B. Sudret, J. Wiart, Polynomial-chaos-based Kriging, Int. J. Uncertain. Quantif. 5 (2) (2015) 171–193.
[44] G. Balokas, B. Kriegesmann, S. Czichon, A. Böttcher, R. Rolfes, Metamodel-based uncertainty quantification for the mechanical behavior of braided composites, in: M. Petrolo (Ed.), Advances in Predictive Models and Methodologies for Numerically Efficient Linear and Nonlinear Analysis of Composites, Springer International Publishing, 2019, pp. 179–193.
[45] R. Jin, W. Chen, A. Sudjianto, An efficient algorithm for constructing optimal design of computer experiments, J. Statist. Plann. Inference 134 (1) (2005) 268–287.

Chapter 5

Data-Driven Inverse Uncertainty Quantification in the Transverse Tensile Response of Carbon Fiber Reinforced Composites

In this paper, a Bayesian inverse method is applied, able to quantify uncertainties on a microscale level in terms of mean and variance, by enabling experimental data from higher scales. Experimental stiffness and strength data from a UD composite under transverse tension are employed and a polynomial chaos expansion is used as a surrogate model. The methodology is generic and non-intrusive, therefore it can be easily extended to other load cases and setups.

The paper is published in Composites Science and Technology, Volume 211, (2021), 108845.

Composites Science and Technology 211 (2021) 108845

Contents lists available at ScienceDirect

Composites Science and Technology

journal homepage: www.elsevier.com/locate/compscitech

Data-driven inverse uncertainty quantification in the transverse tensile response of carbon fiber reinforced composites

Georgios Balokas [a,*], Benedikt Kriegesmann [a], Raimund Rolfes [b]

[a] Hamburg University of Technology, Structural Optimization for Lightweight Design, Am Schwarzenberg-Campus 4, 21073, Hamburg, Germany
[b] Leibniz University Hannover, Institute of Structural Analysis, Appelstraße 9A, 30167, Hannover, Germany

ARTICLE INFO

Keywords:
Uncertainty quantification
UD fiber composites
Bayesian inference
Surrogate modeling
Polynomial chaos
Sensitivity analysis

ABSTRACT

Uncertainty quantification is critical for the full exploitation of composite materials' potential. Inverse methods offer the possibility of indirectly characterizing the uncertainty of microscopic parameters by employing data sets from standard structural tests in higher scales. Two crucial requirements though, are the efficient modeling especially for the nonlinear prediction, and the measurement error availability from the tests which affects the updated scatter. This study employs effective stiffness and strength experimental data in order to quantify uncertainties of a carbon fiber UD composite in the microscale. A polynomial chaos surrogate model is trained from finite element simulations, able to efficiently predict the homogenized stiffness and strength for the uncertainty quantification procedure. The random parameters which are influential enough to be updated, are identified via a variance-based global sensitivity analysis. The inverse problem is solved with the Bayesian inference method, which updates any prior estimation of the probability models of the input parameters, based on output observations from the tests. Results show significant uncertainty reduction in comparison with typically used variance values in the literature and can be used to enrich the composite material databases. The proposed methodology is applied for the transverse tensile load case, although its non-intrusive nature allows applications for more load cases and various setups.

1. Introduction

The heterogeneity of composite materials combined with their manufacturing processes, introduces uncertainties which are observed as variability in their mechanical response. The variability is apparent in their material properties, e.g. stiffness, strength etc., but also on a structural level (displacement, buckling capacity etc.). These uncertainties include the material properties of the different phases, as well as geometrical parameters like the fiber volume fraction and defects on lower scales and the ply thickness, fiber orientation and imperfections on higher scales. In the design of composites, these uncertainties are accounted for by applying knockdown factors, implicitly assuming that multiple effects are present at the same time. This conservatism hinders the full exploitation of composite structures, although it may be overcome by using probabilistic design methods.

Efficient probabilistic methodologies and models are essential for the uncertainty assessment. Over the last 10–20 years, the development of probabilistic methods pertinent to composite structures has flourished. A first indicative classification can be made according to the spatial scale, where the uncertainty is simulated at a microscopic level [1,2], at a mesoscopic level [3,4] and at a structural level [5,6]. The available studies are not limited to typical long-fiber reinforced plastics, but also particle-reinforced and discontinuous composites [7,8]. There is also variety on the type of structure, e.g. cylinders [9], beams [10] etc. Furthermore, a differentiation can be made related to the target of the probabilistic assessment which can be the efficient uncertainty propagation [11,12], the uncertainty quantification (UQ) [13,14], the direct integration of data towards the reliable regeneration of uncertainties [15,16] and lastly the reliability-based or robust design optimization [17,18].

The developed probabilistic models, however, need to be calibrated in terms of statistical information, which requires repeated experiments in order to create statistical samples. A study by Sriramula and Chrysanthopoulos [19] has reviewed and reported significant experimental information on the scatter of different ply-level parameters. The extracted probability models are based on goodness-of-fit tests from repeated experiments. Most studies apply the measured uncertainty from the available data directly to the input properties and afterwards

* Corresponding author.
E-mail address: georgios.balokas@tuhh.de (G. Balokas).

https://doi.org/10.1016/j.compscitech.2021.108845
Received 26 October 2020; Received in revised form 29 March 2021; Accepted 1 May 2021
Available online 8 May 2021

perform forward uncertainty propagation. In Ref. [20], 2D random fields from discrete material measurements on laminate level were generated, allowing for a realistic probability of failure estimation through Monte Carlo evaluations. Kriegesmann et al. [12] followed a similar strategy for random imperfections of composite cylinders, applying additionally an order reduction transformation. Yang et al. [21] developed a UQ method for C/SiC composites integrating probabilistic distributions extracted from sparse data, directly in the constitutive laws.

Nevertheless, there are parameters within the modeling of composites often difficult to measure directly, or requiring expensive test setups for a statistical characterization. A convenient way to identify the uncertainty of these parameters is via inverse or updating approaches, by using available responses from higher scales and standard tests. The distributions of the elastic ply properties have been identified in Refs. [22,23], while in Ref. [24] the effects of measurement errors and modeling uncertainties were investigated via an updating methodology. Regarding the microscopic properties identification, Sakata and Ashida [25] employed optimization for particle-reinforced composites, while Wu et al. [26] calibrated a Mori-Tanaka model based on computational homogenization simulations. However, not all studies employ actual test data, while the identification of strength properties has not been adequately addressed, mainly due to the requirement of a fast nonlinear model necessary for the inverse algorithm. More recently, Hu et al. [27] proposed a nonlinear solver which still led to large errors, while Mustafa et al. [28] developed a FE-based Bayesian inference scheme and used published data to update strength parameters of glass fibers and matrix. However, in both the above studies the lack of detailed statistical information for the data (e.g. the measurement errors) led to several assumptions, while the choice of random parameters is vague. Consequently, it is hard to deduce whether the identified scatters also include epistemic uncertainties (i.e. modeling/measurement errors).

In this study, a methodology able to quantify both elastic and strength microscopic uncertain parameters of fiber reinforced composites is proposed. A numerical homogenization-based multiscale FE procedure is used for the prediction of the effective stiffness and strength properties of a UD composite. The numerical burden of the nonlinear solver encountered by other studies, is bypassed by a polynomial chaos expansion, which reduces the cost of the UQ process to the cost of setting up the surrogate model. As a first step towards UQ, a variance-based global sensitivity analysis (GSA) is performed for both the elastic and the failure behavior. That way a clear perspective on the parameters influential enough to be updated is acquired. The dominant parameters are inserted into a Bayesian inference scheme, which -based on experimental effective stiffness and strength data-offers updated probability distributions. A recently published experimental campaign of carbon fiber reinforced polymers (CFRPs) by Lüders [29] is employed. The detailed test setups including the measurement errors, along with the excellent deterministic agreement of the numerical model with the data, allows this work to focus on the aleatory uncertainty, exempt of systematic errors, and make almost no assumptions which might distort the results. Therefore, a contribution can be made towards the improvement of the composite material databases. While the method is generic, only the transverse tension load case is studied herein, although the non-intrusive nature of the procedures enables applications to other load cases, and consequently the identification of different microscopic parameters.

2. Micromechanical failure modeling

The current section recapitulates the homogenization theory, summarizes the experimental behavior and describes the finite element modeling.

2.1. Brief summary of homogenization theory

The effective properties of a continuous, heterogeneous body under small strains, can be extracted from the solution of a statistically representative volume element (RVE) in a lower scale [30]. The equilibrium and constitutive equations of a RVE with volume, in absence of body forces, are expressed as:

$$\nabla \cdot \boldsymbol{\sigma}(\boldsymbol{x})^T = 0, \quad \forall\, \boldsymbol{x} \in \Omega \tag{1}$$

$$\boldsymbol{\sigma} = C_\Omega : \boldsymbol{\varepsilon} \tag{2}$$

where C_Ω is the stiffness tensor that fluctuates due to the body's heterogeneity. Each phase can have a separate material law. To simulate a progressively damaging microstructure under the spectrum of continuum damage mechanics, the following form is introduced for a phase R:

$$\boldsymbol{\sigma}(\boldsymbol{x}) = (1 - d(\boldsymbol{x}))C_\mathrm{R} : \boldsymbol{\varepsilon}(\boldsymbol{x}), \quad \forall \boldsymbol{x} \in R \subset \Omega \tag{3}$$

where $d \in [0, 1)$ is a scalar damage variable and C_R is the elastic tensor of the phase.

Two basic principles that should be preserved in homogenization theory, are the clear separation and the energy consistency between the spatial scales. Clear separation means that the microstructure consists of heterogeneities orders of magnitude smaller than those of the macroscopic problem. Moreover, the energy consistency between any macroscopic material point associated with a RVE in average, is given by the Hill-Mandel equation:

$$\overline{\boldsymbol{\sigma}} \cdot \overline{\boldsymbol{\varepsilon}} = \frac{1}{|\Omega|} \int_\Omega \boldsymbol{\sigma} \cdot \boldsymbol{\varepsilon}\, d\Omega \tag{4}$$

where $\overline{\boldsymbol{\sigma}}, \overline{\boldsymbol{\varepsilon}}$ are the macro stresses and strains and $\boldsymbol{\sigma}, \boldsymbol{\varepsilon}$ are the ones on the microscale.

To ensure the above, periodic boundary conditions (PBCs) are applied on the RVE, by mapping opposite boundaries and enforcing periodicity on the displacement field $\boldsymbol{u}$ and anti-periodicity on the traction field $\boldsymbol{t}$:

$$\boldsymbol{u}(x^+) = \boldsymbol{u}(x^-), \quad \forall x^+ \in \partial\Omega^+,\ \forall x^- \in \partial\Omega^- \tag{5}$$

$$\boldsymbol{t}(x^+) = -\boldsymbol{t}(x^-), \quad \forall x^+ \in \partial\Omega^+,\ \forall x^- \in \partial\Omega^- \tag{6}$$

The homogenized properties of interest, are calculated by solving the RVE under the appropriate load cases and then using the volume average of either the microscopic stresses, or the strains:

$$\overline{\boldsymbol{\sigma}} = \frac{1}{|\Omega|} \int_\Omega \boldsymbol{\sigma}\, d\Omega \quad , \quad \overline{\boldsymbol{\varepsilon}} = \frac{1}{|\Omega|} \int_\Omega \boldsymbol{\varepsilon}\, d\Omega \tag{7}$$

When damage localizes in the RVE, the formulated problem is no longer valid under the assumptions of PBCs and small strains.

2.2. Experimental data and material properties

The experimental source of this study is a recently published article by Lüders [29], in which six flat, rectangular specimens of a carbon fiber unidirectional (UD) composite were statically tested under uniaxial, transverse tension. The epoxy resin used was tested under uniaxial tension with dog-bone shaped coupons, thus a set of hardening curves characterizing the plasticity is also available.

Transverse failure in composites is a multi-parametric phenomenon and the experimental characterization often results in big scatters. Interfacial strength, thermally induced residual stresses, plasticity and fiber distribution are the main parameters governing damage initiation and evolution [31–34]. Experimental observations typically show nearly vertical cracks, perpendicular to the load direction, that initiate between the different phases.

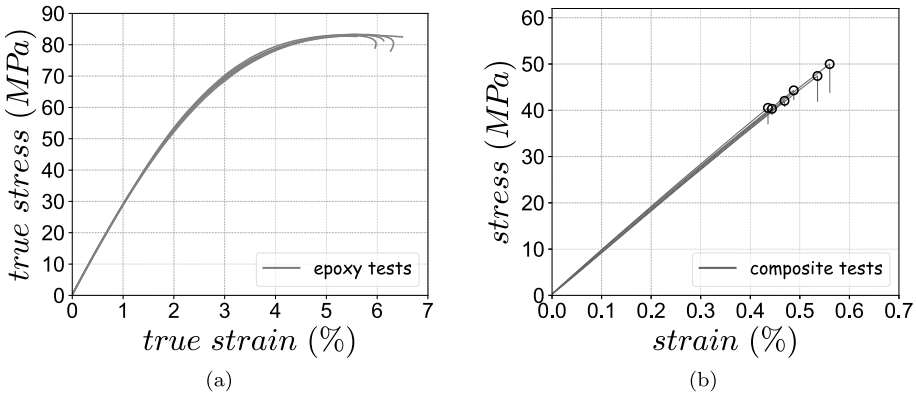

Fig. 1. Experimental stress-strain curves [29]: a) epoxy resin coupons and b) UD composite plates.

Table 1
IM7 carbon fiber and epoxy resin matrix properties [29].

Parameter	E_{f1}(GPa)	E_{f2}(GPa)	G_{f12}(GPa)	G_{f23}(GPa)	ν_{12}	ν_{23}	X_{ft}(MPa)	X_{fc}(MPa)	E_m (GPa)	G_m (GPa)	ν_m	X_{mt} (MPa)	X_{mc} (MPa)
Value	276	19	27	7	0.2	0.357	5180	3200	3.748	1.343	0.395	89	194

The data used herein are shown in Fig. 1. The results of the composite testing (Fig. 1b) reveal an almost linear behavior with a rather brittle failure. This suggests strong fiber-matrix interface properties (otherwise a more ductile behavior would appear) which makes the micro-cracking of the matrix in that area, the triggering failure parameter [29]. In terms of scatter, the mean and standard deviation of the ultimate strength value are $\mu = 44.1$MPa and $\sigma = 3.58$MPa, respectively. The statistical moments of the stiffness value are $\mu = 9.137$GPa and $\sigma = 0.539$GPa. The matrix parameters required for modeling, are calibrated in Ref. [29] from a fitting procedure based on the raw epoxy data (Fig. 1a). The material properties for both carbon fibers and matrix, are reported in Table 1.

2.3. Finite element modeling

The modeling approach is a typical homogenization-based multi-scale FE simulation of a transversely loaded RVE, under PBCs (Eq. (5)). A hexagonal array is sufficient for capturing the actual response of the specimens, as Lüders proved in Ref. [29]. The RVE in-plane dimensions X,Y are calculated conditional to the fiber diameter and volume fraction ($V_f = 62\%$), as $X = 3.145{\cdot}10^{-3}$mm and $Y = 5.447{\cdot}10^{-3}$mm. The RVE thickness (out-of-plane) can be chosen arbitrarily.

Concerning material modeling, the fibers are not critical for the damage behavior of this loading condition, so they are modeled as linear elastic. The epoxy matrix is simulated as an isotropic material following the von Mises plasticity model of Abaqus FE software [35]. This approach is generally not well suited for epoxies as it is not influenced by the hydrostatic pressure above yielding initiation, however it does not have a critical effect for the specific load case and material in hand. The initiation of damage is modeled by the Christensen criterion [36] as:

$$\frac{\sigma_{vm}^2}{X_{mc}X_{mt}} + \left(\frac{1}{X_{mt}} - \frac{1}{X_{mc}}\right) I_1 \geq 1 \tag{8}$$

considering the discrepancy between compressive and tensile strength due to the hydrostatic pressure, where σ_{vm} is the von Mises stress and $I_1 = \sigma_1 + \sigma_2 + \sigma_3$ is the first stress invariant. The matrix

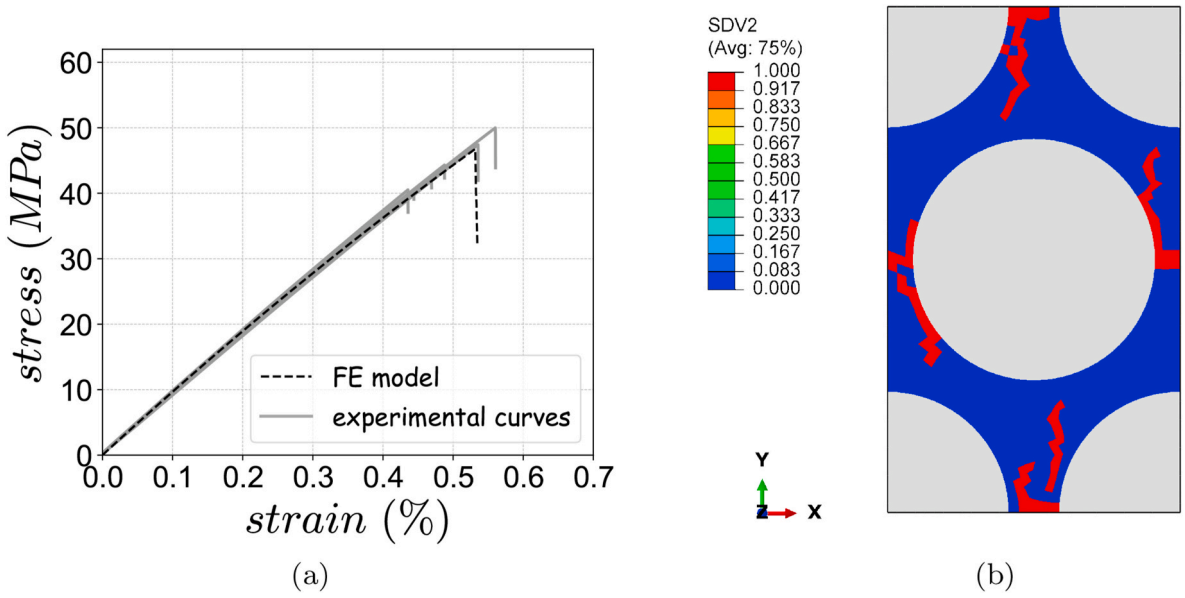

Fig. 2. Finite element prediction: a) stress-strain curve compared with the experimental curves and b) damage pattern at the failure onset.

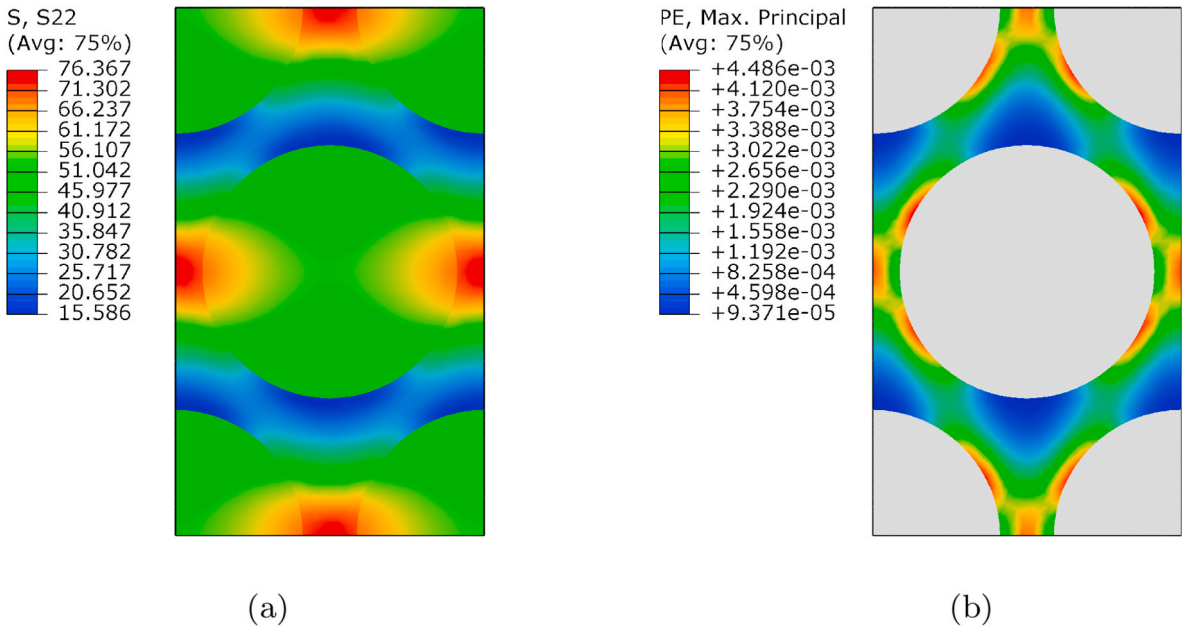

Fig. 3. Contour plots of the RVE before damage localization: a) transverse normal stress distribution b) matrix plastic strain distribution.

strengths in tension and compression are represented with X_{mt} and X_{mc}.

Regarding the damage progression, the model follows an instantaneous stiffness degradation approach (Eq. (3)), where the material properties are reduced to 0.01% of their initial value [29] in a single step once the failure criterion is met. To ensure numerical stability, the stiffness matrix is kept positive by enforcing the physical conditions below [13] and by keeping the off-diagonal terms of the damaged compliance matrix unaffected:

$$v_{12} - \sqrt{\frac{E_1}{E_2}} < 0 \tag{9}$$

$$v_{23} - \sqrt{\frac{E_2}{E_3}} < 0 \tag{10}$$

$$2v_{12}v_{13}v_{23}\frac{E_3}{E_1} + v_{12}^2\frac{E_2}{E_1} + v_{23}^2\frac{E_3}{E_2} + v_{13}^2\frac{E_3}{E_1} - 1 < 0 \tag{11}$$

The progressively damaging algorithm is implemented in Abaqus via a user-defined field (USDFLD) subroutine [16].

After the solution, the homogenized stress-strain curve is extracted with a post-processing script, employing Eq. (7) according to the RVE discretization for each solution step:

$$\overline{\sigma} = \frac{1}{\Omega_{tot}}\sum_{k=1}^{N_p}\sigma^k\Omega^k,\ \overline{\varepsilon} = \frac{1}{\Omega_{tot}}\sum_{k=1}^{N_p}\varepsilon^k\Omega^k \tag{12}$$

where Ω^k is the volume of each element and N_p is the total number of integration points, given that each element has a single integration point (C3D8R elements are used). A practical implementation of the above is given in the appendix of [29]. The resulting curve for the material properties reported in the previous section, is shown in Fig. 2 against the experimental curves, together with the damage pattern of the RVE, a few steps after the peak point of the curve.

The response of the described numerical model is accurate in terms of stiffness and lies well within range regarding failure stress and failure strain, as shown in Fig. 2a. The damage pattern illustrated in Fig. 2b starts at the fiber-matrix interface and has a reasonable orientation, perpendicular to the load direction. The distributions of transverse stresses and plastic strains, right before the damage initiation, are also shown in Fig. 3. Results are in line with similar models from the literature [28,37,38] and verify the consistency of the adopted approach.

3. Inverse uncertainty quantification approach

The FE procedure needs to be bypassed in order to acquire a faster model for the demanding (in terms of model evaluations) UQ methods, i.e. the variance-based sensitivity analysis and the Bayesian inference. The surrogate choice in this study is a non-intrusive polynomial chaos model [39], due to the instant acquisition of the Sobol indices after training without any further calculations and the affordability due to the low stochastic dimension of the problem.

3.1. Polynomial chaos formulation

Assuming a scalar output variable y with finite variance and a vector $\boldsymbol{x} = \{x_i,\ i = 1, \ldots, M\}$ of independent input parameters, the polynomial chaos expansion (PCE) of y approximates the model Ω with an infinite series of orthonormal polynomials:

$$y = \Omega(\boldsymbol{x}) \approx \sum_{\boldsymbol{\alpha}\in\mathbb{N}^M} y_{\boldsymbol{\alpha}}\Psi_{\boldsymbol{\alpha}}(\boldsymbol{x}) \tag{13}$$

where M is the size of the input vector $\boldsymbol{x}$, $y_{\boldsymbol{\alpha}}$ are the coefficients to be computed, $\boldsymbol{\alpha}$ is a M-dimensional multi-index (M-tuple) and $\Psi_{\boldsymbol{\alpha}}(\boldsymbol{x})$ are multivariate orthonormal polynomials. The orthonormal basis of the series is constructed as a product of univariate orthogonal polynomials P:

$$\Psi_{\boldsymbol{\alpha}}(\boldsymbol{x}) = \prod_{i=1}^{M} P_{\alpha_i}^{(i)}(x_i) \tag{14}$$

Every major probability distribution family corresponds to specific known polynomials, e.g. Legendre for Uniform, Hermite for Gaussian, Laguerre for Beta and Jacobi for Gamma distributions. Regarding the truncation and the procedure towards the calculation of the coefficients $y_{\boldsymbol{\alpha}}$, the interested reader is referred to Appendix A.

3.2. Variance-based global sensitivity analysis

The variance-based GSA offers normalized fractions of the total output variance of a model that correspond to each input variable and their possible interactions. For an input variable x_i of a function $y = \Omega(x_i) \in \mathbb{R}$, the first-order sensitivity (or Sobol) index measures the effect of the variable alone and is obtained as a fraction of the unconditional

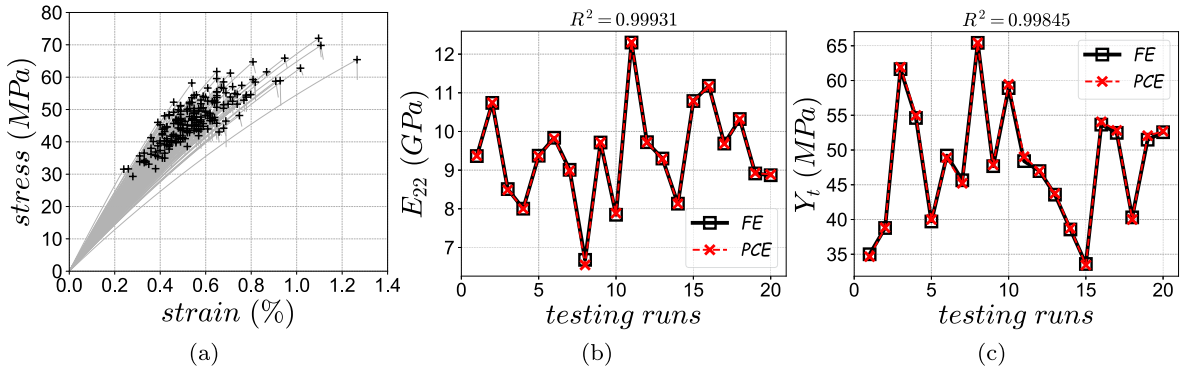

Fig. 4. Polynomial chaos training and verification: a) response of training data set, b) verification for stiffness and c) verification for strength, via comparison for 20 sample points outside the training set.

variance $\sigma^2(y)$:

$$S_i = \frac{\sigma^2_{x_i}\left(E_{x_{\sim i}}(y|x_i)\right)}{\sigma^2(y)} \tag{15}$$

The total Sobol index considers also higher order interactions and is given by Ref. [40]:

$$S_i^T = \frac{E_{x_{\sim i}}\left(\sigma^2_{x_i}(y|x_i)\right)}{\sigma^2(y)} = 1 - \frac{\sigma^2_{x_{\sim i}}(E_{x_i}(y|x_i))}{\sigma^2(y)} \tag{16}$$

The $x_{\sim i}$ notation stands for the set of all variables except x_i. In practice, most models cannot be solved analytically, thus the above expressions are intractable. Instead, several estimators have been proposed [40], which however might require up to 10^5 realizations in order to converge, hence can only be used for costless models.

Nevertheless, an essential advantage of the PCE is that the Sobol indices can be derived immediately after training, without any sort of estimator, simply by post-processing the computed coefficients y_a [41]. The first-order indices are given by the following expression:

$$S_i = \frac{\sum_{a\in A_i} y_a^2}{\sigma^2(y)} \qquad \text{where}: \quad A_i = \left\{a \in \mathbb{N}^M : a_i > 0,\ a_{j\neq i} = 0\right\},\quad \sigma^2(y) = \sum_{\substack{a\in\mathbb{N}^M \\ a\neq 0}} y_a^2 \tag{17}$$

whereas for the total Sobol indices, the subset changes to: $A_i = \{a \in \mathbb{N}^M : a_i > 0\}$. The interested reader on the GSA formulation and the combinations with surrogate modeling is referred to Refs. [11,40,41].

3.3. Inverse identification via Bayesian inference

The acquisition of response data can be used within an inverse UQ framework, in order to improve the knowledge on the input parameters of a system, by updating their statistical information based on the discrepancies between model predictions and observations. In this study, the experimental data of the composite tests are employed in a Bayesian inference scheme, leading to updated information on the scatter of the microscopic parameters.

If Ω is the model between an input x and the response of interest, then the expression:

$$y = \Omega(x) + \varepsilon \tag{18}$$

establishes the deviation/error ε between the observed quantities y and the model response. Based on the Bayes' theorem, the posterior probability density function (PDF) of the input x given a set of observation data y has the form:

$$p(x|y) = \frac{p(y|x)p(x)}{\int p(y|x)p(x)dx} \tag{19}$$

where $p(y|x)$ is the likelihood function, $p(x)$ is the prior PDF and the denominator is a normalizing constant called evidence. Essentially, the prior belief about the probability of the input x, is being updated to the posterior, after observing the data y.

In order to configure the likelihood function, a typical strategy is to consider the errors of Eq. (18) as independent and identically distributed random variables, following a Gaussian distribution $\mathcal{N}(0, \sigma_\varepsilon^2)$, where σ_ε represents the measurement error. It is also common to include potential modeling errors into the same variable [42]. The likelihood function can then be formatted as Gaussian, and the posterior is expressed as:

$$p(x|y) \propto \left(2\pi\sigma_\varepsilon^2\right)^{-n/2} \exp\left\{-\frac{1}{2\sigma_\varepsilon^2}\sum_{i=1}^{n}\left[y_i - \Omega_i(x)\right]^2\right\} p(x) \tag{20}$$

where n is the number of available measurement data. The last equation represents the solution of the inverse Bayesian problem as a proportionality and provides the joint posterior distribution of the input parameters, conditional to the observed data.

An analytical solution for the posterior distribution is usually not possible, thus typically numerical techniques are used in order to sample from an unknown distribution by constructing a Markov Chain. Markov Chain Monte Carlo (MCMC) methods allow the iterative generation of samples which asymptotically behave as the target PDF. In this work the Metropolis-Hastings algorithm is used for that purpose [43]. In brief, starting from a point x^k in space, a so-called random-walk is performed in the neighborhood based on a proposal distribution $Q(x|x^k)$. The candidate point x^* is accepted or rejected according to the following expression:

$$x^{k+1} = \begin{cases} x^* \sim Q\left(x|x^k\right), & \text{if} \quad u \sim U[0,1] < \min\left\{1, \dfrac{p(x^*|y)}{p(x^k|y)}\right\} \\ x^k, & \text{else} \end{cases} \tag{21}$$

where essentially points with higher likelihood are always accepted, otherwise they are either accepted or rejected randomly (based on a comparison with a standard uniform sample) with decreasing probability, the less likely they are.

Some noteworthy points regarding Bayesian inference with MCMC, are the measurement error choice and the spread of the proposal distribution. The measurement error essentially controls the acceptance space of the problem, so it affects the variance of the results. In case it is not available, many studies perform a parametric analysis starting from a reasonable (from an engineering judgment perspective) value. Moreover, the spread of the proposal distribution in MCMC controls the area

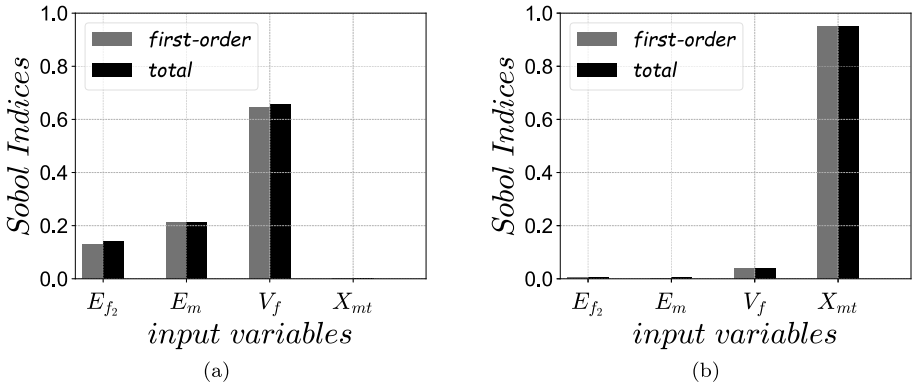

Fig. 5. GSA results for the first order and total indices: a) stiffness response and b) strength response.

covered by the Markov chain samples, hence the efficiency of the method. A small spread leads to correlated samples (meaning ergodicity problems) and slows down convergence, whereas a big spread reduces the acceptance rate, which drives the efficiency of the method. A convenient choice can be found by trial and error, conditional to a desired acceptance rate (usually 40–50%). For more information the reader is referred to Refs. [42,44,45].

4. Uncertainty quantification results

4.1. Surrogate modeling verification

The approach presented in section 3 is applied to quantify the uncertain inputs of the micro-parameters of a UD composite, using the data and model given in section 2. The parameters consisting the random input are: $\boldsymbol{x} = \{E_{f2}, E_m, V_f, X_{mt}\}$. Based on prior experience, those are the governing microscopic parameters for the elastic and damage behavior of the material. The training sample points (also known as design of experiments) were generated by an optimal Latin Hypercube sampling algorithm [46], for an efficient filling of the input space.

A data set of 160 FE model evaluations was generated for training and verification. The scatter of this data set in terms of stress-strain response, is shown in Fig. 4a. The quantities of interest for the current study are the effective stiffness and strength response of the UD composite, as a result two different PCEs are trained. For the stiffness PCE model, a second-order polynomial was used and 60 samples were required, while for the strength model, a third-order polynomial with 140 samples was used. Both PCEs use the 1-norm, without any order reduction (see Appendix A). For the verification of the training, a set of 20 points outside the training set was used to compare the PCE predictions against the original FE model. The coefficient of determination (R^2) is used as an error metric, which is given by the formula:

$$R^2 = 1 - \frac{\sum_{i=1}^{N}\left(y_i - \widehat{y}_i\right)^2}{\sum_{i=1}^{N}\left(y_i - \overline{y}_i\right)^2} \tag{22}$$

where y_i is the true response, $\widehat{y}_i$ is the respective prediction of the constructed PCE, $\overline{y}_i$ is the mean of the true responses and N is the total number of samples. The metric values of R^2 are bounded in [0,1] and the closest the values are to 1, the better is the fit. A point-to-point comparison plot and the coefficient of determination are presented for both PCEs in Fig. 4b and c, where excellent convergence is observed, as the error in both cases is less than 0.2%.

4.2. Variance-based global sensitivity analysis

The Sobol indices for both responses are immediately available after the surrogate training, by post processing the PCE coefficients (Eq. (17)). The results are provided in Fig. 5 for both stiffness and strength, in a bar plot form. The first-order indices and the total ones (including interactions) are directly compared for each input parameter.

Concerning the elastic response (Fig. 5a) the fiber volume fraction is governing the response variability, as it is responsible for almost 65% of the total output scatter. The stiffness properties of the two phases are following with 21% for the matrix and 13% for the fibers. The strength response however (Fig. 5b), is dominated by the matrix tensile strength up to a percentage of 95%. The interactions among the input, observed from the discrepancies between the total and the first-order indices, appear rather low. Therefore, it would be safe to use an order reduction by selecting a q-norm during the PCE construction, which would lead to a more efficient surrogate model in terms of model evaluations (see Appendix A). The results appear realistic from an engineering perspective, and while the strength response is clear, the dominance of V_f for the stiffness response can be interpreted from the inverse rule of mixtures (or Reuss model): $E_2 = (V_f/E_{f2} + (1 - V_f)/E_m)^{-1}$, by calculating the partial derivatives of the denominator:

$$\begin{aligned} \frac{\partial\left(E_2^{-1}\right)}{\partial V_f} &= \frac{1}{E_f} - \frac{1}{E_m} \\ \frac{\partial\left(E_2^{-1}\right)}{\partial E_{f2}} &= -\frac{V_f}{E_{f2}^2} \\ \frac{\partial\left(E_2^{-1}\right)}{\partial E_m} &= -\frac{1 - V_f}{E_m^2} \end{aligned} \tag{23}$$

The derivatives with respect to E_{f2} and E_m have numerators smaller than 1, while the denominators are squared Young's moduli, hence large values. As a result, both expressions are much smaller (absolute value) than the derivative with respect to the volume fraction.

According to the sensitivity results, the microscopic parameters that can be identified when integrated to the Bayesian inference scheme, are the volume fraction based on the stiffness response and the matrix tensile strength based on the failure response. It is of great importance for a sensitivity analysis to precede an inverse identification, as irrational results might appear from the updated distribution of a non-influential parameter.

4.3. Uncertainty quantification via Bayesian inference

4.3.1. Stiffness

The Bayesian inference methodology described in section 3.3, is first applied to identify the volume fraction V_f based on the effective stiffness response of the UD composite. As discussed in the previous section, the elastic variables E_{f2} and E_m also contribute to the output scatter. However, after some trials it was observed that the model is not sensitive enough to those parameters in order for them to be updated, because their posterior distributions were highly dependent on the priors and had mostly larger variance. Therefore, these parameters are considered

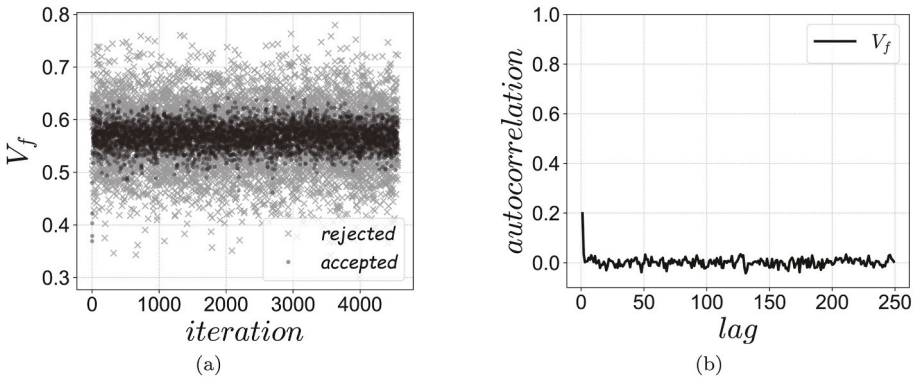

Fig. 6. Evaluation plot of generated MCMC for the stiffness case: a) trace plot and b) autocorrelation plot.

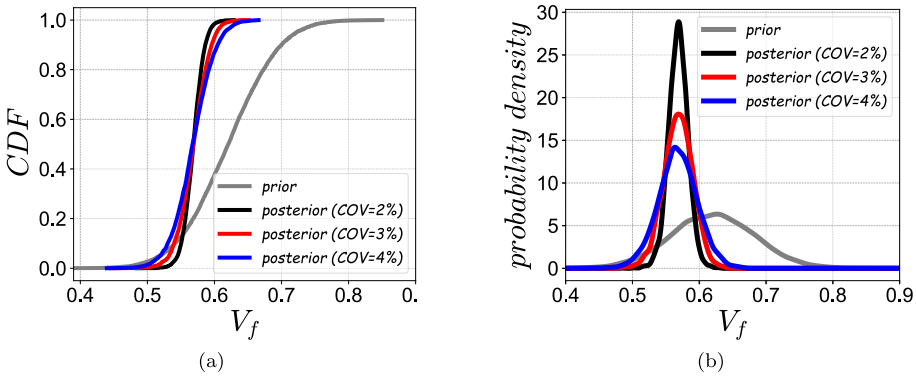

Fig. 7. Comparison of prior and posterior distributions of V_f, for three cases of COV of the parameters which are not updated: a) cumulative distribution and b) probability density.

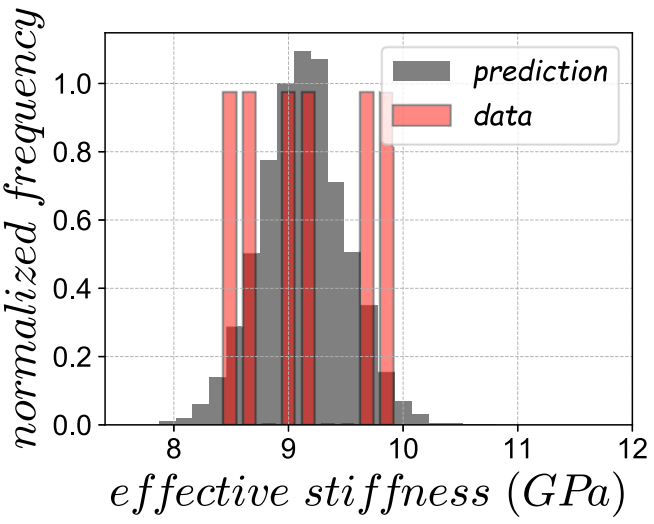

Fig. 8. Response prediction in contrast with experimental data for the stiffness case.

random but they are not updated. The experimental data extracted from the derivative of the curves in Fig. 1 are (in GPa) [9.939, 8.399, 8.979, 9.128, 8.767, 9.699] and the measurement error for this specific test campaign is 0.122 GPa [29]. The availability of the experimental measurement error is of great significance, since it affects the variance of the results, as discussed in section 3.3.

The first performance evaluation concerns the convergence of the MCMC samples. Fig. 6 illustrates the trace plot and the autocorrelation of the generated Markov chains. The prior for V_f is chosen as a Gaussian distribution with a mean value of 0.62 (as given in Ref. [29]) and a 10% coefficient of variation (COV = σ/μ). The starting point of the Markov chain is intentionally chosen quite lower, in order to capture the convergence speed through the trace plot (Fig. 6a). Indeed, the generated samples are mixing well with fast convergence and stationarity. The autocorrelation between accepted samples shows a quick decrease and stays in low levels around zero (Fig. 6b), which is the target as a sample should only depend on the previous sample. These plots also provide clues about the burn-in period which is the amount of samples at the first stages of the Markov chain that are deleted due to high correlation. In this case the burn-in was chosen as 50 samples.

Regarding the updated values of V_f, the mean value decreased from 0.62 to 0.57. For the variance, an assumption must be made on the variance of the random parameters which are not updated. Three cases were considered, with a COV of 0.02, 0.03 and 0.04 for each parameter. The updated variance is lower than the prior (10%) and ranges between 2.5 and 5%. The differences in the mean and variance between the prior and the posterior distributions are also illustrated in Fig. 7, in terms of cumulative distribution and probability density functions.

The response prediction after the update is also directly available with MCMC, with no need for extra model evaluations. The predicted response sample is shown as a histogram in Fig. 8, in contrast with the experimental data. The mean of the response is well captured and all data lie within range. It is worth mentioning that a direct comparison between the predicted variance and the data variance is not reliable, due to the low number of data.

4.3.2. Strength

The Bayesian inference based on the strength response is more straightforward since the GSA identified the matrix strength X_{mt} as the utterly dominant parameter concerning the response variability. The

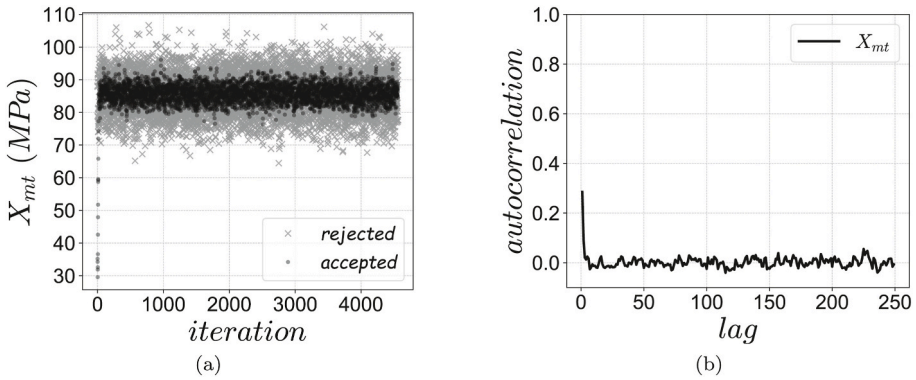

Fig. 9. Evaluation plot of generated MCMC for the strength case: a) trace plot and b) autocorrelation plot.

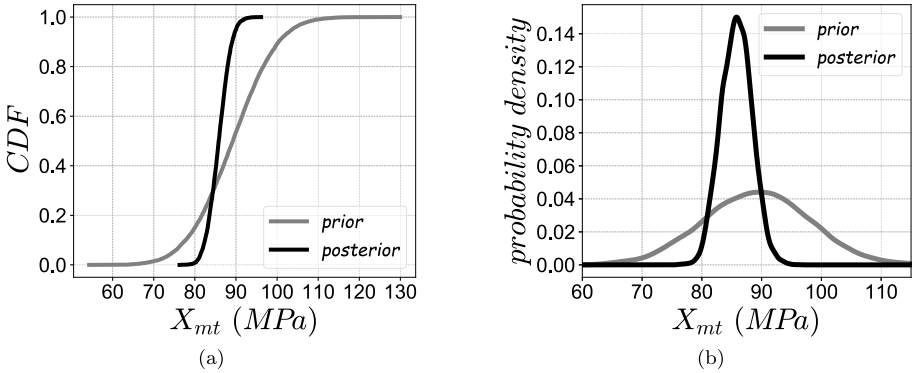

Fig. 10. Comparison of prior and posterior distributions of X_{mt}: a) cumulative distribution and b) probability density.

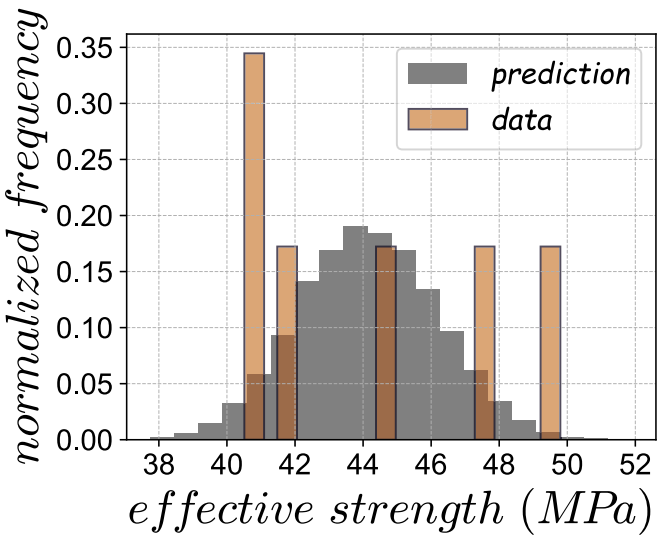

Fig. 11. Response prediction in contrast with experimental data for the strength case.

remaining parameters are considered deterministic. The experimental data as extracted from the curves of Fig. 1 are (in MPa) [40.523, 49.990, 47.413, 42.044, 40.318, 44.306] and the measurement error is 4 MPa [29].

The convergence and autocorrelation plots are shown in Fig. 9. Once more, convergence is established rapidly, even though the initial point of the Markov Chain was selected in a lower value. The autocorrelation plot verifies there are no ergodicity problems and the first 50 samples are deleted as burn-in. The prior is a Gaussian distribution with 89 MPa as mean value, as identified by the fitting procedure in Lüders, while the COV is equal to 10%. The posterior distribution has a reduced mean value of 86 MPa with a COV of 3%. The comparison between prior and posterior is shown in Fig. 10. It appears that the fitting process overestimated X_{mt}.

The histogram of the predicted sample of the response based on the updated posterior, is shown in Fig. 11, together with the data measurements. The mean value of the available data is slightly smaller than the one of the prediction, because of the three measurements within the range of 40–42 MPa. Even though all measurements lie within the predicted range, they appear quite dispersed and their variance, if calculated the conventional way, is bigger than the one of the predicted sample. However, for such a small sample, a different variance estimator is likely to be more appropriate, such as range/4 or range/6. In that case, the variances of the prediction and the data are quite close.

5. Concluding remarks

A full uncertainty quantification framework was presented herein, regarding the most influential microscopic properties of a carbon UD composite material, based on a recently published experimental campaign. A global variance-based sensitivity analysis was initially performed, which identified the governing parameters related to the elastic and the failure response. Afterwards, the prior beliefs of the statistical moments of these parameters were updated, via a Bayesian inverse quantification approach.

A FE multiscale methodology was established for the modeling response, while a polynomial chaos surrogate model was employed to boost the efficiency of the UQ methods, due to the high number of necessary model evaluations. Even though this study only deals with the transverse tension load case, an extension towards other load cases is straightforward, as all methods employed are non-intrusive (PCE, GSA,

Bayesian inference). Hence, a potential follow-up study could integrate the experimental data from Ref. [29] for transverse compression and in-plane shear loads, towards the quantification of more microscopic parameters.

Results showed that the microscopic volume fraction and the matrix tensile strength are the governing parameters for the response variability of the effective stiffness and strength, respectively. The Bayesian inference methodology indicated a shift of their previously determined mean values, namely 57% from 62% for the V_f and 86 from 89 MPa for the X_{mt}. Moreover, a significant uncertainty reduction was observed for both parameters. Starting from a very common prior belief of a 10% COV, the updated V_f lies in the range of 2.5–5% depending on the uncertainty of the phases' elastic parameters, while the posterior of X_{mt} showed a 3% COV. It is worth mentioning that the COV of X_{mt} has been identified as approximately 11% in a similar study [28], which however is very likely to have included measurement errors and uncertainties of other parameters in this scatter.

The availability of the experimental measurement error is really important, as no critical assumptions were made regarding the scatter results. Finally, it is noteworthy that the results of this study are representative solely for the material under investigation. For a different material system where the cohesive properties would be more pronounced, the same methodology can be followed for the UQ of the cohesive stiffness and strength properties under the same load case.

CRediT author statement

Georgios Balokas: conceptualization, methodology, software, validation, writing – original draft; Benedikt Kriegesmann: conceptualization, writing – review and editing, funding acquisition, supervision; Raimund Rolfes: writing – review and editing, funding acquisition.

Declaration of competing interest

The authors declare that they have no known competing financial interests or personal relationships that could have appeared to influence the work reported in this paper.

Acknowledgments

The provided financial support from the European Union's Horizon 2020 programmes FULLCOMP (GA No 642121) and SuCoHS (GA No 769178) is gratefully acknowledged by the authors.

Appendix A. Polynomial chaos truncation and computation of coefficients

For the truncation of the PCE (Eq. (13)), the simplest option consists of confining the total degree of polynomials with an upper bound:

$$A^{M,p} = \left\{ \boldsymbol{\alpha} \in \mathbb{N}^M : |\boldsymbol{\alpha}| \leq p \right\} \tag{A.1}$$

where $|\alpha| = \sum_{i=1}^{M} \alpha_i$ is the total degree of polynomials and p is the maximum degree. The cardinality of this set is:

$$\mathrm{card} A^{M,p} \equiv Z = \frac{(M+p)!}{M!p!} \tag{A.2}$$

hence the set size grows polynomially both in M and p (e.g. for $M = 6$ and $p = 5$, $Z = 210$). The number of model evaluations required for training, needs to be 3–4 times the $\mathrm{card} A^{M,p}$. As a result, this truncation can be expensive when the stochastic dimension M is high. A reduction is achieved with the use of hyperbolic index sets based on q-norms [47]:

$$A_q^{M,p} = \left\{ \boldsymbol{\alpha} \in \mathbb{N}^M : \left(\sum_{i=1}^{M} \alpha_i^q \right)^{\frac{1}{q}} \leq p \right\} \tag{A.3}$$

where $0 < q < 1$. This strategy is suitable for problems with minimal interactions between the stochastic input.

There are various ways to compute the unknown coefficients y_{α} [41]. In this study, a non-intrusive technique (i.e. model independent for generalization purposes) based on minimizing the mean square error between the prediction and the model response for each sample point, is employed. If $\widehat{Y}$ is the vector of the coefficients, then:

$$\widehat{Y} = \arg minE \left\{ \left[\sum_{j=0}^{Z-1} y_j \Psi_j(\boldsymbol{x}) - \Omega(\boldsymbol{x}) \right]^2 \right\} \tag{A.4}$$

And by applying least-square minimization, the final expression is reached:

$$\widehat{Y} = \left(\boldsymbol{A}^T \boldsymbol{A} \right)^{-1} \boldsymbol{A}^T \Omega \tag{A.5}$$

where $\boldsymbol{A} = A_{ij} = \Psi_j(x^{(i)})$ for $\{i = 1, \ldots, M; j = 0, \ldots, Z-1\}$ is the so-called experimental matrix and Ω is the vector of true responses for the sample points. A prediction for any $\boldsymbol{x}$ outside the training sample, is carried out by applying the inferred coefficients $\widehat{Y}$ and the polynomials $\Psi_{\alpha}(\boldsymbol{x})$ to Eq. (13).

References

[1] A. Shaw, S. Sriramula, P.D. Gosling, M.K. Chryssanthopoulos, A critical reliability evaluation of fibre reinforced composite materials based on probabilistic micro and macro-mechanical analysis, Compos. B Eng. 41 (6) (2010) 446–453.

[2] S.L. Omairey, P.D. Dunning, S. Sriramula, Influence of micro-scale uncertainties on the reliability of fibre-matrix composites, Compos. Struct. 203 (2018) 204–216.

[3] N. Carrere, Y. Rollet, F.H. Leroy, J.F. Maire, Efficient structural computations with parameters uncertainty for composite applications, Compos. Sci. Technol. 69 (9) (2009) 1328–1333.

[4] J. Zhang, M. Shields, S. TerMaath, Probabilistic Modeling and Prediction of Out-Of-Plane Unidirectional Composite Lamina Properties, Mechanics of Advanced Materials and Structures, 2020, pp. 1–17.

[5] C. Chen, D. Duhamel, C. Soize, Probabilistic approach for model and data uncertainties and its experimental identification in structural dynamics: case of composite sandwich panels, J. Sound Vib. 294 (1) (2006) 64–81.

[6] H.K. Jeong, R.A. Shenoi, Probabilistic strength analysis of rectangular FRP plates using Monte Carlo simulation, Comput. Struct. 76 (1) (2000) 219–235.
[7] K.M. Hamdia, M. Silani, X. Zhuang, P. He, T. Rabczuk, Stochastic analysis of the fracture toughness of polymeric nanoparticle composites using polynomial chaos expansions, Int. J. Fract. 206 (2) (2017) 215–227.
[8] P. Feraboli, T. Cleveland, P. Stickler, J. Halpin, Stochastic laminate analogy for simulating the variability in modulus of discontinuous composite materials, Compos. Appl. Sci. Manuf. 41 (4) (2010) 557–570.
[9] B. Kriegesmann, E.L. Jansen, R. Rolfes, Semi-analytic probabilistic analysis of axially compressed stiffened composite panels, Compos. Struct. 94 (2) (2012) 654–663.
[10] S. Naskar, T. Mukhopadhyay, S. Sriramula, S. Adhikari, Stochastic natural frequency analysis of damaged thin-walled laminated composite beams with uncertainty in micromechanical properties, Compos. Struct. 160 (2017) 312–334.
[11] G. Balokas, S. Czichon, R. Rolfes, Neural network assisted multiscale analysis for the elastic properties prediction of 3D braided composites under uncertainty, Compos. Struct. 183 (2018) 550–562.
[12] B. Kriegesmann, R. Rolfes, C. Hühne, A. Kling, Fast probabilistic design procedure for axially compressed composite cylinders, Compos. Struct. 93 (12) (2011) 3140–3149.
[13] L. Cappelli, G. Balokas, M. Montemurro, F. Dau, L. Guillaumat, Multi-scale identification of the elastic properties variability for composite materials through a hybrid optimisation strategy, Compos. B Eng. 176 (2019), 107193.
[14] L. Mehrez, A. Doostan, D. Moens, D. Vandepitte, Stochastic identification of composite material properties from limited experimental databases, Part II: uncertainty modelling, Mech. Syst. Signal Process. 27 (2012) 484–498.
[15] A. Vanaerschot, B.N. Cox, S.V. Lomov, D. Vandepitte, Experimentally validated stochastic geometry description for textile composite reinforcements, Compos. Sci. Technol. 122 (2016) 122–129.
[16] G. Balokas, B. Kriegesmann, S. Czichon, R. Rolfes, Stochastic modeling techniques for textile yarn distortion and waviness with 1D random fields, Compos. Appl. Sci. Manuf. 127 (2019), 105639.
[17] C.C. António, L.N. Hoffbauer, An approach for reliability-based robust design optimisation of angle-ply composites, Compos. Struct. 90 (1) (2009) 53–59.
[18] M. Kalantari, C. Dong, I.J. Davies, Multi-objective robust optimisation of unidirectional carbon/glass fibre reinforced hybrid composites under flexural loading, Compos. Struct. 138 (2016) 264–275.
[19] S. Sriramula, M.K. Chryssanthopoulos, Quantification of uncertainty modelling in stochastic analysis of FRP composites, Compos. Appl. Sci. Manuf. 40 (11) (2009) 1673–1684.
[20] P. Sasikumar, A. Venketeswaran, R. Suresh, S. Gupta, A data driven polynomial chaos based approach for stochastic analysis of CFRP laminated composite plates, Compos. Struct. 125 (2015) 212–227.
[21] Q. Yang, C. Xu, G. Cheng, S. Meng, W. Xie, Uncertainty quantification method for mechanical behavior of C/SiC composite and its experimental validation, Compos. Struct. 230 (2019), 111516.
[22] C. Gogu, W. Yin, R. Haftka, P. Ifju, J. Molimard, R. Le Riche, A. Vautrin, Bayesian identification of elastic constants in multi-directional laminate from moiré interferometry displacement fields, Exp. Mech. 53 (4) (2013) 635–648.
[23] K. Sepahvand, S. Marburg, Identification of composite uncertain material parameters from experimental modal data, Probabilist. Eng. Mech. 37 (2014) 148–153.
[24] T. He, L. Liu, A. Makeev, Uncertainty analysis in composite material properties characterization using digital image correlation and finite element model updating, Compos. Struct. 184 (2018) 337–351.
[25] S. Sakata, F. Ashida, Stochastic multiscale stress analysis via identification of microscopic randomness, IOP Conf. Ser. Mater. Sci. Eng. 10 (2010), 012203.
[26] L. Wu, L. Adam, L. Noels, A micromechanics-based inverse study for stochastic order reduction of elastic UD fiber reinforced composite analyses, Int. J. Numer. Methods Eng. 115 (2018) 1430–1456.
[27] N. Hu, J. Fish, C. McAuliffe, An adaptive stochastic inverse solver for multiscale characterization of composite materials, Int. J. Numer. Methods Eng. 109 (2017) 1679–1700.
[28] G. Mustafa, A. Suleman, C. Crawford, Probabilistic first ply failure prediction of composite laminates using a multi-scale M-SaF and Bayesian inference approach, J. Compos. Mater. 52 (2) (2018) 169–195.
[29] C. Lüders, Nonlinear-elastic orthotropic material modeling of an epoxy-based polymer for predicting the material behavior of transversely loaded fiber-reinforced composites, Journal of Composites Science 4 (2) (2020) 46.
[30] C. Miehe, A. Koch, Computational micro-to-macro transitions of discretized microstructures undergoing small strains, Arch. Appl. Mech. 72 (4–5) (2002) 300–317.
[31] B. Fiedler, M. Hojo, S. Ochiai, K. Schulte, M. Ochi, Finite-element modeling of initial matrix failure in CFRP under static transverse tensile load, Compos. Sci. Technol. 61 (1) (2001) 95–105.
[32] G. Ernst, M. Vogler, C. Hühne, R. Rolfes, Multiscale progressive failure analysis of textile composites, Compos. Sci. Technol. 70 (1) (2010) 61–72.
[33] T. Vaughan, C. McCarthy, Micromechanical modelling of the transverse damage behaviour in fibre reinforced composites, Compos. Sci. Technol. 71 (3) (2011) 388–396.
[34] L. Yang, Y. Yan, Y. Liu, Z. Ran, Microscopic failure mechanisms of fiber-reinforced polymer composites under transverse tension and compression, Compos. Sci. Technol. 72 (15) (2012) 1818–1825.
[35] ABAQUS, Documentation, Dassault Systèmes Simulia Corp, 2014. Providence RI.
[36] R.M. Christensen, A comprehensive theory of yielding and failure for isotropic materials, J. Eng. Mater. Technol. 129 (2) (2007) 173–181.
[37] L.E. Govaert, H.J. Schellens, H.J.M. Thomassen, R.J.M. Smit, L. Terzoli, T. Peijs, A micromechanical approach to time-dependent failure in off-axis loaded polymer composites, Compos. Appl. Sci. Manuf. 32 (12) (2001) 1697–1711.
[38] M.-f. Ren, X.-w. Zhang, C. Huang, B. Wang, T. Li, An integrated macro/micro-scale approach for in situ evaluation of matrix cracking in the polymer matrix of cryogenic composite tanks, Compos. Struct. 216 (2019) 201–212.
[39] D. Xiu, G.E. Karniadakis, The wiener-askey polynomial chaos for stochastic differential equations, SIAM J. Sci. Comput. 24 (2) (2002) 619–644.
[40] A. Saltelli, P. Annoni, I. Azzini, F. Campolongo, M. Ratto, S. Tarantola, Variance based sensitivity analysis of model output. Design and estimator for the total sensitivity index, Comput. Phys. Commun. 181 (2) (2010) 259–270.
[41] B. Sudret, Global sensitivity analysis using polynomial chaos expansions, Reliab. Eng. Syst. Saf. 93 (7) (2008) 964–979.
[42] Y.M. Marzouk, H.N. Najm, L.A. Rahn, Stochastic spectral methods for efficient Bayesian solution of inverse problems, J. Comput. Phys. 224 (2) (2007) 560–586.
[43] W.K. Hastings, Monte Carlo sampling methods using Markov chains and their applications, Biometrika 57 (1) (1970) 97–109.
[44] W.R. Gilks, S. Richardson, D. Spiegelhalter, Markov Chain Monte Carlo in Practice, Chapman and Hall/CRC, 1995.
[45] J.L. Beck, S.-K. Au, Bayesian updating of structural models and reliability using Markov chain Monte Carlo simulation, J. Eng. Mech. 128 (4) (2002) 380–391.
[46] R. Jin, W. Chen, A. Sudjianto, An efficient algorithm for constructing optimal design of computer experiments, J. Stat. Plann. Inference 134 (1) (2005) 268–287.
[47] G. Blatman, B. Sudret, Adaptive sparse polynomial chaos expansion based on least angle regression, J. Comput. Phys. 230 (6) (2011) 2345–2367.

Chapter 6

Validation of FE Modeling at Mesoscale level and CT Data Integration

This chapter consists of two subsections and provides experimental validation for some of the numerical models and methodologies presented in the previous chapters. In the first subsection, the mesoscale FE modeling (middle part of Fig.1.5) is validated against experimental data from the literature in terms of stiffness and strength prediction. The comparison is performed based on a triaxially braided composite material under uniaxial tension.

The second part of this chapter verifies the feasibility of the methodology proposed in Chapter 3 for the stochastic characterization of distorted yarns. The methodology is applied on CT-scan data of a carbon-fiber braided tubular specimen through the following steps: a) a statistical sample of distortions is initially extracted via image processing, b) the sample measurements are used for the generation of a random distortion input with the same statistical properties, and c) the realistic distortion uncertainty is propagated through the developed probabilistic framework to the effective stiffness response.

6.1 Validation of mesoscale modeling against experimental data

The modeling approach for the mesoscale braided structure is based on the synergy of TexGen and Abaqus software, as described in detail in Chapters 2, 3 and 4. The stiffness accuracy has been verified in Chapter 2 for both the longitudinal and transverse direction, using literature test data for three different braid angle values. The mesoscale strength prediction accuracy of the framework of this thesis (Fig.1.5) and, consequently, the integrated progressive failure algorithm are validated in this section by the test data provided in (Miravete et al., 2006). The same test data, although filtered, were used for validating the modeling approach in (Xu, Jin, and Ha, 2015), as most of the essential information for creating a representative model are included.

The yarn material properties used are shown in Table 6.1 for both stiffness and strength. The elastic matrix properties are reported in Table 6.2. Concerning the specimen, a coupon with a regular triaxial braid (2/2) and a braid angle of 30° was tested according to ASTM D 3039/D 3039M. Even though the yarn volume fraction within the mesoscale RVE is not explicitly stated, it can be extracted as follows: the fiber volume content in the yarns is 80% and the measured fiber volume content of the specimen was equal to 39%, consequently their ratio provides the yarn volume fraction in the RVE as 48.75%. The exact dimensions of the yarn sections are not disclosed.

The results of FE modeling with the current progressive failure framework and the test curve under uniaxial tension are shown in Fig.6.1. Regarding the discretization, 376740 voxels were used to mesh the mesoscopic RVE with an aspect of 0.02mm each. The experimental curve is quite unstable before the failure peak, but the overall stiffness convergence is satisfactory.

TABLE 6.1: UD carbon/epoxy yarn material properties (Miravete et al., 2006)

Parameter	Value	Units
E_1	168.6	GPa
E_2	21.99	GPa
G_{12}	9.035	GPa
G_{23}	8.654	GPa
v_{12}	0.287	-
v_{23}	0.269	-
X_t	2175	MPa
X_c	2511	MPa
Y_t	53.53	MPa
Y_c	53.53	MPa
S_{12}	43.3	MPa

TABLE 6.2: Epoxy Hexcel RTM-6 matrix properties (Miravete et al., 2006)

Parameter	Value	Units
E	2.89	GPa
v	0.3	GPa

The ultimate strength and strain values are close and the slight difference could be partially explained by the general underestimation of the Hashin failure criterion observed by other researchers, e.g. in (Gu and Chen, 2017). Furthermore, the damage accumulation is in agreement with both (Miravete et al., 2006) and (Xu, Jin, and Ha, 2015), as matrix damage is initially observed on the weft yarns, and as soon as fiber damage occurs within the axial tows which carry most of the load, ultimate failure follows (see also Chapter 4 for details).

For the case of micromechanical models predicting the mechanical response of the yarns (left part of Fig.1.5), it is noted that the numerical microscopic RVE configurations have been verified in Chapter 4 against analytical models. In addition, Chapter 5 provides validation with test data for the transverse tensile case.

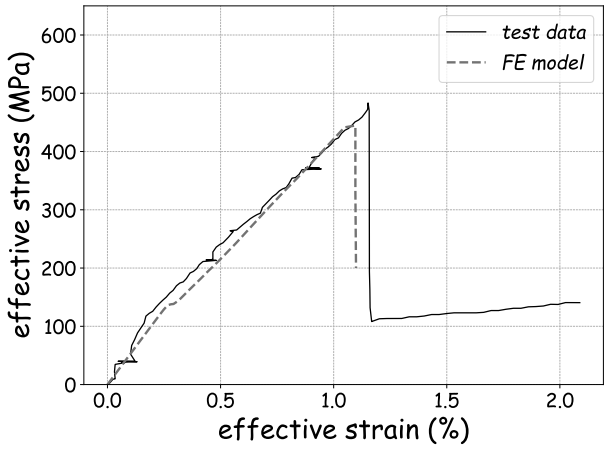

FIGURE 6.1: Comparison between the FE model prediction and experimental data from (Miravete et al., 2006) in terms of effective stress-strain behavior, for a triaxially braided composite with a 30° braid angle under uniaxial tension.

6.2 Geometrical Uncertainty Propagation for a Braided Tube based on CT Data

This section describes an application of the stochastic framework for yarn distortion modeling with random fields presented in Chapter 3 to a tubular braided composite part, verifying the feasibility of the proposed approach in the presence of data. A CT scan of the part was performed at ILK of TU Dresden (Institute of Lightweight Engineering and Polymer Technology, Technical University of Dresden, Germany) in order to extract a statistical sample concerning distorted yarn shapes. The geometrical uncertainty is then propagated to the elastic effective response of the structure via Monte Carlo simulations. As the exact material properties of the braided specimen were not disclosed, the elastic fiber modulus was inversely identified from compression tests performed at KVWEB of TUHH (Institute of Polymers and Composites, Hamburg University of Technology, Germany).

6.2.1 Methodology

Image processing

The first step consists of processing the images extracted from the CT scan. An isometric view of the scanned part is shown in Fig.6.2 in which the yarn pattern is visible. The target is to identify several distorted yarn shapes from the cross-section images, in order to create a sample. Ideally, an automated procedure shall be compiled, in which a threshold is applied to the greyscale images to convert them into binary, and finally perform boundary detection. However, this is not possible due to the low resolution and similar densities of carbon and resin. A manual image processing strategy was instead employed, based on improving the visibility with a spatial filter and adjusting the contrast within Matlab software and, finally, identifying the distorted shapes with the open source software ImageJ.

FIGURE 6.2: Isometric CT view of the scanned specimen.

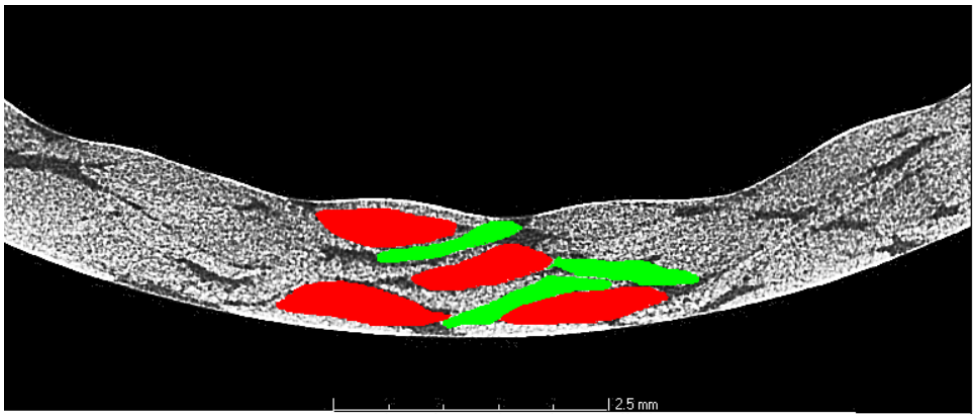

FIGURE 6.3: Processed cross-sectional image of the braided specimen: representation of 3 axial yarns (red color) and 3 binding yarns (green color).

A cross-section illustration is presented in Fig.6.3 where two types of yarns can be identified. The axial yarns (red color) have bigger volumes and were approximated by an elliptical shape in previous chapters, while the binding yarns (green color) are thinner and were modeled with a lenticular cross-section. The distortion due to compaction is evident especially for the binding yarns. In total, two different samples of yarn edges were created, one for axial yarns and one for binding yarns, with 50 sections each. The data were collected from different locations within the scanned specimen. Moreover, the braid angle was measured equal to 38.4° from a front view of the specimen, as shown in Fig.6.4.

Stochastic modeling

After extracting the distorted yarn data, the stochastic modeling approach proposed in Chapter 3 is employed for the geometric uncertainty recreation via random fields. Initially, a geometric shape is fitted to the points of each section of the sample by solving a nonlinear least-squares problem that minimizes the distances of each point from the shape. Ellipses are fitted to the axial yarn data and lenticular shapes to the binding yarn data. An example is shown in Fig.6.5A for an elliptical shape, in which the red points are the distorted yarn data extracted from image processing and the solid gray curve is the fitted ellipse resulted from the optimization problem.

Afterwards, the distortions in terms of radial distances of each point from the fitted shape are calculated. This can be easily done by transforming the data from the Cartesian to the polar coordinate system. As described in Chapter 3, the calculated distances can be sufficiently approximated by a Fourier series, given that the upper limit, and consequently the number of

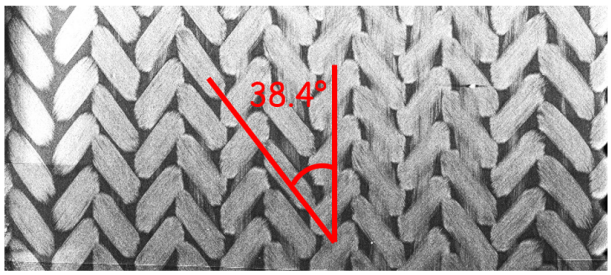

FIGURE 6.4: Processed image of the outer surface of the braided specimen and braiding angle measurement.

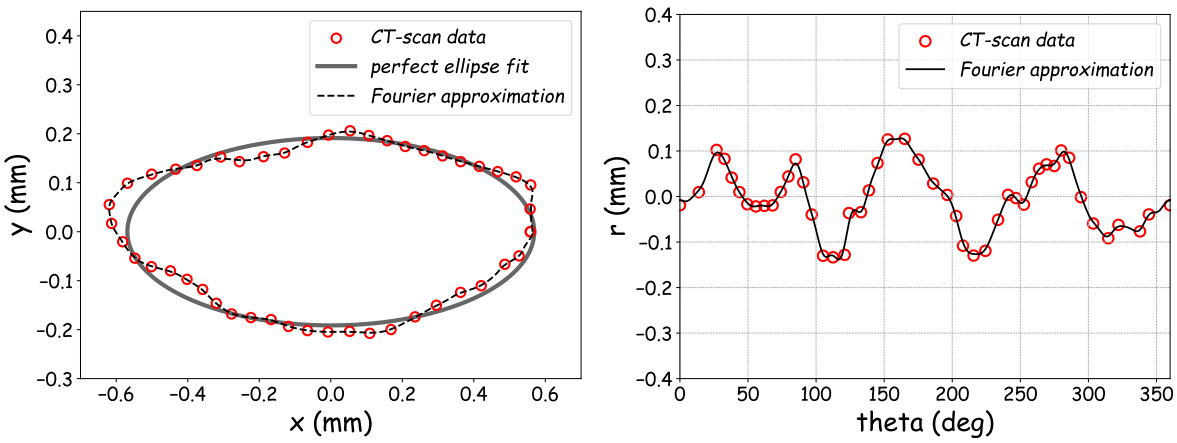

(A) Cartesian coordinates (B) Polar coordinates

FIGURE 6.5: Illustration of ellipse fitting and Fourier approximation to data points of a distorted yarn section: Cartesian coordinate system (A) and polar coordinate system (B).

coefficients, is carefully chosen. The accuracy of such an approximation is illustrated in Fig.6.5B for the polar coordinate system and in Fig.6.5A for the Cartesian system (dashed black line).

The above procedure is followed for all yarns in the sample. In order to generate random input with the same statistical characteristics as the data extracted, a variant of the discrete Karhunen-Loève transformation is used, which decorrelates the random vector of the Fourier coefficients. If $\mathbf{x}$ is the latter vector, $\boldsymbol{\mu}$ its mean vector and $\mathbf{C}$ its covariance matrix, the following formula connects $\mathbf{x}$ with a vector $\mathbf{z}$ of zero mean and unitary standard deviation:

$$\mathbf{x} = \boldsymbol{\mu} + \mathbf{V}\sqrt{\mathbf{D}}\,\mathbf{z} \tag{6.1}$$

where $\mathbf{D}$ is the eigenvalue diagonal matrix and $\mathbf{V}$ is the eigenvector matrix coming from the spectral decomposition of the covariance matrix $\mathbf{C}$, as follows:

$$\mathbf{C} = \mathbf{V}\mathbf{D}\mathbf{V}^{\intercal} \tag{6.2}$$

The reader is referred to (Kriegesmann, 2012) for more details.

Uncertainty propagation

With the realistic random input of the described stochastic modeling, Monte Carlo simulations can be performed based on the FE methods described in the previous chapters and scatter predictions for the macroscopic mechanical properties can be extracted (see also Fig.1.5). The target of this section is to quantify the response variability of the axial stiffness of the braided structure due to the measured geometric uncertainties of the distorted yarns.

Concerning the material properties, carbon fibers have been used during production, however, the exact type and values were not disclosed by the manufacturer. The tube was cut in half and the resulting two specimens were tested under compression towards the stiffness extraction. By calculating the section stiffness and using a trial-and-error strategy, the fiber stiffness in the longitudinal direction was tuned so that the deterministic macroscopic stiffness of the model would approximate the median of the test results. The fiber stiffness outcome was 100GPa indicating a low modulus pitch-based carbon type (Frank, Hermanutz, and Buchmeiser, 2012),

which is reasonable considering the specimen was a bicycle handle part and, hence, low cost materials would be selected.

Another noteworthy element emerging from the section image of Fig.6.3, is the apparent over-braiding (i.e. braiding the same preform more than once to form multiple layers) resulting in three nested layers due to high compaction (i.e. interpenetration of yarns to neighboring layers). The modeling approach of the previous chapters accounts for one layer with periodic boundary conditions also in the out-of-plane direction, so implicitly considers multiple plies. A comparison was performed between the adopted approach and a 3-layer model with a nested configuration from TexGen, with the results being almost identical. Therefore, the single-layer model used throughout the thesis was employed for efficiency.

6.2.2 Results and discussion

In total, 300 Monte Carlo simulations were performed in order to collect the scatter of macroscopic stiffness in the longitudinal direction E_x, accounting for random yarn distortions based on CT measurements. The evolution of the first two statistical moments over the number of simulations is shown in Fig.6.6. The mean evidently converges fast (Fig.6.6A), while the coefficient of variation (COV) requires at least 200 simulations to converge (Fig.6.6B).

The response variability results are plotted in a histogram form in Fig.6.7 together with the two test values extracted from the compression tests. The COV of the sample equals to 3.6% and the test results fall within the range of the predictions. In fact, the test data are located within the $\pm 1\sigma$ region of the sample, within which 68.27% of the sample points are located assuming a symmetric unimodal distribution (e.g. Gaussian). However, a few more test data would provide a clearer perspective on whether this range is representative or one of the values is possibly an outlier.

Moreover, it is known that the volume fraction is the governing parameter for the elastic response of composites. This is confirmed by the scatter plot of Fig.6.8A which correlates the longitudinal stiffness scatter with the yarn-to-matrix volume content of the mesoscale RVEs. However, it is noteworthy that for the case of the axial yarns of the braided specimen fitted with elliptical shapes, the contribution of their thickness and width to the overall area variation, and consequently to the volume fraction, is quite balanced, as shown in Fig.6.8B where the width and thickness of the 50 yarns included in the original sample are plotted against the sectional

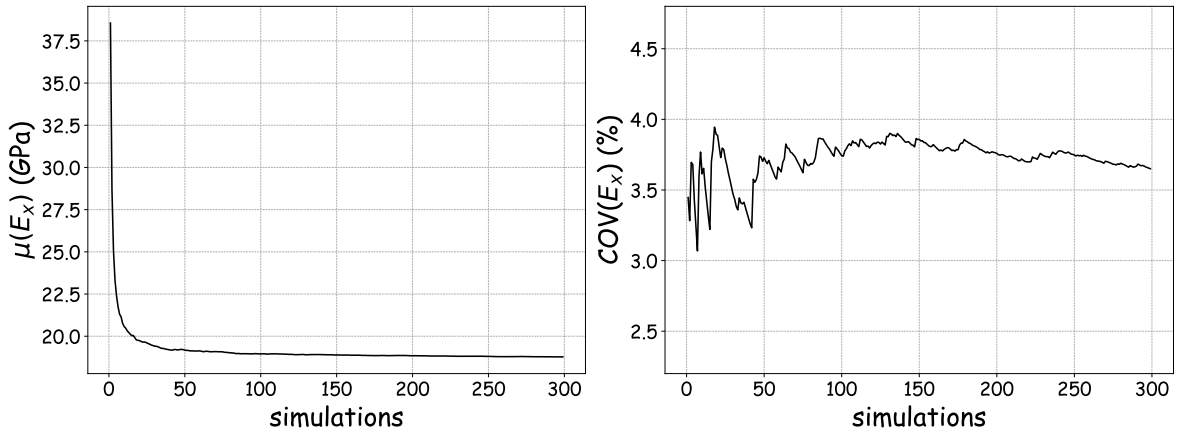

(A) Convergence of mean value (B) Convergence of coefficient of variation

FIGURE 6.6: Convergence of statistics for the longitudinal stiffness scatter: mean (A) and coefficient of variation (B).

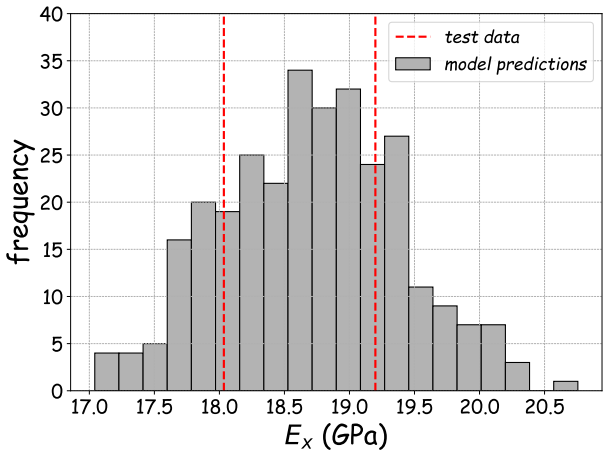

FIGURE 6.7: Histogram of the response sample for the longitudinal stiffness superimposed with the test values of the specimen.

yarn area. The thickness variation is strongly correlated to the area while the width influence is slightly weaker, as opposed to (Bodaghi et al., 2017) where measurements from a woven carbon fabric revealed almost no sensitivity of the width variation. This is probably due to the flattened shape of the woven yarns, as the major axis is more than 10 times larger than the minor axis in the latter study.

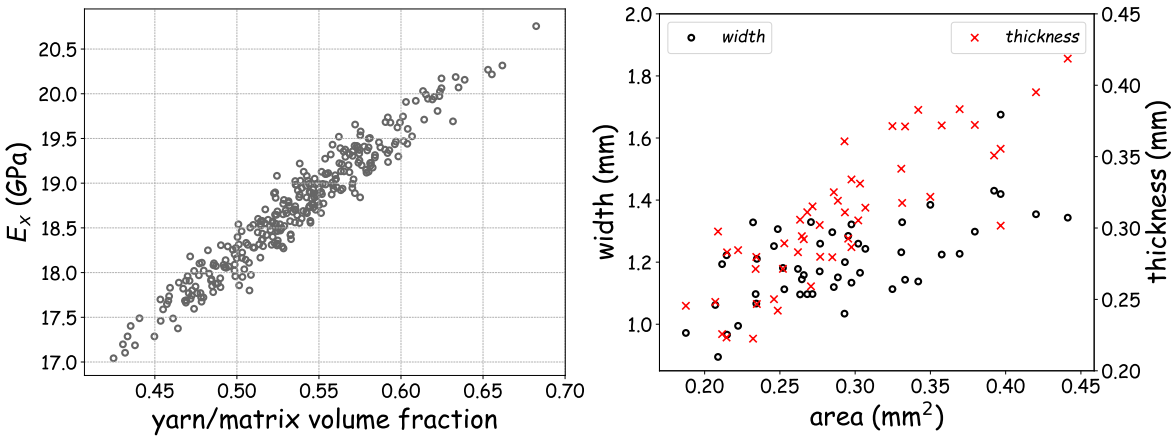

(A) Axial stiffness against measured yarn-to-matrix volume fraction

(B) Width and thickness of the elliptical yarns against the yarn sectional area

FIGURE 6.8: Scatter plots and correlations: stiffness against yarn-to-matrix volume fraction (A) and variations of width and thickness of axial yarns against the overall yarn area (B).

Chapter 7

Summary and Outlook

7.1 Summary

This thesis presents the development of a comprehensive, probabilistic, virtual-testing framework towards the uncertainty quantification of braided composites, based on intelligent and efficient metamodeling techniques. Uncertainties of material and geometric parameters at lower scales can be propagated to the homogenized stiffness and strength response via the proposed multiscale scheme and can be assessed both qualitatively and quantitatively. In order to overcome the computational cost of the probabilistic runs, various surrogate modeling techniques were applied and a novel hybrid metamodel was developed for the emulation of the failure response. All the integrated stochastic algorithms are non-intrusive and purely data-driven, in the sense that no modifications are required within their structure in case of a different FE model. Hence, the extension of the framework towards more load cases or even different textile setups is straightforward.

The application presented in Chapter 2 for the linear elastic case towards the effective stiffness prediction under uncertainty, revealed the fiber volume content of the yarns and the braiding angle variation as the most influential parameters overall for a triaxially braided composite. The geometric randomness introduced to the mesoscale RVE caused slight skewness to some response parameters, while the efficiency of artificial neural networks is indisputable with only 30-40 samples needed for training.

Random geometric imperfections in terms of yard distortion and yarn waviness were modeled with random fields in Chapter 3. The modeling approaches were based on Fourier series and Kriging for a straightforward calibration of the variance and correlation in the presence of measurement data. The uncertainty propagation application for a braided composite showed that the variability levels due to the above uncertainties are non-negligible, especially for the ultimate strength response. Stochastic deviations on the nominal path of the binding yarns caused significant scatter to the transverse elastic properties as well.

The surrogate modeling of the stochastic failure response for braided composites was addressed in Chapter 4. Due to the complex response surface, a novel hybrid metamodeling technique was developed able to make use of low and high fidelity data. The metamodel integrates an artificial neural network in the kernel of the hierarchical Kriging model to boost the training performance. A fast transition from the microscale to the yarn properties was achieved with two artificial neural networks per load case. The step size of the solution algorithm was chosen as the fidelity level to reduce the numerical cost by 7.5 times. The proposed model was employed for the global sensitivity analysis of the failure response and indicated strong interactions between the input properties.

A Bayesian inference scheme for the inverse uncertainty quantification of microscopic composite properties was presented in Chapter 5. The FE multiscale methodology was substituted by a

polynomial chaos surrogate model in order to boost efficiency, but also provide the sensitivity of each random input to the elastic and failure response by processing its coefficients. The test data of a carbon UD composite plate from a published experimental campaign were integrated towards the identification of the first two statistical moments of the most influential parameters. A significant uncertainty reduction was observed compared to typical prior beliefs, while the results are exempt of systematic errors due to the availability of the epistemic uncertainty. The mean properties were also corrected from the chosen values during the initial calibration.

Finally, the numerical multiscale prediction algorithms were validated in Chapter 6 based on test data from the literature. The resulting effective stress-strain response for a triaxially braided composite under uniaxial tension was sufficiently approximated by the FE model adopted in this thesis. Furthermore, the feasibility of the proposed modeling approach of Chapter 3 was verified by calibrating random yarn distortions based on CT-scan measurements. After processing the section images, the Fourier-based methodology was used to tailor random fields around the distorted sections with the same statistical characteristics extracted from the data. The uncertainty was propagated to the effective stiffness of the specimen and revealed a noteworthy response variability.

7.2 Outlook

Even though the effective elastic properties can be statistically characterized for all load cases, stochastic failure prediction has been developed solely for the uniaxial tensile case. Therefore, a direct extension for compressive, shear, transverse or even biaxial load cases can be pursued, considering also the non-intrusive nature of the framework, which allows the straightforward integration of different FE models and cases. This extension can lead to a unified framework for full material characterization under uncertainty, with powerful potential for industrial practice. Nevertheless, several challenges must be addressed for the success of this next step.

Modeling the compressive failure of textile composites is not trivial as complex failure modes occur, including phenomena of stability loss within the yarns. Furthermore, the automated meshing strategy with voxels has been verified for the cases studied in this thesis, but is likely to produce inaccurate results for shear, compressive and biaxial load cases. This is part of a bigger issue regarding conformal meshing algorithms able to automatically re-mesh complex geometries after modifications in every iteration. Lots of research projects have made attempts in this regard, as it is also relevant for topology optimization applications. But a universal solution for all textiles is yet to come, as e.g. meshing braided structures is harder than it is for woven.

Another aspect which can be enhanced is the progressive failure modeling approach based on the elastic-damage model. Different approaches with the potential to capture the majority of load cases can be investigated, e.g. peridynamics (able to predict interaction of damages) or phase-field modeling. A constant consideration, however, should be to avoid extremely expensive algorithms due to the probabilistic runs required for the data generation of the machine learning algorithms. Extensions regarding cohesive modeling within the mesoscale RVEs shall also be pursued.

Having such a unified probabilistic framework available, brings the engineering community one step closer towards the disengagement from the unfavourable safety factors of current industrial practices. As described in Chapter 1, the quantification of uncertainty for the statistical modeling necessary for probabilistic analyses is one of the main barriers for industry. In the short term, testing 10 composite coupons for a specific load case is, of course, more expensive than testing 3 as is the current practice. However, these 10 values could be enough to quantify and model

uncertain parameters that can be used for a full probabilistic approach, leading to higher design allowables for the studied part and, thus, major cost savings in the long term.

As stated earlier in the thesis, machine learning applications to composite materials is an active research topic during the last three years. There is a lot of ground yet to be covered, as it is crucial to surrogate as many response surfaces as possible. Mappings of different nature in order to connect different parameters and responses with mathematical models is often not straightforward, especially for failure and damage responses as displayed in Chapter 4. The emulation of more response surfaces will assist processes like optimization, reliability and sensitivity analysis and will shift engineering science further towards data-driven methods.

An extension related to the latter point concerns the fidelity level choice when employing multi-fidelity strategies. The step size of the solution algorithm used in Chapter 4 was applied in order not to compromise the accuracy due to voxel meshing and geometric uncertainties. The cost reduction was satisfactory but further reductions could be achieved by testing fidelity correlations related to the damage progression algorithms and meshing strategies. Regarding damage progression, simplified approaches like instantaneous stiffness degradation or even first-ply failure could be applied for the low fidelity level and detailed damage models for high fidelity. Similar approaches apply for the mesh, e.g. with coarse voxels for low fidelity and dense conformal meshes for high fidelity.

Another important aspect is also the application of quantified uncertainties to individual parts or components for structural safety assessment. Uncertainty quantification on the material properties and mechanical behavior is valuable, but it has been observed that some responses and macroscale models are not so much affected. Furthermore, the correlation magnitude is the decisive parameter on whether random variables or random fields are appropriate for modeling. Hence, this should be further studied and quantified. Finally, as illustrated in Chapter 3, it is challenging to employ surrogate models when the input is modeled with random fields, so further research in that direction is reasonable.

Bibliography

Alpaydin, E. (2020). *Introduction to Machine Learning*. Ed. by F. Bach. 4th ed. Adaptive Computation and Machine Learning series. Cambridge, MA, USA: MIT Press.

Aranda-Iglesias, D. et al. (2021). "Multiscale modelling of the mechanical response of 3D multiaxial knitted 3D spacer composites". In: *Composite Structures* 257, p. 113139.

Bigaud, D., L. Dréano, and P. Hamelin (2005). "Models of interactions between process, microstructure and mechanical properties of composite materials—a study of the interlock layer-to-layer braiding technique". In: *Composite Structures* 67.1, pp. 99–114.

Bishop, C. (2006). *Pattern Recognition and Machine Learning*. Information Science and Statistics. New York: Springer-Verlag.

Bodaghi, M. et al. (2017). "On the stochastic variations of intra-tow permeability induced by internal geometry variability in a 2/2 twill carbon fabric". In: *Composites Part A: Applied Science and Manufacturing* 101, pp. 444–458.

Bostanabad, R. et al. (2018). "Uncertainty quantification in multiscale simulation of woven fiber composites". In: *Computer Methods in Applied Mechanics and Engineering* 338, pp. 506–532.

Buryachenko, V. A. et al. (2003). "Quantitative description and numerical simulation of random microstructures of composites and their effective elastic moduli". In: *International Journal of Solids and Structures* 40.1, pp. 47–72.

Byun, J.-H. (2000). "The analytical characterization of 2-D braided textile composites". In: *Composites Science and Technology* 60.5, pp. 705–716.

Cai, Y. et al. (2021). "Size-dependency of the transverse-tensile failure behavior for triaxially braided composites". In: *Composites Science and Technology* 206, p. 108672.

Cappelli, L. et al. (2019). "Multi-scale identification of the elastic properties variability for composite materials through a hybrid optimisation strategy". In: *Composites Part B: Engineering* 176, p. 107193.

Carey, J. P. (2016). *Handbook of Advances in Braided Composite Materials: Theory, Production, Testing and Applications*. Amsterdam: Woodhead Publishing.

Chen, N.-Z. and C. Guedes Soares (2008). "Spectral stochastic finite element analysis for laminated composite plates". In: *Computer Methods in Applied Mechanics and Engineering* 197.51, pp. 4830–4839.

Ching Quek, S. et al. (2004). "Compressive response and failure of braided textile composites: Part 1—experiments". In: *International Journal of Non-Linear Mechanics* 39.4, pp. 635–648.

Cichosz, J. et al. (2016). "Failure and damage characterization of (±30°) biaxial braided composites under multiaxial stress states". In: *Composites Part A: Applied Science and Manufacturing* 90, pp. 748–759.

Clément, A., C. Soize, and J. Yvonnet (2013). "Uncertainty quantification in computational stochastic multiscale analysis of nonlinear elastic materials". In: *Computer Methods in Applied Mechanics and Engineering* 254, pp. 61–82.

Constantine, P. G. (2015). *Active Subspaces*. SIAM Spotlights. Society for Industrial and Applied Mathematics.

Dang, H. et al. (2020). "A new analytical method for progressive failure analysis of two-dimensional triaxially braided composites". In: *Composites Science and Technology* 186, p. 107936.

Díaz, J., M. Cid Montoya, and S. Hernández (2016). "Efficient methodologies for reliability-based design optimization of composite panels". en. In: *Advances in Engineering Software* 93, pp. 9–21.

Dey, S., T. Mukhopadhyay, and S. Adhikari (2017). "Metamodel based high-fidelity stochastic analysis of composite laminates: A concise review with critical comparative assessment". In: *Composite Structures* 171, pp. 227–250.

Dey, S. et al. (2016). "Uncertainty Quantification in Natural Frequency of Composite Plates - An Artificial Neural Network Based Approach". In: *Advanced Composites Letters* 25.2.

Dey, S. et al. (2019). "Probabilistic characterisation for dynamics and stability of laminated soft core sandwich plates". In: *Journal of Sandwich Structures & Materials* 21.1, pp. 366–397.

Dixit, A. and H. S. Mali (2013). "Modeling techniques for predicting the mechanical properties of woven-fabric textile composites: a Review". In: *Mechanics of Composite Materials* 49.1, pp. 1–20.

El Said, B. et al. (2016). "Multi-scale modelling of strongly heterogeneous 3D composite structures using spatial Voronoi tessellation". In: *Journal of the Mechanics and Physics of Solids* 88, pp. 50–71.

El Said, B. et al. (2018). "An iterative multiscale modelling approach for nonlinear analysis of 3D composites". In: *International Journal of Solids and Structures* 132-133, pp. 42–58.

Ernst, G. et al. (2010). "Multiscale progressive failure analysis of textile composites". In: *Composites Science and Technology* 70.1, pp. 61–72.

Fang, G. and J. Liang (2011). "A review of numerical modeling of three-dimensional braided textile composites". In: *Journal of Composite Materials* 45.23, pp. 2415–2436.

Fang, G. et al. (2016). "Smoothing artificial stress concentrations in voxel-based models of textile composites". In: *Composites Part A: Applied Science and Manufacturing* 80, pp. 270–284.

Feyel, F. (1999). "Multiscale FE2 elastoviscoplastic analysis of composite structures". In: *Computational Materials Science* 16.1, pp. 344–354.

Feyel, F. and J.-L. Chaboche (2000). "FE2 multiscale approach for modelling the elastoviscoplastic behaviour of long fibre SiC/Ti composite materials". In: *Computer Methods in Applied Mechanics and Engineering* 183.3, pp. 309–330.

Frangopol, D. M. and S. Recek (2003). "Reliability of fiber-reinforced composite laminate plates". In: *Probabilistic Engineering Mechanics* 18.2, pp. 119–137.

Frank, E., F. Hermanutz, and M. R. Buchmeiser (2012). "Carbon Fibers: Precursors, Manufacturing, and Properties". In: *Macromolecular Materials and Engineering* 297.6, pp. 493–501.

Fukuda, H. and T.-W. Chou (1982). "A probabilistic theory of the strength of short-fibre composites with variable fibre length and orientation". In: *Journal of Materials Science* 17.4, pp. 1003–1011.

Gao, X. et al. (2020). "Prediction of mechanical properties on 3D braided composites with void defects". In: *Composites Part B: Engineering* 197, p. 108164.

Ge, J. et al. (2018). "A coupled elastic-plastic damage model for the mechanical behavior of three-dimensional (3D) braided composites". In: *Composites Science and Technology* 157, pp. 86–98.

Ge, L. et al. (2021). "Micro-CT based trans-scale damage analysis of 3D braided composites with pore defects". In: *Composites Science and Technology* 211, p. 108830.

Ghiasi, H. et al. (2010). "Optimum Structural and Manufacturing Design of a Braided Hollow Composite Part". In: *Applied Composite Materials* 17.2, pp. 159–173.

Gogu, C. et al. (2013). "Bayesian Identification of Elastic Constants in Multi-Directional Laminate from Moiré Interferometry Displacement Fields". In: *Experimental Mechanics* 53.4, pp. 635–648.

Grigoriu, M. D. (2002). *Stochastic Calculus: Applications in Science and Engineering*. Birkhäuser Basel, Springer.

Gu, J. and P. Chen (2017). "Some modifications of Hashin's failure criteria for unidirectional composite materials". In: *Composite Structures* 182, pp. 143–152.

Guedes Soares, C. (1997). "Reliability of components in composite materials". In: *Reliability Engineering & System Safety* 55.2, pp. 171–177.

Guo-dong, F., L. Jun, and W. Bao-lai (2009). "Progressive damage and nonlinear analysis of 3D four-directional braided composites under unidirectional tension". In: *Composite Structures* 89.1, pp. 126–133.

Guo-dong, F. et al. (2009). "The effect of yarn distortion on the mechanical properties of 3D four-directional braided composites". In: *Composites Part A: Applied Science and Manufacturing* 40.4, pp. 343–350.

Gusev, A. A., P. J. Hine, and I. M. Ward (2000). "Fiber packing and elastic properties of a transversely random unidirectional glass/epoxy composite". In: *Composites Science and Technology* 60.4, pp. 535–541.

Guyader, G., A. Gabor, and P. Hamelin (2013). "Analysis of 2D and 3D circular braiding processes: Modeling the interaction between the process parameters and the pre-form architecture". In: *Mechanism and Machine Theory* 69, pp. 90–104.

Hallal, A., R. Younes, and F. Fardoun (2013). "Review and comparative study of analytical modeling for the elastic properties of textile composites". In: *Composites Part B: Engineering* 50, pp. 22–31.

Hans, T. et al. (2015). "Finite element simulation of the braiding process for arbitrary mandrel shapes". en. In: *Composites Part A: Applied Science and Manufacturing* 77, pp. 124–132.

Hasani, H. et al. (2017). "Biaxial weft-knitted fabrics as composite reinforcements: A review". In: *Journal of Industrial Textiles* 46.7, pp. 1439–1473.

He, C. et al. (2019). "A multiscale elasto-plastic damage model for the nonlinear behavior of 3D braided composites". In: *Composites Science and Technology* 171, pp. 21–33.

He, C. et al. (2020). "A hierarchical multiscale model for the elastic-plastic damage behavior of 3D braided composites at high temperature". In: *Composites Science and Technology* 196, p. 108230.

He, C. et al. (2021). "From microscale to mesoscale: The non-linear behavior prediction of 3D braided composites based on the SCA2 concurrent multiscale simulation". In: *Composites Science and Technology* 213, p. 108947.

He, T., L. Liu, and A. Makeev (2018). "Uncertainty analysis in composite material properties characterization using digital image correlation and finite element model updating". In: *Composite Structures* 184, pp. 337–351.

Henkes, A., I. Caylak, and R. Mahnken (2021). "A deep learning driven pseudospectral PCE based FFT homogenization algorithm for complex microstructures". In: *Computer Methods in Applied Mechanics and Engineering* 385, p. 114070.

Hong, Y. et al. (2019). "Predicting the Elastic Properties of 3D N-Directional Braided Composites Via a Theoretical Method". In: *Mechanics of Composite Materials* 55.1, pp. 95–106.

Hu, N., J. Fish, and C. McAuliffe (2017). "An adaptive stochastic inverse solver for multiscale characterization of composite materials". In: *International Journal for Numerical Methods in Engineering* 109.12, pp. 1679–1700.

Huang, T. et al. (2021a). "Stochastic nonlinear analysis of unidirectional fiber composites using image-based microstructural uncertainty quantification". In: *Composite Structures* 260, p. 113470.

Huang, W. et al. (2021b). "Data-driven multiscale simulation of FRP based on material twins". In: *Composite Structures* 256, p. 113013.

Huang, Z. (2000). "The mechanical properties of composites reinforced with woven and braided fabrics". In: *Composites Science and Technology* 60.4, pp. 479–498.

Imbert, M., H. Finckh, and G. T. Gresser (2021). "Mechanical analytical modelling of non-axisymmetric overbraiding". In: *Journal of Composite Materials* 55.10, pp. 1385–1404.

Jeong, H. K. and R. A. Shenoi (2000). "Probabilistic strength analysis of rectangular FRP plates using Monte Carlo simulation". In: *Computers & Structures* 76.1, pp. 219–235.

Jiang, D. et al. (2015). "Prediction of uncertain elastic parameters of a braided composite". In: *Composite Structures* 126, pp. 123–131.

Jiang, P., Q. Zhou, and X. Shao (2020). *Surrogate Model-Based Engineering Design and Optimization*. Springer Tracts in Mechanical Engineering. Springer Singapore.

Jolliffe, I. T. (2002). *Principal Component Analysis*. 2nd ed. Springer Series in Statistics. New York: Springer-Verlag.

Kamiński, M. and M. Kleiber (2000). "Perturbation based stochastic finite element method for homogenization of two-phase elastic composites". In: *Computers & Structures* 78.6, pp. 811–826.

Kanouté, P. et al. (2009). "Multiscale Methods for Composites: A Review". In: *Archives of Computational Methods in Engineering* 16.1, pp. 31–75.

Kessels, J. F. A. and R. Akkerman (2002). "Prediction of the yarn trajectories on complex braided preforms". In: *Composites Part A: Applied Science and Manufacturing* 33.8, pp. 1073–1081.

Kim, H. J. and C. C. Swan (2003). "Voxel-based meshing and unit-cell analysis of textile composites". In: *International Journal for Numerical Methods in Engineering* 56.7, pp. 977–1006.

Kim, S. (2017). "Simulation of maypole braiding process with multi-layer interlocking yarns". In: *The Journal of The Textile Institute* 108.4, pp. 579–585.

Ko, F. K. (1987). *Engineered materials handbook. Vol. 1: Composites*. ASM International.

Koley, S., P. M. Mohite, and C. S. Upadhyay (2019). "A micromechanical study and uncertainty quantification for effective properties of unidirectional fibre reinforced composites". In: *Composite Structures* 225, p. 111141.

Kolmogorov, A. N. (1950). *Foundations of the theory of probability*. Chelsea Pub. Co.

Kosztowny, C. J. R. and A. M. Waas (2021). "Postbuckling response of unitized stiffened textile composite panels: Computational modeling". In: *International Journal of Non-Linear Mechanics*, p. 103815.

Kriegesmann, B., E. L. Jansen, and R. Rolfes (2012). "Semi-analytic probabilistic analysis of axially compressed stiffened composite panels". In: *Composite Structures* 94.2, pp. 654–663.

Kriegesmann, B. et al. (2011). "Fast probabilistic design procedure for axially compressed composite cylinders". In: *Composite Structures* 93.12, pp. 3140–3149.

Kriegesmann, Benedikt (2012). "Probabilistic Design of Thin-Walled Fiber Composite Structures". Mitteilungen des Instituts für Statik und Dynamik der Leibniz Universität Hannover 15/2012, ISSN 1862-4650. Hannover, Germany: Gottfried Wilhelm Leibniz Universität Hannover.

Kästner, M., G. Haasemann, and V. Ulbricht (2011). "Multiscale XFEM-modelling and simulation of the inelastic material behaviour of textile-reinforced polymers". In: *International Journal for Numerical Methods in Engineering* 86.4-5, pp. 477–498.

Kyosev, Y. (2014). *Braiding Technology for Textiles: Principles, Design and Processes*. Waltham, MA: Woodhead Publishing.

Larsen, R. J. and M. L. Marx (2010). *An Introduction to Mathematical Statistics and Its Applications*. 5th edition. Boston: Pearson Education Limited.

Li, D.-S. et al. (2011). "High strain rate behavior and failure mechanism of three-dimensional five-directional carbon/phenolic braided composites under transverse compression". In: *Composites Part B: Engineering* 42.2, pp. 309–317.

Li, D.-S. et al. (2014). "Experimental investigation on the compression properties and failure mechanism of 3D braided composites at room and liquid nitrogen temperature". In: *Composites Part B: Engineering* 56, pp. 647–659.

Li, G. et al. (2018). "Stochastic Elastic Properties of Composite Matrix Material with Random Voids Based on Radial Basis Function Network". In: *International Journal of Computational Methods* 15.01, p. 1750082.

Li, L. Y., P. H. Wen, and M. H. Aliabadi (2011). "Meshfree modeling and homogenization of 3D orthogonal woven composites". In: *Composites Science and Technology* 71.15, pp. 1777–1788.

Li, Z.-M. (2014). "Thermal postbuckling behavior of 3D braided beams with initial geometric imperfection under different type temperature distributions". In: *Composite Structures* 108, pp. 924–936.

Li, Z.-M. and H.-S. Shen (2009). "Postbuckling analysis of 3D braided composite cylindrical shells under torsion in thermal environments". In: *Composite Structures* 87.3, pp. 242–256.

Lin, H., L. P. Brown, and A. C. Long (2011). "Modelling and Simulating Textile Structures Using TexGen". In: *Advanced Materials Research* 331, pp. 44–47.

Lin, H. et al. (2012). "Automated geometric modelling of textile structures". In: *Textile Research Journal* 82.16. Publisher: SAGE Publications Ltd STM, pp. 1689–1702.

Liu, X. et al. (2017). "Two-step homogenization of textile composites using mechanics of structure genome". In: *Composite Structures* 171, pp. 252–262.

Liu, X. et al. (2019). "Initial failure strength prediction of woven composites using a new yarn failure criterion constructed by deep learning". In: *Composite Structures* 230, p. 111505.

Liu, X. et al. (2021). "A review of artificial neural networks in the constitutive modeling of composite materials". In: *Composites Part B: Engineering* 224, p. 109152.

Liu, Z. and C. T. Wu (2019). "Exploring the 3D architectures of deep material network in data-driven multiscale mechanics". In: *Journal of the Mechanics and Physics of Solids* 127, pp. 20–46.

Lomov, S. V. (2011). *Non-Crimp Fabric Composites: Manufacturing, Properties and Applications*. New edition. Oxford: Woodhead Publishing.

Lomov, S. V. et al. (2007). "Meso-FE modelling of textile composites: Road map, data flow and algorithms". In: *Composites Science and Technology* 67.9, pp. 1870–1891.

Lomov, S. V. et al. (2011). "Modeling three-dimensional fabrics and three-dimensional reinforced composites: challenges and solutions". In: *Textile Research Journal* 81.1, pp. 28–41.

Ma, X., Y. Dong, and Y. Wang (2016). "Matrix Algorithm for Braiding Simulation of Three-Dimensional Four-Step Braided Composites". In: *Mathematical Problems in Engineering* 2016, p. 9280865.

Madke, R. R. and R. Chowdhury (2019). "A multiscale continuum model for inelastic behavior of woven composite". In: *Composite Structures* 226, p. 111267.

Mardanshahi, A. et al. (2020). "Detection and classification of matrix cracking in laminated composites using guided wave propagation and artificial neural networks". In: *Composite Structures* 246, p. 112403.

Matveev, M. et al. (2018). "Uncertainty in geometry of fibre preforms manufactured with Automated Dry Fibre Placement and its effects on permeability". In: *Journal of Composite Materials* 52.16, pp. 2255–2269.

McGregor, C. J. et al. (2007). "Simulation of progressive damage development in braided composite tubes under axial compression". In: *Composites Part A: Applied Science and Manufacturing* 38.11, pp. 2247–2259.

McGregor, C. J. et al. (2008). "A Constitutive Model for Progressive Compressive Failure of Composites". In: *Journal of Composite Materials* 42.25, pp. 2687–2716.

Mei, H. et al. (2020). "Process modelling of 3D hexagonal braids". In: *Composite Structures* 252, p. 112679.

Melro, A. R., P. P. Camanho, and S. T. Pinho (2008). "Generation of random distribution of fibres in long-fibre reinforced composites". In: *Composites Science and Technology* 68.9, pp. 2092–2102.

Mendoza, A. et al. (2019). "Measuring yarn deformations induced by the manufacturing process of woven composites". In: *Composites Part A: Applied Science and Manufacturing* 120, pp. 127–139.

Miravete, A. et al. (2006). "3D mesomechanical analysis of three-axial braided composite materials". In: *Composites Science and Technology* 66.15, pp. 2954–2964.

Mises, R. von (1981). *Probability, Statistics, and Truth*. Courier Corporation.

Montesano, J. et al. (2013). "Fatigue damage characterization and modeling of a triaxially braided polymer matrix composite at elevated temperatures". In: *Composite Structures* 101, pp. 129–137.

Mouritz, A. P. et al. (1999). "Review of applications for advanced three-dimensional fibre textile composites". In: *Composites Part A: Applied Science and Manufacturing* 30.12, pp. 1445–1461.

Mustafa, G., A. Suleman, and C. Crawford (2018). "Probabilistic first ply failure prediction of composite laminates using a multi-scale M-SaF and Bayesian inference approach". In: *Journal of Composite Materials* 52.2, pp. 169–195.

Na, W.-J. et al. (2014). "Prediction of the braid pattern on arbitrary-shaped mandrels using the minimum path condition". In: *Composites Science and Technology* 91, pp. 30–37.

Naskar, S., T. Mukhopadhyay, and S. Sriramula (2019). "Spatially varying fuzzy multi-scale uncertainty propagation in unidirectional fibre reinforced composites". In: *Composite Structures* 209, pp. 940–967.

Nasution, M. R. E. et al. (2014). "A novel asymptotic expansion homogenization analysis for 3-D composite with relieved periodicity in the thickness direction". In: *Composites Science and Technology* 97, pp. 63–73.

Nezamabadi, S. et al. (2015). "Compressive failure of composites: A computational homogenization approach". In: *Composite Structures* 127, pp. 60–68.

Ni, C. and G. Wei (2016). "Geometric Model and Elastic Constant Prediction of 3D Four-Step Braided Composites Based on the Cubic Spline Curve". In: *International Journal of Applied Mechanics* 08.02, p. 1650019.

Nobeen, N. S. et al. (2016). "Constituent materials micro-damage modeling in predicting progressive failure of braided fiber composites". In: *Composite Structures* 145, pp. 194–202.

Olivier, A., M. D. Shields, and L. Graham-Brady (2021). "Bayesian neural networks for uncertainty quantification in data-driven materials modeling". In: *Computer Methods in Applied Mechanics and Engineering* 386, p. 114079.

Omairey, S. L., P. D. Dunning, and S. Sriramula (2018). "Influence of micro-scale uncertainties on the reliability of fibre-matrix composites". In: *Composite Structures* 203, pp. 204–216.

Onkar, A. K., C. S. Upadhyay, and D. Yadav (2007). "Probabilistic failure of laminated composite plates using the stochastic finite element method". In: *Composite Structures* 77.1, pp. 79–91.

Patel, D. K., A. M. Waas, and C.-F. Yen (2018). "Direct numerical simulation of 3D woven textile composites subjected to tensile loading: An experimentally validated multiscale approach". In: *Composites Part B: Engineering* 152, pp. 102–115.

Pepper, N., F. Montomoli, and S. Sharma (2021). "Identification of missing input distributions with an inverse multi-modal Polynomial Chaos approach based on scarce data". In: *Probabilistic Engineering Mechanics* 65, p. 103138.

Petrolo, M. and E. Carrera (2020). "On the use of neural networks to evaluate performances of shell models for composites". In: *Advanced Modeling and Simulation in Engineering Sciences* 7.1, p. 31.

– (2021). "Selection of element-wise shell kinematics using neural networks". In: *Computers & Structures* 244, p. 106425.

Phoenix, S. L. (1978). "Stochastic strength and fatigue of fiber bundles". In: *International Journal of Fracture* 14.3, pp. 327–344.

Potluri, P. et al. (2003). "Geometrical modelling and control of a triaxial braiding machine for producing 3D preforms". In: *Composites Part A: Applied Science and Manufacturing*. ICMAC 2001 - International Conference for Manufacturing of Advanced Composites 34.6, pp. 481–492.

Qi, Z. et al. (2019). "Prediction of mechanical properties of carbon fiber based on cross-scale FEM and machine learning". In: *Composite Structures* 212, pp. 199–206.

Rana, S. and R. Fangueiro, eds. (2015). *Braided Structures and Composites: Production, Properties, Mechanics, and Technical Applications*. CRC Press.

Rauter, N. (2021). "A computational modeling approach based on random fields for short fiber-reinforced composites with experimental verification by nanoindentation and tensile tests". In: *Computational Mechanics* 67.2, pp. 699–722.

Ravenhorst, J. H. van and R. Akkerman (2014). "Circular braiding take-up speed generation using inverse kinematics". In: *Composites Part A: Applied Science and Manufacturing* 64, pp. 147–158.

– (2016). "A yarn interaction model for circular braiding". In: *Composites Part A: Applied Science and Manufacturing* 81, pp. 254–263.

Rice, J. A. (2007). *Mathematical Statistics and Data Analysis*. Cengage Learning.

Rouf, K., X. Liu, and W. Yu (2018). "Multiscale structural analysis of textile composites using mechanics of structure genome". In: *International Journal of Solids and Structures* 136-137, pp. 89–102.

Roy, S. S., P. Potluri, and C. Soutis (2017). "Tensile Response of Hoop Reinforced Multiaxially Braided Thin Wall Composite Tubes". In: *Applied Composite Materials* 24.2, pp. 397–416.

Sakata, S. and F. Ashida (2010). "Stochastic multiscale stress analysis via identification of microscopic randomness". In: *IOP Conference Series: Materials Science and Engineering* 10, p. 012203.

Sakata, S. et al. (2008). "Three-dimensional stochastic analysis using a perturbation-based homogenization method for elastic properties of composite material considering microscopic uncertainty". In: *International Journal of Solids and Structures* 45.3, pp. 894–907.

Sasikumar, P., R. Suresh, and S. Gupta (2015). "Stochastic model order reduction in uncertainty quantification of composite structures". In: *Composite Structures* 128, pp. 21–34.

Sasikumar, P. et al. (2015). "Experimental characterisation of random field models for CFRP composite panels". In: *Composite Structures* 120, pp. 451–471.

Savvas, D., I. Papaioannou, and G. Stefanou (2020). "Bayesian identification and model comparison for random property fields derived from material microstructure". In: *Computer Methods in Applied Mechanics and Engineering* 365, p. 113026.

Schatz, M. E., A. Hermanutz, and H. J. Baier (2017). "Multi-criteria optimization of an aircraft propeller considering manufacturing". In: *Structural and Multidisciplinary Optimization* 55.3, pp. 899–911.

Sepahvand, K. and S. Marburg (2014). "Identification of composite uncertain material parameters from experimental modal data". In: *Probabilistic Engineering Mechanics* 37, pp. 148–153.

Shaw, A. et al. (2010). "A critical reliability evaluation of fibre reinforced composite materials based on probabilistic micro and macro-mechanical analysis". In: *Composites Part B: Engineering* 41.6, pp. 446–453.

Shokrieh, M. M. and M. S. Mazloomi (2012). "A new analytical model for calculation of stiffness of three-dimensional four-directional braided composites". In: *Composite Structures* 94.3, pp. 1005–1015.

Spahn, J. et al. (2014). "A multiscale approach for modeling progressive damage of composite materials using fast Fourier transforms". In: *Computer Methods in Applied Mechanics and Engineering* 268, pp. 871–883.

Sriramula, S. and M. K. Chryssanthopoulos (2009). "Quantification of uncertainty modelling in stochastic analysis of FRP composites". In: *Composites Part A: Applied Science and Manufacturing* 40.11, pp. 1673–1684.

Stefanou, G., D. Savvas, and M. Papadrakakis (2015). "Stochastic finite element analysis of composite structures based on material microstructure". In: *Composite Structures* 132, pp. 384–392.

– (2017). "Stochastic finite element analysis of composite structures based on mesoscale random fields of material properties". In: *Computer Methods in Applied Mechanics and Engineering* 326, pp. 319–337.

Sturm, R. and F. Heieck (2015). "Energy absorption capacity of braided frames under bending loads". en. In: *Composite Structures* 134, pp. 957–965.

Sun, B., F. Liu, and B. Gu (2005). "Influence of the strain rate on the uniaxial tensile behavior of 4-step 3D braided composites". In: *Composites Part A: Applied Science and Manufacturing* 36.11, pp. 1477–1485.

Sun, X. and C. Sun (2004). "Mechanical properties of three-dimensional braided composites". In: *Composite Structures* 65.3, pp. 485–492.

Swery, E. E. et al. (2017). "Complete simulation process chain for the manufacturing of braided composite parts". In: *Composites Part A: Applied Science and Manufacturing* 102, pp. 378–390.

Tan, P., L. Tong, and G. P. Steven (1997). "Modelling for predicting the mechanical properties of textile composites—A review". In: *Composites Part A: Applied Science and Manufacturing* 28.11, pp. 903–922.

Tan, V. B. C., K. Raju, and H. P. Lee (2020). "Direct FE2 for concurrent multilevel modelling of heterogeneous structures". In: *Computer Methods in Applied Mechanics and Engineering* 360, p. 112694.

Tao, W. et al. (2020a). "Uncertainty quantification of mechanical properties for three-dimensional orthogonal woven composites. Part I: Stochastic reinforcement geometry reconstruction". In: *Composite Structures* 235, p. 111763.

– (2020b). "Uncertainty quantification of mechanical properties for three-dimensional orthogonal woven composites. Part II: Multiscale simulation". In: *Composite Structures* 235, p. 111764.

Tate, J. S. and A. D. Kelkar (2008). "Stiffness degradation model for biaxial braided composites under fatigue loading". In: *Composites Part B: Engineering* 39.3, pp. 548–555.

Thapa, M., S. B. Mulani, and R. W. Walters (2019). "Stochastic multi-scale modeling of carbon fiber reinforced composites with polynomial chaos". In: *Composite Structures* 213, pp. 82–97.

Thapa, M. et al. (2021). "Uncertainty quantification and global sensitivity analysis for progressive failure of fiber-reinforced composites". In: *Structural and Multidisciplinary Optimization* 63.1, pp. 245–265.

Tian, S. and W. Yu (2021). "Adaptive sampling assisted surrogate modeling of initial failure envelopes of composite structures". In: *Composite Structures* 269, p. 113985.

Tian, Z. et al. (2016). "Parameterized unit-cell models for stiffness performance analyses of three-dimensional n-directional braided composites". In: *Journal of Reinforced Plastics and Composites* 35.19, pp. 1371–1386.

Tian, Z. et al. (2018). "Progressive damage and failure analysis of three-dimensional braided composites subjected to biaxial tension and compression". In: *Composite Structures* 185, pp. 496–507.

Tikarrouchine, E. et al. (2021). "Non-linear FE2 multiscale simulation of damage, micro and macroscopic strains in polyamide 66-woven composite structures: Analysis and experimental validation". In: *Composite Structures* 255, p. 112926.

Vanaerschot, A. et al. (2013). "Stochastic framework for quantifying the geometrical variability of laminated textile composites using micro-computed tomography". In: *Composites Part A: Applied Science and Manufacturing* 44, pp. 122–131.

Vanaerschot, A. et al. (2017). "Stochastic characterisation methodology for 3-D textiles based on micro-tomography". In: *Composite Structures* 173, pp. 44–52.

Verpoest, I. and S. V. Lomov (2005). "Virtual textile composites software WiseTex: Integration with micro-mechanical, permeability and structural analysis". In: *Composites Science and Technology* 65.15, pp. 2563–2574.

Wang, B. et al. (2018). "Progressive damage analysis of 3D braided composites using FFT-based method". In: *Composite Structures* 192, pp. 255–263.

Wang, B. et al. (2020). "Efficient multiscale analysis method for the compressive progressive damage of 3D braided composites based on FFT". In: *Acta Mechanica* 231.12, pp. 5047–5061.

Wang, X. et al. (2021). "Modeling method of irregular cross section annular axis braided preform based on finite element simulation". In: *Journal of Engineered Fibers and Fabrics* 16, pp. 1–9.

Wehrkamp-Richter, T., N. V. De Carvalho, and S. T. Pinho (2018a). "A meso-scale simulation framework for predicting the mechanical response of triaxial braided composites". In: *Composites Part A: Applied Science and Manufacturing* 107, pp. 489–506.

– (2018b). "Predicting the non-linear mechanical response of triaxial braided composites". In: *Composites Part A: Applied Science and Manufacturing* 114, pp. 117–135.

Wehrkamp-Richter, T., R. Hinterhölzl, and S. T. Pinho (2017). "Damage and failure of triaxial braided composites under multi-axial stress states". In: *Composites Science and Technology* 150, pp. 32–44.

Wu, C. and A. Viquerat (2017). "Natural frequency optimization of braided bistable carbon/epoxy tubes: Analysis of braid angles and stacking sequences". In: *Composite Structures* 159, pp. 528–537.

Wu, L., L. Adam, and L. Noels (2018). "A micromechanics-based inverse study for stochastic order reduction of elastic UD fiber reinforced composites analyses". In: *International Journal for Numerical Methods in Engineering* 115.12, pp. 1430–1456.

Xu, K. and X. Qian (2016). "Analytical prediction of the elastic properties of 3D braided composites based on a new multiunit cell model with consideration of yarn distortion". In: *Mechanics of Materials* 92, pp. 139–154.

Xu, L., C. Z. Jin, and S. K. Ha (2015). "Ultimate strength prediction of braided textile composites using a multi-scale approach". In: *Journal of Composite Materials* 49.4, pp. 477–494.

Xu, R. et al. (2020). "Data-driven multiscale finite element method: From concurrence to separation". In: *Computer Methods in Applied Mechanics and Engineering* 363, p. 112893.

Yan, S. et al. (2020). "An efficient multiscale surrogate modelling framework for composite materials considering progressive damage based on artificial neural networks". In: *Composites Part B: Engineering* 194, p. 108014.

Yang, C. et al. (2020). "Prediction of composite microstructure stress-strain curves using convolutional neural networks". In: *Materials & Design* 189, p. 108509.

Ye, W. et al. (2019). "A mixed-form solution to the macroscopic elastic properties of 2D triaxially braided composites based on a concentric cylinder model and the rule of mixture". In: *Composites Part B: Engineering* 156, pp. 355–367.

Zeng, T., L.-Z. Wu, and L.-C. Guo (2004). "Mechanical analysis of 3D braided composites: a finite element model". In: *Composite Structures* 64.3, pp. 399–404.

Zhang, C., W. K. Binienda, and L. W. Kohlman (2014). "Analytical Model and Numerical Analysis of the Elastic Behavior of Triaxial Braided Composites". In: *Journal of Aerospace Engineering* 27.3, pp. 473–483.

Zhang, C., J. L. Curiel-Sosa, and T. Q. Bui (2018). "Meso-scale progressive damage modeling and life prediction of 3D braided composites under fatigue tension loading". In: *Composite Structures* 201, pp. 62–71.

Zhang, C. et al. (2015). "Progressive damage simulation of triaxially braided composite using a 3D meso-scale finite element model". In: *Composite Structures* 125, pp. 104–116.

Zhang, J., M. Shields, and S. TerMaath (2020). "Probabilistic modeling and prediction of out-of-plane unidirectional composite lamina properties". In: *Mechanics of Advanced Materials and Structures* 0.0, pp. 1–17.

Zhao, Z. et al. (2019). "Modeling the transverse tensile and compressive failure behavior of triaxially braided composites". In: *Composites Science and Technology* 172, pp. 96–107.

Zhou, K. et al. (2021). "Harnessing deep learning for physics-informed prediction of composite strength with microstructural uncertainties". In: *Computational Materials Science* 197, p. 110663.

Zhou, X.-Y. and P. D. Gosling (2018). "Influence of stochastic variations in manufacturing defects on the mechanical performance of textile composites". In: *Composite Structures* 194, pp. 226–239.

Zhou, X.-Y. et al. (2016). "Perturbation-based stochastic multi-scale computational homogenization method for woven textile composites". In: *International Journal of Solids and Structures* 80, pp. 368–380.

Zhu, H., D.-S. Li, and L. Jiang (2020). "Mesoscale progressive damage and strength analysis of three-dimensional braided composites under tension". In: *Engineering Fracture Mechanics* 237, p. 107221.

Zohdi, T. I. and P. Wriggers (2005). *An Introduction to Computational Micromechanics*. Lecture Notes in Applied and Computational Mechanics. Berlin Heidelberg: Springer-Verlag.